

Computational Study of Vibrational Qubits in Anharmonic Linear Ion Traps

Lei Wang
Marquette University

Recommended Citation

Wang, Lei, "Computational Study of Vibrational Qubits in Anharmonic Linear Ion Traps" (2012). *Dissertations (2009 -)*. Paper 199.
http://epublications.marquette.edu/dissertations_mu/199

COMPUTATIONAL STUDY OF VIBRATIONAL QUBITS IN
ANHARMONIC LINEAR ION TRAPS

by

Lei Wang, B.S., M.S.

A Dissertation submitted to the Faculty of the Graduate School,
Marquette University,
in Partial Fulfillment of the Requirements for
the Degree of Doctor of Philosophy

Milwaukee, Wisconsin

May, 2012

ABSTRACT

COMPUTATIONAL STUDY OF VIBRATIONAL QUBITS IN
ANHARMONIC LINEAR ION TRAPS

Lei Wang, B.S., M.S.

Marquette University, 2012

A string of cold ions confined in a linear trap represents a man-made quantum object with a broad range of applications in atomic and molecular spectroscopy, such as high-precision measurement of atomic properties. An efficient isolation from the environment guarantees excellent coherent properties of such systems and makes them suitable for practical realization of the quantum information processing. The pioneering theoretical [Cirac and Zoller] and experimental [Wineland and Monroe] work in 1990s resulted in the explosive expansion of this field during the last decade. In this dissertation an alternative new method for controlling the quantized motional/vibrational states of ions in a trap is explored theoretically. It is proposed to create small anharmonicity in the trapping potential which would modify the spectrum of states and allow addressing the state-to-state transitions selectively. In this approach all ions remain in the ground electronic state and their motion is controlled adiabatically and coherently by applying the optimally shaped electric fields (RF). The optimal control theory, accurate numerical calculation of the energies and wavefunctions, and numerical propagation of wave packets are employed. Two sources of vibrational anharmonicity are studied: the intrinsic Coulomb anharmonicity due to the ion-ion interactions and the external anharmonicity of the trapping potential. It is shown that the magnitude of Coulomb anharmonicity is insufficient for the control. In contrast, anharmonicity of the trapping potential allows controlling the motion of ions very accurately. It is demonstrated that one ion in a slightly anharmonic trap can be easily controlled and used to represent one qubit. A multi-qubit system can be created by employing a long progression of states of a single ion, or by trapping multiple ions and controlling several normal vibration modes of the ion string. Up to four qubits are modeled in this work and accurate pulses are optimized for a set of universal quantum gates: NOT, conditional NOT (CNOT) and Hadamard transformation. The control field for Shor's algorithm (quantum algorithm for factorization onto prime numbers) is also obtained. It is demonstrated that a careful choice of system properties allows achieving very high accuracy of qubit transformations, up to 0.999.

ACKNOWLEDGEMENTS

Lei Wang, B.S., M.S.

To begin with, I would like to convey my deepest appreciation to my research advisor, Dr. Dmitri Babikov, who initiated me into the area of “ion trap quantum computation”. His continuous help and inspiring guidance throughout all these years is a constant source of encouragement to me. It has been my great honor to be a member of his research group.

I would also like to thank Dr. Scott Reid and Dr. Qadir Timerghazin for the time they have taken to serve in my dissertation committee. Their moral support and patience have led to my successful completing of dissertation.

From the heart, I am grateful to my friends, research group members and all the people who have helped me during my project years.

At last, I would like to express my sincere gratitude to my parents. Their love and encouragement have made me grow.

Table of Contents

ACKNOWLEDGEMENTS	i
LIST OF TABLES	vi
LIST OF FIGURES	viii
Chapter 1: Introduction	1
1.1 Ion-trap quantum computation and the background	1
1.2 The linear Paul trap	3
1.3 The Los Alamos ion-trap quantum computing experiment	4
1.3.1 Doppler cooling of calcium ions.....	7
1.3.2 Sideband cooling of calcium.....	8
1.4 Motivation of the study	9
1.5 Summary of our project	11
Chapter 2: Theoretical methods with applications to adiabatic and optimal control of one ion in the trap	16
2.1 Trapping potential	16
2.2 Schrödinger equation and basis set expansion	18
2.3 Construction of the potential energy matrix and kinetic energy matrix	21
2.4 Matrix diagonalization and convergence studies	24
2.5 Analysis of results	27
2.6 The control scheme and the transition matrix	32
2.7 Optimal control theory (OCT)	37
2.8 Numerical propagation of vibrational wavepackets	43
2.9 Quantum bits (qubits), quantum gates and quantum computation	47
2.10 Examples of pulse optimization.....	51
a) Qubit flips	52
b) Gate NOT	55

C) Hadamard gate, phase control.....	57
2.11 Conclusions.....	59
Chapter 3: Feasibility of Encoding Shor's Algorithm into the Motional States of Ion in the Anharmonic Trap	61
3.1 The model system	61
3.2 The quantum algorithm.....	66
3.3 OCT pulse shaping.....	74
3.4 Results and discussion	76
3.5 Conclusions.....	86
Chapter 4: Study of the two-ion system.....	89
4.1 Two ions in the harmonic trapping potential	89
4.1.1 Harmonic trapping potential	89
4.1.2 Minimization Method	91
4.1.3 Normal vibration modes	95
4.1.4 Hamiltonian and transformation of coordinates	97
4.1.5 Harmonic Approximation	101
4.1.6 2D Basis set expansion	105
4.1.7 Convergence Studies.....	106
4.1.8 Results and analysis	109
4.1.9 Two-dimensional wavefunctions and transition matrix.....	113
4.2 Two ions in the anharmonic trapping potential	116
4.2.1 Anharmonic trapping potential	116
4.2.2 Analysis of the PES	123
4.3 Conclusions.....	127
Chapter 5: Three-ion system.....	128
5.1 Three ions in the harmonic trapping potential	128
5.1.1 Harmonic trapping potential	128

5.1.2 Minimization Method	131
5.1.3 Normal vibration modes	133
5.1.4 Hamiltonian and transformation of coordinates	135
5.1.5 Basis set expansion	139
5.1.6 Results and analysis	140
5.1.7 Three dimensional wavefunctions and transition matrix	144
5.1.8 Effect of Coulomb interaction	150
5.2 Three ions in the anharmonic trapping potential	152
5.2.1 Anharmonic trapping potential	152
5.2.2 Three-dimensional wavefunctions and transition matrix	159
5.2.3 Effect of Coulomb anharmonicity	163
5.3 Conclusions.....	165
Chapter 6: Three ions in the combined potential traps with applications to adiabatic and optimal control of three ions in the trap.....	167
6.1 Combined anharmonic potential	167
6.2 Inverted combined potential ($\alpha < 0, \beta > 0$).....	169
6.3 Three-dimensional wavefunctions and the transition matrix.....	176
6.4 Study of anharmonicity.....	180
6.5 Optimal control of three-ion system	182
a) One qubit control and the gate NOT.....	183
b) Two-qubit control and the Conditional NOT Gate (CNOT)	188
c) Phase control and the Hadamard Gate	194
6.6 Conclusions.....	200
Chapter 7: Future research directions	202
BIBLIOGRAPHY.....	205
Appendix A.....	212
Appendix B	219

Appendix C	234
Appendix D	237
Appendix E	240
Appendix F	242
Appendix G	245
Appendix H	257
Appendix I	260
Appendix J	263
Appendix K	272
Appendix L	284

LIST OF TABLES

Table 2. 1: Eigenvalues, assignments and deviations (from the harmonic model) of the vibrational states of $^{111}\text{Cd}^+$ ion in a slightly anharmonic trap.	31
Table 2. 2: Values of transition matrix (11×11) of $^{111}\text{Cd}^+$ ion in the harmonic trapping potential (values are in units of ea_0).	36
Table 2. 3: Values of transition matrix (11×11) of $^{111}\text{Cd}^+$ ion in the anharmonic trapping potential (values are in units of ea_0).	36
Table 3. 1: Eigenvalues, transition frequencies, qubit state assignments, optimized transformations and their characteristic probabilities for sixteen lower vibrational states in a model of $^{111}\text{Cd}^+$ ion in a weakly anharmonic Paul trap.	63
Table 4. 1: Eigenvalues, assignments and deviations (from the harmonic model) of the vibrational states of two $^{111}\text{Cd}^+$ ions in a harmonic trap.	110
Table 4. 2: Eigenvalues, assignments and deviations (from the harmonic model) of the vibrational states of two $^{111}\text{Cd}^+$ ions in $\sim z^4$ potential trap.	120
Table 5. 1: Eigenvalues, assignments and deviations (from the harmonic model) of the vibrational states of three $^{111}\text{Cd}^+$ ions in a harmonic trap.	141
Table 5. 2: Coefficients of the fit by the Dunham expansion formula, Eq. (5.1.6.3), of the numerically calculated spectrum in Table 5.1 (vibrational states in the harmonic trap). The shift parameter was $D/2\pi = -1.757 \times 10^{-5}$ MHz.	143
Table 5. 3: Eigenvalues, assignments and deviations (from the harmonic model) of the vibrational states of three $^{111}\text{Cd}^+$ ions in a strongly anharmonic trap.	156
Table 5. 4: Coefficients of the fit by the Dunham expansion formula, Eq. (5.1.6.3), of the numerically calculated spectrum in Table 5.3 (vibrational states in the strongly anharmonic trap). The shift parameter was $D/2\pi = -5.269 \times 10^{-4}$ MHz.	159

Table 6. 1: Eigenvalues, assignments and deviations (from the harmonic model) of the vibrational states of three $^{111}\text{Cd}^+$ ions in a combined inverted trap with $\alpha = -100$ and $\beta = 1$. See text for details.	174
Table 6. 2: Coefficients of the fit by the Dunham expansion formula, Eq. (5.1.6.3), of the numerically calculated spectrum in Table 6.1 (vibrational states in the combined inverted trap). The shift parameter was $D/2\pi = -2.115 \times 10^{-2}$ MHz.	175
Table 6. 3: Coefficients of the fit by the Dunham expansion formula, Eq. (5.1.6.3), of the numerically calculated spectrum (vibrational states in the strongly anharmonic combined inverted trap). The shift parameter was $D/2\pi = -0.331$ MHz.	182

LIST OF FIGURES

Fig. 1. 1: Seven ions in a linear Paul trap interacting with a laser beam (from Ref. [61]).	2
Fig. 1. 2: Schematic of four conducting electrodes of a linear paul trap (from Ref. [62]).	3
Fig. 1. 3: The trap built at Los Alamos for quantum computation (from Ref. [3]).	5
Fig. 1. 4: Stepping to lower vibrational states by sideband cooling (from Ref. [3]).	8
Fig. 2. 1: One $^{111}\text{Cd}^+$ ion in the harmonic and anharmonic potential traps. Solid line: harmonic case; dotted line: anharmonic case.....	16
Fig. 2. 2: Spectrum of energies of $^{111}\text{Cd}^+$ ion in the anharmonic potential trap calculated numerically using basis sets of different sizes $N = 10, 20, 30, 40, 50$. In all calculations $z_{\max} = 650$ Bohr and $\Delta z = 10$ Bohr ($\mathcal{N} = 131$) are used. Arrows indicate inaccurate results.....	26
Fig. 2. 3: Spectrum of the lower eleven states for $^{111}\text{Cd}^+$ ion in the harmonic and anharmonic traps.....	28
Fig. 2. 4: Energy difference between the anharmonic spectrum and the harmonic spectrum of $^{111}\text{Cd}^+$ ion (from Table 2.1).	29
Fig. 2. 5: Green line is the anharmonic trapping potential $V_a(z) = \frac{1}{2}kz^2 + \frac{1}{4!}k'z^4$, red line is the harmonic part of this potential and blue line is the anharmonic part. Black solid line describes the wavefunctions and energy levels of $^{111}\text{Cd}^+$ ion in the harmonic trapping potential and the dotted line is that of anharmonic case.	31
Fig. 2. 6: Transition matrix of $^{111}\text{Cd}^+$ ion in the harmonic trapping potential.	34
Fig. 2. 7: Transition matrix of $^{111}\text{Cd}^+$ ion in the anharmonic trapping potential.....	35

Fig. 2. 8: Pulse optimization for the qubit flip: $ 0\rangle \rightarrow 1\rangle$ in the $^{111}\text{Cd}^+$ ion trap. (a) The guess field. (b) – (k) The optimized pulse and evolution of state populations after 1, 11, 101, 1001 and 2001 iteration steps.	53
Fig. 2. 9: (a) The control pulse for qubit flip $ 0\rangle \rightarrow 1\rangle$ in the $^{111}\text{Cd}^+$ ion trap. (b) Switching of state populations during the transition $ 0\rangle \rightarrow 1\rangle$. (c) Convergence of the iterative procedure and the final transition probability.....	54
Fig. 2. 10: The gate NOT in the $^{111}\text{Cd}^+$ ion trap optimized with two transitions. (a) Optimally shaped electric field. (b) Average probability of the gate. (c) Switching of population between the qubit states during the NOT $ 0\rangle \rightarrow 1\rangle$. (d) Switching of population between the qubit states during the NOT $ 1\rangle \rightarrow 0\rangle$	56
Fig. 2. 11: (a) Optimally shaped pulse for the gate Hadamard in the $^{111}\text{Cd}^+$ ion trap. (b) The convergence of iterations and final fidelity of the qubit transformation.	57
Fig. 2. 12: The gate Hadamard in the $^{111}\text{Cd}^+$ ion trap. (a) Creation of linear superposition of the qubit states as required by HAD $ 0\rangle \rightarrow 1/\sqrt{2}(0\rangle + 1\rangle)$. (b) The same during the HAD $ 1\rangle \rightarrow 1/\sqrt{2}(0\rangle - 1\rangle)$ transformation. (c) The same during the HAD $1/\sqrt{2}(0\rangle + 1\rangle) \rightarrow 0\rangle$ transformation. (d) The same during the HAD $1/\sqrt{2}(0\rangle - 1\rangle) \rightarrow 1\rangle$ transformation.	59
Fig. 3. 1: Weakly anharmonic trapping potential in the model system. Energies of thirty-two quantized motional states of one trapped $^{111}\text{Cd}^+$ ion are indicated by horizontal lines. Effect of anharmonicity is clearly seen. Sixteen lower states (used to encode qubits) are indicated by solid lines. Upper states (included for completeness) are shown by dashed lines. Assignment of states of the four-qubit system is indicated in brackets.	62

Fig. 3. 2: Transition moment matrix for sixteen lower vibrational states in a model system of $^{111}\text{Cd}^+$ ion in a weakly anharmonic Paul trap. Color indicates magnitudes of matrix elements in the logarithmic scale (dark red corresponds $\mu_{14,15} = 1.08 \times 10^2 \text{ } ea_0$ ($\sim 2.75 \times 10^2 \text{ D}$) and light blue corresponds $\mu_{0,5} = 4.98 \times 10^{-4} \text{ } ea_0$ ($\sim 1.27 \times 10^{-3} \text{ D}$). See text for further details).	65
Fig. 3. 3: Quantum circuit diagram for the phase estimation part of Shor's algorithm for factorizing number 15 using four qubits (read from left to right). See text for details....	67
Fig. 3. 4: (a) Optimally shaped 50 μs pulse for Shor's algorithm in the $^{111}\text{Cd}^+$ ion trap. (b) Windowed Fourier transform of the pulse. Horizontal dashed lines indicate frequencies of the state-to-state transitions. Dotted curves encircle two spectral features that correspond to the ladder climbing. See text for details.	76
Fig. 3. 5: Time evolution of state populations induced by the pulse optimized for Shor's algorithm in three representative cases: (a) Transformation #1 in Table 3.1. (b) Transformation #3 in Table 3.1. (c) Transformation #11 in Table 3.1. Thicker color lines indicate population of the initial and final states. Thinner black lines indicate population of intermediate states.	78
Fig. 3. 6: Fourier spectrum of the pulse optimized for Shor's algorithm in the $^{111}\text{Cd}^+$ ion trap: (a) broad range of frequencies (up to $\omega_{n,n+9}$). (b) focus on the frequency range of the main spectral structure ($\omega_{n,n+1}$ transitions). (c) focus on the frequency range of the overtone spectral structure ($\omega_{n,n+3}$ transitions). Arrows indicate frequencies of the state-to-state transitions from Table 3.1.	82
Fig. 4. 1: Two $^{111}\text{Cd}^+$ ions in the harmonic potential trap: (a) Equilibrium positions of ions and minimum energy of the two-ion string. (b) Vibrational spectrum of this system and possible encoding of states of the two-qubit system.....	90
Fig. 4. 2: Potential energy surface of two $^{111}\text{Cd}^+$ ions in the harmonic potential trap using Cartisian coordinates. Anharmonicities due to Coulomb repulsion of ions are clearly seen.	91
Fig. 4. 3: Minimization from four different arbitrary initial positions.....	93

Fig. 4. 4: Change of potential energy of the system during minimization from four different guess positions.	94
Fig. 4. 5: Potential energy surface of two $^{111}\text{Cd}^+$ ions in the harmonic potential trap using normal mode coordinates.	104
Fig. 4. 6: Convergence study with different integration limits ($\zeta_{\max} = 1000, 500, 400$ Bohr). $\Delta\zeta = 6.25$ Bohr and $N = 20$	107
Fig. 4. 7: Convergence study with different integration steps ($\Delta\zeta = 6.25, 10, 20$ Bohr). $\zeta_{\max} = 500$ Bohr and $N = 20$	108
Fig. 4. 8: Convergence study with different number of basis functions $N = 10, 15, 20, 25$. $\Delta\zeta = 10$ Bohr and $\zeta_{\max} = 500$ Bohr.	109
Fig. 4. 9: Effect of anharmonicity for two modes of the vibrational spectrum of two $^{111}\text{Cd}^+$ ions in a harmonic ($\sim z^2$) potential trap.	111
Fig. 4. 10: Description of the ion motions for two vibrational motion modes.	112
Fig. 4. 11: Wavefunctions of two $^{111}\text{Cd}^+$ ions in the harmonic potential trap.	114
Fig. 4. 12: Transition matrix for two $^{111}\text{Cd}^+$ ions in the harmonic potential trap. (black corresponds $\mu_{5,6} = 1.06 \times 10^2$ ea_0 ($\sim 2.69 \times 10^2$ D) and orange corresponds $\mu_{0,1} = 43.22$ ea_0 ($\sim 1.10 \times 10^2$ D) between states of mode 1).	115
Fig. 4. 13: Two $^{111}\text{Cd}^+$ ions in the $\sim z^4$ potential trap: (a) Equilibrium positions of ions and minimum energy of the two-ion string. (b) Vibrational spectrum of this system and the encoding of two-qubit states.	117
Fig. 4. 14: PES of two $^{111}\text{Cd}^+$ ions in the anharmonic potential trap using Cartesian coordinates. Anharmonicities due to Coulomb repulsion of ions are clearly seen.	118

Fig. 4. 15: PES of two $^{111}\text{Cd}^+$ ions in the anharmonic potential trap using normal mode coordinates.....	119
Fig. 4. 16: Effect of anharmonicity for two modes of the vibrational spectrum of two $^{111}\text{Cd}^+$ ions in an anharmonic ($\sim z^4$) potential trap.	121
Fig. 4. 17: Components of the potential according to different orders of ζ_2	126
Fig. 5. 1: Three $^{111}\text{Cd}^+$ ions in the harmonic potential trap: (a) Equilibrium positions of ions and minimum energy of the three-ion string; (b) Vibrational spectrum of this system and the encoding of two-qubit states proposed in this work.....	129
Fig. 5. 2: PES of three $^{111}\text{Cd}^+$ ions in the harmonic potential trap using Cartesian coordinates. Three slices through the 3D-surface are shown: (a) perpendicular to z_1 through $z_1 = 0$, (b) perpendicular to z_2 through $z_2 = 0$ and (c) perpendicular to z_3 through $z_3 = 0$	130
Fig. 5. 3: Potential energy difference between two consequent steps of the system during the minimization.	131
Fig. 5. 4: Absolute values of position difference between two consequent steps during the minimization.	132
Fig. 5. 5: PES of three $^{111}\text{Cd}^+$ ions in the harmonic potential trap using the normal mode coordinates. Three slices through the 3D-surface are shown: (a) perpendicular to ζ_1 through $\zeta_1 = 0$, (b) perpendicular to ζ_2 through $\zeta_2 = 0$ and (c) perpendicular to ζ_3 through $\zeta_3 = 0$. Note that the Coulomb repulsion part (white) goes parallel to ζ_1 everywhere.....	139
Fig. 5. 6: Effect of anharmonicity on three modes of the vibrational spectrum of three $^{111}\text{Cd}^+$ ions in a harmonic ($\sim z^2$) potential trap.	142
Fig. 5. 7: Wavefunctions of the lower 40 states of three $^{111}\text{Cd}^+$ ions in the harmonic trapping potential.	145

Fig. 5. 8: Description of the motions of ions for three vibrational modes in the harmonic trapping potential. Length of the arrows indicates the vibrational motion amplitude of each ion.	148
Fig. 5. 9: Transition matrix of three $^{111}\text{Cd}^+$ ions in the harmonic potential trap and the diagram of allowed state-to-state transitions in this system. (black corresponds $\mu_{4,5} = 1.18 \times 10^2 \text{ } ea_0$ ($\sim 3.00 \times 10^2 \text{ D}$) and pink corresponds $\mu_{0,1} = 52.94 \text{ } ea_0$ ($\sim 1.35 \times 10^2 \text{ D}$) between states of mode 1).....	149
Fig. 5. 10: Relations between the equilibrium distances, normal mode frequencies and vibrational anharmonicities for three $^{111}\text{Cd}^+$ ions in the harmonic potential trap.	151
Fig. 5. 11: Three $^{111}\text{Cd}^+$ ions in the $\sim z^4$ potential trap: (a) Equilibrium positions of ions and minimum energy of the three-ion string. (b) Vibrational spectrum of this system and the encoding of two-qubit states proposed in this work.	153
Fig. 5. 12: PES of three $^{111}\text{Cd}^+$ ions in the strongly anharmonic potential trap ($\sim z^4$) using the normal mode coordinates. Three slices through the 3D-surface are shown: (a) perpendicular to ζ_1 through $\zeta_1 = 0$, (b) perpendicular to ζ_2 through $\zeta_2 = 0$ and (c) perpendicular to ζ_3 through $\zeta_3 = 0$	154
Fig. 5. 13: Effect of anharmonicity on three modes of the vibrational spectrum of three $^{111}\text{Cd}^+$ ions in a strongly anharmonic ($\sim z^4$) potential trap.	157
Fig. 5. 14: Wavefunctions of the lower 40 states of three $^{111}\text{Cd}^+$ ions in the $\sim z^4$ trapping potential.....	160
Fig. 5. 15: Description of the motions of ions for three vibrational motion modes in the $\sim z^4$ trapping potential. Length of the arrows indicates the vibrational motion amplitude of each ion.....	161
Fig. 5. 16: Transition matrix of three $^{111}\text{Cd}^+$ ions in the $\sim z^4$ potential trap and the diagram of allowed state-to-state transitions in this system. (black corresponds	

$\mu_{4,5} = 33.57 \text{ } ea_0$ ($\sim 85.33 \text{ D}$) between states of mode 1 and light yellow corresponds $\mu_{0,1} = 3.50 \text{ } ea_0$ ($\sim 8.90 \text{ D}$) between states of mode 3).....	162
Fig. 5. 17: Relations between the equilibrium distances, normal mode frequencies and vibrational anharmonicities for three $^{111}\text{Cd}^+$ ions in the strongly ($\sim z^4$) anharmonic potential trap.	164
Fig. 6. 1: Relations between the equilibrium distances, normal mode frequencies and vibrational anharmonicities for three $^{111}\text{Cd}^+$ ions in the anharmonic combined potential trap ($\alpha \frac{1}{2} kz^2 + \beta \frac{1}{4!} k' z^4, \alpha > 0, \beta > 0$).	168
Fig. 6. 2: (a) Equilibrium positions of $^{111}\text{Cd}^+$ ions and minimum energy of a three-ion string trapped in a flat anharmonic potential of the form $\alpha \frac{1}{2} kz^2 + \beta \frac{1}{4!} k' z^4$. (b) Vibrational spectrum of this system and the encoding of two-qubit states proposed in this work.	170
Fig. 6. 3: PES of three $^{111}\text{Cd}^+$ ions in the inverted combined potential trap using the normal mode coordinates. Three slices through the 3D-surface are shown: (a) perpendicular to ζ_1 through $\zeta_1 = 0$, (b) perpendicular to ζ_2 through $\zeta_2 = 0$ and (c) perpendicular to ζ_3 through $\zeta_3 = 0$	172
Fig. 6. 4: Effect of anharmonicity on three modes of the vibrational spectrum of three $^{111}\text{Cd}^+$ ions in an inverted combined potential trap (with $\alpha = -100$ and $\beta = 1$).	175
Fig. 6. 5: Wavefunctions of 40 states with excitation to the first and the third modes of three $^{111}\text{Cd}^+$ ions in the inverted combined trapping potential.....	177
Fig. 6. 6: Description of the motions of ions for three vibrational motion modes in inverted combined trapping potential with $\alpha = -100$ and $\beta = 1$. Length of the arrows indicates the vibrational motion amplitude of each ion.	178
Fig. 6. 7: Transition matrix of three $^{111}\text{Cd}^+$ ions in inverted combined potential trap with $\alpha = -100$ and $\beta = 1$ and the diagram of allowed state-to-state transitions in this system.	

Color indicates magnitudes of matrix elements in the logarithmic scale (dark purple corresponds $\mu_{4,5} = 82.77 \text{ } ea_0$ ($\sim 2.10 \times 10^2 \text{ D}$) between states of mode 1 and light pink corresponds $\mu_{0,1} = 7.90 \text{ } ea_0$ ($\sim 20.08 \text{ D}$) between states of mode 3).	179
Fig. 6. 8: Relations between the equilibrium distances, normal mode frequencies and vibrational anharmonicities for three $^{111}\text{Cd}^+$ ions in the inverted combined potential trap.	180
Fig. 6. 9: Optimally shaped electric field of the gate NOT in the $^{111}\text{Cd}^+$ ion trap with inverted combined potential optimized with four transitions. ($\alpha_0 = 2.0 \times 10^{12}$)	184
Fig. 6. 10: The gate NOT on second qubit in the $^{111}\text{Cd}^+$ ion trap with inverted combined potential. (a) Switching of population between the qubit states during the $\text{NOT} 00\rangle \rightarrow 01\rangle$. (b) Switching of population between the qubit states during the $\text{NOT} 10\rangle \rightarrow 11\rangle$. (c) The same during $\text{NOT} 01\rangle \rightarrow 00\rangle$ transformation. (d) The same during $\text{NOT} 11\rangle \rightarrow 10\rangle$ transformation.	185
Fig. 6. 11: Fourier analysis of the pulse in Fig 6.9 for the gate NOT.	187
Fig. 6. 12: Optimally shaped electric field of the gate CNOT for the two-qubit system in the $^{111}\text{Cd}^+$ ion trap with inverted combined potential. Large penalty factor $\alpha_0 = 6.0 \times 10^{12}$	188
Fig. 6. 13: The gate CNOT for the two-qubit control in the $^{111}\text{Cd}^+$ ion trap optimized with four transitions. Large penalty factor $\alpha_0 = 6.0 \times 10^{12}$. (a) Switching of population between the qubit states during the $\text{CNOT} 00\rangle \rightarrow 00\rangle$. (b) Switching of population between the qubit states during the $\text{CNOT} 10\rangle \rightarrow 11\rangle$. (c) The same during $\text{CNOT} 01\rangle \rightarrow 01\rangle$ transformation. (d) The same during $\text{CNOT} 11\rangle \rightarrow 10\rangle$ transformation.	189

Fig. 6. 14: Fourier analysis of the pulse in Fig 6.12 for the gate CNOT.	190
Fig. 6. 15: Optimally shaped electric field of the gate CNOT for the two-qubit control in the $^{111}\text{Cd}^+$ ion trap with inverted combined potential. Small penalty factor $\alpha_0 = 8.0 \times 10^{11}$	191
Fig. 6. 16: The gate CNOT for the two-qubit control in the $^{111}\text{Cd}^+$ ion trap optimized with four transitions. Small penalty factor $\alpha_0 = 8.0 \times 10^{11}$. (a) Switching of population between the qubit states during the $\text{CNOT} 00\rangle \rightarrow 00\rangle$. (b) Switching of population between the qubit states during the $\text{CNOT} 10\rangle \rightarrow 11\rangle$. (c) The same during $\text{CNOT} 01\rangle \rightarrow 01\rangle$ transformation. (d) The same during $\text{CNOT} 11\rangle \rightarrow 10\rangle$ transformation.	192
Fig. 6. 17: Fourier analysis of the pulse in Fig 6.15 for the gate CNOT.	193
Fig. 6. 18: Optimally shaped electric field of the gate Hadamard on the second qubit in the $^{111}\text{Cd}^+$ ion trap with inverted combined potential optimized with five transitions. ($\alpha_0 = 1.0 \times 10^{12}$)	195
Fig. 6. 19: The gate Hadamard on the second qubit in the $^{111}\text{Cd}^+$ ion trap optimized with five transitions. (a) Switching of population between the qubit states during the $\text{HAD} 00\rangle \rightarrow \frac{1}{\sqrt{2}}(00\rangle + 01\rangle)e^{i\varphi_1}$. (b) Switching of population between the qubit states during the $\text{HAD} 01\rangle \rightarrow \frac{1}{\sqrt{2}}(00\rangle - 01\rangle)e^{i\varphi_2}$. (c) The same during $\text{HAD} 10\rangle \rightarrow \frac{1}{\sqrt{2}}(10\rangle + 11\rangle)e^{i\varphi_3}$ transformation. (d) The same during $\text{HAD} 11\rangle \rightarrow \frac{1}{\sqrt{2}}(10\rangle - 11\rangle)e^{i\varphi_4}$ transformation.	196
Fig. 6. 20: The gate Hadamard on the second qubit in the $^{111}\text{Cd}^+$ ion trap. Frames (e) and (f): Switching of population of states $ 00\rangle$ and $ 01\rangle$ during the	

$\text{HAD} \frac{1}{2}(00\rangle + 01\rangle + 10\rangle + 11\rangle) \rightarrow \frac{1}{\sqrt{2}}(00\rangle + 10\rangle) e^{i\varphi_5}$	(g) Average transition probability.
(h) Gate fidelity as functions of number of iterations.....	197
Fig. 6. 21: Fourier analysis of the pulse in Fig 6.18 for the gate Hadamard (lower frequency part).....	198
Fig. 6. 22: Fourier analysis of the pulse in Fig 6.18 for the gate Hadamard (higher frequency part).....	199
Fig. 7. 1: A four-ion string trapped in a flat anharmonic potential of the form	
$\alpha \frac{1}{2} kz^2 + \beta \frac{1}{4!} k' z^4$	203

Chapter 1: Introduction

“...It seems that the laws of physics present no barrier to reducing the size of computers until bits are the size of atoms, and quantum behavior holds dominant sway.”

—R. P. Feynman, 1985

1.1 Ion-trap quantum computation and the background

In a classical computer, the unit of memory is bit, where each bit represents either a one or a zero. In contrast, in a quantum computer, which requires a very special physical environment, a sequence of quantum bits (qubits) is needed [1-3]. For quantum computation, a single qubit can represent a one, a zero, or, crucially, any quantum superposition of these: $|\Psi\rangle = \alpha|0\rangle + \beta|1\rangle$, where α and β are coefficients such that $\alpha^2 + \beta^2 = 1$. That means: a n bits classical computer can only be in one of these 2^n states at one time; while a n qubits quantum computer can be in an arbitrary superposition up to 2^n different states simultaneously, leading to the exponential increase of computer power. Further, because of the interaction between the quantum state and the environment, a quantum operation must be performed on the qubits before those states decohere. On the one hand, to limit decoherence, interaction between the qubits and the environment should be negligible. On the other hand, to

manipulate the quantum state, implement quantum algorithms and read out the result of a calculation, qubits must be easily accessible from the outside and must interact strongly with each other.

The original proposal of Cirac and Zoller [4] advanced a possible solution to this dilemma, where a linear radio frequency quadrupole (RFQ) ion trap, or a linear Paul Trap using time-varying electric fields to trap ions was employed to hold a line of ions in place, see Fig. 1.1. A string of atomic ions trapped and cooled in a linear Paul trap represents a man-made quantum system well isolated from the environment. In this method, the ions serve as the physical qubits of the quantum computer. States of qubits are encoded into electronic states of the ions, and quantum gates are

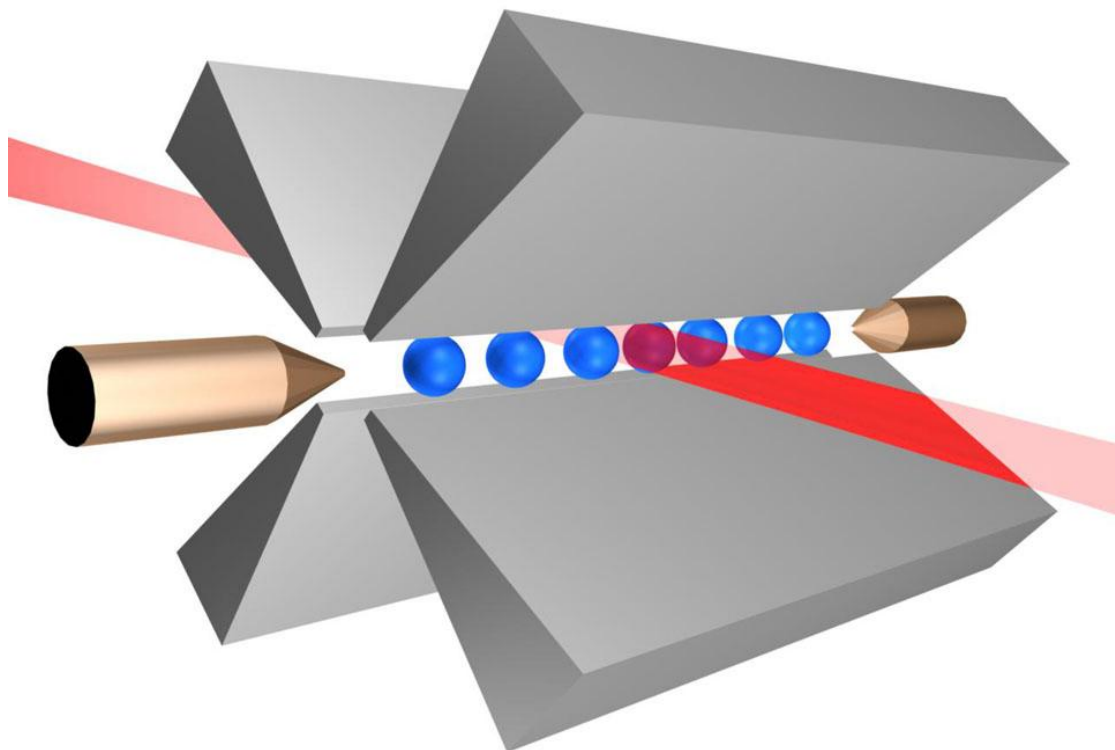


Fig. 1. 1: Seven ions in a linear Paul trap interacting with a laser beam (from Ref. [61]).

achieved by excitation of ions with sharply focused laser beams [5-16]. The interaction between the individual ions is mediated by the Coulomb force between the charged particles, while the motional mode of ions in the trapping potential is used to create entanglement. Favorable properties of this system, such as long coherence time and possibility of fast and reliable manipulations with its quantum states, make it suitable for practical realization of quantum computation. Realization of this proposal in the experiment [17] led to many fascinating developments and explosive growth of the field [18-60].

1.2 The linear Paul trap

Imagine a positively charged ion floating in free space and surrounded by

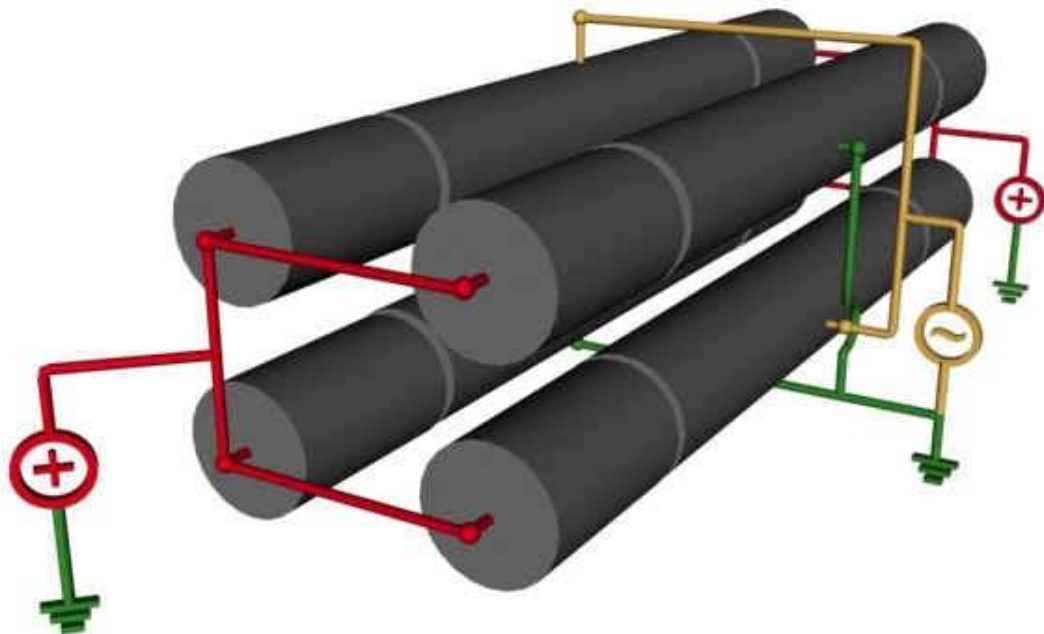


Fig. 1. 2: Schematic of four conducting electrodes of a linear paul trap (from Ref. [62]).

four infinitely long conducting rods [3]. Two opposing rods can be connected to one pole of a RF voltage source, whereas the remaining two to the other pole, see Fig. 1.2.

Then one pair of opposing rods is charged positively and the other pair negatively.

The positively charged conductors will give a repulsive force to the positive ion and

push it toward the center of the trap. At the same time, the negatively charged

conductors produce an attractive force to the ion and pull it outwards. If the polarity

of the four electrodes is reversed, the ion motion will begin to reverse. Because the

heavy ion which has too much inertia cannot respond to this fast change of electric

field quickly, it becomes stuck in a rapid back-and-forth motion. Since the minimum

of electric fields locates at the trap axis, the ion is pushed toward the center by an

effective force, where it becomes trapped. In Fig 1.1, we show a schematic of linear

Paul trap which is from the website of the research group of R. Blatt in the

University of Innsbruck [61]. In Fig. 1.2, we show a connection of electrodes of a

linear Paul trap [62]. The axis of symmetry between the rods is the trap axis [3].

If a positive direct-current (DC) component to the RF voltage is introduced, the mass selectivity in the Paul trap can be generated. Positive ions outside a certain mass range feel less of a restoring force from the pseudo potential and are kicked out of the trap by the repulsive DC field.

1.3 The Los Alamos ion-trap quantum computing experiment

An experiment developed at Los Alamos uses calcium ions to implement the ion-trap quantum computation [3]. Theoretically, many different ion species can be used as qubits and numerous qubit schemes are possible, if the qubits satisfy the following condition: a) the trapped ions have two long-lived internal states (electronic states); b) the trap's vibrational modes can serve as the qubits communicating with each other. Using relatively inexpensive diode lasers it is possible to produce the entire range of wavelengths needed for cooling and manipulation of the calcium ions; In addition, a reasonable number of coherent operations can be performed during the lifetime of the metastable state and the calcium isotope of interest which is most abundant can easily be loaded into the trap.

Any element that displays an ionic-level structure similar to that of calcium can be used in the basic quantum computational schemes. Recently strontium was

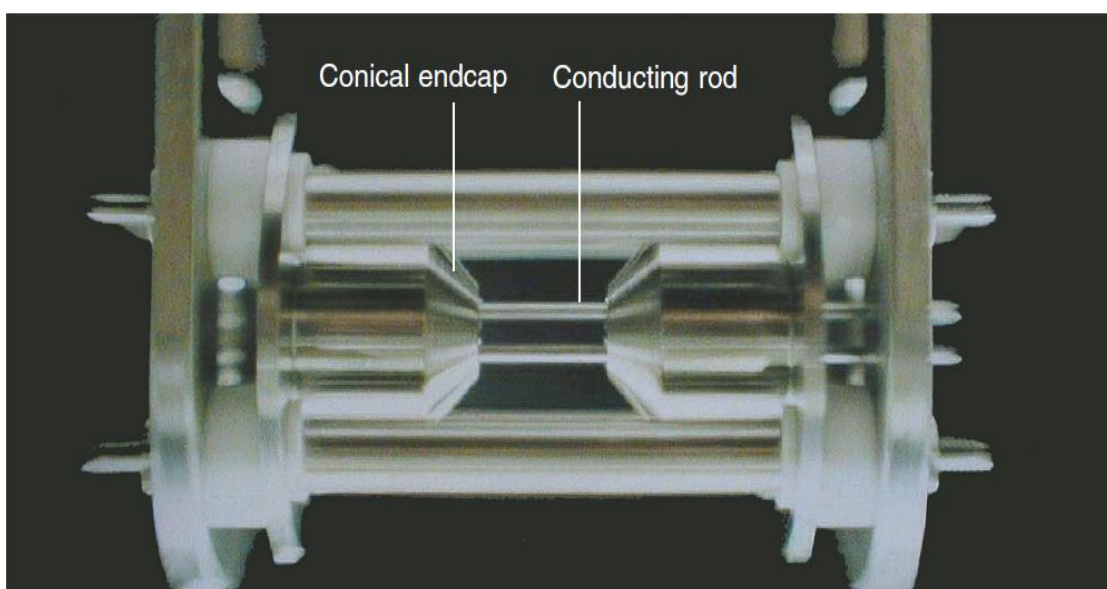


Fig. 1. 3: The trap built at Los Alamos for quantum computation (from Ref. [3]).

employed in the quantum computing experiment for mostly technical reasons.

Moreover, with slightly different technical approaches, ions like mercury and

ytterbium are also applicable to quantum computation because of proper level

schemes [3].

A schematic diagram of the internal-level structure of calcium ions is as

follows: The $4^2S_{1/2}$ ground state and the metastable $3^2D_{5/2}$ excited state are used to

form the logical qubit states $|0\rangle$ and $|1\rangle$, respectively. Because the decoherence is

spontaneous emission from the excited state, a large number of computational steps

should be performed before decoherence can destroy the internal state of the quantum

register. The lifetime of metastable excited state is about 1 second and that is long

enough.

Authors including Cirac and Zoller (1995) present the initial state of the

computer as follows [4]: all qubits are in their electronic and vibrational ground states.

For example, in a four-qubit system this corresponds to

$$|0000\rangle. \quad (1.3.1)$$

However, because of the energy from a combination of the temperature of the

calcium oven and that imparted to the ion by the electric field, the temperature of the

newly trapped ions is very high. In order to initialize state of quantum system and

perform quantum logic operations, the temperature must be reduced to its lowest

possible value. Two steps of cooling the ions are described in the next two sections.

1.3.1 Doppler cooling of calcium ions

In Doppler cooling, a laser which has a frequency below the resonance frequency of a transition in the ion is used. Only when the ion is moving at a certain velocity toward the laser it can absorb these “off-resonance” photons, because only then does it “see” the laser frequency shift into resonance. However, due to its random jiggling, the ion has a probability to emit photons at any frequency within its Doppler broadened emission line profile. The ion has a greater probability to emit a photon with a higher frequency than the absorbed photon. On average, more energy is emitted than absorbed, which leads to a cooling of the ion [3].

In the momentum space, after emitting a photon in one direction, the ion will recoil in the opposite direction with a momentum which is equal to the photon momentum. The heating effect of this recoil energy eventually counteracts any cooling process, which means Doppler cooling has its limits. For calcium ions, the temperature of the Doppler limit is about 3 microkelvins. Because the kinetic energy of the ions is significantly less than the mutual Coulomb repulsion, they do not have enough kinetic energy to leap-frog each other. Eventually, the cold ions remain frozen in their relative locations and form a string, see Fig. 1.1. However, even at this low temperature of 3 microkelvins, the ions have enough energy to occupy any of several

vibrational modes, with many phonons per mode. After Doppler cooling, the ions in the trap can typically occupy the common mode states from $|n = 10\rangle$ to about $|n = 30\rangle$. So, it requires an additional cooling scheme to get the qubits into the common-mode ground state ($|n = 0\rangle$).

1.3.2 Sideband cooling of calcium

Because of the limit of Doppler cooling, experimentalists cannot get to the quantum ground state of the motion. The sideband cooling is employed to cool the system beyond Doppler cooling. The internal degrees of freedom of ions in the trap can couple with their external motion which leads to sidebands at $\omega_0 \pm \omega_1$, where ω_0 is the internal ionic transition frequency and ω_1 is the common-mode motional/vibrational frequency. Thus, an ion can absorb photons not only at the carrier frequency ω_0 of their internal $|g\rangle \rightarrow |e\rangle$ transition but also on the upper and

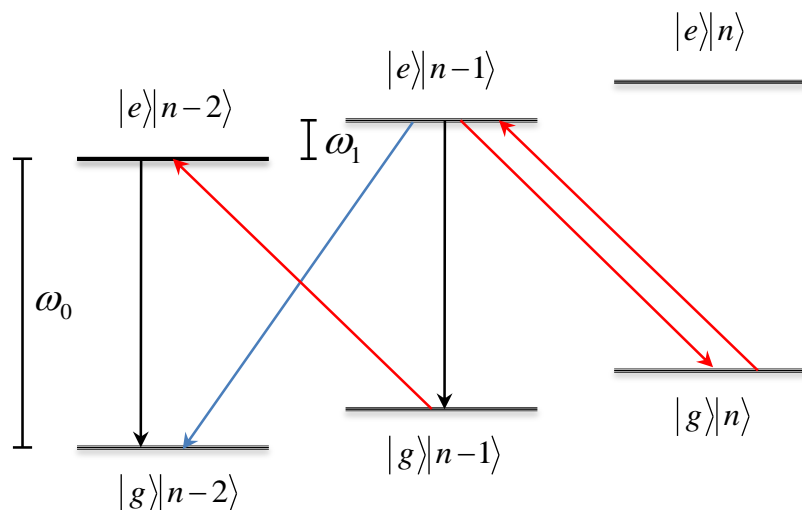


Fig. 1. 4: Stepping to lower vibrational states by sideband cooling (from Ref. [3]).

lower sidebands at the frequencies $\omega_0 \pm \omega_1$. Assuming all ions are in the state $|g\rangle|n\rangle$, it is possible to tune a laser with a suitably narrow linewidth to the red sideband — photon energy $E_- = \hbar(\omega_0 - \omega_1)$ and excite one of the ions to the state $|e\rangle|n-1\rangle$, see Fig. 1.4. In essence, energy is removed from the vibrational mode (the occupation number is reduced by one phonon) and is used to make up the deficit in photon energy. After its radiative lifetime, the ion can decay to one of three states: the state $|g\rangle|n-2\rangle$, by emitting a photon with energy $E_+ = \hbar(\omega_0 + \omega_1)$; the state $|g\rangle|n-1\rangle$, by emitting a photon with energy $E_0 = \hbar\omega_0$; or a return to its initial state, by emitting a photon with energy $E_- = \hbar(\omega_0 - \omega_1)$. On average, the ion loses one vibrational photon of energy $E = \hbar\omega_1$ for each excitation–decay cycle. Because usually it is started somewhere around $|n = 30\rangle$, it requires about 30 cycles to bring the vibrational mode to its ground state [3].

1.4 Motivation of the study

While the architecture of Cirac and Zoller rely mostly on the electronic states of *individual* ions, the quantized states of *collective* vibrational motion of ions along the trap axis are also employed. These states represent quantized eigenstates and form the normal-mode progressions (somewhat similar to the vibrational states of naturally occurring molecules). In a standard setup the trapping potential is harmonic (quadratic) and the vibrational states are all equidistant, like the states of multi-

dimensional harmonic oscillator. Frequencies of transitions between these states are usually in the few MHz region, but selective excitation/control of these states using the microwave fields is impossible, because all state-to-state transitions of the “ladder” have the same frequency and occur simultaneously. In a standard set up of Cirac and Zoller, the control is achieved by pumping the population of one vibrational state to the excited electronic state and dumping it onto another vibrational state (of the ground electronic state), see Fig. 1.4.

Recently, a new alternative method for adiabatic coherent control of the quantized motional states of ions in a Paul trap was suggested by Zhao and Babikov [63]. They proposed to modify the harmonic trapping potential along the axial direction of the Paul trap in order to introduce small anharmonicity into the spectrum of collective motional/vibrational states of ions. When the spectrum of motional states is slightly anharmonic, different state-to-state transitions occur at slightly different frequencies and in principle can be controlled selectively by applying electric fields of appropriate amplitude, duration, phase and frequency (in the MHz range). In such control scenario all ions remain in the ground electronic state and the dynamics is adiabatic. The phase of motion can also be controlled [63], which makes this scheme potentially useful for coherent manipulations with ions and for quantum computation. In the numerical simulations of Ref. [63] the qubit states were encoded into two

lowest motional states $|0\rangle$ and $|1\rangle$ of a single trapped ion. But this new control scheme is not restricted to only two quantum states. The progression of multiple motional states like $|0\rangle, |1\rangle, |2\rangle, |3\rangle, \dots$ can also be controlled and used for the quantum information processing. In such architecture the simple quantum algorithms could be executed using a single trapped ion. If several ions are trapped, the multi-qubit system can be created by encoding different qubits into different motional modes. For example, different qubits can be encoded into different normal vibration modes of the ion chain (*e.g.*, the center-of-mass motion mode and the asymmetric stretching mode) and addressed selectively using different frequencies. Addressing of individual ions is unnecessary. Opportunity of using the vibrational states of ion chains for encoding qubits and the time varying electric fields for applying quantum gates is very attractive and should be explored. Nowadays the techniques of ion trapping are improved quickly and multiple ion traps are placed on a single microchip [64-67]. Some control tasks can be performed using the electric fields instead of lasers, which could facilitate the ongoing miniaturization and the practical implementation of scalability in the future.

1.5 Summary of our project

In their first paper on this topic, Ref. [63], Zhao and Babikov considered only the simplest case – single ion in an anharmonic trap, and employed an approximate

analytic model in order to introduce anharmonicity into the spectrum of motional states. The state-to-state transition moment matrix was also described analytically and approximately. The optimal control theory (OCT) was employed to derive shaped pulses for several major quantum gates such as qubit flips, phase shifts, NOT and Hadamard transformation. They showed that the value of anharmonicity parameter on the order of 1% of the trap frequency is sufficient in order to obtain simply-shaped pulses optimized for accurate state-to-state transitions and for the quantum logics gates. Durations of predicted pulses were in the ten microsecond range; the field amplitudes were on the order of few mV/cm. It was suggested that the practical realization of this approach is within the reach of today's technology.

In this work we go well beyond the assumptions of Zhao and Babikov and employ accurate numerically converged methods to characterize the system and carry out modeling of the adiabatic coherent control. We also go beyond the one-ion case and explore the control of two and three ions in several different trap architectures.

In Chapter 2, we present a very detailed study of the one-ion system in the anharmonic ion trap. Spectra of the motional states are computed accurately and analysis of the anharmonicities is carried out. Then we use OCT method to derive shaped pulses for several universal quantum gates, the results are consistent with the study of Zhao and Babikov in Ref. [63].

We see two methods of expanding this approach to the ion trap quantum computation onto larger number of qubits. The first method of scaling, discussed in Chapter 3, is to use more than one excited vibrational state. Indeed, even if we use just one single ion in an anharmonic ion trap, we may be able to access and control multiple excited vibrational states: $|0\rangle, |1\rangle, |2\rangle, |3\rangle, \dots$. If the control of state-to-state transitions in this system is feasible, it should be relatively straightforward to use a fair number of such states for encoding and processing the quantum information. In Chapter 3 we focus onto this method of scaling. Based on results of the OCT calculations, we argue that one should be able to control accurately the state-to-state transitions between sixteen lower vibrational states – enough to encode a four-qubit system and implement the phase estimation part of Shor’s algorithm for factorizing the number 15 [53, 68].

A second method of scaling is to employ more than one ion. If a linear chain of trapped ions is employed, different qubits can be encoded into different normal vibration modes of the system. Clear advantage of this approach is that such qubits are relatively easy to control selectively using fields of different frequencies. Indeed, although all ions are identical, the normal mode frequencies of the multiple-ion system are quite different [69, 70]. Another advantage of this scaling method is that addressing individual ions is unnecessary because the control field is applied globally,

along the axis of the trap. This is researched in Chapter 4 and 5, where we study two and three ions in the harmonic ($\sim z^2$) and anharmonic ($\sim z^4$) ion traps. For each of these systems, we first compute accurate vibrational eigenstates and characterize anharmonicities of the system. Two sources of anharmonicity are considered: the intrinsic Coulomb anharmonicity and the anharmonicity from the trapping potential. Unfortunately, our calculations show that anharmonicities in these systems are not large enough. An extensive analysis of this problem is presented.

In a search for possible solution of this problem, we found a new architecture of the trapping potential [32, 71, 72] able to provide large enough anharmonicity for the control. It requires to create a very wide and highly anharmonic trapping potential by combining $\sim z^2$ and $\sim z^4$ potential terms, which is researched in Chapter 6. The center-of-mass motion mode and the asymmetric stretching mode in this system are used to represent two qubits. The overall ground vibrational state, the first excited state of each mode, and the combination state were used to encode four states of the two-qubit system: $|00\rangle$, $|01\rangle$, $|10\rangle$ and $|11\rangle$, respectively. Next, we use the OCT to determine the control pulses for various quantum gates such as gate NOT/CNOT and Hadamard transformation. It is found that by carefully choosing the trap parameters, a very accurate control over this system and implementation of the two-qubit gates are possible.

In fact, this second method of scaling is complementary to the first one and can be combined with it in a composite “divide-and-conquer” approach to scaling.

Finally, in Chapter 7 we describe several possible future research directions that have emerged from this study.

Chapter 2: Theoretical methods with applications to adiabatic and optimal control of one ion in the trap

2.1 Trapping potential

In this chapter, we explore and report the fundamental properties of the adiabatic control scheme for ions in a trap using the simplest case: We consider only one ion and restrict its motion to one dimension along the trap (z-axis), which is assumed to be sufficiently uncoupled from the radial motion. Thus, this model is essentially one dimensional. In the vast majority of experiments the trapping potential is harmonic:

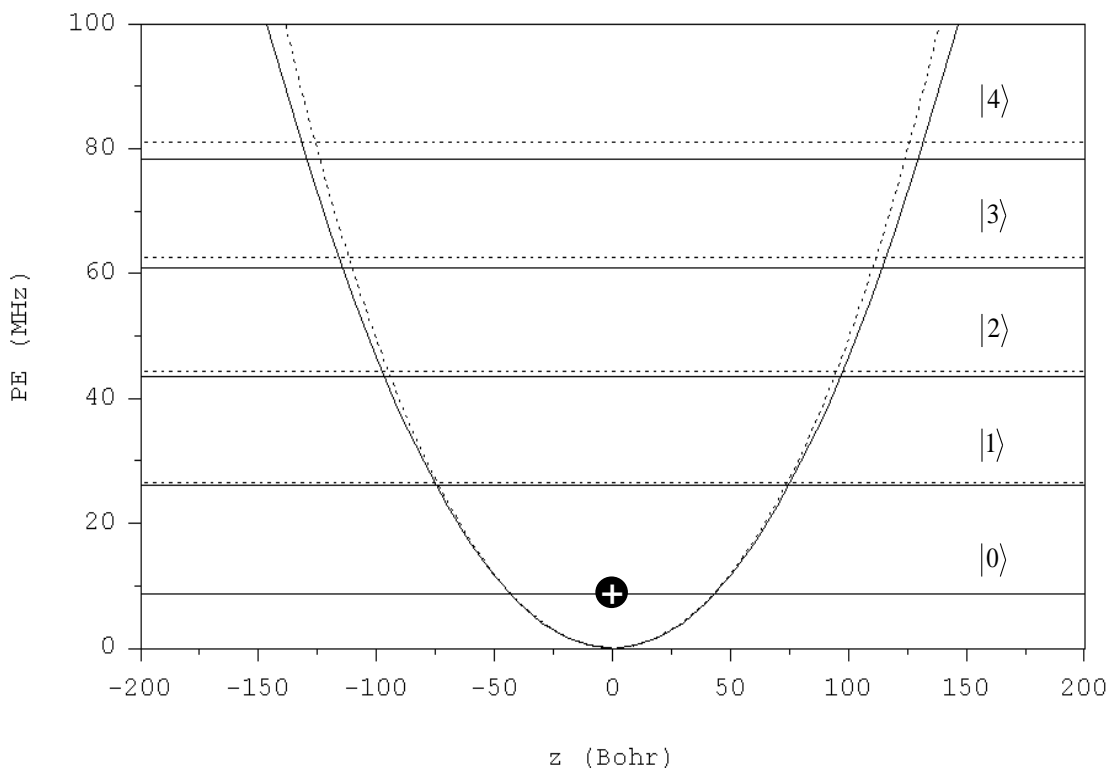


Fig. 2. 1: One $^{111}\text{Cd}^+$ ion in the harmonic and anharmonic potential traps. Solid line: harmonic case; dotted line: anharmonic case.

$$V_h(z) = \frac{1}{2}kz^2, \quad (2.1.1)$$

where k is the force constant. For example, in the work of Monroe group [73-75] the cadmium ions ($^{111}\text{Cd}^+$) are used and the axial frequency is $\omega/2\pi = 2.77$ MHz, related to the force constant through $k = m\omega^2$, with $k/2\pi = 1.483 \times 10^{-3}$ MHz/ a_0^2 . For harmonic oscillator problem, solution of the Schrödinger equation is analytic and leads to the well-known result (atomic units are used in all equations here, a_0 and Bohr are both the length symbol in atomic units):

$$E_h = \omega \left(v + \frac{1}{2} \right), v = 0, 1, 2 \dots \quad (2.1.2)$$

In the harmonic potential trap, as seen from this equation, the transition frequencies between different energy levels are all equal to $\omega = E_{v+1} - E_v$. As a consequence, it is impossible to selectively address and control transitions between two chosen energy levels. In order to achieve the control, we propose to add an *anharmonic* term to the harmonic trapping potential. Now the anharmonic trapping potential is:

$$V_a(z) = \frac{1}{2}kz^2 + <\text{anharmonic term}>. \quad (2.1.3)$$

This should result in a non-equidistant (anharmonic) spectrum of the motional states and should enable the control. In this work we consider the following anharmonic trapping potential:

$$V_a(z) = \frac{1}{2}kz^2 + \frac{1}{4!}k'z^4, \quad (2.1.4)$$

where k' is a parameter which controls anharmonicity. The case of $k' = 0$ correspond to usual harmonic potential. From the previous work by M. Zhao and D. Babikov [63], it is known that the anharmonicity on the order of 1% of the harmonic frequency is enough to achieve robust control. Larger values of k' are better for the control, but may be difficult to create experimentally due to the microscopic size of the trapping region. We studied several different values of $k'/2\pi = 3.558 \times 10^{-6}, 1.423 \times 10^{-7}, 1.067 \times 10^{-7}, 3.558 \times 10^{-9}, 3.558 \times 10^{-10}$ MHz/ a_0^4 to choose a suitable anharmonicity parameter. Based on the above consideration the value of $k'/2\pi = 1.067 \times 10^{-7}$ MHz/ a_0^4 was chosen for the 1D model which was estimated to provide anharmonicity on the order of 1% of the axial trap frequency.

2.2 Schrödinger equation and basis set expansion

The time-independent Schrödinger equation for the axial direction of the ion trap is:

$$\hat{H}\Psi_v(z) = E_v\Psi_v(z), \quad (2.2.1)$$

where

$$\hat{H} = -\frac{1}{2m}\frac{d^2}{dz^2} + V_a(z)q \quad (2.2.2)$$

is 1D Hamiltonian operator, q is the electric charge of the ion and index v lables eigenstates of the system [76-78]. Using basis set expansion, the wavefunctions of the system can be written as:

$$\Psi_v(z) = \sum_{j=1}^N C_{v,j} \varphi_j(z), \quad (2.2.3)$$

where $\varphi_j(z)$ is the basis set of known one dimensional functions of coordinate z , the index j labels basis functions, $C_{v,j}$ are the coefficients of linear combination, N is the number of basis functions which is a convergence parameter determined by try-and-error during convergence studies. In this work, we use the orthonormal basis set of eigenwavefunctions of harmonic oscillator. It has the following form:

$$\varphi_j(z) = A_j H_j(y) e^{-y^2/2}, \quad y = \alpha z, \quad \alpha = \sqrt{m\omega} = \sqrt{k/\omega}. \quad (2.2.4)$$

Here $H_j(y)$ is a Hermite polynomial [79],

$$A_j = [\alpha/\sqrt{\pi} 2^j \cdot j!]^{1/2}, \quad (2.2.5)$$

which is normalization constant. The basis functions are orthonormal

$$\int_{-\infty}^{\infty} \varphi_i(z) \varphi_j(z) dz = \delta_{ij}.$$

In the matrix form, the wavefunction and the basis set expansion can be written as follows:

$$\Psi = \begin{vmatrix} \Psi_1 \\ \Psi_2 \\ \vdots \\ \Psi_N \end{vmatrix}, \quad \Phi = \begin{vmatrix} \varphi_1 \\ \varphi_2 \\ \vdots \\ \varphi_N \end{vmatrix}, \quad \mathbf{C}_{N \times N} = \begin{vmatrix} c_{11} & c_{12} & \cdots & c_{1N} \\ c_{21} & c_{22} & \cdots & c_{2N} \\ \vdots & \vdots & \ddots & \vdots \\ c_{N1} & c_{N2} & \cdots & c_{NN} \end{vmatrix}, \quad (2.2.6)$$

$$\Psi = \mathbf{C}^T \Phi. \quad (2.2.7)$$

The time-independent Schrödinger equation in the matrix form is as follow:

$$\hat{H}\Psi = \mathbf{E}\Psi, \quad (2.2.8)$$

$$\text{where } \hat{H}\Psi = \begin{vmatrix} \hat{H}\Psi_1(z) \\ \hat{H}\Psi_2(z) \\ \vdots \\ \hat{H}\Psi_N(z) \end{vmatrix}, \quad \mathbf{E}_{N \times N} = \begin{vmatrix} E_1 & 0 & \cdots & 0 \\ 0 & E_2 & \cdots & 0 \\ \vdots & \vdots & \ddots & \vdots \\ 0 & 0 & \cdots & E_N \end{vmatrix}. \quad (2.2.9)$$

The transposed matrix of Eqs. (2.2.7) and (2.2.8) are as follows:

$$\Psi^T = \Phi^T \mathbf{C}, \quad (2.2.10)$$

$$\hat{H}\Psi^T = \Psi^T \mathbf{E}, \quad (2.2.11)$$

Substituting Eq. (2.2.10) into Eq. (2.2.11), we obtain:

$$\hat{H}\Phi^T \mathbf{C} = \Phi^T \mathbf{C} \mathbf{E}, \quad (2.2.12)$$

Multiplying Eq. (2.2.12) by Φ^* from the left side, we obtain the following secular equation:

$$\mathbf{H}\mathbf{C} = \mathbf{C}\mathbf{E}, \quad (2.2.13)$$

where $\Phi^* \Phi^T = \mathbf{I}$ (unit matrix) and $\mathbf{H} = \Phi^* \hat{H} \Phi^T$ is the Hamiltonian matrix, which can be written explicitly as follows:

$$\mathbf{H}_{N \times N} = \begin{vmatrix} \langle \varphi_1 | \hat{H} | \varphi_1 \rangle & \langle \varphi_1 | \hat{H} | \varphi_2 \rangle & \cdots & \langle \varphi_1 | \hat{H} | \varphi_N \rangle \\ \langle \varphi_2 | \hat{H} | \varphi_1 \rangle & \langle \varphi_2 | \hat{H} | \varphi_2 \rangle & \cdots & \langle \varphi_2 | \hat{H} | \varphi_N \rangle \\ \vdots & \vdots & \ddots & \vdots \\ \langle \varphi_N | \hat{H} | \varphi_1 \rangle & \langle \varphi_N | \hat{H} | \varphi_2 \rangle & \cdots & \langle \varphi_N | \hat{H} | \varphi_N \rangle \end{vmatrix}. \quad (2.2.14)$$

Here $\langle \varphi_i | \hat{H} | \varphi_j \rangle$, $i, j = 1, 2, \dots, N$ represent integrals over z . After numerical diagonalization of this matrix (see our code Program 1DIONTRAP in Appendix A), we obtain eigenvalues of the system:

$$\mathbf{E} = \mathbf{C}^T \mathbf{H} \mathbf{C}. \quad (2.2.15)$$

Here \mathbf{C} is unitary matrix of eigenvectors obtained after numerical diagonalization

such that $\mathbf{C}^+ \mathbf{C} = \mathbf{I}$, where \mathbf{C}^+ is Hermitian conjugate of \mathbf{C} . Because the wavefunctions and the expansion coefficients are real in this time-independent problem, we have

$\mathbf{C}^* = \mathbf{C}$ and $\mathbf{C}^T \mathbf{C} = \mathbf{I}$. When the matrix \mathbf{C} is known, the wavefunctions of eigenstates of the system can be calculated from Eq. (2.2.7).

The elements of the Hamiltonian matrix Eq. (2.2.14) are computed as follows:

$$\begin{aligned} H_{i,j} &= \langle \varphi_i(z) | \hat{H}(z) | \varphi_j(z) \rangle = \langle \varphi_i(z) | \hat{T}(z) + \hat{V}_a(z) | \varphi_j(z) \rangle \\ &= \left\langle \varphi_i(z) \left| -\frac{1}{2m} \frac{d^2}{dz^2} + \frac{1}{2} kz^2 + \frac{1}{4!} k' z^4 \right| \varphi_j(z) \right\rangle. \end{aligned} \quad (2.2.16)$$

Here we introduce kinetic energy matrix $T_{i,j}$ and potential energy matrix $V_{i,j}$ separately to represent the Hamiltonian matrix:

$$H_{i,j} = T_{i,j} + V_{i,j}, \quad (2.2.17)$$

$$T_{i,j} = -\frac{1}{2m} \left\langle \varphi_i(z) \left| \frac{d^2}{dz^2} \varphi_j(z) \right. \right\rangle, \quad (2.2.18)$$

$$V_{i,j} = \left\langle \varphi_i(z) \left| \frac{1}{2} kz^2 + \frac{1}{4!} k' z^4 \right| \varphi_j(z) \right\rangle. \quad (2.2.19)$$

2.3 Construction of the potential energy matrix and kinetic energy matrix

Integrals of Eqs. (2.2.18) and (2.2.19) can be computed numerically or analytically. For the potential energy part we can rewrite Eq. (2.2.19) in another form:

$$V_{i,j} = \int_{-\infty}^{+\infty} \varphi_i^*(z) \left(\frac{1}{2} kz^2 + \frac{1}{4!} k' z^4 \right) \varphi_j(z) dz. \quad (2.3.1)$$

In our codes, instead of the integral from negative infinity to positive infinity, we only

need to determine certain integration limits and calculate the integral between them which gives reliable numerical results. Here we define them as z_{min} and z_{max} with $z_{min} = -z_{max}$. Then the Eq. (2.3.1) can be written as follows:

$$V_{i,j} = \int_{z_{min}}^{z_{max}} \varphi_i^*(z) \left(\frac{1}{2} kz^2 + \frac{1}{4!} k' z^4 \right) \varphi_j(z) dz. \quad (2.3.2)$$

In the 1D code we use the straightforward Equally-Spaced Abscissas method to calculate the integral [80], so we have to choose a relatively small distance step Δz and replace the integral by the product of Δz and the sum of values of the integrand in different points z_n :

$$V_{i,j} = \Delta z \sum_{n=1}^{\mathcal{N}} \varphi_i^*(z_n) \left(\frac{1}{2} kz_n^2 + \frac{1}{4!} k' z_n^4 \right) \varphi_j(z_n), \quad (2.3.3)$$

here \mathcal{N} is the number of integration points and n is used to label the points. \mathcal{N} is calculated using the following equation:

$$\mathcal{N} = \frac{z_{max} - z_{min}}{\Delta z} + 1. \quad (2.3.4)$$

The value $n = 1$ corresponds to z_{min} and $n = \mathcal{N}$ corresponds to z_{max} . Because \mathcal{N} is integer, we change \mathcal{N} to obtain desirable distance step size Δz . Since the wavefunctions are real, $\varphi_i^* = \varphi_i$.

For the kinetic energy part, because $\varphi_i(z)$ is a known analytic function from Eq. (2.2.4), the second derivative of the basis function can be calculated analytically using rules of Hermite polynomials:

$$\begin{aligned} \frac{d^2}{dz^2} \varphi_j(z) &= A_j \left(H_j''(y) e^{-y^2/2} + 2H_j'(y) (e^{-y^2/2})' \right. \\ &\quad \left. + H_j(y) (e^{-y^2/2})'' \right). \end{aligned} \quad (2.3.5)$$

It is easy to calculate the first and second derivatives of $e^{-y^2/2}$, which are

$$(e^{-y^2/2})' = -\alpha y e^{-y^2/2} = -\alpha^2 z e^{-\alpha^2 z^2/2}, \quad (2.3.6)$$

$$(e^{-y^2/2})'' = \alpha^2 (y^2 - 1) e^{-y^2/2} = \alpha^2 (\alpha^2 z^2 - 1) e^{-\alpha^2 z^2/2}. \quad (2.3.7)$$

When we calculate the derivatives of Hermite polynomials, we can use the following property:

$$H_j'(z) = 2jH_{j-1}(z). \quad (2.3.8)$$

Now we can calculate the terms of interest.

$$H_j'(y) = H_j'(\alpha z) = \alpha H_j'(y) = \alpha H_j'(\alpha z), \quad (2.3.9)$$

$$\begin{aligned} H_j''(y) &= H_j''(\alpha z) = [H_j'(\alpha z)]' \\ &= [\alpha H_j'(\alpha z)]' = 2\alpha j [H_{j-1}(\alpha z)]' = 2j\alpha^2 H_{j-1}'(\alpha z). \end{aligned} \quad (2.3.10)$$

Substituting Eqs. (2.3.5) - (2.3.10) into Eq. (2.2.18) we obtain the following formula for the kinetic part:

$$\begin{aligned} T_{i,j} &= -\frac{1}{2m} \langle \varphi_i(z) | A_j \left(4j(j-1)\alpha^2 H_{j-2}(\alpha z) e^{-\alpha^2 z^2/2} \right. \\ &\quad \left. + 4j\alpha H_{j-1}(\alpha z) (-\alpha^2 z e^{-\alpha^2 z^2/2}) \right. \\ &\quad \left. + H_j(\alpha z) (\alpha^2 (\alpha^2 z^2 - 1) e^{-\alpha^2 z^2/2}) \right) \rangle. \end{aligned} \quad (2.3.11)$$

Using Eq. (2.2.4), Eq. (2.3.11) can be integrated analytically [81]. For the upper triangle of the matrix, the result is:

$$\begin{aligned}
T_{i,j} &= -\frac{1}{2m} \langle \varphi_i(z) | \sqrt{4j(j-1)} \alpha^2 \varphi_{j-2}(z) \\
&\quad - 2\sqrt{2j}\alpha^3 z \varphi_{j-1}(z) + \alpha^2(\alpha^2 z^2 - 1) \varphi_j(z) \rangle \\
&= -\frac{k}{4\alpha^2} \left(4\sqrt{j(j-1)} \delta_{i,j-2} - 4\sqrt{j} (\sqrt{i+1} \delta_{i,j-2} + \sqrt{i} \delta_{i,j}) \right. \\
&\quad \left. - 2\delta_{i,j} + \left((2i+1)\delta_{i,j} + \sqrt{(i+1)(i+2)} \delta_{i,j-2} \right) \right). \quad (2.3.12)
\end{aligned}$$

Alternatively, we can generate Hermite polynomials and their first derivatives numerically using a subroutine OTHPL [82] and calculate the integral of Eq. (2.3.11) numerically, which serves as a check of the analytic expressions. Similar to Eq. (2.3.3) of the potential part, we calculate the integral along the axial z using the Equally-Spaced Abscissas method:

$$\begin{aligned}
T_{i,j} &= -\frac{1}{2m} A_i A_j \Delta z \sum_{n=1}^N H_i(\alpha z_n) e^{-\alpha^2 z_n^2/2} (4j(j-1) \alpha^2 H_{j-2}(\alpha z_n) \\
&\quad e^{-\alpha^2 z_n^2/2} + 4j\alpha H_{j-1}(\alpha z_n) (-\alpha^2 z_n e^{-\alpha^2 z_n^2/2}) \\
&\quad + H_j(\alpha z_n) (\alpha^2 (\alpha^2 z_n^2 - 1) e^{-\alpha^2 z_n^2/2})). \quad (2.3.13)
\end{aligned}$$

2.4 Matrix diagonalization and convergence studies

After the elements of Hamiltonian matrix are calculated, we need to diagonalize the matrix to obtain its eigenvalues (energies) and the eigenvectors (parameter matrix \mathbf{C}). Computer code 1DIONTRAP was written using FORTRAN language to carry out these calculations. The code is attached in Appendix A.

In my work, my FORTRAN program jobs are run at remote computer at

NERSC which is high performance scientific computing facility for research sponsored by the U.S. Department of Energy Office of Science. I used several computer system provided by NERSC to do my calculation. For example, Jacquard Linux system was used for the first two and half years of my research. After its retirement, I switched to Franklin, then to the newest one, Hopper, which I use until now.

Rigorous convergence studies were carried out in order to obtain reliable results and save the computer time. First, using very small step size $\Delta z = 1.0$ Bohr and very large size of basis set $N = 50$, we did calculations with different grid limits ($z_{max} = 500, 650$ and 900 Bohr) to determine the optimal value of z_{max} . The value of $z_{max} = 650$ Bohr was chosen for further calculations. With this z_{max} , the energy of eigenstates up to $v = 10$ (v is quantum number) is accurate within 10^{-9} MHz. Second, using $z_{max} = 650$ Bohr and $N = 50$, we studied the effect of the number of points. We carried out calculations with the number of points ($\mathcal{N} = 101, 131, 501, 1001, 1501$ and 2501) along the axial direction. The value $\mathcal{N} = 131$ (corresponding to $\Delta z = 10$ Bohr) was chosen. With this grid the deviation of energy for the state $v = 10$ from the most accurate results ($\mathcal{N} = 2501$) is lower than 10^{-9} MHz. Finally, using $z_{max} = 650$ Bohr and $\Delta z = 10$ Bohr we investigated the effect of the size of the basis set with $N = 10, 20, 30, 40$ and 50 . Results of all these

calculations are summarized in Fig. 2.2 which shows E_v as a function of quantum number in different calculations. One feature seen in these calculations is that results for some upper states calculated with smaller basis sets are noticeably different from those calculated with larger basis sets. For example, comparing the results obtained with $N = 40$ basis functions against those obtained with $N = 50$ basis functions, one can see apparent differences when the quantum number comes to about $v = 33$. In the numerical method, we can only use a limited number of basis functions in the

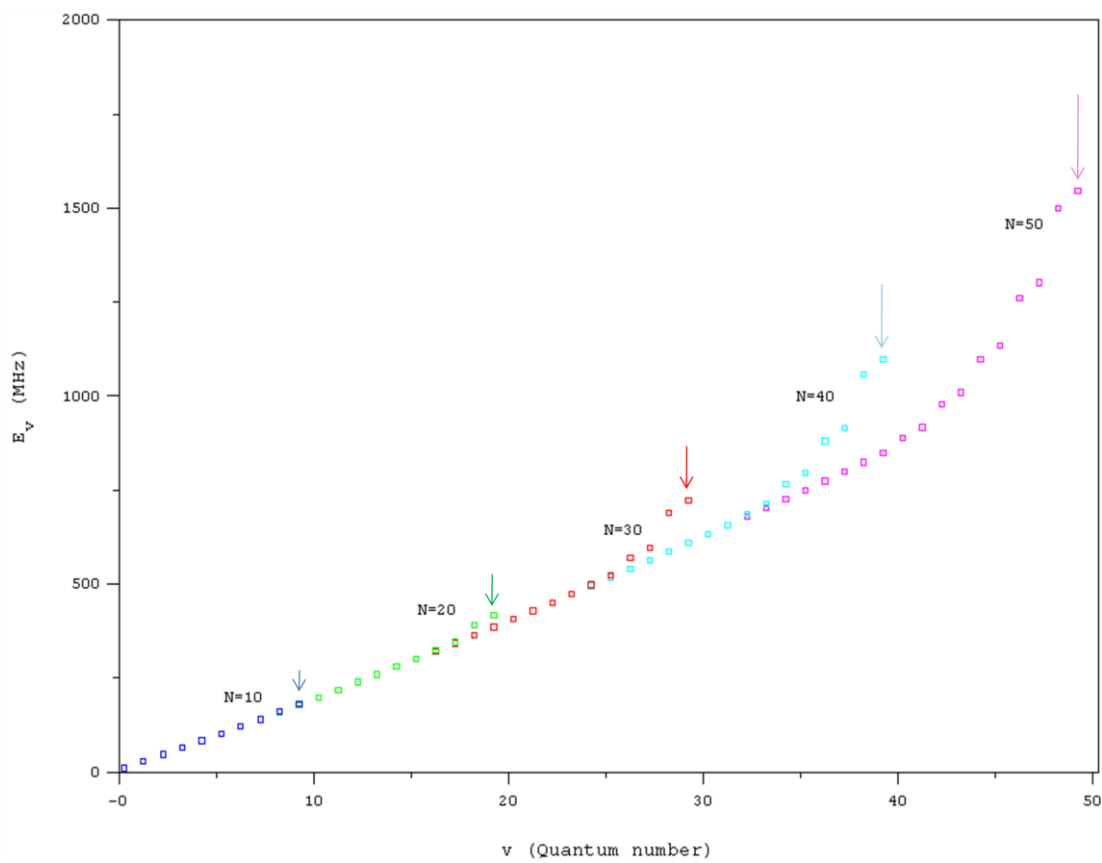


Fig. 2. 2: Spectrum of energies of $^{111}\text{Cd}^+$ ion in the anharmonic potential trap calculated numerically using basis sets of different sizes $N = 10, 20, 30, 40, 50$. In all calculations $z_{\max} = 650$ Bohr and $\Delta z = 10$ Bohr ($\mathcal{N} = 131$) are used. Arrows indicate inaccurate results.

calculation, so there are always some deviations between calculated results with true values for the upper states. We have to use larger sizes of basis set if we want to obtain accurate results for upper states. Similarly, in calculations with $N = 40$ basis functions we cannot achieve 40 accurate eigenvalues, we need to compare their results with more accurate data from larger sizes of basis set to make sure how accurate they are. Recall that in our system the anharmonicity is small and the deviation of anharmonic results from harmonic ones is also small. In order to see this effect, the error of energy eigenvalues should be lower than 1% of anharmonicity, which is about 0.001 MHz. From our study, when the size of basis set is $N = 20$, the states up to $|v\rangle = 10$ are converged to 10^{-9} MHz compared to the more accurate results from $N = 50$. This is accurate enough for our purpose, so our final 1D calculations are carried out with $z_{max} = 650$ Bohr, $\mathcal{N} = 131$ (Equally-Spaced Abscissas method with $\Delta z = 10$ Bohr) and $N = 20$ basis functions.

2.5 Analysis of results

Figure 2.3 shows energy eigenvalues of the states with quantum number $v = 0, 1, \dots, 10$. Results for the harmonic potential trap (plus) are calculated analytically using Eq. (2.1.2). Results for the anharmonic potential trap (circle) are from our numerical calculations. The third set of data points (box) in Fig. 2.3 corresponds to Dunham expansion formula [83]:

$$E_v = D + \Omega \left(v + \frac{1}{2} \right) - \Delta \left(v + \frac{1}{2} \right)^2. \quad (2.5.1)$$

We used the first three numerical values ($v = 0, 1, 2$) of the calculated anharmonic spectrum to fit the Dunham expansion formula and obtained the following values of the coefficients:

$$\Omega/2\pi = 2.771 \text{ MHz},$$

$$\Delta/2\pi = -2.179 \times 10^{-2} \text{ MHz},$$

$$D/2\pi = -5.214 \times 10^{-3} \text{ MHz}.$$

Note that the value of Ω is practically equivalent to the harmonic frequency, which

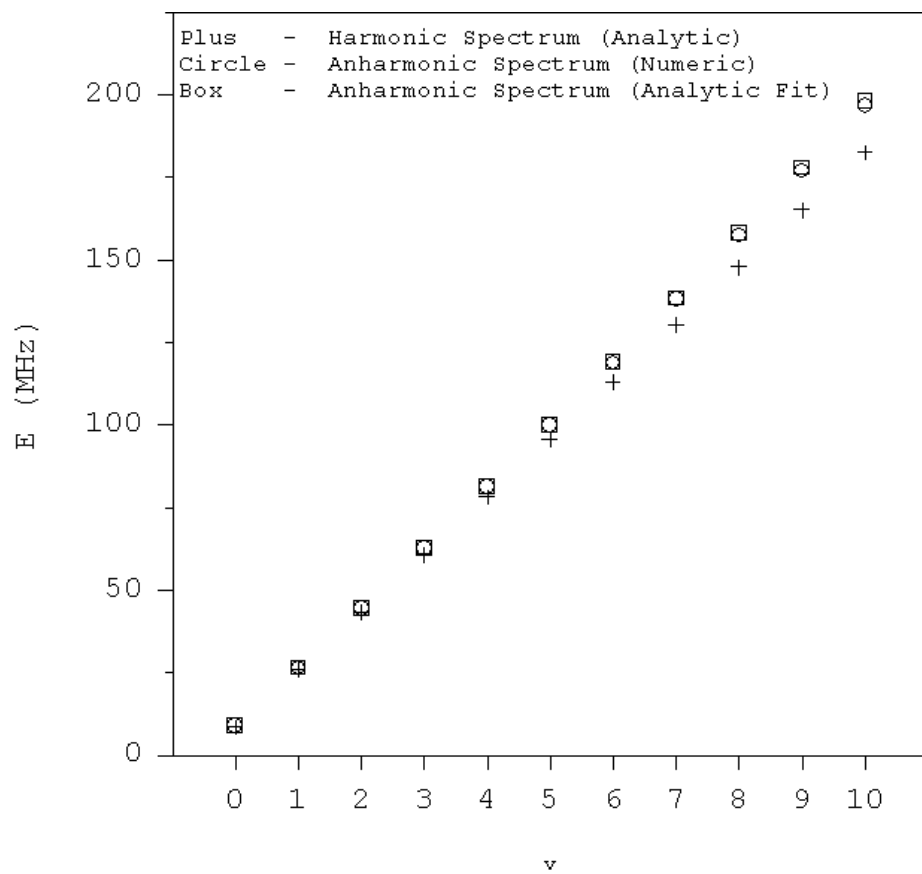


Fig. 2. 3: Spectrum of the lower eleven states for $^{111}\text{Cd}^+$ ion in the harmonic and anharmonic traps.

means that the Dunham expansion describes the low part of the spectrum very accurately. Also, the value of $\Delta \approx -0.008 \Omega$, which is about 0.8% of Ω . As expected, it should be enough for the successful control.

From Fig. 2.3 it is also apparent that results of the anharmonic case are different from the analytic harmonic results. When $v = 0$, the difference is vanishingly small (smaller than 0.1 MHz), but with the increase of the quantum number the difference increases. When $v = 10$, the deviation is about 20 MHz. To find out the trend of the difference between the harmonic and anharmonic spectra, we

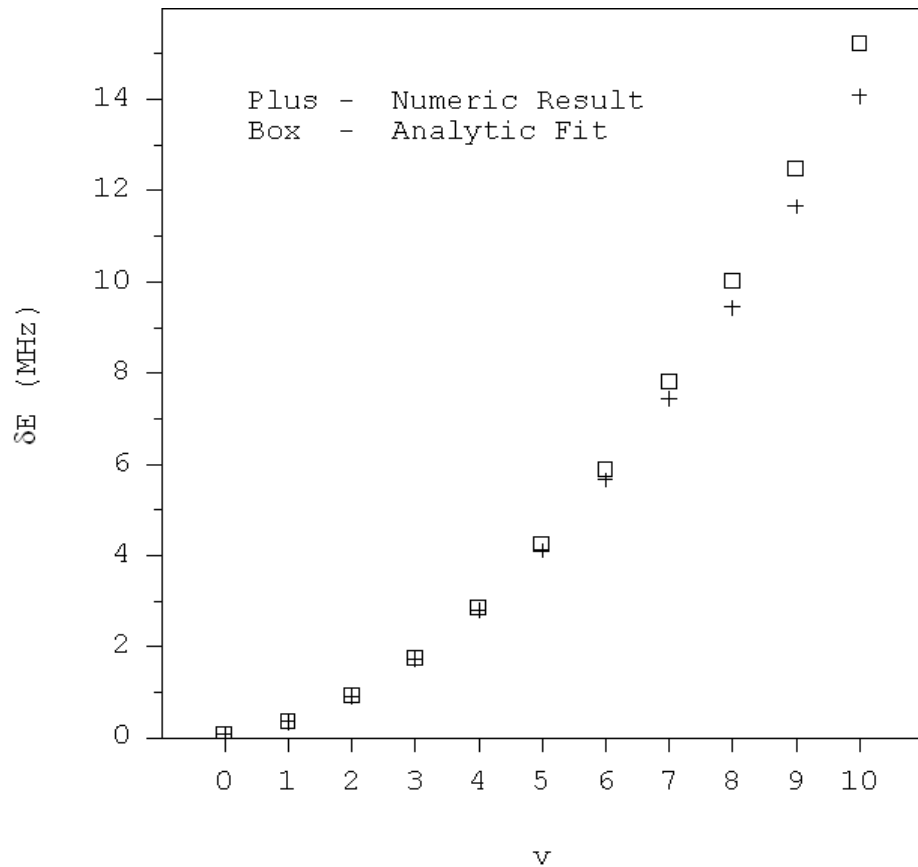


Fig. 2. 4: Energy difference between the anharmonic spectrum and the harmonic spectrum of $^{111}\text{Cd}^+$ ion (from Table 2.1).

plotted in Fig. 2.4 the energy differences:

$$\delta E = E_v - E_h, \quad (2.5.2)$$

The anharmonic results from numerical calculation (Table 2.1) and from the Dunham fit (Eq. (2.5.1)) are both used. The data in Fig. 2.4 show that the energy differences increase with a trend of parabola which is the evidence that the spectrum of ion in the anharmonic potential trap is non-equidistant. If the numerical spectrum is harmonic, the data in Fig. 2.4 would show a straight line. Also note that the spectrum from numerical calculations is close to the results calculated from Dunham expansion formula for small values of v , which tells us that our fit values are qualitatively correct. But when the quantum number becomes larger, they are somewhat different. This means we can reproduce very accurately the results for several lower states with the Dunham fit using the lowest three states. All data used in Fig. 2.3 and 2.4 are summarized in Table 2.1.

In addition to analysis of the spectrum, we can also analyze wavefunctions of states of the trap. Because the matrix **C** is obtained during the diagonalization of the Hamiltonian matrix, the wavefunctions of the system can be calculated from the Eq. (2.2.7). In Fig. 2.5, the harmonic (red) and anharmonic(green) trapping potentials are both plotted, the anharmonic term (blue) of the anharmonic potential is also included. We also draw the wavefunctions of different energy levels in the ion traps and it can

Table 2. 1: Eigenvalues, assignments and deviations (from the harmonic model) of the vibrational states of $^{111}\text{Cd}^+$ ion in a slightly anharmonic trap.

# of state	E_h (MHz)	E_v (numerical) (MHz)	Anharmonic spectrum from Dunham expansion (MHz)	δE between E_v (numerical) and E_h (MHz)	δE between anharmonic (Dunham fit) and E_h (MHz)
0	8.7022	8.7740	8.7740	0.0718	0.0718
1	26.1066	26.4619	26.4619	0.3552	0.3552
2	43.5110	44.4236	44.4236	0.9126	0.9126
3	60.9154	62.6480	62.6592	1.7326	1.7437
4	78.3198	81.1251	81.1686	2.8053	2.8488
5	95.7242	99.8458	99.9519	4.1216	4.2276
6	113.1287	118.8018	119.0090	5.6731	5.8804
7	130.5331	137.9855	138.3401	7.4524	7.8070
8	147.9375	157.3898	157.9449	9.4524	10.0075
9	165.3419	177.0085	177.8237	11.6666	12.4818
10	182.7463	196.8353	197.9763	14.0891	15.2300

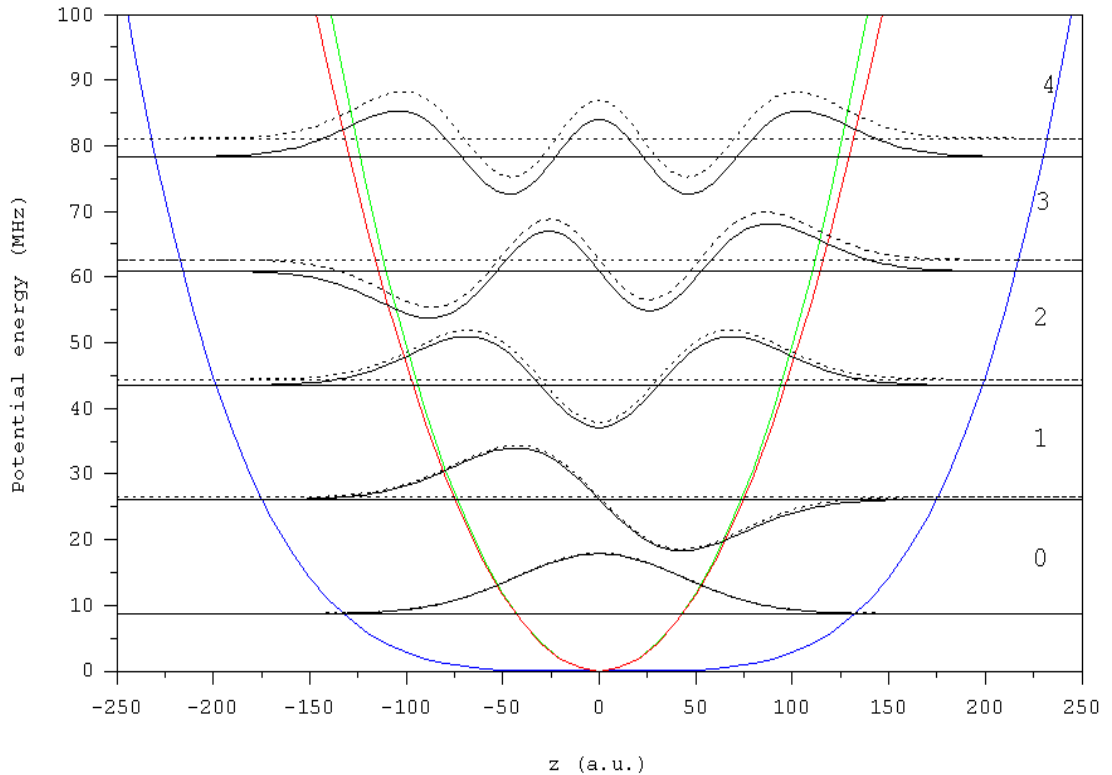


Fig. 2. 5: Green line is the anharmonic trapping potential $V_a(z) = \frac{1}{2}kz^2 + \frac{1}{4!}k'z^4$, red line is the harmonic part of this potential and blue line is the anharmonic part. Black solid line describes the wavefunctions and energy levels of $^{111}\text{Cd}^+$ ion in the harmonic trapping potential and the dotted line is that of anharmonic case.

line is the harmonic part of this potential and blue line is the anharmonic part. Black solid line describes the wavefunctions and energy levels of $^{111}\text{Cd}^+$ ion in the harmonic trapping potential and the dotted line is that of anharmonic case.

help us understand the system in terms of the probability distribution for different states. From Fig. 2.5, it is shown that the anharmonic trapping potential is a little sharper than the harmonic potential which induces a shift up of the anharmonic energy levels compared to the energy levels of the harmonic case. The differences between energy levels of harmonic and anharmonic trap increase with the quantum number, which is consistent with Fig. 2.4. Because the anharmonicity is quite small, the shape of anharmonic potential trap is very similar to the harmonic trap which leads to the nearly same wavefunctions of two systems. However, the sharper anharmonic potential results in the slightly smaller axial extent of the corresponding wavefunctions compared to the harmonic case. This small effect is seen in Fig. 2.5.

2.6 The control scheme and the transition matrix

In order to control motion of the ion we propose to apply an additional time-dependent electric field $\varepsilon(z, t)$ along the axis of the trap, so that the Hamiltonian becomes: $\hat{H}_{ion} = \hat{H} + \Phi(z, t)q$, where \hat{H} is the Hamiltonian from Eq. (2.2.2), $\Phi(z, t) = -\int_0^z \varepsilon(z, t)dz$ is the electric potential, and q is electric charge of the ion. The easiest approach is to create a spatially homogeneous field with the time-dependent amplitude $\varepsilon(t)$ which after trivial analytic integration gives:

$$\hat{H}_{ion} = \hat{H} - \varepsilon(t)zq. \quad (2.6.1)$$

Note that this problem is very similar to the coherent control problem of

molecular vibrations using the ultra-fast optimally shaped laser pulses [8, 33, 37, 44, 84-88]. Indeed, the semiclassical molecule-light interaction is given by:

$$\hat{H}_{mol} = \hat{H} - \epsilon(t)\mu(r). \quad (2.6.2)$$

Here \hat{H} is molecular Hamiltonian, $\epsilon(t)$ is intensity of the time-dependent laser field and $\mu(r)$ is the molecular dipole moment function. The dipole moment of non-polar molecules executing small amplitude vibrational motion is a linear function of the internuclear distance:

$$\mu(r) \approx \left(\frac{\partial \mu}{\partial r} \right)_{r=r_{eq}} r + \dots \quad (2.6.3)$$

If only keeping the first term, the total molecular Hamiltonian becomes:

$$\hat{H}_{mol} = \hat{H} - \epsilon(t)r\mu'_{r_{eq}}. \quad (2.6.4)$$

Since this expression is mathematically equivalent to Eq. (2.6.1), the optimal control theory methods developed for molecular vibrations can be utilized to control the motion of ions in a trap [84].

Similar to the molecular dipole moment function $\mu(r)$, for convenience, we introduce the dipole moment function $d(z)$ of one-ion in a trap:

$$d(z) = qz. \quad (2.6.5)$$

Using this definition, the control Hamiltonian of Eq. (2.6.1) can be rewritten as:

$$\hat{H}_{ion} = \hat{H} - \epsilon(t)d(z). \quad (2.6.6)$$

The transition matrix elements of ion in the trap (needed in the following

section) are calculated as follows:

$$M_{v,v'} = \langle \Psi_v(z) | d(z) | \Psi_{v'}(z) \rangle. \quad (2.6.7)$$

Here Ψ_v and $\Psi_{v'}$ are two wavefunctions of the ion which can be calculated from Eq. (2.2.3) for any pair of eigenstates. So the equation is rewritten as:

$$\begin{aligned} M_{v,v'} &= \left\langle \sum_{i=1}^N C_{v,i} \varphi_i(z) | qz | \sum_{j=1}^N C_{v',j} \varphi_j(z) \right\rangle \\ &= q \int_{-\infty}^{+\infty} \left(\sum_{i=1}^N C_{v,i} \varphi_i(z) \right)^* \left(\sum_{j=1}^N C_{v',j} \varphi_j(z) \right) zdz \\ &= \frac{q}{\sqrt{2m\omega}} \sum_{i,j=1}^N C_{v,i}^* C_{v',j} (\sqrt{i}\delta_{i,j+1} + \sqrt{i+1}\delta_{i,j-1}). \end{aligned} \quad (2.6.8)$$

Here m is the mass of $^{111}\text{Cd}^+$ ion, ω is the axial frequency (see Eq. (2.2.4)) and N is the number of basis functions which are used to represent wavefunctions of the

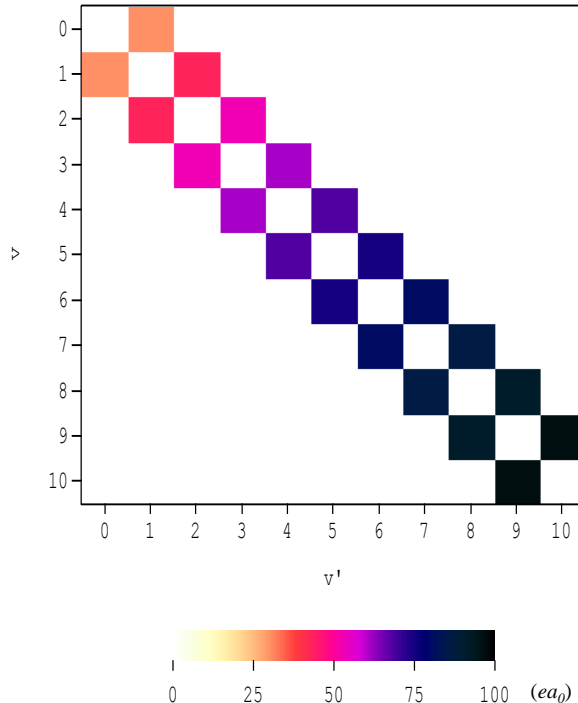


Fig. 2. 6: Transition matrix of $^{111}\text{Cd}^+$ ion in the harmonic trapping potential.

system. Alternatively, we can calculate the elements of transition matrix numerically using the following equation which serves as a test:

$$\begin{aligned}
 M_{v,v'} &= q\Delta z \sum_{n=1}^N z_n \Psi_v(z_n)^* \Psi_{v'}(z_n) \\
 &= q\Delta z \sum_{n=1}^N z_n \left(\sum_{i=1}^N C_{v,i} \varphi_i(z_n) \right)^* \left(\sum_{j=1}^N C_{v',j} \varphi_j(z_n) \right). \quad (2.6.9)
 \end{aligned}$$

The code for calculation of transition matrix is program 1DIONTRAP (Appendix

A, lines 264-286) using the numerical integral with Eq. (2.6.9).

If the trapping potential is harmonic, wavefunctions of the system are just basis functions from Eq. (2.2.4). In this case, the sum of Eq. (2.6.8) simplifies to only one term:

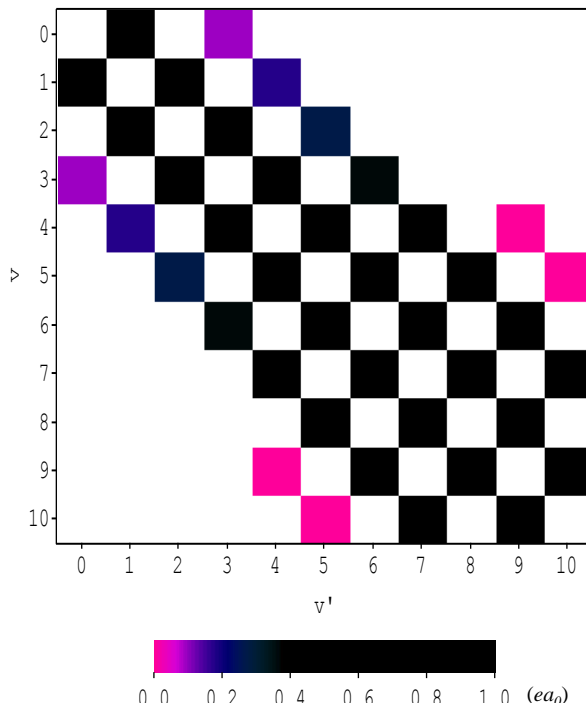


Fig. 2. 7: Transition matrix of $^{111}\text{Cd}^+$ ion in the anharmonic trapping potential.

Table 2. 2: Values of transition matrix (11×11) of $^{111}\text{Cd}^+$ ion in the harmonic trapping potential (values are in units of ea_0).

	0	1	2	3	4	5	6	7	8	9	10
0	0.00	30.56	0.00	0.00	0.00	0.00	0.00	0.00	0.00	0.00	0.00
1	30.56	0.00	43.22	0.00	0.00	0.00	0.00	0.00	0.00	0.00	0.00
2	0.00	43.22	0.00	52.94	0.00	0.00	0.00	0.00	0.00	0.00	0.00
3	0.00	0.00	52.94	0.00	61.13	0.00	0.00	0.00	0.00	0.00	0.00
4	0.00	0.00	0.00	61.13	0.00	68.34	0.00	0.00	0.00	0.00	0.00
5	0.00	0.00	0.00	0.00	68.34	0.00	74.87	0.00	0.00	0.00	0.00
6	0.00	0.00	0.00	0.00	0.00	74.87	0.00	80.87	0.00	0.00	0.00
7	0.00	0.00	0.00	0.00	0.00	0.00	80.87	0.00	86.45	0.00	0.00
8	0.00	0.00	0.00	0.00	0.00	0.00	0.00	86.45	0.00	91.69	0.00
9	0.00	0.00	0.00	0.00	0.00	0.00	0.00	0.00	91.69	0.00	96.65
10	0.00	0.00	0.00	0.00	0.00	0.00	0.00	0.00	0.00	96.65	0.00

Table 2. 3: Values of transition matrix (11×11) of $^{111}\text{Cd}^+$ ion in the anharmonic trapping potential (values are in units of ea_0).

	0	1	2	3	4	5	6	7	8	9	10
0	0.000	30.318	0.000	0.095	0.000	0.001	0.000	0.000	0.000	0.000	0.000
1	30.318	0.000	42.547	0.000	0.181	0.000	0.001	0.000	0.000	0.000	0.000
2	0.000	42.547	0.000	51.731	0.000	0.273	0.000	0.002	0.000	0.000	0.000
3	0.095	0.000	51.731	0.000	59.322	0.000	0.370	0.000	0.003	0.000	0.000
4	0.000	0.181	0.000	59.322	0.000	65.888	0.000	0.469	0.000	0.004	0.000
5	0.001	0.000	0.273	0.000	65.888	0.000	71.724	0.000	0.571	0.000	0.007
6	0.000	0.001	0.000	0.370	0.000	71.724	0.000	77.005	0.000	0.673	0.000
7	0.000	0.000	0.002	0.000	0.469	0.000	77.005	0.000	81.848	0.000	0.878
8	0.000	0.000	0.000	0.003	0.000	0.571	0.000	81.848	0.000	86.332	0.000
9	0.000	0.000	0.000	0.000	0.004	0.000	0.673	0.000	86.332	0.000	94.448
10	0.000	0.000	0.000	0.000	0.000	0.007	0.000	0.878	0.000	94.448	0.000

$$M_{v,v'} = q\langle \varphi_v | z | \varphi_{v'} \rangle = \frac{q}{\sqrt{2m\omega}} (\sqrt{v}\delta_{v,v'+1} + \sqrt{v+1}\delta_{v,v'-1}). \quad (2.6.10)$$

Figure 2.6 shows elements of 11×11 transition matrix for one ion in the *harmonic*

trapping potential calculated using this analytic formula. As in the infrared

spectroscopy, the selection rule $\Delta v = \pm 1$ is revealed. Elements of 11×11 transition

matrix for one ion in the *anharmonic* trapping potential calculated numerically using

Eq. (2.6.9) are shown in Fig. 2.7. Because we only add a small anharmonicity to harmonic potential, the difference between the harmonic transition matrix and the anharmonic one is quite small. In Fig. 2.7, besides the $\Delta\nu = \pm 1$ transitions, $\Delta\nu = \pm 3, \pm 5 \dots$ transitions also occur which are the contributions of the double sum in Eq. (2.6.8), and it is the effect of anharmonicity. All the data of Figs. 2.6 and 2.7 are summarized in the Tables 2.2 and 2.3.

2.7 Optimal control theory (OCT)

The purpose of optimal control theory is to design theoretically the pulse shape $\varepsilon(t)$ which maximizes the transfer probability from a given initial state ϕ_i to a chosen target state ϕ_f (both can be eigenstates or superposition states). The optimization can be achieved by maximizing the objective functional with the monotonically convergent numerical algorithm of Rabitz [8], where the objective functional is defined as:

$$J = \left| \langle \vec{\Psi}(T) | \phi_f \rangle \right|^2 - \int_0^T \alpha(t) |\varepsilon(t)|^2 dt - 2Re \left\{ \langle \vec{\Psi}(T) | \phi_f \rangle \int_0^T \langle \vec{\Psi}(t) | i\hat{H}_{ion} + \partial/\partial t | \vec{\Psi}(t) \rangle dt \right\}. \quad (2.7.1)$$

Here T presents duration of the pulse, $\vec{\Psi}(t)$ is the time-dependent wave function driven by $\varepsilon(t)$ from its *initial* state $\vec{\Psi}(t=0) = \phi_i$ to the *final* state $\vec{\Psi}(t=T) = \phi_f$ and $\vec{\Psi}(t)$ is the backward driven wave function. The first term in Eq. (2.7.1) is an overlap of the final wave function with the target state which is maximized; the

second term is required to minimize energy of the laser field and constrain its smooth switching on and off; the last term serves to satisfy the time-dependent Schrödinger equation with the evolution of the wave functions $\vec{\Psi}(t)$ and $\overleftarrow{\Psi}(t)$. The function $\alpha(t)$ is a penalty function, which has the following form [48]:

$$\alpha(t) = \frac{\alpha_0}{s(t)} \quad (2.7.2)$$

where α_0 is a constant penalty factor, $s(t)$ plays a role of the smooth switching-on and switching-off of the pulse:

$$s(t) = \sin^2\left(\pi \frac{t}{T}\right) \quad (2.7.3)$$

The brackets $\langle | \rangle$ in Eq. (2.7.1) denote integration over the spatial coordinate z , which is omitted here for simplicity. This approach can be used, for example, for state flips like $|0\rangle \rightarrow |1\rangle$, when both the initial and the final states are uniquely defined.

In quantum computation, however we have to deal with more complicated gate transformations of the vibrational qubit. For example, for the logical gate NOT we have to find a pulse to induce two transitions between the qubit states simultaneously:

$$\text{NOT}|0\rangle \rightarrow |1\rangle \quad (2.7.4)$$

$$\text{NOT}|1\rangle \rightarrow |0\rangle \quad (2.7.5)$$

This means, the system should be driven into the state $|1\rangle$ if it was initially in the vibrational state $|0\rangle$, but if it was initially in the state $|1\rangle$ it should be driven into the

state $|0\rangle$. One universal gate pulse should be able to achieve the population transfer for two transitions of interest simultaneously, which transition is actually performed depends only on the initial state of the qubit. This can be achieved by maximizing the functional where the sum over the two transitions of interest (Eqs. (2.7.4) and (2.7.5)) is introduced:

$$J = \frac{1}{K} \sum_{k=1,2} \left| \langle \vec{\Psi}^k(T) | \phi_f^k \rangle \right|^2 - \int_0^T \alpha(t) |\varepsilon(t)|^2 dt - 2 \sum_{k=1,2} \operatorname{Re} \left\{ \langle \vec{\Psi}^k(T) | \phi_f^k \rangle \int_0^T \langle \vec{\Psi}^k(t) | i\hat{H}_{ion} + \partial/\partial t | \vec{\Psi}^k(t) \rangle dt \right\}. \quad (2.7.6)$$

Here index k labels $K = 2$ transitions of interest. For example, for the gate NOT we set: $\phi_i^1 = |0\rangle$, $\phi_f^1 = |1\rangle$, and $\phi_i^2 = |1\rangle$, $\phi_f^2 = |0\rangle$ according to Eqs. (2.7.4) and (2.7.5). The $\vec{\Psi}^k(t)$ and $\vec{\Psi}^k(t)$, $k = \{1,2\}$, are the laser-driven time-dependent wave functions for two transitions of the gate, and $\varepsilon(t)$ is the universal gate field.

In practice, the measure of success of the control pulse is the value of overlap $\langle \vec{\Psi}(T) | \phi_f \rangle$ between the actual final wave function and wave function of the target state. The control pulse designed to induce *multiple* state-to-state transitions (e.g., different transitions of the quantum gate) can be assessed by the value of cumulative transition probability defined as:

$$P = \frac{1}{K} \sum_k \left| \langle \vec{\Psi}(T) | \phi_f^k \rangle \right|^2. \quad (2.7.7)$$

Here the index k labels K transitions we want to optimize simultaneously, $1 \leq k \leq K$.

The goal of this theory is to derive the equations for calculation of the optimal pulse $\varepsilon(t)$. The procedure of this is very similar to the maximization of the Eq. (2.7.1) described in detail in the literature [89]. It is required to maximize the functional with respect to variations in five functions: $\bar{\Psi}^k(t)$, $\bar{\Psi}^k(t)$, $k = \{1,2\}$, and $\varepsilon(t)$. We start with the variation of $\bar{\Psi}^k(t)$, $k = \{1,2\}$. We get:

$$\begin{aligned}\delta_{\bar{\Psi}^k} J &= J(\bar{\Psi}^k(t), \bar{\Psi}^k(t) + \delta\bar{\Psi}^k(t), \varepsilon(t)) - J(\bar{\Psi}^k(t), \bar{\Psi}^k(t), \varepsilon(t)) \\ &= -2Re \left\{ \langle \bar{\Psi}^k(T) | \phi_f^k \rangle \int_0^T \langle \delta\bar{\Psi}^k(t) | i\hat{H}_{ion} + \partial/\partial t | \bar{\Psi}^k(t) \rangle dt \right\}. \quad (2.7.8)\end{aligned}$$

Because $\delta\bar{\Psi}^k$ is chosen arbitrarily, Eq. (2.7.8) can only be satisfied if

$$\left(i\hat{H}_{ion} + \frac{\partial}{\partial t} \right) \bar{\Psi}^k(t) = 0 \quad (2.7.9)$$

By applying variations to the backward propagated wavefunctions $\bar{\Psi}^k(t)$ in Eq.

(2.7.6) separately, we obtain the following equations for each k , $k = \{1,2\}$:

$$\begin{aligned}i \frac{\partial}{\partial t} \bar{\Psi}^k(t) &= \hat{H}_{ion} \bar{\Psi}^k(t), \\ \bar{\Psi}^k(0) &= \phi_i^k, \quad (2.7.10)\end{aligned}$$

These are two time-dependent Schrödinger equations to propagate forward in time, each with its own initial condition ϕ_i^k .

In the similar way, variations of $\bar{\Psi}^1(t)$ and $\bar{\Psi}^2(t)$ in the Eq. (2.7.6) give:

$$\begin{aligned}\delta_{\bar{\Psi}^k} J &= J(\bar{\Psi}^k(t) + \delta\bar{\Psi}^k(t), \bar{\Psi}^k(t), \varepsilon(t)) - J(\bar{\Psi}^k(t), \bar{\Psi}^k(t), \varepsilon(t)) \\ &= \langle \bar{\Psi}^k(T) + \delta\bar{\Psi}^k(T) | \phi_f^k \rangle \langle \phi_f^k | \bar{\Psi}^k(T) + \delta\bar{\Psi}^k(T) \rangle - \langle \bar{\Psi}^k(T) | \phi_f^k \rangle \langle \phi_f^k | \bar{\Psi}^k(T) \rangle \\ &\quad - 2Re \left\{ \langle \bar{\Psi}^k(T) | \phi_f^k \rangle \int_0^T \langle \bar{\Psi}^k(t) | i\hat{H}_{ion} + \partial/\partial t | \delta\bar{\Psi}^k(t) \rangle dt \right\}\end{aligned}$$

$$\begin{aligned}
& -2Re \left\{ \langle \delta \vec{\Psi}^k(T) | \phi_f^k \rangle \int_0^T \langle \vec{\Psi}^k(t) | i\hat{H}_{ion} + \partial/\partial t | \vec{\Psi}^k(t) + \delta \vec{\Psi}^k(t) \rangle dt \right\} \\
& \approx 2Re \langle \vec{\Psi}^k(T) | \phi_f^k \rangle \langle \phi_f^k | \delta \vec{\Psi}^k(T) \rangle \\
& -2Re \left\{ \langle \vec{\Psi}^k(T) | \phi_f^k \rangle \int_0^T \langle \vec{\Psi}^k(t) | i\hat{H}_{ion} + \partial/\partial t | \delta \vec{\Psi}^k(t) \rangle dt \right\} \\
& -2Re \left\{ \langle \delta \vec{\Psi}^k(T) | \phi_f^k \rangle \int_0^T \langle \vec{\Psi}^k(t) | i\hat{H}_{ion} + \partial/\partial t | \vec{\Psi}^k(t) \rangle dt \right\}. \quad (2.7.11)
\end{aligned}$$

Here we omit terms that depend quadratically on $\delta \vec{\Psi}^k$. From Eq. (2.7.9), the last term in Eq. (2.7.11) vanishes and we obtain:

$$\delta_{\vec{\Psi}^k} J = 2Re \left[\langle \vec{\Psi}^k(T) | \phi_f^k \rangle \left(\langle \phi_f^k | \delta \vec{\Psi}^k(T) \rangle - \int_0^T \langle \vec{\Psi}^k(t) | i\hat{H}_{ion} + \partial/\partial t | \delta \vec{\Psi}^k(t) \rangle dt \right) \right]. \quad (2.7.12)$$

Due to the choice of a time-independent $\delta \vec{\Psi}^k(t) = \delta \vec{\Psi}^k$, the time derivative $\partial/\partial t$ vanishes. By moving the operator $i\hat{H}_{ion}$ to the left, it was indicated it will work on $\vec{\Psi}^k(t)$, and then we get:

$$\delta_{\vec{\Psi}^k} J = 2Re \left[\langle \vec{\Psi}^k(T) | \phi_f^k \rangle \times \left(\langle \phi_f^k | \delta \vec{\Psi}^k \rangle - \int_0^T \langle -i\hat{H}_{ion} \vec{\Psi}^k(t) | \delta \vec{\Psi}^k \rangle dt \right) \right]. \quad (2.7.13)$$

Eq. (2.7.13) holds for a $\vec{\Psi}^k(t)$ satisfying the Schrödinger equation with boundary condition $\vec{\Psi}^k(T) = \phi_f^k$, so we obtain the following equation for each k , $k = \{1,2\}$:

$$\begin{aligned}
& i \frac{\partial}{\partial t} \vec{\Psi}^k(t) = \hat{H}_{ion} \vec{\Psi}^k(t), \\
& \vec{\Psi}^k(T) = \phi_f^k, \quad (2.7.14)
\end{aligned}$$

These are two time-dependent Schrödinger equations propagated backward in time, each one with its own target state ϕ_f^k as a boundary condition.

Finally, the variations $\varepsilon(t)$ lead to the optimal field:

$$\begin{aligned}
\delta_E J &= J(\vec{\Psi}^k(t), \vec{\Psi}^k(t), \varepsilon(t) + \delta\varepsilon(t)) - J(\vec{\Psi}^k(t), \vec{\Psi}^k(t), \varepsilon(t)) \\
&= \alpha_0 \int_0^T \frac{|\varepsilon(t)|^2}{s(t)} dt - \alpha_0 \int_0^T \frac{|\varepsilon(t) + \delta\varepsilon(t)|^2}{s(t)} dt \\
&\quad - 2 \sum_{k=1,2} \operatorname{Re} \left\{ \langle \vec{\Psi}^k(T) | \phi_f^k \rangle \int_0^T \langle \vec{\Psi}^k(t) | -i\delta\varepsilon(t)d(z) | \vec{\Psi}^k(t) \rangle dt \right\} \\
&= -\alpha_0 \int_0^T \frac{2\varepsilon(t)\delta\varepsilon(t) + \delta\varepsilon^2(t)}{s(t)} dt \\
&\quad - 2 \sum_{k=1,2} \operatorname{Im} \left\{ \int_0^T \langle \vec{\Psi}^k(T) | \phi_f^k \rangle \langle \vec{\Psi}^k(t) | d(z) | \vec{\Psi}^k(t) \rangle \delta\varepsilon(t) dt \right\} \\
&\approx - \int_0^T \left\{ 2\alpha_0 \frac{\varepsilon(t)}{s(t)} + 2 \sum_{k=1,2} \operatorname{Im} \langle \vec{\Psi}^k(T) | \phi_f^k \rangle \langle \vec{\Psi}^k(t) | d(z) | \vec{\Psi}^k(t) \rangle \right\} \delta\varepsilon(t) dt \quad (2.7.15)
\end{aligned}$$

Eq. (2.6.1) was used here. Eq. (2.7.15) can be satisfied for all $\delta E(t)$ only when

$$\alpha_0 \frac{\varepsilon(t)}{s(t)} + \sum_{k=1,2} \operatorname{Im} \langle \vec{\Psi}^k(T) | \phi_f^k \rangle \langle \vec{\Psi}^k(t) | d(z) | \vec{\Psi}^k(t) \rangle = 0. \quad (2.7.16)$$

From Eqs. (2.7.10) and (2.7.14), we can obtain:

$$\frac{d \langle \vec{\Psi}^k(t) | \vec{\Psi}^k(t) \rangle}{dt} = 0. \quad (2.7.17)$$

So,

$$\langle \vec{\Psi}^k(t) | \vec{\Psi}^k(t) \rangle = \langle \vec{\Psi}^k(T) | \vec{\Psi}^k(T) \rangle, \quad (2.7.18)$$

Finally, we obtain the equation of the field:

$$\varepsilon(t) = -\frac{s(t)}{\alpha_0} \operatorname{Im} \sum_{k=1,2} \langle \vec{\Psi}(t) | \vec{\Psi}(t) \rangle \langle \vec{\Psi}(t) | d(z) | \vec{\Psi}(t) \rangle, \quad (2.7.19)$$

here the sum is over the two optimized transitions of interest and the four Schrödinger

equations (2.7.10) and (2.7.14) are coupled only through this field equation (2.7.19).

2.8 Numerical propagation of vibrational wavepackets

The forward and backward propagation of the time-dependent Schrödinger equation is achieved by expanding the time-dependent wavefunction $\vec{\Psi}(z, t)$ and $\overleftarrow{\Psi}(z, t)$ over the basis set of eigenstates $\Psi_v(z)$ of the system with time-dependent complex coefficients $a_v(t)$ and $b_{v'}(t)$:

$$i \dot{\Psi}(z, t) = \hat{H}_{ion} \Psi(z, t), \quad (2.8.1)$$

$$\vec{\Psi}(z, t) = \sum_{v=1}^L a_v(t) e^{-iE_v t} \Psi_v(z), \quad (2.8.2)$$

$$\overleftarrow{\Psi}(z, t) = \sum_{v'=1}^L b_{v'}(t) e^{-iE_{v'} t} \Psi_{v'}(z), \quad (2.8.3)$$

where \hat{H}_{ion} is from Eq. (2.6.1). Indexes v and v' label eigenstates of the system and L is the total number of states in the expansion used for the propagation ($L \leq N$).

Probability of the system in states v and v' can be computed as $|a_v(t)|^2$ and $|b_{v'}(t)|^2$.

Substituting $\vec{\Psi}(z, t)$ from Eq. (2.8.2) into Eq. (2.8.1), we can obtain the following coupled equations for time evolution of coefficient $a_v(t)$ for the forward propagation:

$$\begin{aligned} i \sum_{v=1}^L & \{ \dot{a}_v(t) e^{-iE_v t} + a_v(t) e^{-iE_v t} (-iE_v) \} \Psi_v \\ &= \sum_{v=1}^L a_v(t) e^{-iE_v t} \hat{H} \Psi_v - \sum_{v=1}^L a_v(t) e^{-iE_v t} \varepsilon(t) d(z) \Psi_v. \end{aligned} \quad (2.8.4)$$

In Dirac form, it can be rewritten as follows:

$$\begin{aligned}
& i \sum_{v=1}^L \{ \dot{a}_v(t) e^{-iE_v t} + a_v(t) e^{-iE_v t} (-iE_v) \} |v\rangle \\
& = \sum_{v=1}^L a_v(t) e^{-iE_v t} E_v |v\rangle - \sum_{v=1}^L a_v(t) e^{-iE_v t} \varepsilon(t) d(z) |v\rangle. \tag{2.8.5}
\end{aligned}$$

Or,

$$i \sum_{v=1}^L e^{-iE_v t} \dot{a}_v(t) |v\rangle = -\varepsilon(t) \sum_{v=1}^L e^{-iE_v t} d(z) a_v(t) |v\rangle. \tag{2.8.6}$$

Multiplying Eq. (2.8.6) by $e^{iE_{v'} t} \langle v' |$ from the left and integrating, we obtain:

$$i \dot{a}_{v'}(t) = -\varepsilon(t) \sum_{v=1}^L e^{-i(E_v - E_{v'})t} M_{v,v'} a_v(t). \tag{2.8.7}$$

Here $M_{v,v'}$ is the element of the transition matrix defined in Eq. (2.6.7).

If we split Eq. (2.8.7) into its real and imaginary parts, the following equations are obtained ($v \leq L$):

$$\dot{a}_{v'}^R(t) = \varepsilon(t) \sum_{v=1}^L (a_v^R(t) \sin \theta_{v,v'} - a_v^I(t) \cos \theta_{v,v'}) M_{v,v'}, \tag{2.8.8}$$

$$\dot{a}_{v'}^I(t) = \varepsilon(t) \sum_{v=1}^L (a_v^R(t) \cos \theta_{v,v'} + a_v^I(t) \sin \theta_{v,v'}) M_{v,v'}, \tag{2.8.9}$$

where $\theta_{v,v'} = (E_v - E_{v'})t$ is the phase shift. $\dot{a}_{v'}^R(t)$ and $\dot{a}_{v'}^I(t)$ represent real and imaginary parts of complex coefficient $\dot{a}_{v'}(t)$.

Similarly, if we follow the same procedure to derive the equations for the backward propagation, we will come to the same equations as Eqs. (2.8.7)-(2.8.9) (but $a(t)$ substituted by $b(t)$). For simplicity, in the following derivation we only show

the equations for forward propagation.

The optimized field $\varepsilon(t)$ in Eqs. (2.8.8) and (2.8.9) is calculated using Eq. (2.7.19). Expansions for $\vec{\Psi}(t)$ and $\tilde{\Psi}(t)$ are needed during the calculation:

$$\vec{\Psi}(t) = \sum_{v=1}^L a_v(t) e^{-iE_v t} |v\rangle, \quad (2.8.10)$$

$$\tilde{\Psi}(t) = \sum_{v'=1}^L b_{v'}(t) e^{-iE_{v'} t} |v'\rangle, \quad (2.8.11)$$

Substituting Eqs. (2.8.10) and (2.8.11) into Eq. (2.7.19), the different parts of Eq. (2.7.19) are rewritten as follows:

$$\langle \vec{\Psi}(t) | \tilde{\Psi}(t) \rangle = \sum_{v=1}^L a_v^*(t) b_v(t), \quad (2.8.12)$$

$$\langle \vec{\Psi}(t) | \tilde{\Psi}(t) \rangle^R = \sum_{v=1}^L (a_v^R(t) b_v^R(t) + a_v^I(t) b_v^I(t)), \quad (2.8.13)$$

$$\langle \vec{\Psi}(t) | \tilde{\Psi}(t) \rangle^I = \sum_{v=1}^L (a_v^R(t) b_v^I(t) - a_v^I(t) b_v^R(t)), \quad (2.8.14)$$

$$\begin{aligned} \langle \tilde{\Psi}(t) | d(z) | \vec{\Psi}(t) \rangle &= \sum_{v=1}^L \sum_{v'=1}^L [(\text{Re}_{v,v'} \cos \theta_{v,v'} + \text{Im}_{v,v'} \sin \theta_{v,v'}) \\ &\quad + i(\text{Im}_{v,v'} \cos \theta_{v,v'} - \text{Re}_{v,v'} \sin \theta_{v,v'})] M_{v,v'}, \end{aligned} \quad (2.8.15)$$

where

$$\text{Re}_{v,v'} = a_v^R(t) b_{v'}^R(t) + a_v^I(t) b_{v'}^I(t), \quad (2.8.16)$$

$$\text{Im}_{v,v'} = a_v^I(t) b_{v'}^R(t) - a_v^R(t) b_{v'}^I(t). \quad (2.8.17)$$

Now everything is ready for solving Eqs. (2.8.8) and (2.8.9).

Note that the forward and backward propagation follow the same equations which simplifies our calculations a lot. But one thing we need to point out is that the initial condition of the forward and backward propagation have to be set up differently. Assume that the initial and final target states are given by:

$$\phi_i = \sum_{v'=1}^L \tilde{a}_{v'}, |v'\rangle, \quad (2.8.18)$$

$$\phi_f = \sum_{v'=1}^L \tilde{b}_{v'}, |v'\rangle. \quad (2.8.19)$$

For the forward propagation, because at $t = 0$ the phase term in Eq. (2.8.10) is equal to 1, the wave function at $t = 0$ can be written as:

$$\vec{\Psi}(t = 0) = \sum_{v'=1}^L a_{v'}(t = 0) |v'\rangle. \quad (2.8.20)$$

Comparing Eqs. (2.8.18) and (2.8.20) we see that the initial boundary values are equal to the input coefficients: $a_{v'}(t = 0) = \tilde{a}_{v'}$.

For the backward propagation, the setup becomes more complicated. The wave function at $t = T$ is:

$$\vec{\Psi}(t = T) = \sum_{v'=1}^L b_{v'}(t = T) e^{-iE_{v'}T} |v'\rangle, \quad (2.8.21)$$

The final boundary values for backward propagation are obtained from $b_{v'}(t = T) e^{-iE_{v'}T} = \tilde{b}_{v'}$. Now the phase term cannot be neglected any more, so we have to find out the relationship between $b_{v'}(t = T)$ and $\tilde{b}_{v'}$ in order to start propagation of

the wave function backward. After some mathematical manipulation, the equations

for $b_{v'}(t = T)$ are obtained:

$$b_{v'}^R(t = T) = \tilde{b}_{v'}^R \cos E_{v'} T - \tilde{b}_{v'}^I \sin E_{v'} T, \quad (2.8.22)$$

$$b_{v'}^I(t = T) = \tilde{b}_{v'}^R \sin E_{v'} T + \tilde{b}_{v'}^I \cos E_{v'} T, \quad (2.8.23)$$

Where $b_{v'}^R$ and $b_{v'}^I$, are the real and imaginary part of $b_{v'}$, $\tilde{b}_{v'}^R$ and $\tilde{b}_{v'}^I$, are the real and imaginary parts of the input value of $\tilde{b}_{v'}$, for backward propagation.

When the boundary conditions are set up, we can solve the Eqs. (2.8.8) and (2.8.9) both forward and backward by the fourth-order Runge-Kutta method using RK4 subroutine of the numerical recipes [80]. The general optimization code (Program MAIN, see Appendix B) was initially written by Dr. Babikov, but was substantially modified for this work [63, 84, 85, 90, 91]. The code solves Eqs. (2.8.8), (2.8.9) iteratively and calculates the field $\varepsilon(t)$ using Eq. (2.7.19). The spectra of eigenvalues and the transition matrix, which are obtained from code 1DIONTRAP in Appendix A, are needed as input files for this code.

2.9 Quantum bits (qubits), quantum gates and quantum computation

An electrical circuit containing wires and logic gates; a quantum computer is theoretically built from a quantum circuit containing wires and elementary quantum gates which is analogous to the way a classical computer is built from. Changes occurring to a quantum state can be described using the language of quantum

computation in order to carry around and manipulate the quantum information. The simplest case is the single qubit gates [53].

Just as a classical bit has a state – either $\{0\}$ or $\{1\}$ – a qubit also has a state. Two possible states for a qubit are the states $|0\rangle$ and $|1\rangle$, which as you might guess correspond to the states $\{0\}$ and $\{1\}$ for a classical bit. The difference between bits and qubits is that a qubit can be in a state other than $|0\rangle$ and $|1\rangle$. It is also possible to form linear combinations of states, often called superpositions:

$$|\Psi\rangle = \alpha|0\rangle + \beta|1\rangle. \quad (2.9.1)$$

The numbers α and β are complex numbers. Differently, we cannot examine a qubit to determine its quantum state, the values of α and β . When we measure a qubit we get either the result 0, with probability $|\alpha|^2$, or the result 1, with probability $|\beta|^2$. Naturally, $|\alpha|^2 + |\beta|^2 = 1$, since the probabilities must sum to one. The state of a qubit is a vector in a two-dimensional complex vector space. The special states $|0\rangle$ and $|1\rangle$ are known as computational basis states, and form an orthonormal basis for this vector space.

Classical computer circuits consist of wires and logic gates. The wires are used to carry information around the circuit. The logic gates perform manipulations of the information and convert it from one form to another. For example, classical single bit logic gates – the only non-trivial member of this class is the NOT gate. The

operation of gate NOT is defined by its truth table, in which $\text{NOT}\{0\} \rightarrow \{1\}$ and $\text{NOT}\{1\} \rightarrow \{0\}$, that means, the $\{0\}$ and $\{1\}$ states are interchanged by the action of this gate.

To define an analogous quantum NOT gate using qubits, we can imagine that we had some process which took the state $|0\rangle$ to the state $|1\rangle$, and vice versa. Such a process would obviously be a good candidate for a quantum analogue to the NOT gate. However, specifying the action of the gate on the states $|0\rangle$ and $|1\rangle$ does not tell us what happens to superpositions of the states $|0\rangle$ and $|1\rangle$, without further knowledge about the properties of quantum gates. In fact, the quantum NOT gate acts linearly, that is, it takes the state

$$\alpha|0\rangle + \beta|1\rangle \quad (2.9.2)$$

to the corresponding state in which the role of $|0\rangle$ and $|1\rangle$ have been interchanged,

$$\alpha|1\rangle + \beta|0\rangle. \quad (2.9.3)$$

There is a convenient way of representing the quantum NOT gate in matrix form. Suppose we define a matrix U_{NOT} to represent the quantum NOT gate as follows:

$$U_{\text{NOT}} = \begin{vmatrix} 0 & 1 \\ 1 & 0 \end{vmatrix}. \quad (2.9.4)$$

If the quantum state $\alpha|0\rangle + \beta|1\rangle$ is written in a vector notation as

$$\begin{bmatrix} \alpha \\ \beta \end{bmatrix}, \quad (2.9.5)$$

with the top entry corresponding to the amplitude for $|0\rangle$ and the bottom entry the amplitude for $|1\rangle$, then the corresponding output from the quantum NOT gate is

$$U_{\text{NOT}} \begin{bmatrix} \alpha \\ \beta \end{bmatrix} = \begin{vmatrix} 0 & 1 \\ 1 & 0 \end{vmatrix} \begin{bmatrix} \alpha \\ \beta \end{bmatrix} = \begin{bmatrix} \beta \\ \alpha \end{bmatrix}. \quad (2.9.6)$$

Notice that the action of the NOT gate is to take the state $|0\rangle$ and replace it by the state corresponding to the first column of the matrix U_{NOT} . Similarly, the state $|1\rangle$ is replaced by the state corresponding to the second column of the matrix U_{NOT} .

So quantum gates on a single qubit can be described by two-by-two matrices. Recall that the normalization condition requires $\alpha^2 + \beta^2 = 1$ for a quantum state $\alpha|0\rangle + \beta|1\rangle$. This must also be true of the quantum state $|\Psi'\rangle = \alpha'|0\rangle + \beta'|1\rangle$ after the gate has acted. It turns out that the appropriate condition on the matrix representing the gate is that the matrix U describing the single qubit gate be unitary, that is $U^+U = I$, where U^+ is the Hermitian conjugate of U .

Amazingly, this unitarity constraint is the only constraint on quantum gates. Any unitary matrix specifies a valid quantum gate. The interesting implication is that in contrast to the classical case, where only one non-trivial single bit gate exists – the NOT gate. There are many non-trivial single qubit gates. One important is the Hadamard gate,

$$U_{\text{HAD}} = \frac{1}{\sqrt{2}} \begin{vmatrix} 1 & 1 \\ 1 & -1 \end{vmatrix}. \quad (2.9.7)$$

This gate is sometimes described as being like a “square-root of NOT” gate, in

that it turns a $|0\rangle$ into $(|0\rangle + |1\rangle)/\sqrt{2}$ (first column of U_{HAD}), “halfway” between $|0\rangle$ and $|1\rangle$, and turns $|1\rangle$ into $(|0\rangle - |1\rangle)/\sqrt{2}$ (second column of U_{HAD}), which is also “halfway” between $|0\rangle$ and $|1\rangle$.

$$U_{\text{HAD}} \begin{bmatrix} 1 \\ 0 \end{bmatrix} = \frac{1}{\sqrt{2}} \begin{vmatrix} 1 & 1 \\ 1 & -1 \end{vmatrix} \begin{bmatrix} 1 \\ 0 \end{bmatrix} = \frac{1}{\sqrt{2}} \begin{bmatrix} 1 \\ 1 \end{bmatrix}, \quad (2.9.8)$$

$$U_{\text{HAD}} \begin{bmatrix} 0 \\ 1 \end{bmatrix} = \frac{1}{\sqrt{2}} \begin{vmatrix} 1 & 1 \\ 1 & -1 \end{vmatrix} \begin{bmatrix} 0 \\ 1 \end{bmatrix} = \frac{1}{\sqrt{2}} \begin{bmatrix} 1 \\ -1 \end{bmatrix}. \quad (2.9.9)$$

The other important gate is the π -rotation gate (U_π):

$$U_\pi = \begin{vmatrix} 1 & 0 \\ 0 & e^{i\pi} \end{vmatrix} = \begin{vmatrix} 1 & 0 \\ 0 & -1 \end{vmatrix}, \quad (2.9.10)$$

which leaves the state populations unchanged, but introduces the phase difference between the states $|0\rangle$ and $|1\rangle$:

$$U_\pi \begin{bmatrix} 1 \\ 0 \end{bmatrix} = \begin{vmatrix} 1 & 0 \\ 0 & -1 \end{vmatrix} \begin{bmatrix} 1 \\ 0 \end{bmatrix} = \begin{bmatrix} 1 \\ 0 \end{bmatrix}, \quad (2.9.11)$$

$$U_\pi \begin{bmatrix} 0 \\ 1 \end{bmatrix} = \begin{vmatrix} 1 & 0 \\ 0 & -1 \end{vmatrix} \begin{bmatrix} 0 \\ 1 \end{bmatrix} = \begin{bmatrix} 0 \\ -1 \end{bmatrix}. \quad (2.9.12)$$

It is important to note that these three gates, together with the conditional two-qubit gate CNOT and the conditional three-qubit Toffoli gate (See section 3.2 and 6.5), form a universal set of quantum gates sufficient to represent any quantum algorithm.

2.10 Examples of pulse optimization

Although the optimal control theory methods developed for molecular vibrations can be used to control the motion of ions in a trap, the computational aspect of the trapped ion is complicated by several special properties: i) the spatial extent of

the motional wave functions $\Psi(z)$ of ion in a trap (~ 50 nm) is 500 times larger than the amplitude of a typical molecular vibration; ii) The energy differences between the motional states of ions in a trap (~ 1 MHz) is about 10^7 times smaller than that in the molecules; iii) The time scale of ionic motion (and control) is 10^8 times longer than the femtosecond scale of molecular motion. Due to these features, the time step for numerical propagation of ionic wavefunctions was very large, $dt \approx 3.3$ ns. The penalty factor was chosen to be a large number ($\alpha_0 = 10^{12}$) to reduce the field amplitude to the optimal level. The overall convergence of iterations was very slow and $\sim 10^4$ forward-backward propagation cycles were necessary to converge $\varepsilon(t)$.

In order to start the iterative improvement of the field, we use the “guess” pulse in the following form:

$$\varepsilon_{ini}(t) = A * \sin(|E_2 - E_1|t). \quad (2.10.1)$$

Here A is a guessed amplitude of the electric field, E_1 and E_2 are the energies of the ground and first excited states, $|0\rangle$ and $|1\rangle$. During the propagation, α_0 from Eq. (2.7.19) is used to restrict the amplitude of the field and the shape of the pulse is modified step by step under the influence of Eq. (2.7.19).

a) Qubit flips

Here, as the simplest example, we optimize the pulse for a transition: $|0\rangle \rightarrow |1\rangle$, which gives general understanding of our optimal control approach. We

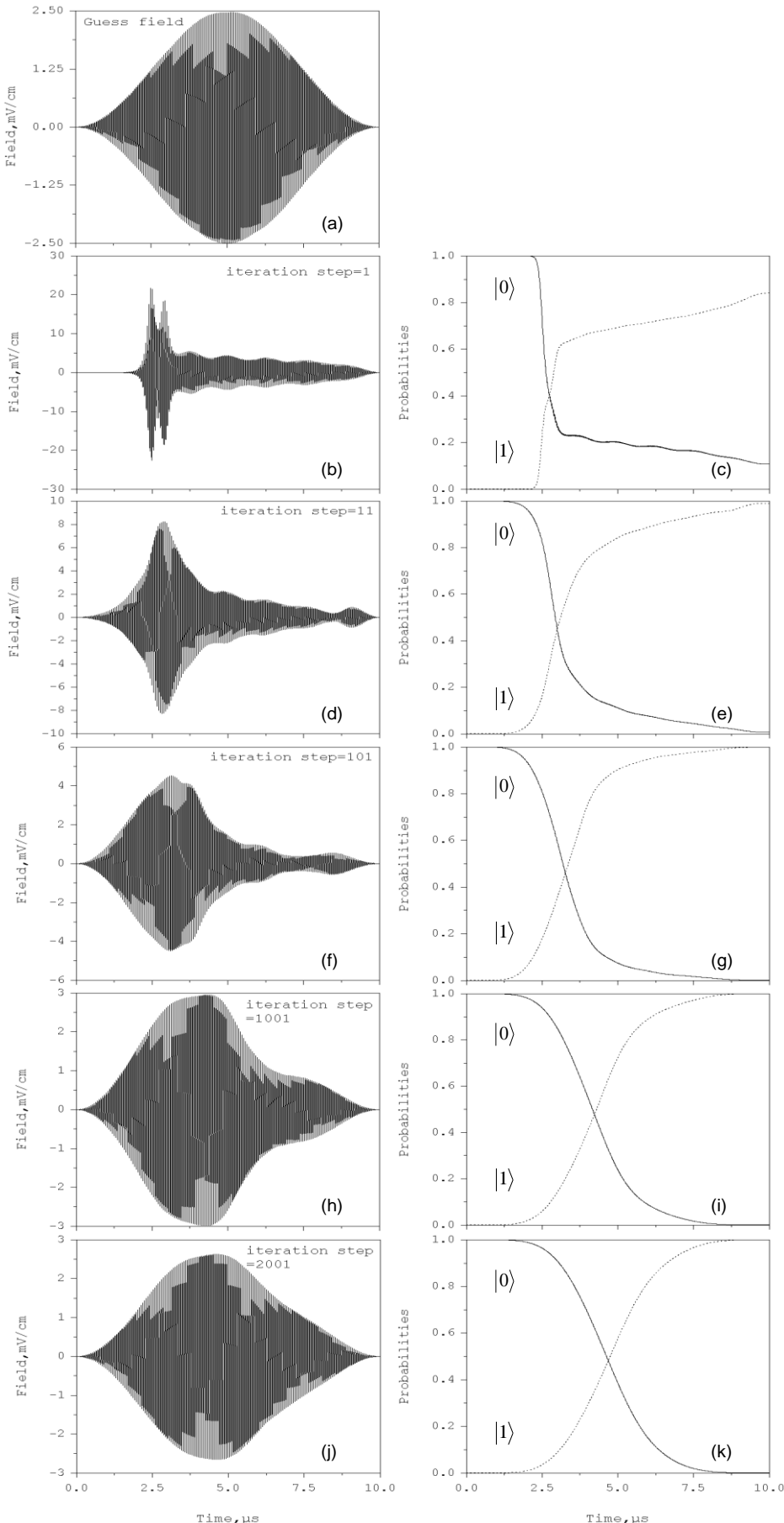


Fig. 2.8: Pulse optimization for the qubit flip: $|0\rangle \rightarrow |1\rangle$ in the $^{111}\text{Cd}^+$ ion trap. (a) The guess field. (b) – (k) The optimized pulse and evolution of state populations after 1, 11, 101, 1001 and 2001 iteration steps.

numerically solve Eq. (2.7.19) to calculate the optimal pulses for this qubit flip with the ground vibrational state $|0\rangle$ being the initial boundary condition and the first excited vibrational state $|1\rangle$ being the final boundary condition. In Fig. 2.8 (a) we present the initial guess field with target time $T = 10 \mu\text{s}$. The process of optimization procedure is demonstrated in Fig. 2.8 (b) – (i) where the pulses after 1, 11, 101, 1001 and 2001 iterations are shown. The guess field is from Eq. (2.10.1). Such field carries single frequency. The amplitude changes gradually according to simple and symmetric function. The transition probabilities are shown together with the pulse and

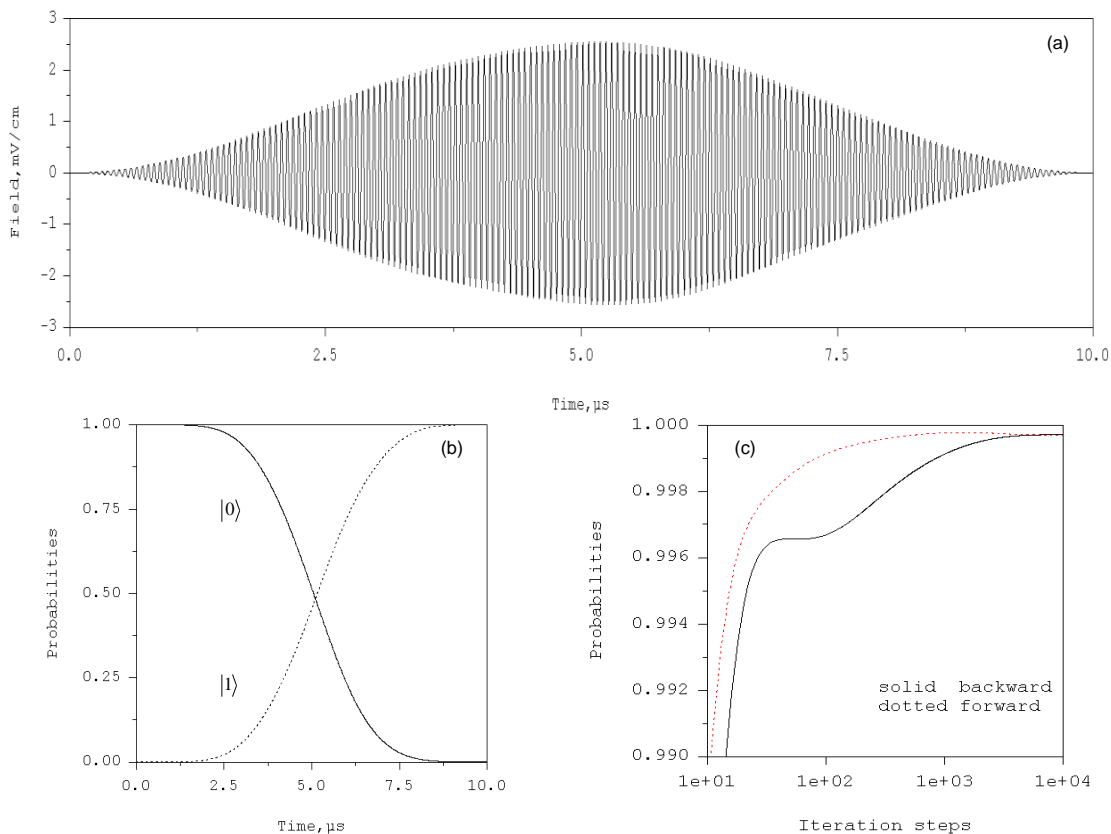


Fig. 2. 9: (a) The control pulse for qubit flip $|0\rangle \rightarrow |1\rangle$ in the $^{111}\text{Cd}^+$ ion trap. (b) Switching of state populations during the transition $|0\rangle \rightarrow |1\rangle$. (c) Convergence of the iterative procedure and the final transition probability.

they go up as iterations proceed. Fig. 2.9 (a) shows the optimized pulse $\varepsilon(t)$ for the transition $|0\rangle \rightarrow |1\rangle$ after 10,001 iteration steps, target time $T = 10 \mu\text{s}$. The optimized pulse shape is quite simple and nearly symmetric with the maximum amplitude about 2.8 mV/cm. Figure 2.9 (b) shows time evolution of the probabilities in two vibrational states during the pulse action. At $t = 0$, the ion is in state $v = |0\rangle$ with probability equal to 1. During the pulse, the probability in state $|0\rangle$ decreases, while the probability in state $|1\rangle$ increases. In the end $t = T$, the probability is transferred to state $v = |1\rangle$ almost completely (up to 0.999).

Convergence study was carried out to make sure that our results are reliable. The transition probabilities of forward and backward propagations are plotted in Fig. 2.9 (c), the curves are smooth and the results begin to converge after about 4000 iteration steps with accuracy approaching to 0.999.

b) Gate NOT

More complicated qubit transformation is presented by the gate NOT, where we need to control two transitions simultaneously from Eqs. (2.7.4) and (2.7.5). For the gate NOT: as many as 20,001 forward-backward iteration cycles were required to achieve convergence. The results are summarized in Fig. 2.10. The formulas of the average transition probability are given by the following equations:

$$P_i = \frac{1}{2} \sum_{k=1}^K |\langle \phi_i^k | \tilde{\Psi}^k(t=0) \rangle|^2, \quad (2.10.2)$$

$$P_f = \frac{1}{2} \sum_{k=1}^K |\langle \phi_f^k | \vec{\Psi}^k(t=T) \rangle|^2. \quad (2.10.3)$$

Where $K = 2$ is the number of transitions optimized simultaneously.

From Fig. 2.10, we can see that the optimized pulse of gate NOT is quite simple and nearly symmetric with the maximum amplitude about 2.8 mV/cm. The

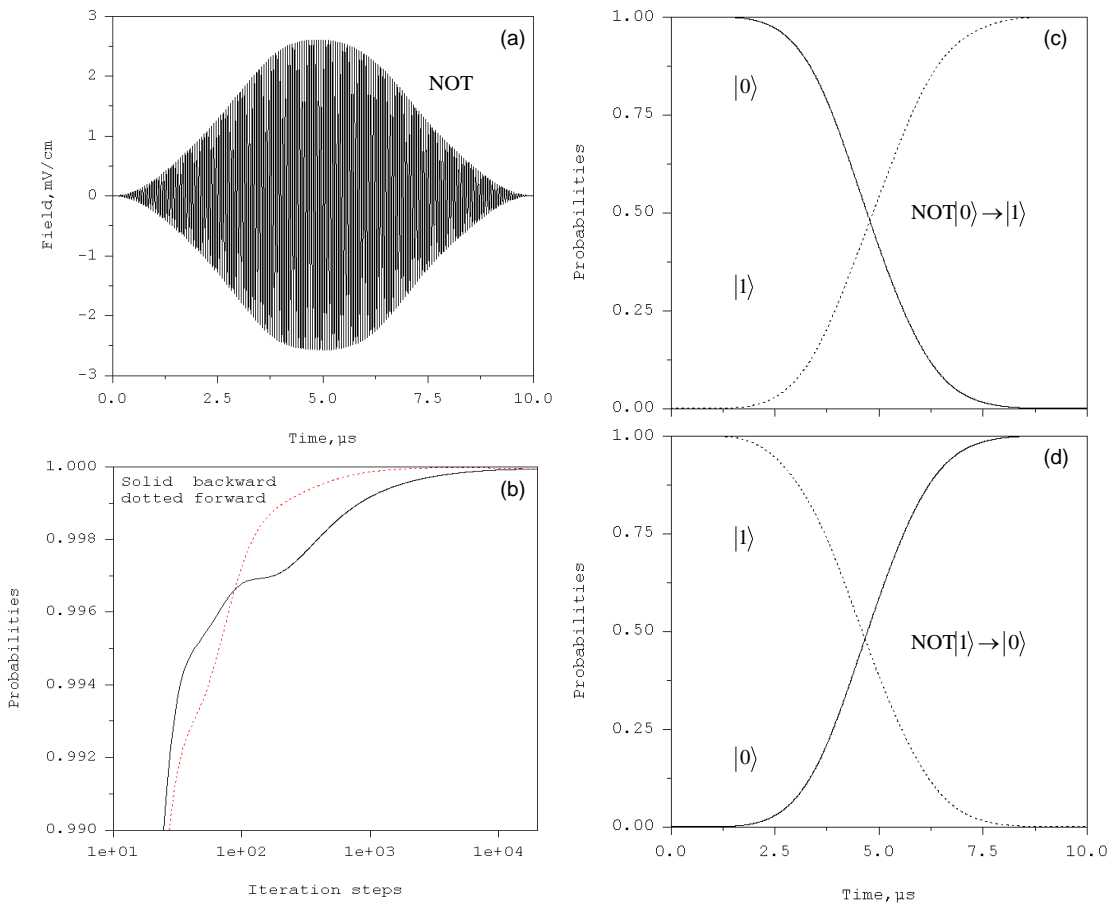


Fig. 2. 10: The gate NOT in the $^{111}\text{Cd}^+$ ion trap optimized with two transitions. (a) Optimally shaped electric field. (b) Average probability of the gate. (c) Switching of population between the qubit states during the $\text{NOT}|0\rangle \rightarrow |1\rangle$. (d) Switching of population between the qubit states during the $\text{NOT}|1\rangle \rightarrow |0\rangle$.

pulse duration is 10 μs . The results converge very fast – within about 4000 iterations.

Both transitions are controlled accurately, up to 0.999. If the state is first in $v = |0\rangle$, it is excited to $v = |1\rangle$. In contrast, if it is first in $v = |1\rangle$, population is transferred into stat $v = |0\rangle$ after the action of the pulse.

C) Hadamard gate, phase control

For the gates like Hadamard transformation:

$$\text{HAD}|0\rangle \rightarrow \frac{1}{\sqrt{2}}(|0\rangle + |1\rangle), \quad (2.10.4)$$

$$\text{HAD}|1\rangle \rightarrow \frac{1}{\sqrt{2}}(|0\rangle - |1\rangle). \quad (2.10.5)$$

The phase information is important and gate fidelity, F , should be computed as a

coherent sum over the optimized transitions.

$$F_i = \frac{1}{K^2} \left| \sum_{k=1}^K \langle \phi_i^k | \bar{\Psi}^k(t=0) \rangle \right|^2, \quad (2.10.6)$$

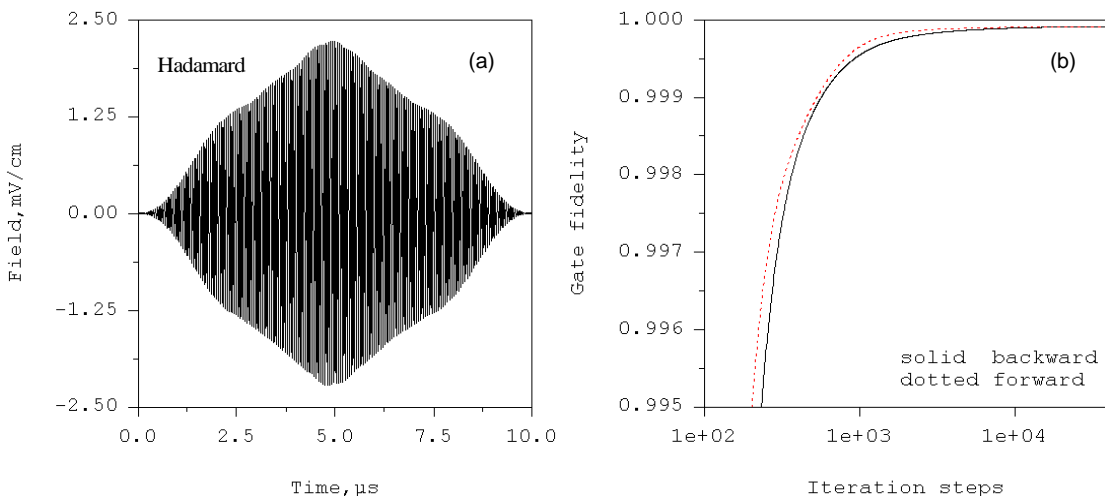


Fig. 2. 11: (a) Optimally shaped pulse for the gate Hadamard in the $^{111}\text{Cd}^+$ ion trap.
(b) The convergence of iterations and final fidelity of the qubit transformation.

$$F_f = \frac{1}{K^2} \left| \sum_{k=1}^K \langle \phi_f^k | \vec{\Psi}^k(t = T) \rangle \right|^2. \quad (2.10.7)$$

Here $K = 2$.

It was shown in the literature [85, 92] that optimizing just two transitions is not enough. At least one (or two) additional transitions should be included into the optimization process, in order to constrain the common phase. For example, the transition

$$\text{HAD} \frac{1}{\sqrt{2}} (|0\rangle + |1\rangle) \rightarrow |0\rangle, \quad (2.10.8)$$

and/or

$$\text{HAD} \frac{1}{\sqrt{2}} (|0\rangle - |1\rangle) \rightarrow |1\rangle, \quad (2.10.9)$$

must be optimized simultaneously with transitions of Eqs. (2.10.4) and (2.10.5). Such calculations were carried out, and converged results were obtained after 40,001 iteration steps. They are summarized in the Fig. 2.11 and 2.12. The pulse shape in Fig. 2.11 is simple with the maximum amplitude about 2.3 mV/cm. Because we optimize four transitions simultaneously, the pulse is almost symmetric. Such a pulse is easy to create in the experiment. From Fig. 2.12 we can see that the transitions to the target states for Hadamard gate are not straight forward. For example, in Fig. 2.12(a), the population in states $|0\rangle$ and $|1\rangle$ is nearly 0.5 at about 5.5 μ s. However it does not stop there, the population of state $|0\rangle$ is transferred further into state $|1\rangle$. At the end of the pulse duration, it returns to 0.5. Still, the transition probabilities for all four transitions

are very high simultaneously. The fidelity of Hadamard transformation is ~ 0.999 .

Iterations begin to converge after about 3000 forward-backward loops.

2.11 Conclusions

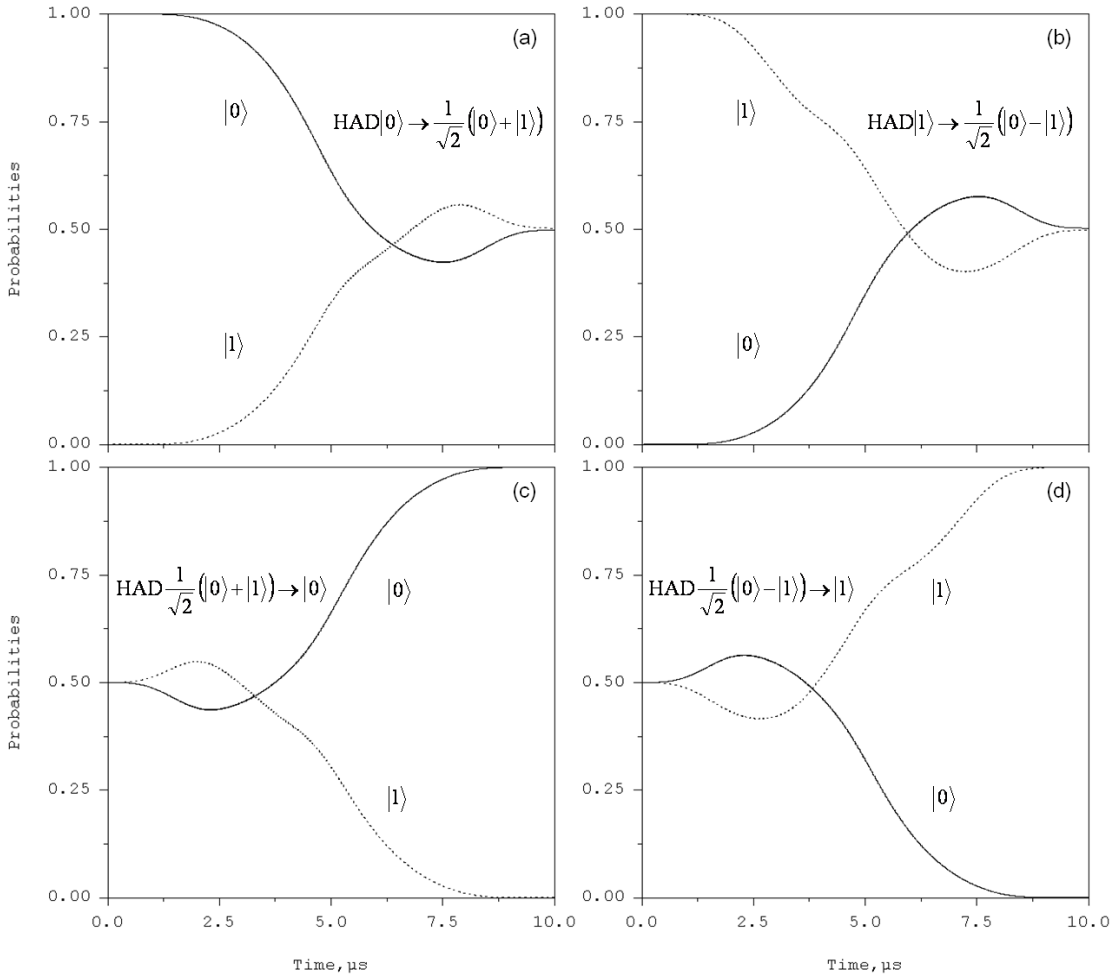


Fig. 2. 12: The gate Hadamard in the $^{111}\text{Cd}^+$ ion trap. (a) Creation of linear superposition of the qubit states as required by $\text{HAD}|0\rangle \rightarrow 1/\sqrt{2}(|0\rangle + |1\rangle)$. (b) The same during the $\text{HAD}|1\rangle \rightarrow 1/\sqrt{2}(|0\rangle - |1\rangle)$ transformation. (c) The same during the $\text{HAD}\frac{1}{\sqrt{2}}(|0\rangle + |1\rangle) \rightarrow |0\rangle$ transformation. (d) The same during the $\text{HAD}\frac{1}{\sqrt{2}}(|0\rangle - |1\rangle) \rightarrow |1\rangle$ transformation.

In this chapter, we developed general theory, numerical methodology and computer codes to calculate the eigenvalues and wavefunctions of one ion in the anharmonic trap. Small anharmonictiy ($\Delta = 0.008\Omega$) was found large enough to carry our very accurate state-to-state transformations [55, 63, 69, 70, 84, 90, 91, 93]. Pulses for a set of major quantum gates were optimized, such as qubit flips, gate NOT, CNOT and Hadamard transformation. The fidelity of all the transformations is very high, ~ 0.999 . The field patameters obtained after optimization are $\varepsilon_{max} \approx 2.5$ mV/cm and $T = 10$ μ s. Because the optimized pulses are simple and symmetric, such pulses should be easy to create in the experiment.

Chapter 3: Feasibility of Encoding Shor's Algorithm into the Motional States of Ion in the Anharmonic Trap

Those gates we optimized in Chapter 2 are used to control one-qubit encoded into states $|0\rangle$ and $|1\rangle$. One can expand this idea onto larger number of qubits by controlling more states. In general, in order to represent n qubits we need 2^n quantum states. Here we consider 16 lowest vibrational states of one ion in the anharmonic trap to represent a four-qubit system.

3.1 The model system

In this study we applied the same anharmonic system (the trapping potential is from Eq. (2.1.4)) as in Chapter 2. The two force constants k and k' of the anharmonic trapping potential are of the same values as in Chapter 2, with $k/2\pi = 1.483 \times 10^{-3}$ MHz/ a_0^2 and $k'/2\pi = 1.067 \times 10^{-7}$ MHz/ a_0^4 . The resultant anharmonic potential along the axial direction of the trap is shown in Fig. 3.1. Energy eigenvalues for the lower sixteen vibrational states are given in Table 3.1. The vibrational quantum number, v , is assigned to each state. Since anharmonicity is relatively small, wave functions of these states (not shown here) look very similar to the wave functions of harmonic oscillator. However, the effect of anharmonicity is easy to spot if one looks at the transition frequencies. The frequencies for excitation of one quantum of vibration, $\omega_{n,n+1}$, and three quanta of vibration, $\omega_{n,n+3}$, are also

given in Table 3.1 for each state. These frequencies increase as the vibrational quantum number increases. For example, for single excitation of the ground state the frequency is $\omega_{0,1}/2\pi = 2.8151$ MHz, while for the 16th state it is $\omega_{15,16}/2\pi = 3.3376$ MHz, which is about 19% higher. Effect of similar magnitude is found if we compare frequencies for excitation of three quanta of vibration:

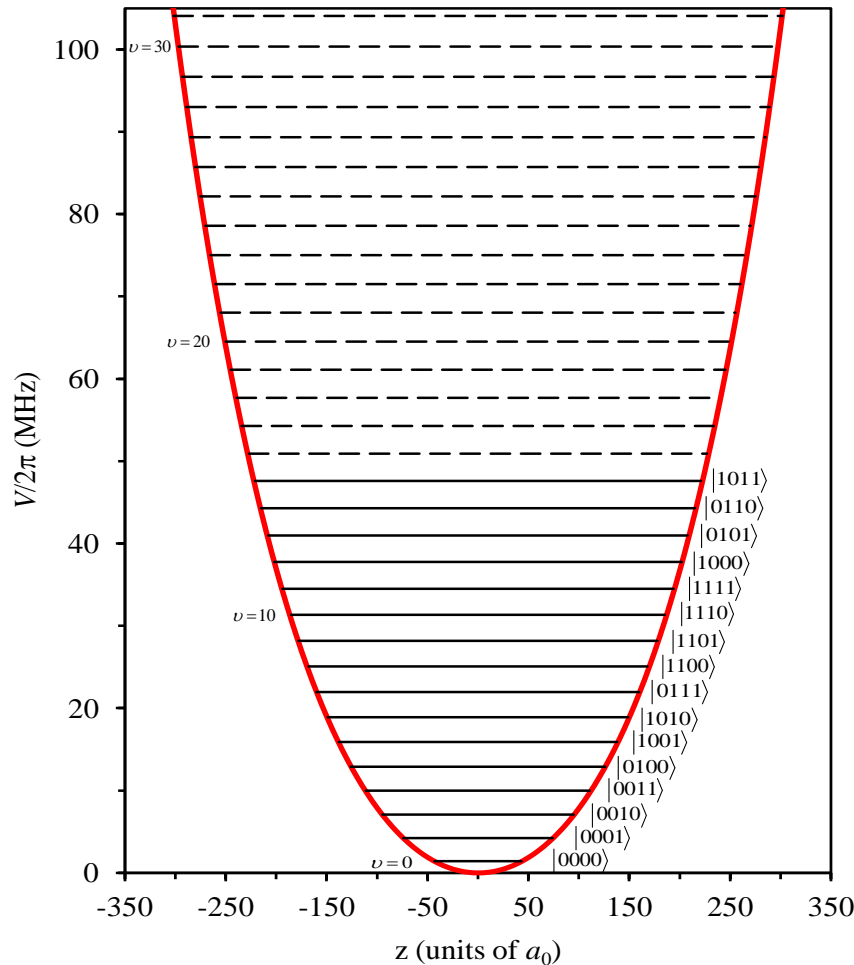


Fig. 3. 1: Weakly anharmonic trapping potential in the model system. Energies of thirty-two quantized motional states of one trapped $^{111}\text{Cd}^+$ ion are indicated by horizontal lines. Effect of anharmonicity is clearly seen. Sixteen lower states (used to encode qubits) are indicated by solid lines. Upper states (included for completeness) are shown by dashed lines. Assignment of states of the four-qubit system is indicated in brackets.

Table 3. 1: Eigenvalues, transition frequencies, qubit state assignments, optimized transformations and their characteristic probabilities for sixteen lower vibrational states in a model of $^{111}\text{Cd}^+$ ion in a weakly anharmonic Paul trap.

v	$E/2\pi$ (MHz)	$\omega_{n,n+1}/2\pi$ (MHz)	$\omega_{n,n+3}/2\pi$ (MHz)	Qubit states	Transformations of the Shor's algorithm		Characteristic Probabilities
0	1.3964	2.8151	8.5743	$ 0000\rangle$	#1	$ 0\rangle \rightarrow \frac{1}{2}(1\rangle + 2\rangle + 5\rangle - 6\rangle)$	0.9977
1	4.2115	2.8587	8.6999	$ 0001\rangle$	#2	$ 1\rangle \rightarrow 0\rangle$	0.9979
2	7.0702	2.9005	8.8207	$ 0010\rangle$	#3	$ 2\rangle \rightarrow 3\rangle$	0.9995
3	9.9707	2.9407	8.9372	$ 0011\rangle$	#4	$ 3\rangle \rightarrow \frac{1}{2}(1\rangle + 2\rangle - 5\rangle + 6\rangle)$	0.9977
4	12.9115	2.9795	9.0496	$ 0100\rangle$	#5	$ 4\rangle \rightarrow \frac{1}{2}(1\rangle - 2\rangle + 5\rangle + 6\rangle)$	0.9992
5	15.8910	3.0169	9.1584	$ 1001\rangle$	#6	$ 5\rangle \rightarrow \frac{1}{2}((1+i) 4\rangle + (1-i) 8\rangle)$	0.9991
6	18.9079	3.0532	9.2639	$ 1010\rangle$	#7	$ 6\rangle \rightarrow \frac{1}{2}((1+i) 7\rangle + (1-i) 11\rangle)$	0.9981
7	21.9611	3.0883	9.3662	$ 0111\rangle$	#8	$ 7\rangle \rightarrow \frac{1}{2}(- 1\rangle + 2\rangle + 5\rangle + 6\rangle)$	0.9990
8	25.0494	3.1224	9.4657	$ 1100\rangle$	#9	$ 8\rangle \rightarrow \frac{1}{2}(9\rangle + i 10\rangle + 13\rangle - i 14\rangle)$	0.9985
9	28.1718	3.1555	9.5626	$ 1101\rangle$	#10	$ 9\rangle \rightarrow \frac{1}{2}((1-i) 4\rangle + (1+i) 8\rangle)$	0.9986
10	31.3273	3.1878	9.6569	$ 1110\rangle$	#11	$ 10\rangle \rightarrow \frac{1}{2}((1-i) 7\rangle + (1+i) 11\rangle)$	0.9986
11	34.5151	3.2192	9.7489	$ 1111\rangle$	#12	$ 11\rangle \rightarrow \frac{1}{2}(i 9\rangle + 10\rangle - i 13\rangle + 14\rangle)$	0.9994
12	37.7343	3.2499	9.8387	$ 1000\rangle$	#13	$ 12\rangle \rightarrow \frac{1}{2}(9\rangle - i 10\rangle + 13\rangle + i 14\rangle)$	0.9991
13	40.9842	3.2798	9.9265	$ 0101\rangle$	#14	$ 13\rangle \rightarrow 12\rangle$	0.9995
14	44.2640	3.3090	10.0123	$ 0110\rangle$	#15	$ 14\rangle \rightarrow 15\rangle$	0.9996
15	47.5731	3.3376	10.0963	$ 1011\rangle$	#16	$ 15\rangle \rightarrow \frac{1}{2}(-i 9\rangle + 10\rangle + i 13\rangle + 14\rangle)$	0.9982

$\omega_{0,3}/2\pi = 8.5743$ MHz against $\omega_{15,18}/2\pi = 10.0963$ MHz.

Another way to quantify anharmonicity of the spectrum is to fit the spectrum by Dunham's analytic expression from Eq. (2.5.1) [83]. Using numerical values of energies of three lower states ($v=0, 1$ and 2 from Table 3.1) we obtained:

$$D/2\pi = -5.214 \times 10^{-3} \text{ MHz}, \quad (3.1.1a)$$

$$\Omega/2\pi = 2.771 \text{ MHz}, \quad (3.1.1b)$$

$$\Delta/2\pi = -2.179 \times 10^{-2} \text{ MHz}. \quad (3.1.1c)$$

Using numerical values of energies of three upper states ($v = 13, 14$ and 15 from Table 3.1) we obtained:

$$D/2\pi = -4.312 \times 10^{-1} \text{ MHz}, \quad (3.1.2a)$$

$$\Omega/2\pi = 2.870 \text{ MHz}, \quad (3.1.2b)$$

$$\Delta/2\pi = -1.462 \times 10^{-2} \text{ MHz}. \quad (3.1.2c)$$

These data show that the value of anharmonicity parameter, Δ , is close to 0.8% of the trap frequency for the lower part of spectrum and is about 0.5% for the upper part of spectrum. The value of Ω from this fit is close to the harmonic frequency ω (within the effect of small anharmonicity).

Using the numerically computed wave functions $\psi_v(z)$ of vibrational eigenstates we calculated matrix elements of the transition dipole moment matrix for this system. The 16×16 part of this matrix is shown in Fig. 3.2, for the lower 16 states. Due to symmetry, only transitions characterized by odd values of Δv are allowed, *e.g.*:

$$\Delta v = \pm 1, \pm 3, \pm 5, \pm 7, \text{ etc.} \quad (3.1.3)$$

Figure 3.2 shows that the dipole moment matrix is clearly dominated by $\Delta v = \pm 1$ transitions, which is consistent with low anharmonicity of the system. For example,

the matrix element $\mu_{0,1} = 30.32 \text{ } ea_0$ ($\sim 77.07 \text{ D}$) is two orders of magnitude larger than the element $\mu_{0,3} = 9.47 \times 10^{-2} \text{ } ea_0$ ($\sim 0.24 \text{ D}$), which in turn is two orders of magnitude larger than $\mu_{0,5} = 4.98 \times 10^{-4} \text{ } ea_0$ ($\sim 1.27 \times 10^{-3} \text{ D}$). This property suggests that excitation of multiple quanta of vibration in this system might be easier to achieve by inducing a ladder of consecutive state-to-state transitions. For example:

$$|v=0\rangle \rightarrow |v=1\rangle \rightarrow |v=2\rangle \rightarrow |v=3\rangle,$$

rather than $|v=0\rangle \rightarrow |v=3\rangle$ directly.

Another relevant property of the dipole moment matrix is that, when we go

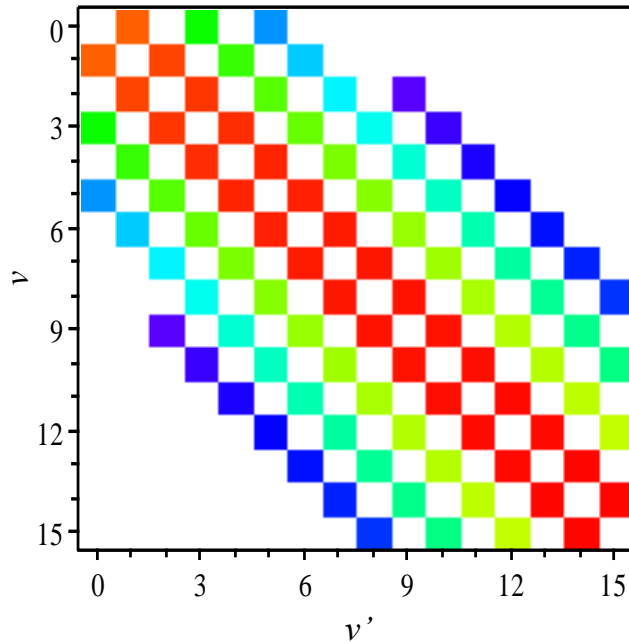


Fig. 3. 2: Transition moment matrix for sixteen lower vibrational states in a model system of $^{111}\text{Cd}^+$ ion in a weakly anharmonic Paul trap. Color indicates magnitudes of matrix elements in the logarithmic scale (dark red corresponds $\mu_{14,15} = 1.08 \times 10^2 \text{ } ea_0$ ($\sim 2.75 \times 10^2 \text{ D}$) and light blue corresponds $\mu_{0,5} = 4.98 \times 10^{-4} \text{ } ea_0$ ($\sim 1.27 \times 10^{-3} \text{ D}$)). See text for further details).

down along its near-diagonal line that represents the dominant $\Delta\nu = \pm 1$ transitions

(see Fig. 3.2), the values of matrix elements slightly increase. For example,

$\mu_{6,7} = 77.01 \text{ } ea_0 (\sim 1.96 \times 10^2 \text{ D})$ is a factor of 2.5 larger than $\mu_{0,1}$, and is a factor of

1.4 smaller than $\mu_{14,15} = 1.08 \times 10^2 \text{ } ea_0 (\sim 2.75 \times 10^2 \text{ D})$. Again, this behavior is

reminiscent of the harmonic oscillator.

3.2 The quantum algorithm

Sixteen lower vibrational states are used in this work to encode states of the four-qubit system with the purpose of implementing, in the computational experiments, the four-qubit version of Shor's algorithm for factorizing number 15 [53, 68]. The quantum circuit diagram for the phase-estimation part of this well known algorithm is shown in Fig. 3.3. Here qubits 1 and 2 represent the argument-register, while qubits 3 and 4 represent the function-register. The algorithm involves three major steps:

- i) Preparation of the argument-register in an equally weighted coherent superposition of states. This is achieved by Hadamard gates on qubits 1 and 2 and is indicated by gray background in Fig. 3.3.
- ii) Modular exponentiation of the function-register. This is achieved by a sequence of three conditional three-qubit gates, working as a controlled SWAP operation, also known as Fredkin-gate, and indicated by blue

background in Fig. 3. Qubits 2, 3 and 4 are involved.

iii) Inverse quantum Fourier transform of the argument-register. This is achieved by a sequence of three CNOT gates on qubits 1 and 2, known also as SWAP gate (green background in Fig. 3) with following Hadamard and conditional rotation gates (purple).

In the overall factorizing algorithm, the phase estimation part described above is

followed by measurement of populations of the qubit states.

In the matrix form the preparation part of the algorithm (Hadamard transformation of two qubits) is described by the following unitary transformation matrix acting on four states:

$$\overline{U}_1 = \frac{1}{2} \begin{pmatrix} 1 & 1 & 1 & 1 \\ 1 & -1 & 1 & -1 \\ 1 & 1 & -1 & -1 \\ 1 & -1 & -1 & 1 \end{pmatrix}. \quad (3.2.1)$$

The modular exponentiation step creates a maximally entangled state and is given by

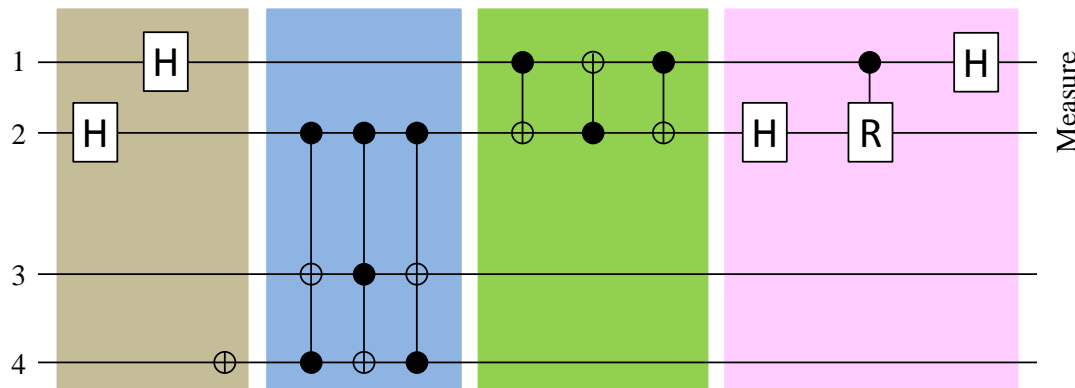


Fig. 3. 3: Quantum circuit diagram for the phase estimation part of Shor's algorithm for factorizing number 15 using four qubits (read from left to right). See text for details.

the following matrix acting in the three-qubit space (eight states):

$$\overline{U}_2 = \begin{pmatrix} 1 & 0 & 0 & 0 & 0 & 0 & 0 & 0 \\ 0 & 1 & 0 & 0 & 0 & 0 & 0 & 0 \\ 0 & 0 & 1 & 0 & 0 & 0 & 0 & 0 \\ 0 & 0 & 0 & 1 & 0 & 0 & 0 & 0 \\ 0 & 0 & 0 & 0 & 1 & 0 & 0 & 0 \\ 0 & 0 & 0 & 0 & 0 & 0 & 1 & 0 \\ 0 & 0 & 0 & 0 & 0 & 1 & 0 & 0 \\ 0 & 0 & 0 & 0 & 0 & 0 & 0 & 1 \end{pmatrix}. \quad (3.2.2)$$

A sequence of three two-qubit gates CNOT is given by

$$\overline{U}_3 = \begin{pmatrix} 1 & 0 & 0 & 0 \\ 0 & 0 & 1 & 0 \\ 0 & 1 & 0 & 0 \\ 0 & 0 & 0 & 1 \end{pmatrix}. \quad (3.2.3)$$

This transformation is also known as SWAP. Finally, a sequence of Hadamard,

conditional rotation and Hadamard gates for two qubits is given by:

$$\overline{U}_4 = \frac{1}{2} \begin{pmatrix} 1 & 1 & 1 & 1 \\ 1 & -1 & 1 & -1 \\ 1 & i & -1 & -i \\ 1 & -i & -1 & i \end{pmatrix}. \quad (3.2.4)$$

Each of these matrixes can be easily expanded onto the entire space of four qubits (sixteen states) by adding the needed number of identity-blocks and zero-blocks to create the 16×16 matrixes: U_1 , U_2 , U_3 and U_4 , able to act on sixteen states of the entire four-qubit system. Then, the overall Shor's algorithm can be represented by a single 16×16 unitary matrix obtained as a matrix product: $U_{\text{Shor}} = U_4 U_3 U_2 U_1$. We let readers to carry out these matrix manipulations. The final result is [33]:

$$U_{\text{Shor}} = \frac{1}{2} \begin{pmatrix} 0 & 2 & 0 & 0 & 0 & 0 & 0 & 0 & 0 & 0 & 0 & 0 & 0 & 0 & 0 & 0 & 0 \\ 1 & 0 & 0 & 1 & 1 & 0 & 0 & -1 & 0 & 0 & 0 & 0 & 0 & 0 & 0 & 0 & 0 \\ 1 & 0 & 0 & 1 & -1 & 0 & 0 & 1 & 0 & 0 & 0 & 0 & 0 & 0 & 0 & 0 & 0 \\ 0 & 0 & 2 & 0 & 0 & 0 & 0 & 0 & 0 & 0 & 0 & 0 & 0 & 0 & 0 & 0 & 0 \\ \dots & \dots \\ 0 & 0 & 0 & 0 & 0 & 0 & 0 & 0 & 0 & 0 & 1+i & 0 & 0 & 0 & 1-i & 0 & 0 \\ 0 & 0 & 0 & 0 & 0 & 0 & 0 & 0 & 0 & 1 & 0 & 0 & i & 1 & 0 & 0 & -i \\ 0 & 0 & 0 & 0 & 0 & 0 & 0 & 0 & 0 & i & 0 & 0 & 1 & -i & 0 & 0 & 1 \\ 0 & 0 & 0 & 0 & 0 & 0 & 0 & 0 & 0 & 0 & 0 & 1+i & 0 & 0 & 0 & 1-i & 0 \\ \dots & \dots \\ 0 & 0 & 0 & 0 & 0 & 2 & 0 & 0 & 0 & 0 & 0 & 0 & 0 & 0 & 0 & 0 & 0 \\ 1 & 0 & 0 & -1 & 1 & 0 & 0 & 1 & 0 & 0 & 0 & 0 & 0 & 0 & 0 & 0 & 0 \\ -1 & 0 & 0 & 1 & 1 & 0 & 0 & 1 & 0 & 0 & 0 & 0 & 0 & 0 & 0 & 0 & 0 \\ 0 & 0 & 0 & 0 & 0 & 0 & 2 & 0 & 0 & 0 & 0 & 0 & 0 & 0 & 0 & 0 & 0 \\ \dots & \dots \\ 0 & 0 & 0 & 0 & 0 & 0 & 0 & 0 & 0 & 0 & 1-i & 0 & 0 & 0 & 1+i & 0 & 0 \\ 0 & 0 & 0 & 0 & 0 & 0 & 0 & 0 & 0 & 1 & 0 & 0 & -i & 1 & 0 & 0 & i \\ 0 & 0 & 0 & 0 & 0 & 0 & 0 & 0 & 0 & -i & 0 & 0 & 1 & i & 0 & 0 & 1 \\ 0 & 0 & 0 & 0 & 0 & 0 & 0 & 0 & 0 & 0 & 0 & 1-i & 0 & 0 & 0 & 1+i & 0 \end{pmatrix} \quad (3.2.5)$$

This unitary matrix acts on the vector of sixteen states of the four-qubit system

arranged in the following usual order:

$$\Psi = \begin{pmatrix} |0000\rangle \\ |0001\rangle \\ |0010\rangle \\ |0011\rangle \\ |0100\rangle \\ |0101\rangle \\ |0110\rangle \\ |0111\rangle \\ |1000\rangle \\ |1001\rangle \\ |1010\rangle \\ |1011\rangle \\ |1100\rangle \\ |1101\rangle \\ |1110\rangle \\ |1111\rangle \end{pmatrix} \quad (3.2.6)$$

In principle, the sixteen vibrational states could be used in their normal order to

encode these qubit states, namely:

$$\Psi = \left| v=0 \right\rangle \left| v=1 \right\rangle \left| v=2 \right\rangle \left| v=3 \right\rangle \left| v=4 \right\rangle \left| v=5 \right\rangle \left| v=6 \right\rangle \left| v=7 \right\rangle \left| v=8 \right\rangle \left| v=9 \right\rangle \left| v=10 \right\rangle \left| v=11 \right\rangle \left| v=12 \right\rangle \left| v=13 \right\rangle \left| v=14 \right\rangle \left| v=15 \right\rangle \quad (3.2.7)$$

However, we found that this straightforward way of encoding is not the best. The difficulties created by this choice are easy to spot if one looks at the state-to-state transitions generated by applying the unitary matrix U_{Shor} of Eq. (3.2.5) to the state vector of Eq. (3.2.7). For example, if the initial state is $|0000\rangle$, represented by the vibrational state $|v=0\rangle$, the unitary matrix U_{Shor} leads to the following transformation:

$$U_{\text{Shor}}|v=0\rangle \rightarrow \frac{1}{2}(|v=1\rangle + |v=2\rangle + |v=9\rangle - |v=10\rangle). \quad (3.2.8)$$

Analogously, for the initial state $|1111\rangle$, represented by $|v=15\rangle$, we obtain

$$U_{\text{Shor}}|v=15\rangle \rightarrow \frac{1}{2}(-i|v=5\rangle + |v=6\rangle + i|v=13\rangle + |v=14\rangle). \quad (3.2.9)$$

We see that these two transformations require transferring 10 quanta of vibrational excitation, which is quite difficult to implement with the near-diagonal dipole moment matrix, as one presented in Fig. 3.2. Two other difficult to implement transformations associated with the straightforward encoding of Eq. (3.2.7) are:

$$U_{\text{Shor}}|\nu = 13\rangle \rightarrow \frac{1}{2}((1-i)|\nu = 4\rangle + (1+i)|\nu = 12\rangle), \quad (3.2.10)$$

$$U_{\text{Shor}}|\nu = 3\rangle \rightarrow \frac{1}{2}(|\nu = 1\rangle + |\nu = 2\rangle - |\nu = 9\rangle + |\nu = 10\rangle) \quad (3.2.11)$$

These transformations require transferring 9 and 7 quanta of the vibrational excitation. In order to avoid such far state-to-state transitions, one has to search for an alternative, more convenient encoding of the qubit states.

We analyzed several alternative ways to encode the four-qubit states into the sixteen lower vibrational states and have, finally, chosen the following order of the vibrational states:

$$\Psi = \left| \begin{array}{l} v=0 \\ v=1 \\ v=2 \\ v=3 \\ v=4 \\ v=13 \\ v=14 \\ v=7 \\ v=12 \\ v=5 \\ v=6 \\ v=15 \\ v=8 \\ v=9 \\ v=10 \\ v=11 \end{array} \right\rangle \quad (3.2.12)$$

This way of encoding is also outlined in Table 3.1, where states of the four-qubit system are assigned to sixteen vibrational states, and all transformations of the initial states are indicated, as dictated by unitary matrix of Shor's algorithm, Eq. (3.2.5).

Among those transitions, some of the most difficult to implement are:

$$U_{\text{Shor}} |v=0\rangle \rightarrow \frac{1}{2} (|v=1\rangle + |v=2\rangle + |v=5\rangle - |v=6\rangle), \quad (3.2.13)$$

$$U_{\text{Shor}} |v=8\rangle \rightarrow \frac{1}{2} (|v=9\rangle + i|v=10\rangle + |v=13\rangle - i|v=14\rangle). \quad (3.2.14)$$

They require excitation of only up to 6 quanta of vibration, compared to 10 quanta in the case of straightforward encoding. Two other difficult to implement transitions are:

$$U_{\text{Shor}} |v=6\rangle \rightarrow \frac{1}{2} ((1+i)|v=7\rangle + (1-i)|v=11\rangle), \quad (3.2.15)$$

$$U_{\text{Shor}} |v=3\rangle \rightarrow \frac{1}{2} (|v=1\rangle + |v=2\rangle - |v=5\rangle + |v=6\rangle). \quad (3.2.16)$$

These transformations require excitation of only up to 5 and 3 quanta of vibration, compared to 9 and 7 quanta in the case of straightforward encoding. So, advantages offered by the encoding of Eq. (3.2.12) are clearly seen.

Another useful (and exactly equivalent) viewpoint onto the same issue is this: Instead of changing the order of vibrational states in the state vector of Eq. (3.2.7), one could permute the order of qubit states in the vector of Eq. (3.2.6) which corresponds to permuting, simultaneously, the corresponding columns and rows of the unitary matrix U_{Shor} in Eq. (3.2.5). The purpose is to obtain new unitary matrix U'_{Shor} that will be as close to the diagonal matrix as only possible. Indeed, the original matrix U_{Shor} of Eq. (3.2.5) has several non-zero off-diagonal elements that are very far from the diagonal line. These matrix elements are responsible for those far state-to-state transitions listed in Eqs. (3.2.8) – (3.2.11). Alternatively, the unitary matrix U'_{Shor} , which corresponds to the encoding of Eq. (3.2.12), is given by:

$$U'_{\text{Shor}} = \frac{1}{2} \begin{pmatrix} 0 & 2 & 0 & 0 & 0 & 0 & 0 & 0 & 0 & 0 & 0 & 0 & 0 & 0 & 0 & 0 \\ 1 & 0 & 0 & 1 & 1 & 0 & 0 & -1 & 0 & 0 & 0 & 0 & 0 & 0 & 0 & 0 \\ 1 & 0 & 0 & 1 & -1 & 0 & 0 & 1 & 0 & 0 & 0 & 0 & 0 & 0 & 0 & 0 \\ 0 & 0 & 2 & 0 & 0 & 0 & 0 & 0 & 0 & 0 & 0 & 0 & 0 & 0 & 0 & 0 \\ 0 & 0 & 0 & 0 & 0 & 1+i & 0 & 0 & 0 & 1-i & 0 & 0 & 0 & 0 & 0 & 0 \\ 1 & 0 & 0 & -1 & 1 & 0 & 0 & 1 & 0 & 0 & 0 & 0 & 0 & 0 & 0 & 0 \\ -1 & 0 & 0 & 1 & 1 & 0 & 0 & 1 & 0 & 0 & 0 & 0 & 0 & 0 & 0 & 0 \\ 0 & 0 & 0 & 0 & 0 & 0 & 1+i & 0 & 0 & 0 & 1-i & 0 & 0 & 0 & 0 & 0 \\ 0 & 0 & 0 & 0 & 0 & 1-i & 0 & 0 & 0 & 1+i & 0 & 0 & 0 & 0 & 0 & 0 \\ 0 & 0 & 0 & 0 & 0 & 0 & 0 & 0 & 1 & 0 & 0 & i & 1 & 0 & 0 & -i \\ 0 & 0 & 0 & 0 & 0 & 0 & 0 & i & 0 & 0 & 1 & -i & 0 & 0 & 0 & 1 \\ 0 & 0 & 0 & 0 & 0 & 0 & 1-i & 0 & 0 & 0 & 1+i & 0 & 0 & 0 & 0 & 0 \\ 0 & 0 & 0 & 0 & 0 & 0 & 0 & 0 & 0 & 0 & 0 & 0 & 0 & 2 & 0 & 0 \\ 0 & 0 & 0 & 0 & 0 & 0 & 0 & 0 & 1 & 0 & 0 & -i & 1 & 0 & 0 & i \\ 0 & 0 & 0 & 0 & 0 & 0 & 0 & 0 & -i & 0 & 0 & 1 & i & 0 & 0 & 1 \\ 0 & 0 & 0 & 0 & 0 & 0 & 0 & 0 & 0 & 0 & 0 & 0 & 0 & 0 & 2 & 0 \end{pmatrix} \quad (3.2.17)$$

Here, the off-diagonal elements describe the transitions of Eqs. (3.2.13-3.2.16), but the overall structure of this matrix is much closer to the near-diagonal one, compared to the original matrix U_{Shor} of Eq. (3.2.5).

3.3 OCT pulse shaping

Optimization of the pulse for the entire quantum algorithm, such as Shor's algorithm, is a formidable task. Indeed, the optimal pulse should be able to carry out each of sixteen transformations listed in the 6th column of Table 3.1 with high accuracy. Finding such a pulse is made feasible by employing a multi-target version of the objective functional [35, 37, 44, 63, 89, 90]. This approach requires propagating a set of sixteen identical Schrödinger equations (forward and backward in

time as explained above), but each with its own initial condition and its own target state, as dictated by transformations of sixteen qubit states (see Table 3.1, 6th column). The common field $\varepsilon(t)$ is iteratively improved using all this information. See Chapter 2, Sec. 2.7 and 2.8 for further details of the method.

Such calculations are quite demanding. Our optimization code was parallelized using the MPI interface and was run in parallel on sixteen processors of Cray machine at NERSC center [94-96]. Numerical propagation of vibrational wave packets was employed. The wave packet was expanded in the basis set of 32 vibrational eigenstates to avoid unphysical reflection of wave packet from the upper states. The overall optimization procedure was semi-automated. Namely, it took many attempts made with different pulse durations, different guess amplitudes and different penalty factors, before the optimal pulse of acceptable accuracy, duration and shape was identified. We found that for this problem it was advantageous to start the search with a guess pulse of very large amplitude of the field, on order of 100 V/m. In the course of iterative improvement the pulse amplitude dropped quickly to only about ~ 0.4 V/m (in the final optimal pulse), but we saw that accuracy of the final pulse was better if amplitude of the initial guess pulse was much larger. The best penalty factors were between $\alpha = 2 \times 10^{12}$ and 4×10^{13} . The number of forward-backward iterations needed for convergence was on order of 10,000 or more. Durations of studies pulses

were between 10 and 50 μs . The number of time steps for numerical wave packet propagation was on order of few hundred thousand.

3.4 Results and discussion

The field optimized for Shor's algorithm is shown in Fig. 3.4 (a). Duration of the pulse is 50 μs . The field amplitude does not exceed 0.4 V/m. The pulse shape is

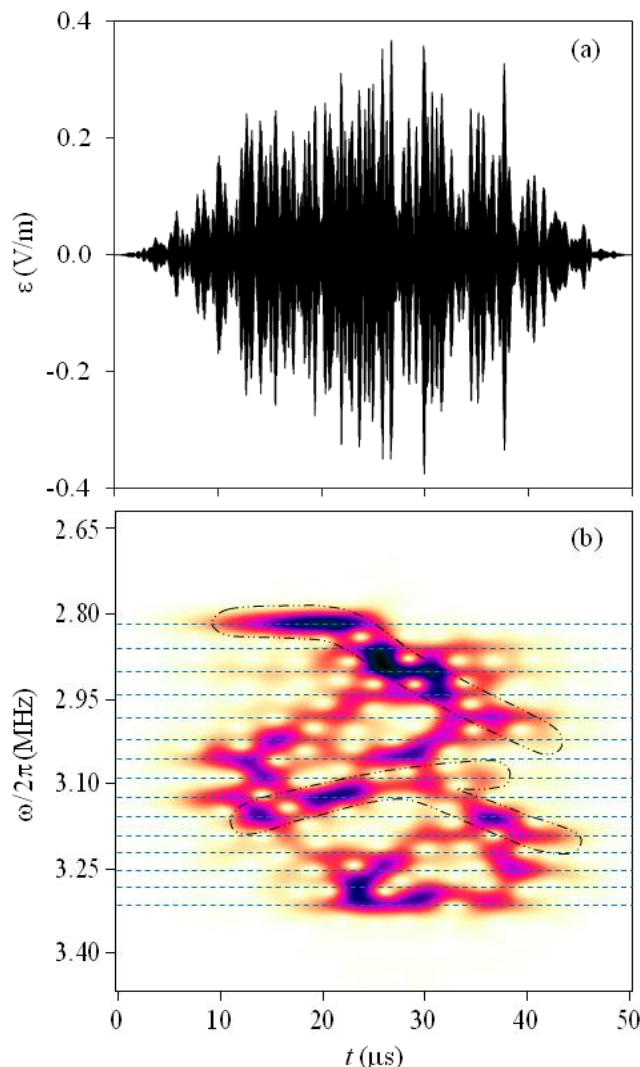


Fig. 3. 4: (a) Optimally shaped 50 μs pulse for Shor's algorithm in the $^{111}\text{Cd}^+$ ion trap. (b) Windowed Fourier transform of the pulse. Horizontal dashed lines indicate frequencies of the state-to-state transitions. Dotted curves encircle two spectral features that correspond to the ladder climbing. See text for details.

quite complicated, as one might expect from complexity of the optimization task that involves sixteen transformations optimized at the same time. Although it is very difficult to derive any useful information simply from the shape of the pulse in Fig. 3.4 (a), this optimized field gives very accurate control of all sixteen transformations given in Table 3.1. For different transformations of the training set the characteristic probabilities vary between 0.9977 and 0.9996 (see last column of Table 3.1) with an average (over sixteen transformations) close to 0.999. From our point of view, this is quite high, taking into account complexity of the optimization problem. Our results also indicate that it is possible to improve the average probability even further by increasing the pulse duration, doing more forward-backward iterations, and delicately changing some other numerical parameters of the method. However, we decided to stick with this set of parameters, as one providing very reasonable accuracy of the qubit state transformations.

A straightforward way to analyze the optimized pulse is to look at the state-to-state transitions induced by this pulse. In Fig. 3.5 we present three examples (out of sixteen optimized transformations) that are quite typical. The first example to discuss is the first transformation of Table 3.1, illustrated by Fig. 3.5 (a). In this case, population of the initial state $|v=0\rangle$ should be transferred in equal amounts to four final states: $|v=1\rangle$, $|v=2\rangle$, $|v=5\rangle$ and $|v=6\rangle$. Thus, each of the final states is expected

to receive the population of $P = 0.25$. The time evolution of state populations in Fig.

3.5 (a) is as follows: In the first 25 μs of the pulse the $|v=0\rangle \rightarrow |v=1\rangle$ transition is

induced and population of the ground state is converted almost entirely into

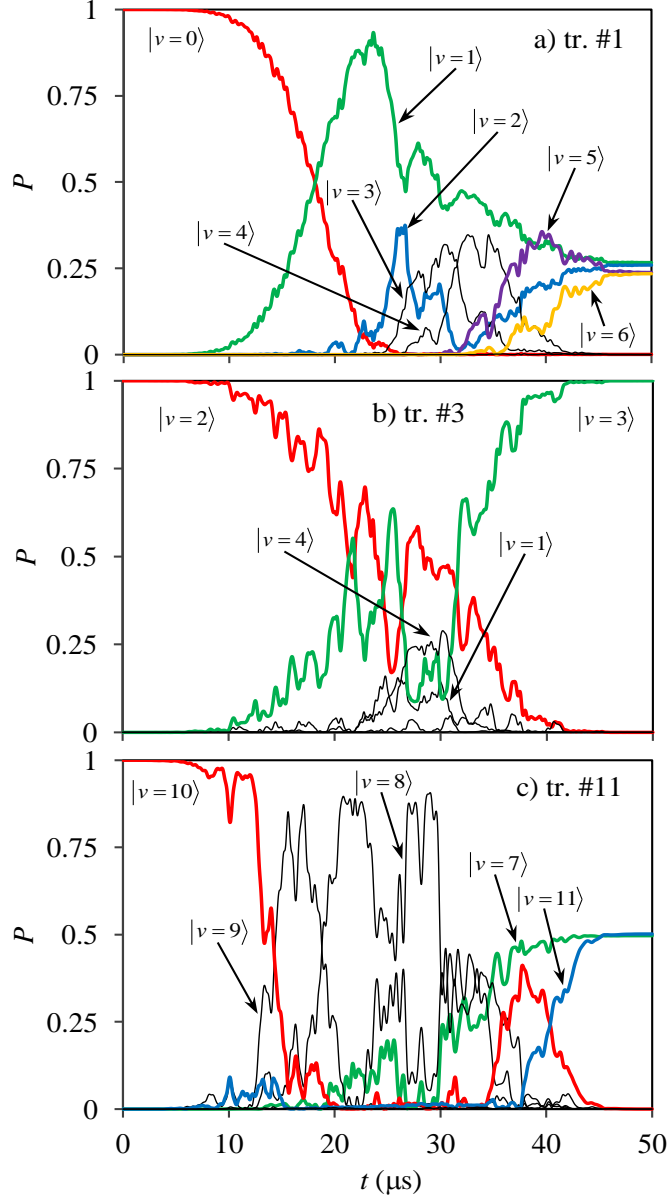


Fig. 3.5: Time evolution of state populations induced by the pulse optimized for Shor's algorithm in three representative cases: (a) Transformation #1 in Table 3.1. (b) Transformation #3 in Table 3.1. (c) Transformation #11 in Table 3.1. Thicker color lines indicate population of the initial and final states. Thinner black lines indicate population of intermediate states.

population of the first excited state. Transition to state $|v=2\rangle$ starts showing up only after the population of state $|v=1\rangle$ reaches a reasonably high value ($P \sim 0.7$ at $t \sim 22$ μs). Also note that the increase of population of state $|v=2\rangle$ mirrors the decrease of population of state $|v=1\rangle$. This certainly means that state $|v=2\rangle$ is populated not directly from the ground state $|v=0\rangle$, but through the state $|v=1\rangle$. Next, the increase of population of state $|v=3\rangle$ occurs only when the population of state $|v=2\rangle$ reaches its maximum ($P \sim 0.4$ at $t \sim 26$ μs) and, again, the population of state $|v=3\rangle$ increases at the same rate as the population of state $|v=2\rangle$ decreases. Same scenario repeats again for transferring population from state $|v=3\rangle$ to state $|v=4\rangle$. The populations of states $|v=3\rangle$ and $|v=4\rangle$ reach $P \sim 0.3$ in the time interval near $t \sim 30$ - 35 μs . Note, however, that these states are expected to be unpopulated at the final moment of time. Indeed, from Fig. 3.5 (a) we can see that they give all of their population either further up to state $|v=5\rangle$, or back down to the $|v=2\rangle$ state. Finally, at $t \sim 35$ - 40 μs , state $|v=6\rangle$ starts receiving population from state $|v=5\rangle$. At the end of the pulse, the final populations of states $|v=1\rangle$ and $|v=2\rangle$ are close to $P \sim 0.2632$, while the final populations of states $|v=5\rangle$ and $|v=6\rangle$ are close to $P \sim 0.2361$. Populations of states $|v=3\rangle$ and $|v=4\rangle$, and of all states above $|v=6\rangle$, are close to zero.

Note that Transformation #1 depicted in Fig. 3.5 (a) is typical to the Shor's algorithm. For example, Transformations #4, #5 and #8 have exactly the same

complexity. We analyzed state populations in those cases too, and observed very similar behavior. The only difference is that during the Transformation #1 (and #8) all population of the initial state is transferred up (down) first and then some part of it is returned down (up), while during the Transformations #4 and #5 the population of initial state is split from the beginning: about 50% of it go up and the remaining 50% go down. The Transformations #9, #12, #13 and #16 are also similar to Transformation #1 (apart from the phases involved). So, our conclusion is that controlling the ladders of consecutive state-to-state transitions is essential for successful implementation of the Shor's algorithm in this architecture.

Next to discuss is Transformation #3 illustrated by Fig. 3.5 (b). Here the population transfer from $|v=2\rangle$ to $|v=3\rangle$ is relatively direct. The neighboring states $|v=1\rangle$ and $|v=4\rangle$ receive some relatively small population “erroneously” during the pulse ($P \sim 0.2$ at $t \sim 23\text{-}33 \mu\text{s}$), which is attributed to the relatively low anharmonicity of the system. However, this process is well controlled: By the end of the pulse this erroneous population is entirely returned to the target state. Final population of the target state is $P \sim 0.9995$. Similar behavior of state populations was observed during the Transformations #2, #14 and #15. These transformations belong to the same type, characterized as a state-to-the-next-state transition.

Finally, Fig. 3.5 (c) illustrates Transformation #11, which is example of

splitting population of the initial state between the two target states. Here, population of the initial state $|v=10\rangle$ is transferred very quickly ($t \sim 15 \mu\text{s}$) and almost entirely into the $|v=9\rangle$ state, and then, also very quickly (by $t \sim 22 \mu\text{s}$) and almost entirely into the $|v=8\rangle$ state. Then, state $|v=7\rangle$ starts receiving population. During the time period $t \sim 20\text{-}30 \mu\text{s}$ population oscillates between the states $|v=7\rangle$, $|v=8\rangle$ and $|v=9\rangle$. At $t \sim 30 \mu\text{s}$ the population is directed further down towards the final state $|v=7\rangle$ and, through the intermediate state $|v=10\rangle$, up into the other final state $|v=11\rangle$. Final populations are $P \sim 0.4972$ and $P \sim 0.5014$. This behavior is typical to Transformations #6, #7 and #10 as well.

Overall, this discussion demonstrates a very pronounced *step-ladder climbing* scenario which, undoubtedly, is a reflection of properties of the dipole moment matrix of this system, discussed in the Sec. 3. 2 above.

Another way to analyze the optimized pulse is to look at its Fourier spectrum. Figure 3.6 (a) shows the spectrum in a broad range of frequencies. It exhibits five very distinct spectral structures. The first structure is in the frequency range of transitions between the neighboring states, $\Delta v = \pm 1$. Among those, the lowest frequency transition is at $\omega_{0 \rightarrow 1}$ and the highest frequency transition is at $\omega_{14 \rightarrow 15}$. Two arrows are given, near the top of the spectral structure in Fig. 3.6 (a), to indicate the corresponding range of frequencies. In the frequency range between these arrows the

spectral structure exhibits a plateau. Outside of this plateau the intensity drops exponentially. The second spectral structure corresponds to the overtone transitions,

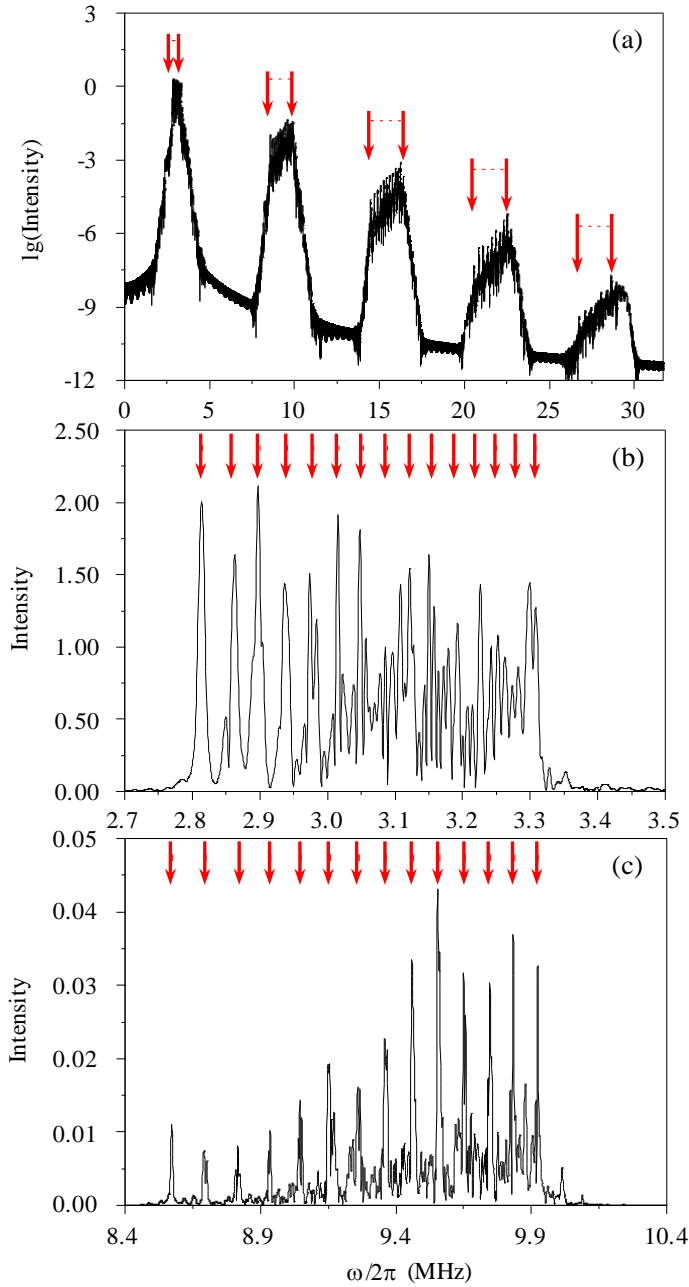


Fig. 3.6: Fourier spectrum of the pulse optimized for Shor's algorithm in the $^{111}\text{Cd}^+$ ion trap: (a) broad range of frequencies (up to $\omega_{n,n+9}$). (b) focus on the frequency range of the main spectral structure ($\omega_{n,n+1}$ transitions). (c) focus on the frequency range of the overtone spectral structure ($\omega_{n,n+3}$ transitions). Arrows indicate frequencies of the state-to-state transitions from Table 3.1.

$\Delta\nu = \pm 3$, with the lowest frequency transition at $\omega_{0 \rightarrow 3}$ and the highest frequency transition at $\omega_{12 \rightarrow 15}$. Those are also indicated by arrows. And so on and so forth, up to the $\Delta\nu = \pm 9$ frequency range included into the Fig. 3.6 (a). Note, however, that the vertical axis in Fig. 3.6 (a) is in the logarithmic scale. When we go from the main spectral structure ($\Delta\nu = \pm 1$) to the next and the next, the intensity drops each time by two-to-three orders of magnitude, on average. This certainly means that the step-ladder climbing transitions (described by the main spectral structure) are dominant, which is totally consistent with behavior observed in Figs. 3.5 (a-c) and discussed above. The overtone transitions, although clearly present in the pulse, play less important role.

Figure 3.6 (b) shows plateau of the main spectral structure in detail (no logarithmic scale for the intensity). Fifteen arrows indicate frequencies of the neighboring state-to-state transitions $\omega_{n,n+1}$. Figure 3.6 (c) shows in detail the plateau of the spectral structure corresponding to the first overtone. Fourteen arrows indicate frequencies of the relevant state-to-state transitions $\omega_{n,n+3}$. Majority of spectral peaks on these two pictures are easily assignable to the corresponding state-to-state transitions. Note that the lower frequency part of spectrum in Fig. 3.6 (b) is particularly “clean” and intensity of the corresponding overtone components in Fig. 3.6 (c) is quite low. In contrast, the higher frequency part of spectrum in Fig. 3.6 (b) is

more “congested” and intensity of the corresponding overtone components in Fig. 3.6 (c) is notably higher. These features have very straightforward interpretation: Recall that selective control of the state-to-state transitions is facilitated by anharmonicity of the spectrum. For a long progression of states, like the sixteen states used in this work, the parameter of anharmonicity can change as we go through the spectrum. As it was shown in Sec. 3.2 above, the lower part of our spectrum is more anharmonic (Δ is close to 0.8% of the trap frequency) compared to the upper part of spectrum (only 0.5%). It appears that when the spectrum is more anharmonic (lower part) the overtone transitions matter less and accurate control can be achieved mostly by means of the $\omega_{n,n+1}$. When the spectrum is less anharmonic (upper part), the role played by the overtone frequency components $\omega_{n,n+3}$ becomes more visible.

The conclusion here is that one could, probably, benefit from using somewhat more anharmonic trapping potential. This would increase the overall anharmonicity of the vibrational spectrum of the system, particularly that in its upper part, and would lead to simpler frequency content of the optimized pulse, which normally translates into simpler pulse shape and higher accuracy of the qubit transformations.

The last thing we did to analyze the optimized pulse was windowed Fourier transform shown in Fig. 3.4 (b). The time-frequency diagram was obtained using Gaussian window with half-width of $\sim 190 \mu\text{s}$, applied at 501 points evenly spaced

along the pulse duration period. Only the frequency range of the main spectral structure is shown in Fig. 3.4 (b), which corresponds to the $\omega_{n,n+1}$ transition frequencies. Fifteen relevant frequencies $\omega_{n,n+1}$ are indicated in Fig. 3.4 (b) by horizontal dashed lines.

It is instructive to analyze Fig. 3.4 (b) together with Fig. 3.5. Thus, a long ladder of state-to-state transitions seen in Fig. 3.5 (a) and discussed in detail above:

$$|v=0\rangle \rightarrow |v=1\rangle \rightarrow |v=2\rangle \rightarrow |v=3\rangle \rightarrow |v=4\rangle \rightarrow |v=5\rangle \rightarrow |v=6\rangle ,$$

is also clearly seen in Fig. 3.4 (b). It is located in the upper part of the figure (lower frequency range) and, for clarity, is encircled by thin dotted line. It spreads over a very broad time interval, $10 \mu\text{s} < t < 40 \mu\text{s}$. This is one of the most pronounced features of the time-frequency diagram in Fig. 3.4 (b). Another important structure in the time-frequency diagram corresponds to the ladder of transitions depicted in Fig.

3.5 (c):

$$|v=10\rangle \rightarrow |v=9\rangle \rightarrow |v=8\rangle \rightarrow |v=7\rangle .$$

This structure is located in the middle part of Fig. 3.4 (b) and, for clarity, is also encircled by dotted line. Interestingly, one can see another ladder that “branches out” of this ladder near $t \sim 35 \mu\text{s}$. It corresponds to the ladder of backward transitions:

$$|v=9\rangle \rightarrow |v=10\rangle \rightarrow |v=11\rangle ,$$

this is totally consistent with discussion of Fig. 3.5 (c) above.

Further analysis of the time-frequency diagram of Fig. 3.4 (b) reveals several other shorter ladders. One can also identify several “forks” (where two ladders are initiated at the same state), and several points where two different ladders cross each other. Overall, the time-frequency diagram of Fig. 3.4 (b) is rather complicated, but it can be rationalized in terms of multiple ladders that can cross each other, form branches and forks. For completeness, the codes of the 1D Fast Fourier Transform (FFT) and 2D Fourier analysis are given in the Appendix C and D.

3.5 Conclusions

The purpose of the work in this chapter is exploratory, rather than predictive. We do not really expect that the Shor pulse obtained here by calculations can be exactly reproduced in the experiment and can lead to exactly the same result under experimental conditions. However, we feel it is reasonable to expect that employment of an advanced experimental pulse optimization technique, such as feedback loop with evolutionary algorithm [33, 34], may lead to experimental result of acceptable quality. Thus, we encourage the members of experimental community to seriously consider this possibility. Computational results outlined in this work could serve as prediction of a reasonable set of parameters for the system and for the pulse.

Let's start with the system. We found that small anharmonicity of the trapping potential, characterized by anharmonicity parameter close to 1% of the trap

frequency, is sufficient to alter the state-to-state transition frequencies and make the control feasible. In the case studied here, the sixteen lower vibrational states (used to encode the four-qubit system) exhibit the excitation frequencies in the range between roughly 2.82 MHz and 3.34 MHz. So, the effect of anharmonicity is apparent. The dipole moment matrix for single trapped ion is dominated by transitions to the nearest states, $\Delta v = \pm 1$, suggesting the ladder-climbing scenario of the population transfer.

As for the pulse, we were able to reach the average (over sixteen states of the four-qubit system) transition probability of 0.999 with the pulse duration of 50 μ s. Our calculations showed that 0.999 is not a limit. We saw clear indications that running more iterations would improve the accuracy of qubit transformations even further. The pulses longer than 50 μ s can exhibit somewhat higher transition probabilities. Amplitude of the optimized control field is relatively small; it does not exceed 0.4 V/m. We should admit that shape of the optimized Shor pulse is rather complicated. Frequency content of the pulse is sharply peaked at the range of frequencies that corresponds to the ladder of state-to-state transitions with $\Delta v = \pm 1$ for the sixteen states involved. Frequencies of the overtone transitions with $\Delta v = \pm 3$, $\Delta v = \pm 5$, etc., are also present in the optimal pulse, but their intensity decreases exponentially as frequency increases. The time-frequency diagram of the pulse contains multiple ladders (that can cross and form branches and forks) and allows

explaining major features of the sequence of sub-pulses of different frequencies.

Chapter 4: Study of the two-ion system

In this chapter we study a two-ion system which represents a 2D quantum problem. Numerical solution of Schrödinger equation requires setting up the basis set in two-dimensions. Since our system is only slightly anharmonic, it is a good idea to use the normal mode coordinates and the normal mode frequencies to define the 1D basis functions for each dimension of the problem.

4.1 Two ions in the harmonic trapping potential

4.1.1 Harmonic trapping potential

In this section, we consider two $^{111}\text{Cd}^+$ ions in the harmonic trapping potential, Eq. (2.1.1). The value of the force constant $k/2\pi = 1.483 \times 10^{-3}$ MHz/ a_0^2 is the same as in the one-ion case studied in Chapters 2 and 3. However, due to the Coulomb interaction, this is a totally different system. We restrict the motions of ions to one dimension along the trap (z-axis). Our initial intention was to use two normal modes of this system to encode two qubits. For example, one can try to use the center-of-mass motion mode to encode the first qubit and the symmetric stretching mode to encode the second qubit. The trapping potential, equilibrium positions, relevant energy levels and the possible encoding of the two-qubit states are shown in Fig. 4.1.

The potential energy of the two ions in the harmonic trapping potential is

expressed as follows (in atomic units):

$$\begin{aligned} V(z_1, z_2) &= V(z_1) + V(z_2) + \frac{1}{|z_2 - z_1|} \\ &= \frac{1}{2} kz_1^2 + \frac{1}{2} kz_2^2 + \frac{1}{|z_2 - z_1|}. \end{aligned} \quad (4.1.1.1)$$

As before, k is the force constant, we use z_1 and z_2 to describe the positions of two ions and set $z_2 > z_1$.

Potential energy surface (PES) of two ions in the trap based on Eq. (4.1.1.1) is

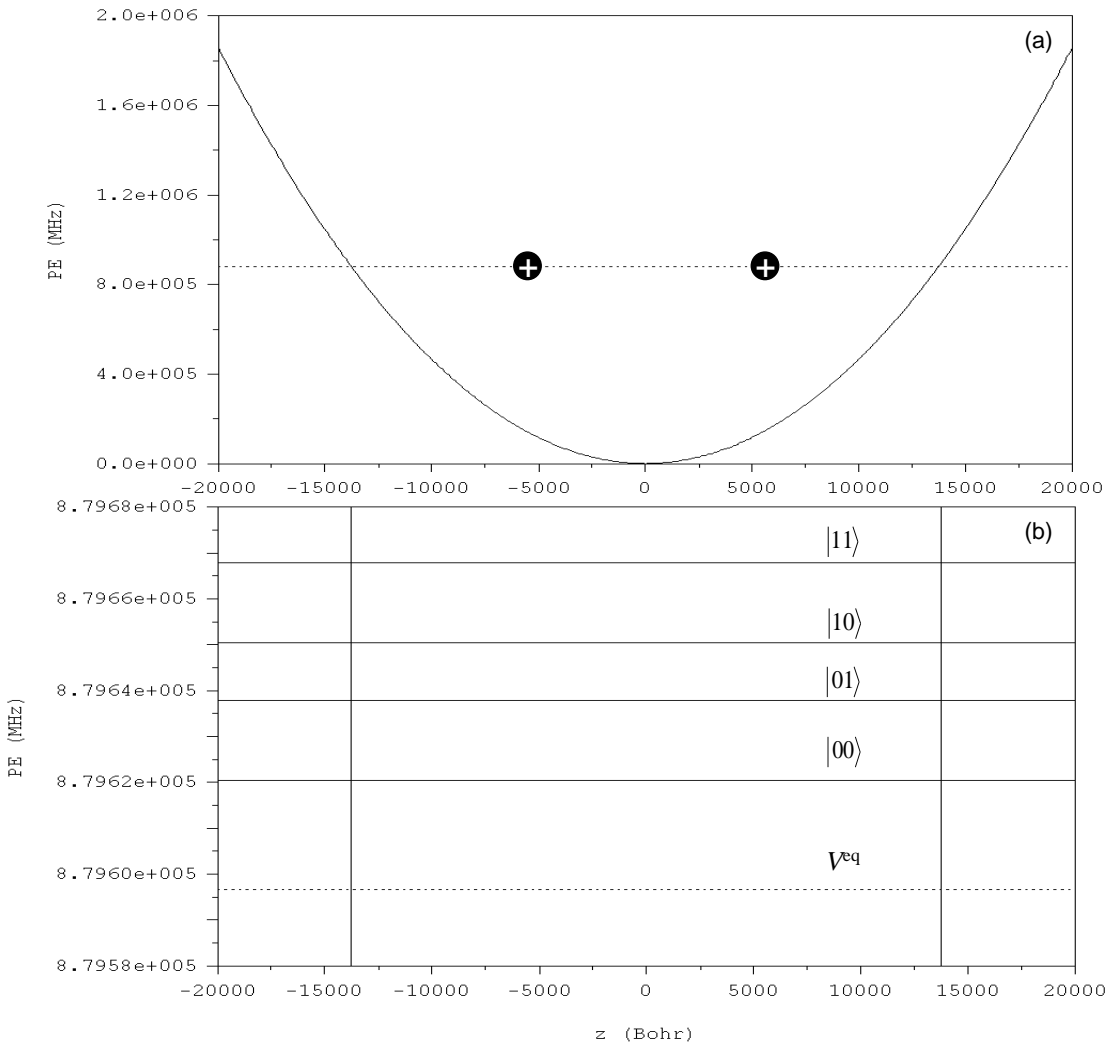


Fig. 4. 1: Two $^{111}\text{Cd}^+$ ions in the harmonic potential trap: (a) Equilibrium positions of ions and minimum energy of the two-ion string. (b) Vibrational spectrum of this system and possible encoding of states of the two-qubit system.

shown in Fig. 4.2. When the two ions come close to each other ($z_1 \approx z_2$), the potential energy approaches infinity which is the effect of Coulomb repulsion. This part of the PES is shown in white color. Second, although the trapping potential from Eq. (2.1.1) is harmonic, the potential energy of the system is anharmonic due to ion-ion Coulomb interaction. The main question here: *is Coulomb interaction of ions enough to introduce anharmonicity sufficient for accurate control?*

4.1.2 Minimization Method

When we consider one ion in the trap, it is obvious that the equilibrium

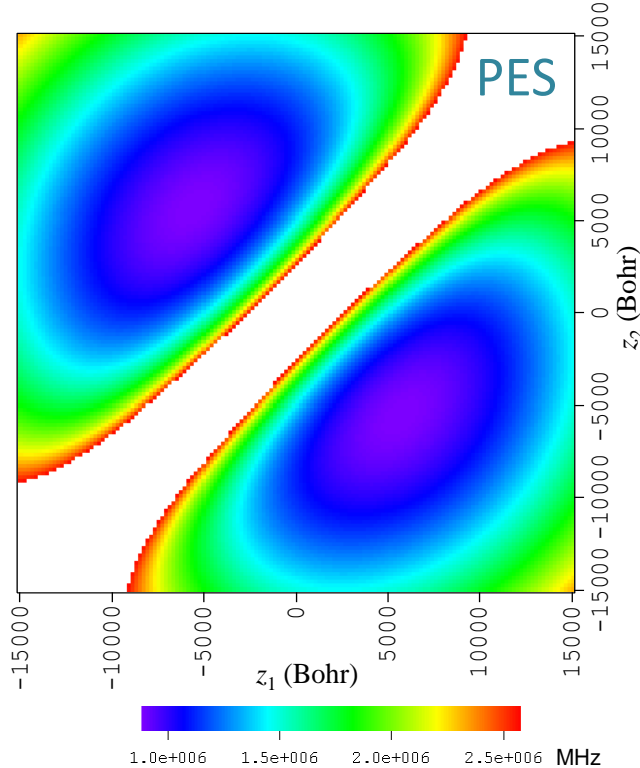


Fig. 4. 2: Potential energy surface of two $^{111}\text{Cd}^+$ ions in the harmonic potential trap using Cartesian coordinates. Anharmonicities due to Coulomb repulsion of ions are clearly seen.

position of the ion is at $z = 0$ (right at the center of the trap). But now there are two ions in the trap and we have to determine the equilibrium positions of these two ions first. The second-order derivative minimization methods represent powerful tools, because they use both the gradients and the second derivatives to locate the minimum. The *Newton-Raphson* (NR) method is the simplest second-order derivative method [97]. To describe this method, it is useful to recall the expression for the Taylor series expansion in the vicinity of z_0 :

$$f(z) = f(z_0) + (z - z_0)f'(z_0) + \frac{1}{2}(z - z_0)^2 f''(z_0) + \dots \quad (4.1.2.1)$$

Keeping only terms through quadratic, we can express the derivative of this function as:

$$f'(z) \approx f'(z_0) + (z - z_0)f''(z_0). \quad (4.1.2.2)$$

At the minimum, which we'll call z_e , the first derivative is zero, thus:

$$f'(z_e) = 0 = f'(z_0) + (z_e - z_0)f''(z_0), \quad (4.1.2.3)$$

$$z_e = z_0 - \frac{f'(z_0)}{f''(z_0)}. \quad (4.1.2.4)$$

This equation allows us to approach the minimum z_e using information about f' and f'' at an arbitrary initial point z_0 from which we start the minimization. On the harmonic PES, the minimum energy point is found in one step. Our PES is anharmonic and iterations are needed. Because our system is two dimensional, in this method we need to calculate the inverse second derivative, which will be an inverse

matrix of second derivatives.

The two dimensional minimization equation is shown as follows:

$$\begin{pmatrix} z_{e1} \\ z_{e2} \end{pmatrix} = \begin{pmatrix} z_{01} \\ z_{02} \end{pmatrix} - f^{n-1} \begin{pmatrix} f'(z_{01}) \\ f'(z_{02}) \end{pmatrix}, \quad (4.1.2.5)$$

where (z_{e1}, z_{e2}) characterizes the equilibrium positions of two ions and (z_{01}, z_{02})

describes a set of arbitrary initial positions.

Since the potential is analytic, the gradient and the second-order derivative are also analytic. From Eq. (4.1.1.1), we obtain the first and second derivatives of the potential energy for two-ion system:

$$\frac{\partial V(z_1, z_2)}{\partial z_1} = kz_1 + \frac{1}{(z_2 - z_1)^2}, \quad (4.1.2.6)$$

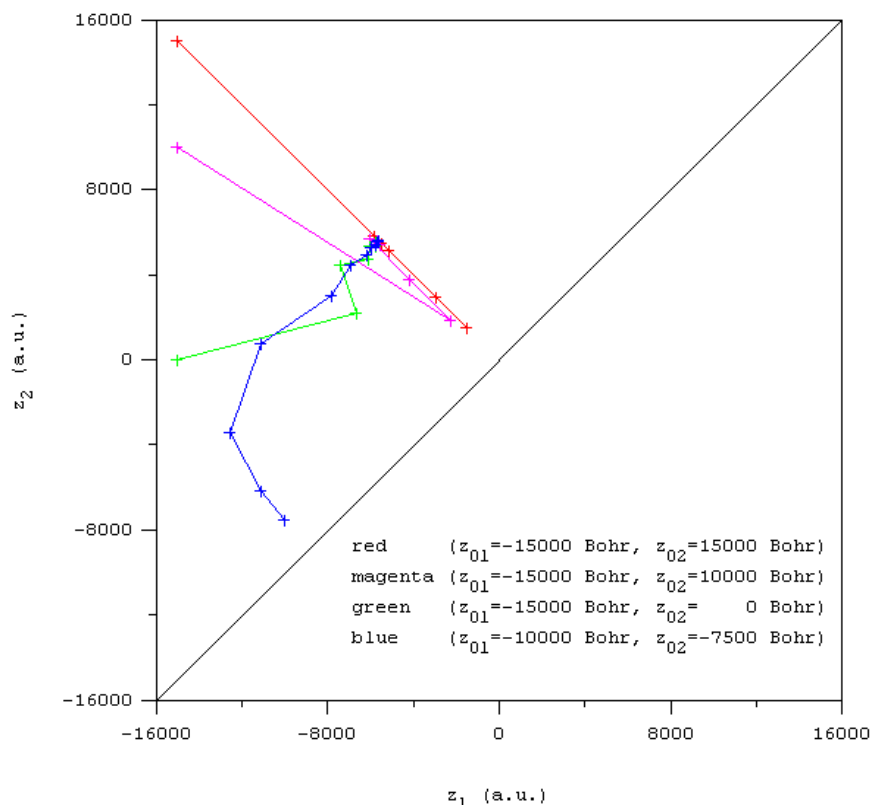


Fig. 4. 3: Minimization from four different arbitrary initial positions.

$$\frac{\partial V(z_1, z_2)}{\partial z_2} = kz_2 - \frac{1}{(z_2 - z_1)^2}, \quad (4.1.2.7)$$

$$\frac{\partial^2 V(z_1, z_2)}{\partial z_1^2} = k + \frac{2}{(z_2 - z_1)^3}, \quad (4.1.2.8)$$

$$\frac{\partial^2 V(z_1, z_2)}{\partial z_2^2} = k + \frac{2}{(z_2 - z_1)^3}, \quad (4.1.2.9)$$

$$\frac{\partial V(z_1, z_2)}{\partial z_1 \partial z_2} = \frac{\partial V(z_1, z_2)}{\partial z_2 \partial z_1} = -\frac{2}{(z_2 - z_1)^3}. \quad (4.1.2.10)$$

These derivatives are used in Eq. (4.1.2.5) to locate the equilibrium positions of these two ions in the trap with NR method. A computer code Program 2DMIN written in FORTRAN language is used to carry out these optimizations numerically (see Appendix E). In the algorithm, the equilibrium position (z_{e1}, z_{e2}) is approached iteratively from an arbitrary initial point (z_{01}, z_{02}) by consecutive application of Eq.

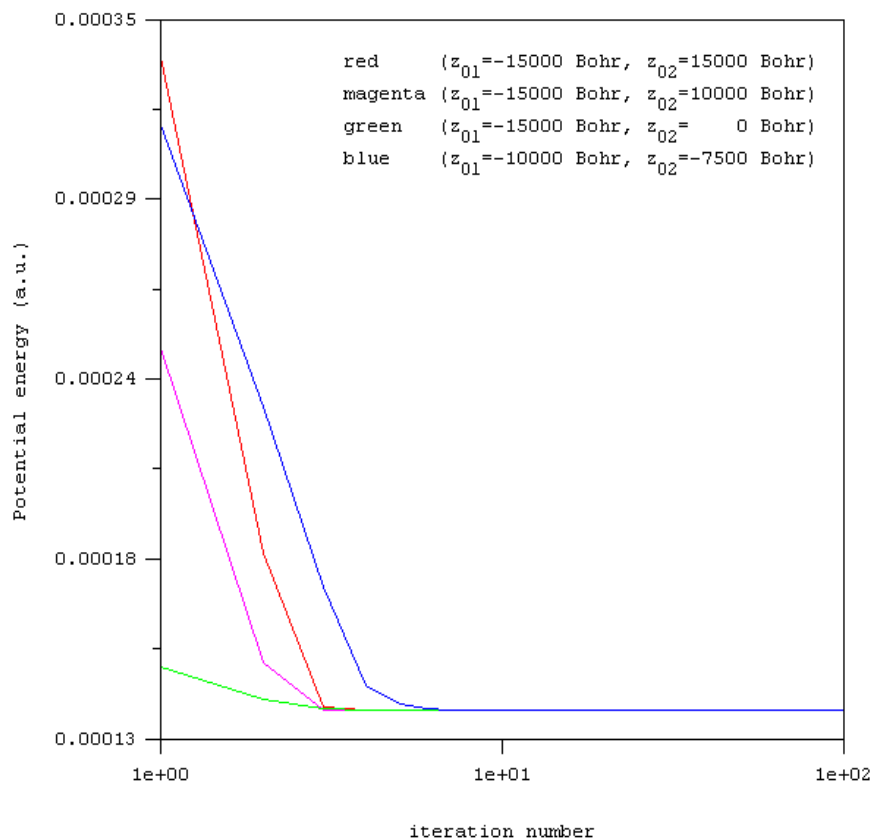


Fig. 4. 4: Change of potential energy of the system during minimization from four different guess positions.

(4.1.2.5) until the convergence is achieved.

Figure 4.3 illustrates the minimization process in four different runs when the initial guess positions were $(z_{01}, z_{02}) = (-15000 \text{ Bohr}, 15000 \text{ Bohr}), (-15000 \text{ Bohr}, 10000 \text{ Bohr}), (-15000 \text{ Bohr}, 0 \text{ Bohr}), (-10000 \text{ Bohr}, -7500 \text{ Bohr})$. All four calculations resulted in the same equilibrium position after about 40 iterations. The results are as follows:

$$z_{e1} = -5.6103 \times 10^3 \text{ Bohr},$$

$$z_{e2} = 5.6103 \times 10^3 \text{ Bohr}.$$

The value of potential energy at this point was $V^{eq} = V(z_{e1}, z_{e2}) = 8.796 \times 10^5 \text{ MHz}$. In Fig. 4.4, we present the change of the potential energy of the system during the minimization and the minimized potential energy was found in the end. In all four runs, the results converged to accuracy up to 10^{-8} Bohr , which is the position difference between two subsequent steps.

4.1.3 Normal vibration modes

At the equilibrium point ($z_1 = z_{e1}$ and $z_2 = z_{e2}$), the Hessian matrix of the system is expressed by the following equation:

$$\mathbf{V}'' = \begin{vmatrix} \frac{\partial^2 V}{\partial z_1^2} & \frac{\partial^2 V}{\partial z_1 \partial z_2} \\ \frac{\partial^2 V}{\partial z_2 \partial z_1} & \frac{\partial^2 V}{\partial z_2^2} \end{vmatrix}_{(z_{e1}, z_{e2})}, \quad (4.1.3.1)$$

To obtain the frequency of two normal vibration modes, the Hessian matrix \mathbf{V}'' of Eq.

(4.1.3.1) must be converted into the matrix \mathbf{F} in mass-weighted coordinates first,

which is presented as follows:

$$\mathbf{F} = \mathbf{M}^{-1/2} \mathbf{V}^T \mathbf{M}^{-1/2}. \quad (4.1.3.2)$$

Substitution of Eqs. (4.1.2.8) - (4.1.2.10) into Eq. (4.1.3.2), the equation of the

Hessian matrix at equilibrium position in mass-weighted coordinates is obtained:

$$\begin{aligned} \mathbf{F} &= \begin{vmatrix} m & 0 \\ 0 & m \end{vmatrix}^{-1/2} \begin{vmatrix} \frac{\partial^2 V}{\partial z_1^2} & \frac{\partial^2 V}{\partial z_1 \partial z_2} \\ \frac{\partial^2 V}{\partial z_2 \partial z_1} & \frac{\partial^2 V}{\partial z_2^2} \end{vmatrix}_{(z_{e1}, z_{e2})} \begin{vmatrix} m & 0 \\ 0 & m \end{vmatrix}^{-1/2} \\ &= \frac{1}{m} \begin{vmatrix} \frac{\partial^2 V}{\partial z_1^2} & \frac{\partial^2 V}{\partial z_1 \partial z_2} \\ \frac{\partial^2 V}{\partial z_2 \partial z_1} & \frac{\partial^2 V}{\partial z_2^2} \end{vmatrix}_{(z_{e1}, z_{e2})} \\ &= \frac{1}{m} \begin{vmatrix} k + \frac{2}{(z_{e2} - z_{e1})^3} & -\frac{2}{(z_{e2} - z_{e1})^3} \\ -\frac{2}{(z_{e2} - z_{e1})^3} & k + \frac{2}{(z_{e2} - z_{e1})^3} \end{vmatrix}. \end{aligned} \quad (4.1.3.3)$$

Eq. (4.1.3.3) can be diagonalized analytically to obtain the eigenvalues and

eigenvectors of the matrix \mathbf{F} . The results are as follows:

$$\begin{aligned} \lambda_1 &= \frac{k}{m} \\ \lambda_2 &= \frac{k}{m} + \frac{\frac{4}{m}}{(z_{e2} - z_{e1})^3} \\ \mathbf{A} &= \begin{vmatrix} a_{11} & a_{12} \\ a_{21} & a_{22} \end{vmatrix} = \begin{vmatrix} \frac{\sqrt{2}}{2} & -\frac{\sqrt{2}}{2} \\ -\frac{\sqrt{2}}{2} & \frac{\sqrt{2}}{2} \end{vmatrix} \end{aligned}$$

Here λ_1 and λ_2 are two eigenvalues of the matrix \mathbf{F} , and the columns in matrix \mathbf{A}

describe two eigenvectors of the system. The first column of matrix \mathbf{A} describes the

first mode with lower frequency which is the center-of-mass motion mode ($\Delta z_1 = \Delta z_2$) and the second column describes the higher frequency mode which is the symmetric stretching mode ($\Delta z_1 = -\Delta z_2$).

The frequency of each normal mode can be calculated from the eigenvalues using the following relationship:

$$\nu_i = \frac{\sqrt{\lambda_i}}{2\pi} = \frac{\omega_i}{2\pi}, \quad (4.1.3.4)$$

here i labels normal vibration modes. Using Eq. (4.1.3.4), we calculate the frequency of these two modes and transfer them from atomic units to MHz. For parameters of the system given on page 17, this gives:

$$\omega_1/2\pi = 2.770 \text{ MHz}$$

$$\omega_2/2\pi = 4.798 \text{ MHz}$$

Note that here for two (and in the later Chapter for three) ions this step can be carried out either analytically or numerically. For four and more ions (in the future work) the numerical procedure is required. In order to test our computer codes we did both numerical and analytic diagonalization and obtained equivalent results. Program 2DHESSIAN in Appendix F shows example of numerical calculations.

4.1.4 Hamiltonian and transformation of coordinates

In the Cartesian coordinates, the Hamiltonian of the system can be written as:

$$\hat{H}(z_1, z_2) = -\frac{1}{2m} \frac{\partial^2}{\partial z_1^2} - \frac{1}{2m} \frac{\partial^2}{\partial z_2^2} + V(z_1, z_2) - V^{eq}, \quad (4.1.4.1)$$

here $V(z_1, z_2)$ is the potential from Eq. (4.1.1.1), z_1 and z_2 are the Cartesian coordinates of two ions. $V^{eq} = V(z_{e1}, z_{e2})$ is the constant energy shift by the minimum potential energy of system when two ions are at their classical minimum energy point (z_{e1}, z_{e2}) . In order to use simple basis functions for numerical solution of this problem, we need to transform the coordinates from Cartesian to the normal mode coordinates. First we transform the coordinates to mass scaled coordinates:

$$\bar{z}_1 = \sqrt{m}z_1, \quad \bar{z}_2 = \sqrt{m}z_2, \quad (4.1.4.2)$$

$$\hat{H}(\bar{z}_1, \bar{z}_2) = -\frac{1}{2} \frac{\partial^2}{\partial \bar{z}_1^2} - \frac{1}{2} \frac{\partial^2}{\partial \bar{z}_2^2} + \hat{V}(\bar{z}_1, \bar{z}_2) - V^{eq}, \quad (4.1.4.3)$$

$$\hat{V}(\bar{z}_1, \bar{z}_2) = \frac{1}{2} \frac{k}{m} \bar{z}_1^2 + \frac{1}{2} \frac{k}{m} \bar{z}_2^2 + \frac{\sqrt{m}}{|\bar{z}_2 - \bar{z}_1|}, \quad (4.1.4.4)$$

here \bar{z}_1 and \bar{z}_2 are the mass scaled coordinates of z_1 and z_2 . Using the following transformation, the expression of Hamiltonian in the mass scaled *displacement* coordinates is achieved:

$$\begin{cases} \bar{z}_1 - \sqrt{m}z_{e1} = \Delta\bar{z}_1 \\ \bar{z}_2 - \sqrt{m}z_{e2} = \Delta\bar{z}_2 \end{cases}, \quad (4.1.4.5)$$

$$\hat{H}(\Delta\bar{z}_1, \Delta\bar{z}_2) = -\frac{1}{2} \frac{\partial^2}{\partial \Delta\bar{z}_1^2} - \frac{1}{2} \frac{\partial^2}{\partial \Delta\bar{z}_2^2} + \hat{V}(\Delta\bar{z}_1, \Delta\bar{z}_2) - V^{eq}, \quad (4.1.4.6)$$

$$\begin{aligned} \hat{V}(\Delta\bar{z}_1, \Delta\bar{z}_2) = & \frac{1}{2} k \left(\frac{\Delta\bar{z}_1}{\sqrt{m}} + z_{e1} \right)^2 + \frac{1}{2} k \left(\frac{\Delta\bar{z}_2}{\sqrt{m}} + z_{e2} \right)^2 \\ & + \frac{\sqrt{m}}{|\Delta\bar{z}_2 - \Delta\bar{z}_1 + \sqrt{m}(z_{e2} - z_{e1})|}, \end{aligned} \quad (4.1.4.7)$$

here $\Delta\bar{z}_1$ and $\Delta\bar{z}_2$ are the mass scaled displacement coordinates for two ions. In the next step, we need to transform coordinates to mass-weighted normal mode

coordinates [98] and the transformation is as follows:

$$\begin{vmatrix} \Delta\bar{z}_1 \\ \Delta\bar{z}_2 \end{vmatrix} = \begin{vmatrix} a_{11} & a_{12} \\ a_{21} & a_{22} \end{vmatrix} \begin{vmatrix} \bar{\zeta}_1 \\ \bar{\zeta}_2 \end{vmatrix} = \begin{vmatrix} -\frac{\sqrt{2}}{2} & -\frac{\sqrt{2}}{2} \\ -\frac{\sqrt{2}}{2} & \frac{\sqrt{2}}{2} \end{vmatrix} \begin{vmatrix} \bar{\zeta}_1 \\ \bar{\zeta}_2 \end{vmatrix}, \quad (4.1.4.8)$$

here $\bar{\zeta}_1$ and $\bar{\zeta}_2$ are the mass-weighted normal mode coordinates of the two-ion system and the matrix of eigenvectors \mathbf{A} is used in the coordinate transformation. From the equations above, the expression of variable $\Delta\bar{z}_1$ and $\Delta\bar{z}_2$ through $\bar{\zeta}_1$ and $\bar{\zeta}_2$ is presented:

$$\begin{cases} \Delta\bar{z}_1 = -\frac{\sqrt{2}}{2}(\bar{\zeta}_1 + \bar{\zeta}_2) \\ \Delta\bar{z}_2 = \frac{\sqrt{2}}{2}(\bar{\zeta}_2 - \bar{\zeta}_1) \end{cases}. \quad (4.1.4.9)$$

Now we know the relation between the mass scaled displacement coordinates and mass scaled normal mode coordinates and we need to find the expression for Hamiltonian in the mass scaled normal mode coordinates.

For the kinetic energy part of the Hamiltonian operator, the transformation to the mass scaled displacement coordinates gives (see Eq. (4.1.4.6)):

$$\hat{T}(\Delta\bar{z}_1, \Delta\bar{z}_2) = -\frac{1}{2} \frac{\partial^2}{\partial \Delta\bar{z}_1^2} - \frac{1}{2} \frac{\partial^2}{\partial \Delta\bar{z}_2^2}. \quad (4.1.4.10)$$

Using Eq. (4.1.4.9), we obtain the following expressions [98]:

$$\frac{\partial}{\partial \bar{\zeta}_1} = \frac{\partial}{\partial \Delta\bar{z}_1} \frac{\partial \Delta\bar{z}_1}{\partial \bar{\zeta}_1} + \frac{\partial}{\partial \Delta\bar{z}_2} \frac{\partial \Delta\bar{z}_2}{\partial \bar{\zeta}_1} = -\frac{1}{\sqrt{2}} \frac{\partial}{\partial \Delta\bar{z}_1} - \frac{1}{\sqrt{2}} \frac{\partial}{\partial \Delta\bar{z}_2}, \quad (4.1.4.11)$$

$$\frac{\partial^2}{\partial \Delta\bar{z}_1 \partial \Delta\bar{z}_2} = \frac{\partial^2}{\partial \Delta\bar{z}_2 \partial \Delta\bar{z}_1}, \quad (4.1.4.12)$$

$$\frac{\partial^2}{\partial \bar{\zeta}_1^2} = -\frac{1}{\sqrt{2}} \left(\frac{\partial^2}{\partial \Delta\bar{z}_1^2} \frac{\partial \Delta\bar{z}_1}{\partial \bar{\zeta}_1} + \frac{\partial^2}{\partial \Delta\bar{z}_1 \partial \Delta\bar{z}_2} \frac{\partial \Delta\bar{z}_2}{\partial \bar{\zeta}_1} \right)$$

$$\begin{aligned}
& + \frac{\partial^2}{\partial \Delta \bar{z}_2 \partial \Delta \bar{z}_1} \frac{\partial \Delta \bar{z}_1}{\partial \bar{\zeta}_1} + \frac{\partial^2}{\partial \Delta \bar{z}_2^2} \frac{\partial \Delta \bar{z}_2}{\partial \bar{\zeta}_1} \Big) \\
& = \frac{1}{2} \left(\frac{\partial^2}{\partial \Delta \bar{z}_1^2} + \frac{\partial^2}{\partial \Delta \bar{z}_2^2} + 2 \frac{\partial^2}{\partial \Delta \bar{z}_1 \partial \Delta \bar{z}_2} \right). \tag{4.1.4.13}
\end{aligned}$$

In the same way, we obtain the second derivative of the second mode:

$$\frac{\partial^2}{\partial \bar{\zeta}_2^2} = \frac{1}{2} \left(\frac{\partial^2}{\partial \Delta \bar{z}_1^2} + \frac{\partial^2}{\partial \Delta \bar{z}_2^2} - 2 \frac{\partial^2}{\partial \Delta \bar{z}_1 \partial \Delta \bar{z}_2} \right). \tag{4.1.4.14}$$

Using Eqs. (4.1.4.13) and (4.1.4.14), we obtain the following final expression of the kinetic energy operator:

$$\frac{\partial^2}{\partial \bar{\zeta}_1^2} + \frac{\partial^2}{\partial \bar{\zeta}_2^2} = \frac{\partial^2}{\partial \Delta \bar{z}_1^2} + \frac{\partial^2}{\partial \Delta \bar{z}_2^2}. \tag{4.1.4.15}$$

This means that in the mass scaled normal mode coordinates the kinetic energy part of Hamiltonian is still in the same form:

$$\hat{T}(\bar{\zeta}_1, \bar{\zeta}_2) = -\frac{1}{2} \frac{\partial^2}{\partial \bar{\zeta}_1^2} - \frac{1}{2} \frac{\partial^2}{\partial \bar{\zeta}_2^2}. \tag{4.1.4.16}$$

By substitution Eq. (4.1.4.9) into Eq. (4.1.4.7), the equation of potential energy part in the mass scaled normal mode coordinates is obtained:

$$\begin{aligned}
\hat{V}(\bar{\zeta}_1, \bar{\zeta}_2) &= \frac{1}{2} k \left(z_{e1} - \frac{\bar{\zeta}_1 + \bar{\zeta}_2}{\sqrt{2m}} \right)^2 + \frac{1}{2} k \left(z_{e2} + \frac{\bar{\zeta}_2 - \bar{\zeta}_1}{\sqrt{2m}} \right)^2 \\
&+ \frac{\sqrt{2m}}{|2\bar{\zeta}_2 + \sqrt{2m}(z_{e2} - z_{e1})|}. \tag{4.1.4.17}
\end{aligned}$$

Here

$$V_{eq} = \frac{1}{2} k z_{e1}^2 + \frac{1}{2} k z_{e2}^2 + \frac{1}{|z_{e2} - z_{e1}|}. \tag{4.1.4.18}$$

If we expand the brackets in Eq. (4.1.4.17), we obtain:

$$\hat{V}(\bar{\zeta}_1, \bar{\zeta}_2) = \frac{1}{2m} \bar{\zeta}_1^2 + \frac{1}{2m} \bar{\zeta}_2^2 + \frac{k \bar{\zeta}_2 (z_{e2} - z_{e1})}{\sqrt{2m}}$$

$$+ \frac{1}{\left| \sqrt{\frac{2}{m}} \bar{\zeta}_2 + (z_{e2} - z_{e1}) \right|} + \frac{k}{2} (z_{e1}^2 + z_{e2}^2). \quad (4.1.4.19)$$

Note that the Coulomb interaction is included only into the term $\frac{1}{\left| \sqrt{\frac{2}{m}} \bar{\zeta}_2 + (z_{e2} - z_{e1}) \right|}$ of

Eq. (4.1.4.19). This term is clearly anharmonic and depends only on the symmetric stretching coordinate $\bar{\zeta}_2$. Also there is no coupling terms between the two vibration modes, so this potential is analytically separable. The first mode is harmonic and the second mode is anharmonic due to the Coulomb.

$$\hat{V}(\bar{\zeta}_1) = \frac{1}{2} \frac{k}{m} \bar{\zeta}_1^2 + \frac{k}{2} z_{e1}^2, \quad (4.1.4.20)$$

$$\hat{V}(\bar{\zeta}_2) = \frac{1}{2} \frac{k}{m} \bar{\zeta}_2^2 + \frac{k \bar{\zeta}_2 (z_{e2} - z_{e1})}{\sqrt{2m}} + \frac{1}{\left| \sqrt{\frac{2}{m}} \bar{\zeta}_2 + (z_{e2} - z_{e1}) \right|} + \frac{k}{2} z_{e2}^2. \quad (4.1.4.21)$$

Finally, the Hamiltonian in mass scaled normal mode coordinates is expressed by the following equation:

$$\hat{H}(\bar{\zeta}_1, \bar{\zeta}_2) = -\frac{1}{2} \frac{\partial^2}{\partial \bar{\zeta}_1^2} - \frac{1}{2} \frac{\partial^2}{\partial \bar{\zeta}_2^2} + \hat{V}(\bar{\zeta}_1) + \hat{V}(\bar{\zeta}_2) - V^{eq}. \quad (4.1.4.22)$$

4.1.5 Harmonic Approximation

It is instructive to consider an approximation to the Hamiltonian in Eq. (4.1.4.19), which allows solving the Schrödinger equation analytically and approximately. We expand the term $\frac{1}{\left| \sqrt{\frac{2}{m}} \bar{\zeta}_2 + (z_{e2} - z_{e1}) \right|}$ in the Taylor Expansion. This leads to the following equation:

$$\begin{aligned}\hat{V}(\bar{\zeta}_1, \bar{\zeta}_2) \approx & \frac{1}{2} \frac{k}{m} \bar{\zeta}_1^2 + \frac{1}{2} \frac{k}{m} \bar{\zeta}_2^2 + \frac{2}{m(z_{e2} - z_{e1})^3} \bar{\zeta}_2^2 \\ & + \frac{k \bar{\zeta}_2 (z_{e2} - z_{e1})}{\sqrt{2m}} - \sqrt{\frac{2}{m}} \frac{\bar{\zeta}_2}{(z_{e2} - z_{e1})^2} \\ & + \frac{k}{2} (z_{e1}^2 + z_{e2}^2) + \frac{1}{z_{e2} - z_{e1}}.\end{aligned}\quad (4.1.5.1)$$

We can define the equilibrium energy as:

$$V_{eq} = V(\bar{\zeta}_1 = 0, \bar{\zeta}_2 = 0) = \frac{1}{2} k z_{e1}^2 + \frac{1}{2} k z_{e2}^2 + \frac{1}{|z_{e2} - z_{e1}|}. \quad (4.1.5.2)$$

Next, from the expression above, using properties of the equilibrium point ($\bar{\zeta}_1 = \bar{\zeta}_2 = 0$, $-z_1^{eq} = z_2^{eq}$ and $\partial V / \partial z^{eq} = 0$) we can obtain approximate analytical expressions

for the equilibrium positions (in the harmonic approximation):

$$z_{e1} \approx -\left(\frac{1}{4k}\right)^{\frac{1}{3}}, \quad (4.1.5.3)$$

$$z_{e2} \approx \left(\frac{1}{4k}\right)^{\frac{1}{3}}, \quad (4.1.5.4)$$

and for the equilibrium energy (in the harmonic approximation):

$$V^{eq} \approx V(z_{e1}, z_{e2}) = \frac{3}{2} \left(\frac{k}{2}\right)^{1/3}. \quad (4.1.5.5)$$

Substituting Eqs. (4.1.5.3) and (4.1.5.4) into Eq. (4.1.5.1), we obtain the following

expression:

$$\hat{V}(\bar{\zeta}_1, \bar{\zeta}_2) \approx \frac{1}{2} \frac{k}{m} \bar{\zeta}_1^2 + \frac{1}{2} \frac{3k}{m} \bar{\zeta}_2^2 + \frac{3}{2} \left(\frac{k}{2}\right)^{\frac{1}{3}} = \hat{V}(\bar{\zeta}_1) + \hat{V}(\bar{\zeta}_2). \quad (4.1.5.6)$$

Substitution Eqs. (4.1.5.5) and (4.1.5.6) in to Eq. (4.1.4.22), the Hamiltonian in

harmonic approximation is obtained:

$$\hat{H}(\bar{\zeta}_1, \bar{\zeta}_2) = -\frac{1}{2} \frac{\partial^2}{\partial \bar{\zeta}_1^2} - \frac{1}{2} \frac{\partial^2}{\partial \bar{\zeta}_2^2} + \frac{1}{2} \frac{k}{m} \bar{\zeta}_1^2 + \frac{1}{2} \frac{3k}{m} \bar{\zeta}_2^2, \quad (4.1.5.7)$$

$$\hat{H}(\bar{\zeta}_1, \bar{\zeta}_2) = -\frac{1}{2} \frac{\partial^2}{\partial \bar{\zeta}_1^2} - \frac{1}{2} \frac{\partial^2}{\partial \bar{\zeta}_2^2} + \frac{1}{2} k \left(\frac{\bar{\zeta}_1}{\sqrt{m}} \right)^2 + \frac{1}{2} k \left(\sqrt{\frac{3}{m}} \bar{\zeta}_2 \right)^2, \quad (4.1.5.8)$$

here $\bar{\zeta}_1$ and $\bar{\zeta}_2$ are mass scaled normal mode coordinates. This approximate Hamiltonian operator is separable and harmonic in $\bar{\zeta}_1$ and $\bar{\zeta}_2$ (two uncoupled harmonic oscillators) and has analytic solutions to energies and wave functions. We found it convenient to introduce the “unscaled” normal mode coordinates ζ_1 and ζ_2 (measured in the units of length, a_0) according to the following:

$$\begin{cases} \mu_1 = \frac{m}{3}, \\ \mu_2 = \frac{m}{3}, \end{cases} \quad \begin{cases} \bar{\zeta}_1 = \sqrt{\mu_1} \zeta_1, \\ \bar{\zeta}_2 = \sqrt{\mu_2} \zeta_2. \end{cases} \quad (4.1.5.9)$$

Here (μ_1, μ_2) are the effective masses. In such unscaled coordinates the Hamiltonian is expressed simply as:

$$\hat{H}(\zeta_1, \zeta_2) = -\frac{1}{2\mu_1} \frac{\partial^2}{\partial \zeta_1^2} - \frac{1}{2\mu_2} \frac{\partial^2}{\partial \zeta_2^2} + \frac{1}{2} k \zeta_1^2 + \frac{1}{2} k \zeta_2^2. \quad (4.1.5.10)$$

The Harmonic frequencies of two modes are (in the harmonic approximation):

$$\omega_1 = \sqrt{k/m} = \omega, \quad (4.1.5.11)$$

$$\omega_2 = \sqrt{k/\left(\frac{m}{3}\right)} = \sqrt{3}\omega. \quad (4.1.5.12)$$

Using parameters of our model we obtain, in the harmonic approximation,
 $z_{e1} = -5.610 \times 10^3 a_0$, $z_{e2} = 5.610 \times 10^3 a_0$, $V^{eq} = 8.796 \times 10^5$ MHz, $\omega_1/2\pi = 2.770$ MHz and $\omega_2/2\pi = 4.798$ MHz. These numbers are close to those obtained numerically at the beginning of this section.

Note that analytical expressions of Eqs. (4.1.5.3) and (4.1.5.4) for the

equilibrium distances, Eqs. (4.1.5.11) and (4.1.5.12) for the vibration frequencies, obtained here within the harmonic approximation, are consistent with results of James and coworkers [69, 70] obtained in a different way, and also with the NIST data [99]. This comparison provides an important benchmark for our theory and clearly demonstrates that the exact framework (beyond the harmonic approximation) developed in this work goes beyond the existing theoretical treatments of the ion chains in Paul traps.

Using conclusions of the discussion above it is convenient to rewrite the exact Hamiltonian of Eq. (4.1.4.22) using the mass-unscaled normal mode coordinates (ζ_1, ζ_2) . The resultant expression is:

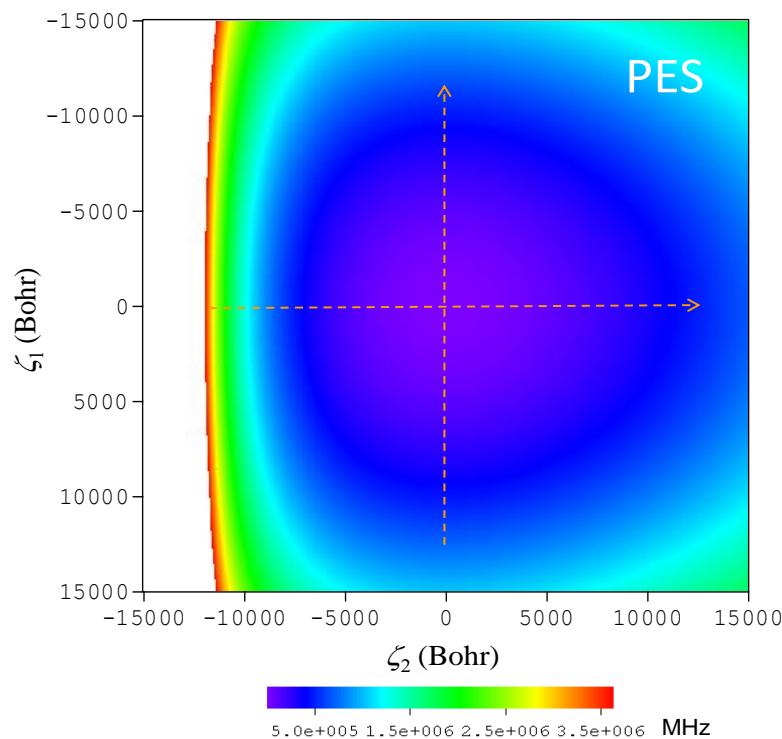


Fig. 4. 5: Potential energy surface of two $^{111}\text{Cd}^+$ ions in the harmonic potential trap using normal mode coordinates.

$$\hat{H}(\zeta_1, \zeta_2) = -\frac{1}{2m} \frac{\partial^2}{\partial \zeta_1^2} - \frac{1}{2 \left(\frac{m}{3} \right)} \frac{\partial^2}{\partial \zeta_2^2} + \hat{V}(\zeta_1) + \hat{V}(\zeta_2) - V^{eq}. \quad (4.1.5.13)$$

$$\hat{V}(\zeta_1) = \frac{1}{2} k \zeta_1^2 + \frac{k}{2} z_{e1}^2, \quad (4.1.5.14)$$

$$\hat{V}(\zeta_2) = \frac{1}{6} k \zeta_2^2 + \frac{k \zeta_2 (z_{e2} - z_{e1})}{\sqrt{6}} + \frac{1}{\left| \sqrt{\frac{2}{3}} \zeta_2 + (z_{e2} - z_{e1}) \right|} + \frac{k}{2} z_{e2}^2. \quad (4.1.5.15)$$

This expression is exact and contains all anharmonicities. It involves no approximations, just the transformation of coordinates. In Fig. 4.5, the PES in the normal mode coordinates (ζ_1, ζ_2) is shown. Only the part of $z_2 > z_1$ is relevant after the transformation. From the picture we can see that: The motion along ζ_1 goes parallel to the white part, where Coulomb interaction is significant. So the motion along this mode does not bring the system towards the region of strong Coulomb interaction. As a result the system remains harmonic. In contrast, the motion along ζ_2 brings the system closer to the Coulomb region, which makes this mode anharmonic.

4.1.6 2D Basis set expansion

Two-dimensional wavefunctions of this system and the corresponding energy eigenvalues are calculated using the direct product basis set expansion method in the normal mode coordinates:

$$\Psi_v(\zeta_1, \zeta_2) = \sum_{i,j}^N C_{v,i,j} \varphi_i(\zeta_1) \varphi_j(\zeta_2), \quad (4.1.6.1)$$

here $\varphi_i(\zeta_1)$ and $\varphi_j(\zeta_2)$ are given by the expression of Eq. (2.2.4). They describe the

basis functions of two vibrational modes of the system. Their vibration frequencies

are ω_1 (center-of-mass motion mode ζ_1) and ω_2 (symmetric stretching mode ζ_2).

Indexes i and j lable basis functions and run from 1 to N . Index v lables states of the

two-ion system; it runs from 1 to N^2 . The $C_{v,i,j}$ are coefficients of linear combination.

In the matrix form they can be written as \mathbf{C}_{N^2, N^2} .

Substituting the basis functions $\varphi_i(\zeta_1)\varphi_j(\zeta_2)$ ($i, j = 1, \dots, N$) into Eq. (2.2.14), we obtain the Hamiltonian matrix of the two-ion system. Similar in form to the one-ion case, but the dimension of this matrix is $N^2 \times N^2$, where N is the number of basis functions for each mode. The kinetic energy part and the potential energy part are calculated numerically using the Equally-Spaced Abscissas method. A computer code named 2DIONTRAP was written to carry out all these calculation numerically (see Appendix G).

4.1.7 Convergence Studies

Rigorous convergence studies were carried out to optimize different parameters in our calculations: the integration limit ζ_{max} , the step size $\Delta\zeta$ and the basis set size N . First, using a small integration step $\Delta\zeta = 6.25$ Bohr and large size of the basis set $N = 20$, we did calculations with different integration limits ($\zeta_{max} = 1000, 500, 400$ Bohr). We defined the numerical accuracy as:

$$\delta E = E_{\zeta_{max}=1000} - E_{\zeta_{max}=400/500}. \quad (4.1.7.1)$$

From Fig. 4.6, we can see the difference between the results computed with $\zeta_{max} = 500$ and 1000 Bohr, and the difference between the results computed with $\zeta_{max} = 400$ and 1000 Bohr. It is found that results obtained with $\zeta_{max} = 500$ Bohr are accurate enough and their differences from those obtained with $\zeta_{max} = 1000$ Bohr is smaller than 10^{-9} MHz up to 400 states. So the value of $\zeta_{max} = 500$ Bohr is used in further calculations.

Next, using $\zeta_{max} = 500$ Bohr and $N = 20$, we studied the effect of the integration step size ($\Delta\zeta = 6.25, 10, 20$ Bohr). We defined the numerical accuracy as:

$$\delta E = E_{\Delta\zeta=6.25} - E_{\Delta\zeta=10/20}. \quad (4.1.7.2)$$

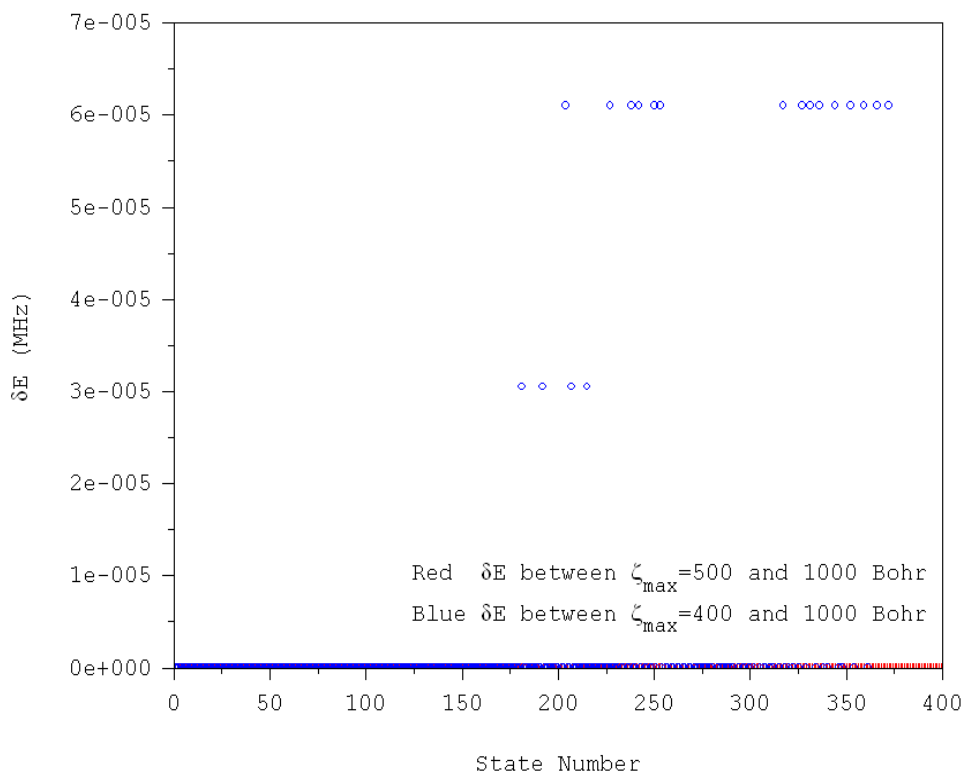


Fig. 4.6: Convergence study with different integration limits ($\zeta_{max} = 1000, 500, 400$ Bohr). $\Delta\zeta = 6.25$ Bohr and $N = 20$.

The value $\Delta\zeta = 10$ Bohr was chosen with this grid: the deviation of energies from the most accurate result ($\Delta\zeta = 6.25$ Bohr) is lower than 10^{-9} MHz for up to 400 states. Finally, we fixed $\zeta_{max} = 500$ Bohr and $\Delta\zeta = 10$ Bohr to study the effect of the size of basis set ($N = 10, 15, 20, 25$). The definition of the numerical accuracy in this case is given by the following expression:

$$\delta E = E_{N=25} - E_{N=10/15/20}. \quad (4.1.7.3)$$

From Fig. 4.8, we see that the results obtained using 15 basis functions per normal mode are good enough for the first 77 states which contain all the vibrational states we need with accuracy better than 10^{-9} MHz. In the final 2D calculations, the

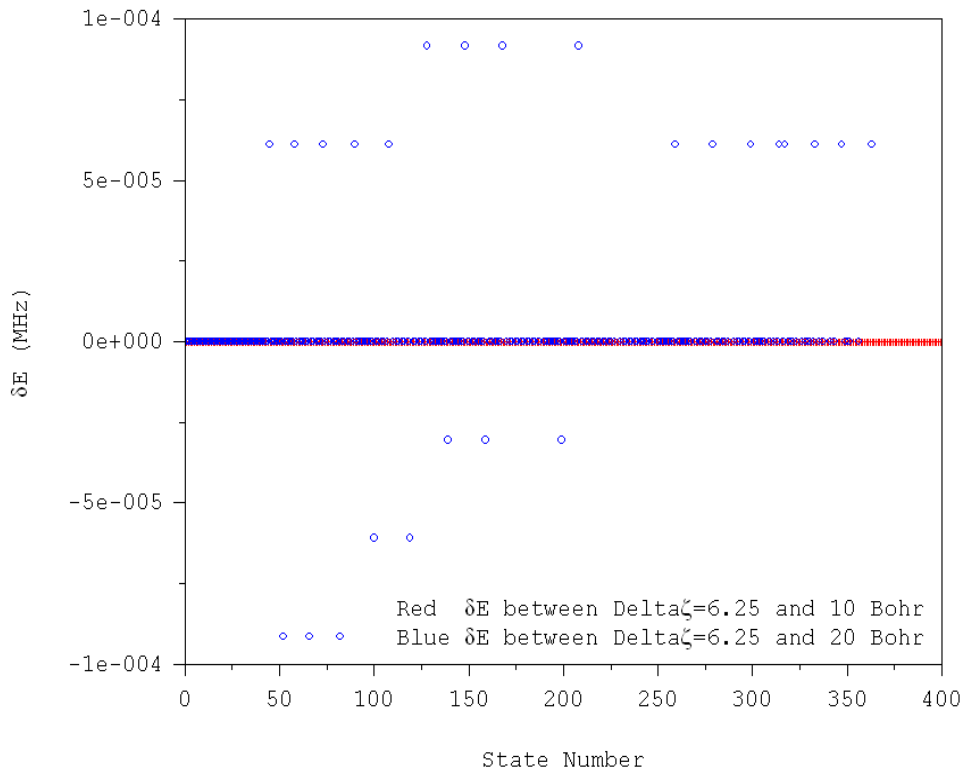


Fig. 4. 7: Convergence study with different integration steps ($\Delta\zeta = 6.25, 10, 20$ Bohr). $\zeta_{max} = 500$ Bohr and $N = 20$.

following parameters are used: $\zeta_{1max} = \zeta_{2max} = 500$ Bohr, $\mathcal{N}_1 = \mathcal{N}_2 = 101$ (Equally-Spaced Abscissas method: $\Delta\zeta_1 = \Delta\zeta_2 = 10$ Bohr) and $N_1 \times N_2 = 15 \times 15$.

4.1.8 Results and analysis

In order to elucidate the effect of Coulomb anharmonicity, we computed deviations of the numerical spectrum from the Harmonic one:

$$\delta E = E_v - E_h, \quad (4.1.8.1)$$

where

$$E_h = \omega_1 \left(v_1 + \frac{1}{2} \right) + \omega_2 \left(v_2 + \frac{1}{2} \right). \quad (4.1.8.2)$$

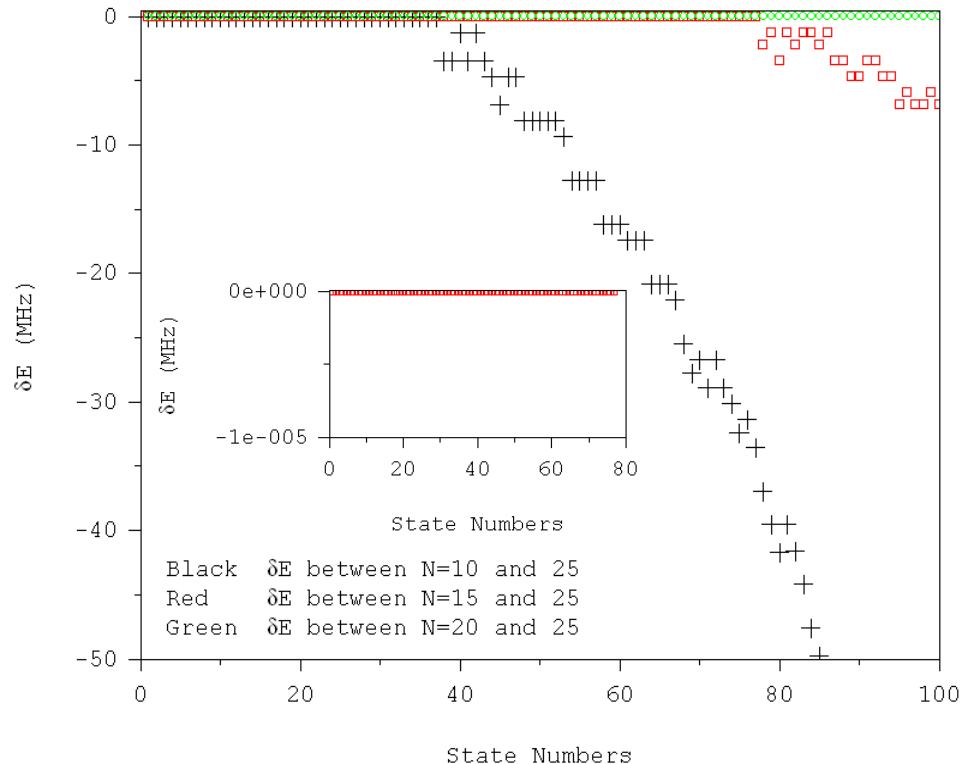


Fig. 4. 8: Convergence study with different number of basis functions $N = 10, 15, 20, 25$. $\Delta\zeta = 10$ Bohr and $\zeta_{max} = 500$ Bohr.

Table 4. 1: Eigenvalues, assignments and deviations (from the harmonic model) of the vibrational states of two $^{111}\text{Cd}^+$ ions in a harmonic trap.

# of state	E_v (MHz)	E_h (MHz)	v_1	v_2	δE (MHz)
1	23.77492	23.77487	0	0	0.00005
2	41.17934	41.17929	1	0	0.00005
3	53.92034	53.92021	0	1	0.00013
4	58.58375	58.58371	2	0	0.00005
5	71.32475	71.32462	1	1	0.00013
6	75.98817	75.98812	3	0	0.00005
7	84.06584	84.06554	0	2	0.00031
8	88.72917	88.72903	2	1	0.00014
9	93.39259	93.39253	4	0	0.00005
10	101.47026	101.46996	1	2	0.00031
11	106.13358	106.13345	3	1	0.00013
12	110.79700	110.79695	5	0	0.00005
13	114.21143	114.21087	0	3	0.00056
14	118.87467	118.87437	2	2	0.00031
15	123.53800	123.53786	4	1	0.00014
16	128.20142	128.20137	6	0	0.00005
17	131.61584	131.61528	1	3	0.00056
18	136.27908	136.27878	3	2	0.00031
19	140.94241	140.94228	5	1	0.00014
20	144.35710	144.35620	0	4	0.00090
21	145.60583	145.60579	7	0	0.00005
26	163.01024	163.01019	8	0	0.00005
29	174.50287	174.50154	0	5	0.00133
32	180.41466	180.41461	9	0	0.00005
40	204.64871	204.64687	0	6	0.00185
53	234.79465	234.79221	0	7	0.00244
67	264.94067	264.93753	0	8	0.00314
82	295.08676	295.08286	0	9	0.00391

Here ω_1 and ω_2 are the normal mode frequencies obtained from diagonalization of Hessian matrix in Sec. 4.1.3.

The eigenvalues calculated numerically, the harmonic spectrum and their assignments in terms of the normal vibration mode quantum numbers (v_1 , v_2) are given in Table 4.1. From Table 4.1, it is found that our numerical results for energies

are a little higher than the analytic spectrum from harmonic approximation. It is because in the harmonic approximation we only keep the first three terms of the Taylor series. The values of deviations from harmonic model, δE , are given in Table 4.1 and are also presented in Fig. 4.9 for the ten lowest states of each normal mode progression. Figure 4.9 shows very clearly that Mode 1 (center-of-mass motion) remains harmonic, while Mode 2 (symmetric stretching) shows a distinct effect of Coulomb anharmonicity. We can understand this effect more directly from Fig. 4.10. In Mode 1 two ions move together along the z -axis as a single pseudo-particle. Such simultaneous center-of-mass motion of two ions does not change the distance between

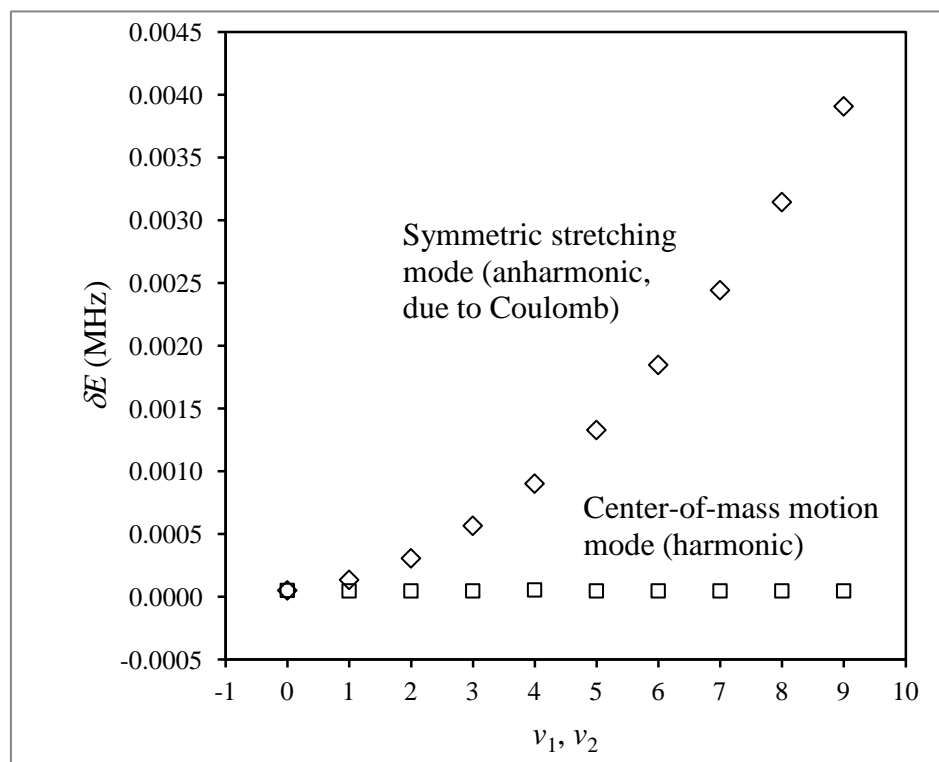


Fig. 4.9: Effect of anharmonicity for two modes of the vibrational spectrum of two $^{111}\text{Cd}^+$ ions in a harmonic ($\sim z^2$) potential trap.

them, and does not change the amount of Coulomb interaction. Excitation of the Mode 2, however, brings ions closer together and takes them further apart, changing the Coulomb repulsion energy of the system.

In order to quantify the effect of Coulomb anharmonicity we calculated the coefficients for the 2D-Dunham expansion [83]:

$$E_{v_1, v_2} = D + \Omega_1 \left(v_1 + \frac{1}{2} \right) - \Delta_1 \left(v_1 + \frac{1}{2} \right)^2 + \Omega_2 \left(v_2 + \frac{1}{2} \right) - \Delta_2 \left(v_2 + \frac{1}{2} \right)^2 - \Delta_{12} \left(v_1 + \frac{1}{2} \right) \left(v_2 + \frac{1}{2} \right), \quad (4.1.8.3)$$

based on numerical values of six eigenstates (ground state, first excited states of each mode, their overtones, and the combination state). The results are:

$$D/2\pi = 6.280 \times 10^{-6} \text{ MHz},$$

$$\Omega_1/2\pi = 2.770 \text{ MHz},$$

$$\Omega_2/2\pi = 4.798 \text{ MHz},$$

$$\Delta_1 \approx 0 \text{ MHz},$$

$$\Delta_2/2\pi = -6.851 \times 10^{-6} \text{ MHz},$$

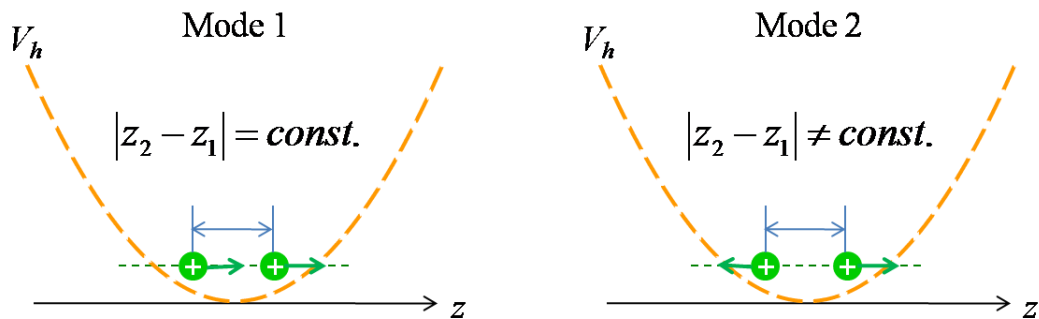


Fig. 4. 10: Description of the ion motions for two vibrational motion modes.

$$\Delta_{12} \approx 0 \text{ MHz}.$$

From these data we see that the center-of-mass motion mode is strictly harmonic ($\Delta_1 \approx 0$). Although the Coulomb interaction introduces some anharmonicity into the spectrum of the symmetric stretching mode, the value of this anharmonicity is too low for the control. The anharmonicity parameter in this case is $\Delta_2 \sim 10^{-6}\Omega_2$, which is about four orders of magnitude smaller than is needed for the successful control. Thus, the Coulomb anharmonicity by itself is clearly insufficient for the control.

4.1.9 Two-dimensional wavefunctions and transition matrix

Using eigenvectors $C_{v_i,j}$ from diagonalization of Hamiltonian matrix and the basis functions $\varphi_i(\zeta_1)\varphi_j(\zeta_2)$ ($i, j = 1, \dots, N$) of the system, the wavefunctions Ψ_v of the eigenstates in the harmonic potential trap can be computed using Eq. (2.2.7). In Fig. 4.11 we present wavefunctions for several lower states. Based on shapes of wavefunctions we can assign the normal mode quantum numbers (v_1, v_2) to these states.

In the two-ion system, the elements in transition matrix are computed as follows:

$$M_{v,v'} = \langle \Psi_v | d(z_1, z_2) | \Psi_{v'} \rangle. \quad (4.1.9.1)$$

Here

$$d(z_1, z_2) = q(z_1 + z_2) \quad (4.1.9.2)$$

is the dipole moment function. The brackets $\langle \parallel \rangle$ in Eq. (4.1.9.1) represent integration over two spatial variables. Note that the wavefunctions are obtained in the normal mode coordinates, while the dipole moment function of Eq. (4.1.9.2) is expressed in Cartesian coordinates. In order to carry out the integration of Eq. (4.1.9.1) using wavefunctions in the normal mode coordinates, one has to transform the dipole moment function into the normal mode coordinates using Eqs. (4.1.4.2), (4.1.4.5), (4.1.4.9) and (4.1.5.9). This can be done using the following expressions:

$$z_1 = -\frac{\sqrt{2}}{2} \left(\zeta_1 + \frac{\zeta_2}{\sqrt{3}} \right) + z_{e1}, \quad (4.1.9.3)$$

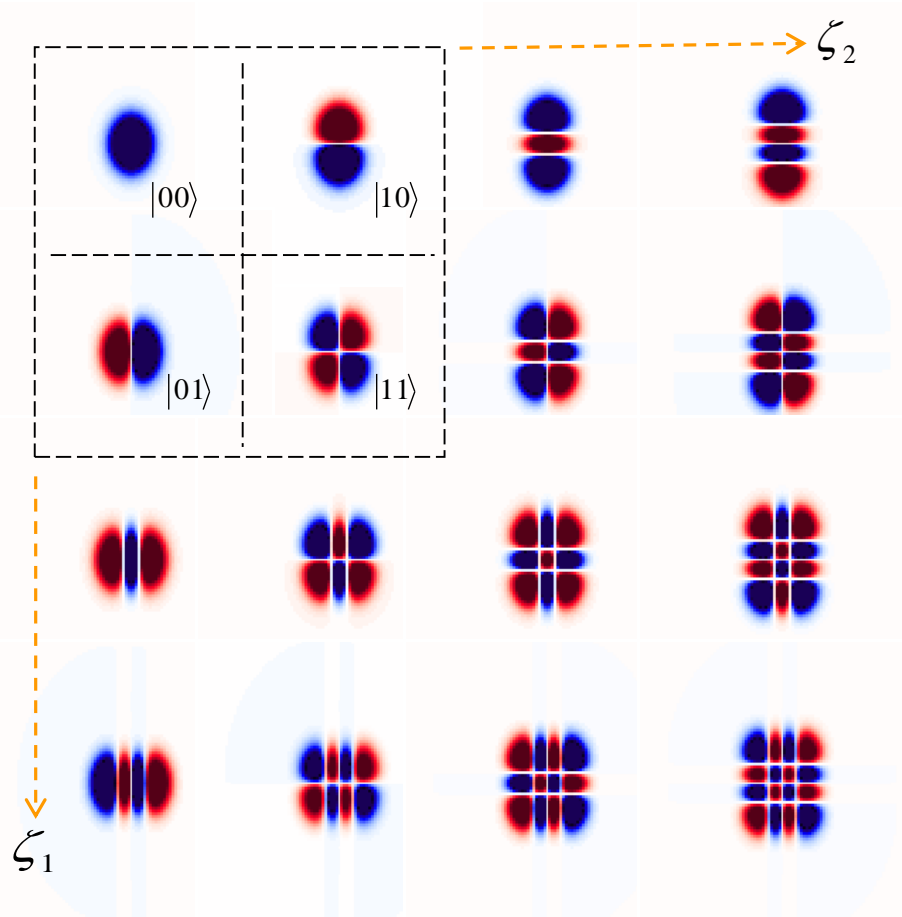


Fig. 4. 11: Wavefunctions of two $^{111}\text{Cd}^+$ ions in the harmonic potential trap.

$$z_2 = -\frac{\sqrt{2}}{2} \left(\zeta_1 - \frac{\zeta_2}{\sqrt{3}} \right) + z_{e2}, \quad (4.1.9.4)$$

$$z_1 + z_2 = -\sqrt{2}\zeta_1. \quad (4.1.9.5)$$

Finally, we use Eq. (4.1.9.5) to rewrite the expression of the dipole moment in the

following form:

$$d(\zeta_1, \zeta_2) = -\sqrt{2}\zeta_1 q = d(\zeta_1) \quad (4.1.9.6)$$

From Eq. (4.1.9.6) we can see that the transition dipole moment depends only on one coordinate ζ_1 . That means there are only state-to-state transitions between states of the first mode, the second mode is “dark” in this two-ion system.

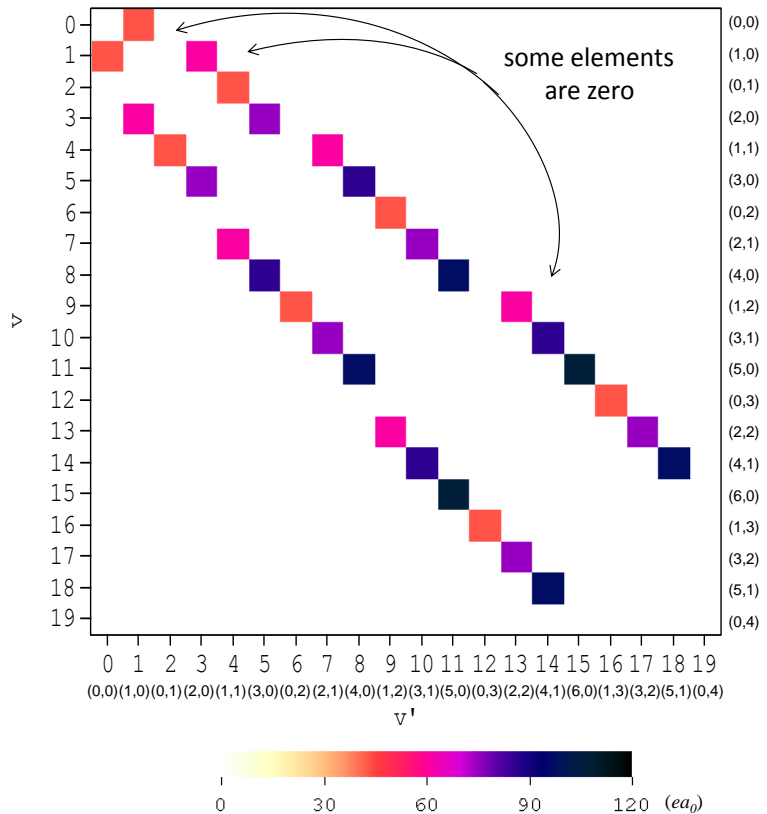


Fig. 4. 12: Transition matrix for two $^{111}\text{Cd}^+$ ions in the harmonic potential trap. (black corresponds $\mu_{5,6} = 1.06 \times 10^2 \text{ } ea_0$ ($\sim 2.69 \times 10^2 \text{ D}$) and orange corresponds $\mu_{0,1} = 43.22 \text{ } ea_0$ ($\sim 1.10 \times 10^2 \text{ D}$) between states of mode 1).

Then the elements of transition matrix in the mass unscaled normal mode coordinates are expressed as:

$$M_{v,v'} = -\sqrt{2}q\langle \Psi_v(\zeta_1, \zeta_2) | \zeta_1 | \Psi_{v'}(\zeta_1, \zeta_2) \rangle. \quad (4.1.9.7)$$

In Fig. 4.12, we show the transition matrix of the lower 20 states, calculated from Eq. (4.1.9.7). The dipole moment function is an anti-symmetric (linear) function of ζ_1 . Thus, the matrix elements are non-zero only for transitions between states of different symmetries (e.g., symmetric-to-asymmetric states and vice versa), leading to the following selection rules:

$$\Delta v = \pm 1, \pm 3, \pm 5 \text{ etc.}, \quad (4.1.9.8)$$

for Modes 1. Mode 2 is “dark” and cannot be controlled using the spatially homogeneous electric field.

4.2 Two ions in the anharmonic trapping potential

4.2.1 Anharmonic trapping potential

Here we explore the possibility of using an anharmonic trapping potential in order to control the two-ion system. We consider the strongly anharmonic quartic trap where the potential is given by:

$$V_a(z) = \frac{1}{4!}k'z^4, \quad (4.2.1.1)$$

where k' is a parameter which controls trap frequency. Here, we present the results of

calculations with $k'/2\pi = 3.558 \times 10^{-11} \text{ MHz}/a_0^4$. This parameter was chosen in order to obtain vibration frequencies similar to the system of two ions in the harmonic trapping potential. In Fig. 4.13 we show the anharmonic trapping potential, the equilibrium positions of two ions and several lower energy levels of the system.

The PES of two ions in the anharmonic trapping potential based on Eq. (4.2.1.1) is shown in Fig. 4.14 using Cartesian coordinates. Overall, it looks similar to

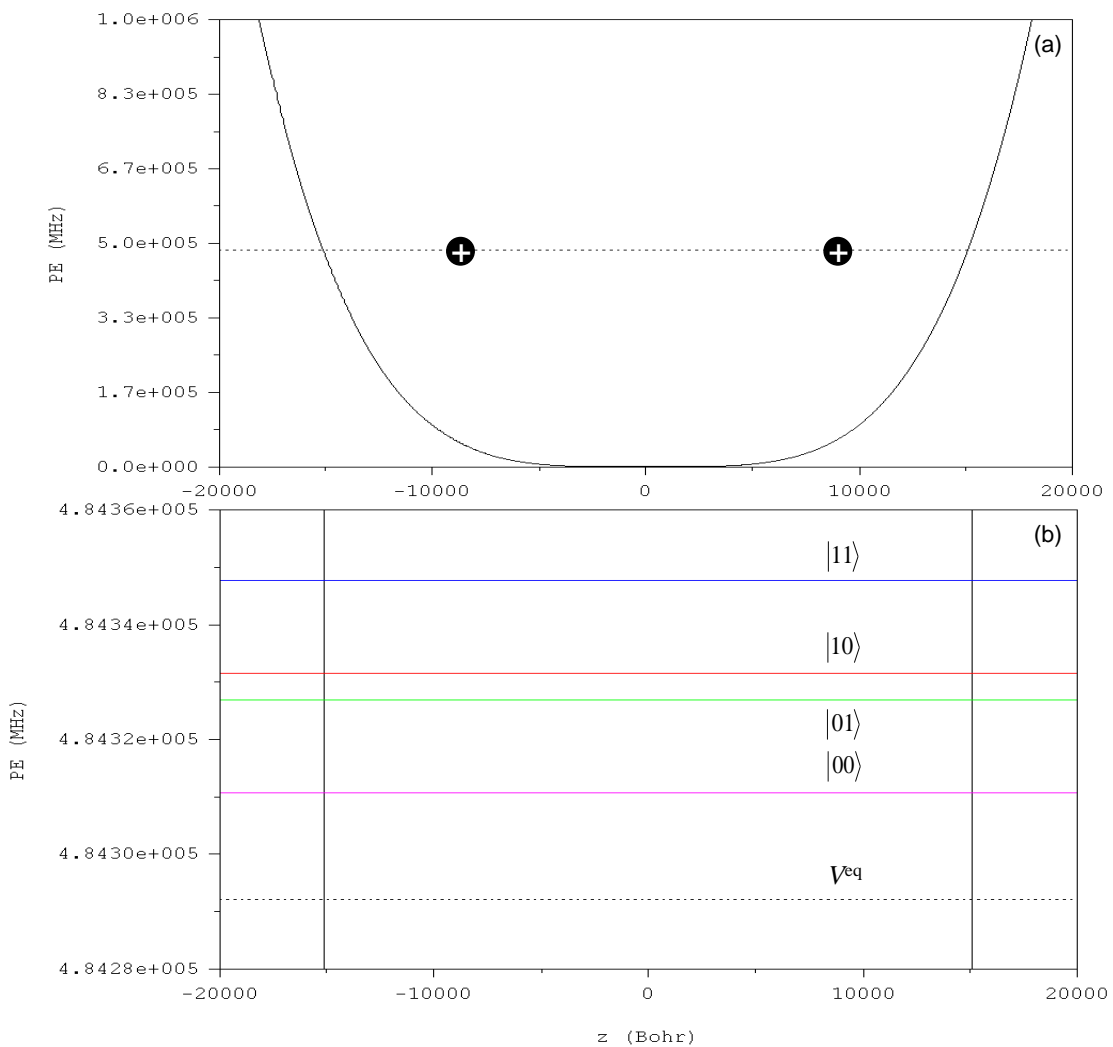


Fig. 4. 13: Two $^{111}\text{Cd}^+$ ions in the $\sim z^4$ potential trap: (a) Equilibrium positions of ions and minimum energy of the two-ion string. (b) Vibrational spectrum of this system and the encoding of two-qubit states.

Fig. 4.2, which is the PES of two ions in the harmonic trapping potential, but some differences are clearly seen. Again, when the two ions come close to each other, the potential energy approaches infinity which is the effect of Coulomb repulsion.

As before, the NR method was used to carry out the minimization and the results obtained for the equilibrium positions were:

$$z_{e1} = -8.4914 \times 10^3 \text{ Bohr},$$

$$z_{e2} = 8.4914 \times 10^3 \text{ Bohr}.$$

The value of potential energy at this point was $V^{eq} = V(z_{e1}, z_{e2}) = 4.843 \times 10^5$ MHz.

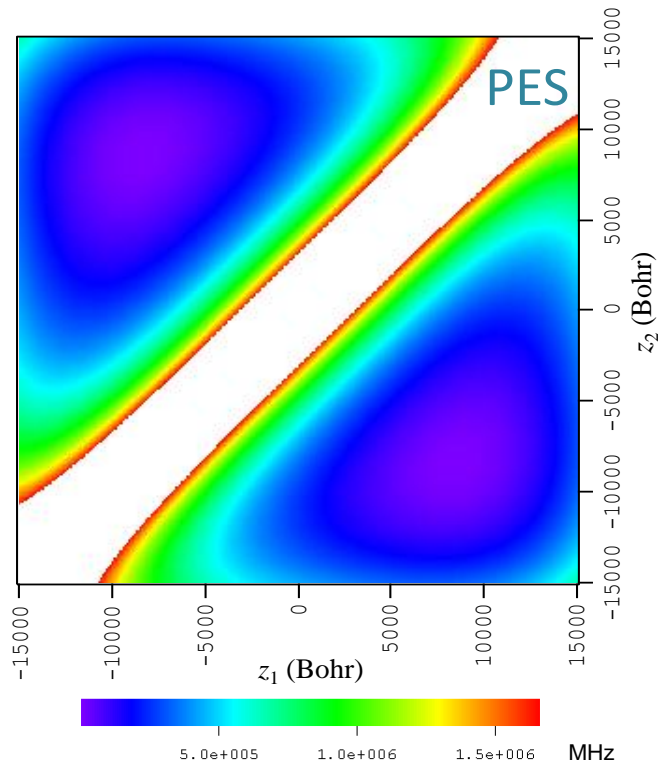


Fig. 4. 14: PES of two $^{111}\text{Cd}^+$ ions in the anharmonic potential trap using Cartesian coordinates. Anharmonicities due to Coulomb repulsion of ions are clearly seen.

In the next step, diagonalization of the Hessian matrix was done and eigenvalues were obtained:

$$\lambda_1 = 6.054 \times 10^{-18} \text{ a.u.}$$

$$\lambda_2 = 1.009 \times 10^{-17} \text{ a.u.}$$

Using Eq. (4.1.3.4), we calculate the frequencies of these two modes and transform to the units of MHz:

$$\omega_1/2\pi = 2.577 \text{ MHz},$$

$$\omega_2/2\pi = 3.326 \text{ MHz.}$$

The eigenvectors were also obtained:

$$\mathbf{A} = \begin{vmatrix} a_{11} & a_{12} \\ a_{21} & a_{22} \end{vmatrix} = \begin{vmatrix} -0.70711 & -0.70711 \\ -0.70711 & 0.70711 \end{vmatrix}.$$

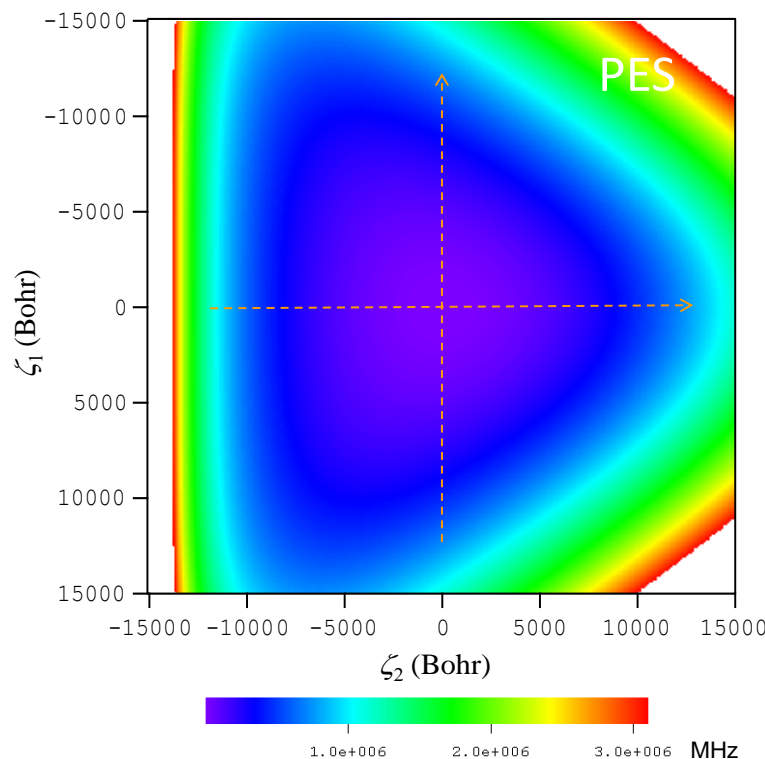


Fig. 4. 15: PES of two $^{111}\text{Cd}^+$ ions in the anharmonic potential trap using normal mode coordinates.

Table 4. 2: Eigenvalues, assignments and deviations (from the harmonic model) of the vibrational states of two $^{111}\text{Cd}^+$ ions in $\sim z^4$ potential trap.

# of state	E (MHz)	E_h (MHz)	v_1	v_2	δE (MHz)
1	18.54483	18.54478	0	0	0.00005
2	34.73405	34.73406	1	0	-0.00001
3	39.44524	39.44506	0	1	0.00019
4	50.92324	50.92335	2	0	-0.00011
5	55.63440	55.63434	1	1	0.00006
6	60.34582	60.34533	0	2	0.00049
7	67.11240	67.11263	3	0	-0.00023
10	81.24658	81.24561	0	3	0.00097
11	83.30153	83.30192	4	0	-0.00038
15	99.49063	99.49120	5	0	-0.00057
16	102.14750	102.14588	0	4	0.00161
20	115.67970	115.68048	6	0	-0.00078
23	123.04859	123.04616	0	5	0.00243
26	131.86874	131.86977	7	0	-0.00103
31	143.94985	143.94644	0	6	0.00341
33	148.05775	148.05905	8	0	-0.00130
41	164.85128	164.84671	0	7	0.00457
52	185.75287	185.74699	0	8	0.00589

Again, the mass unscaled normal mode coordinates were used to set up the 2D basis set and compute the eigenvalues and eigenfunctions of the system. In Fig. 4.15, the PES in the normal mode coordinates is shown. Only the part of $z_2 > z_1$ is relevant after the transformation. From the picture we come to conclusions somewhat similar to the harmonic case: The motion along ζ_1 goes parallel to the white part, where Coulomb interaction is significant. So this mode is somehow harmonic even in the anharmonic trapping potential! In contrast, the motion along ζ_2 clearly brings the system closer to the Coulomb region, which makes this mode anharmonic as expected.

To reduce the computer time, the Gaussian Quadrature Method was used here in order to compute integrals numerically. After the convergence studies the following values were selected: $\mathcal{N}_1 = \mathcal{N}_2 = 91$ (points along the two normal modes, which was probably an overkill.) and $N_1 \times N_2 = 35 \times 35$ (the number of basis functions). Note that the Gaussian Quadrature Method does not require choosing ζ_{mas} [100]. The eigenvalues calculated numerically, the harmonic spectrum to compare with, and their assignments in terms of the normal vibration mode quantum numbers are given in Table 4.2. The values of deviation from the harmonic spectrum, δE , are also given in

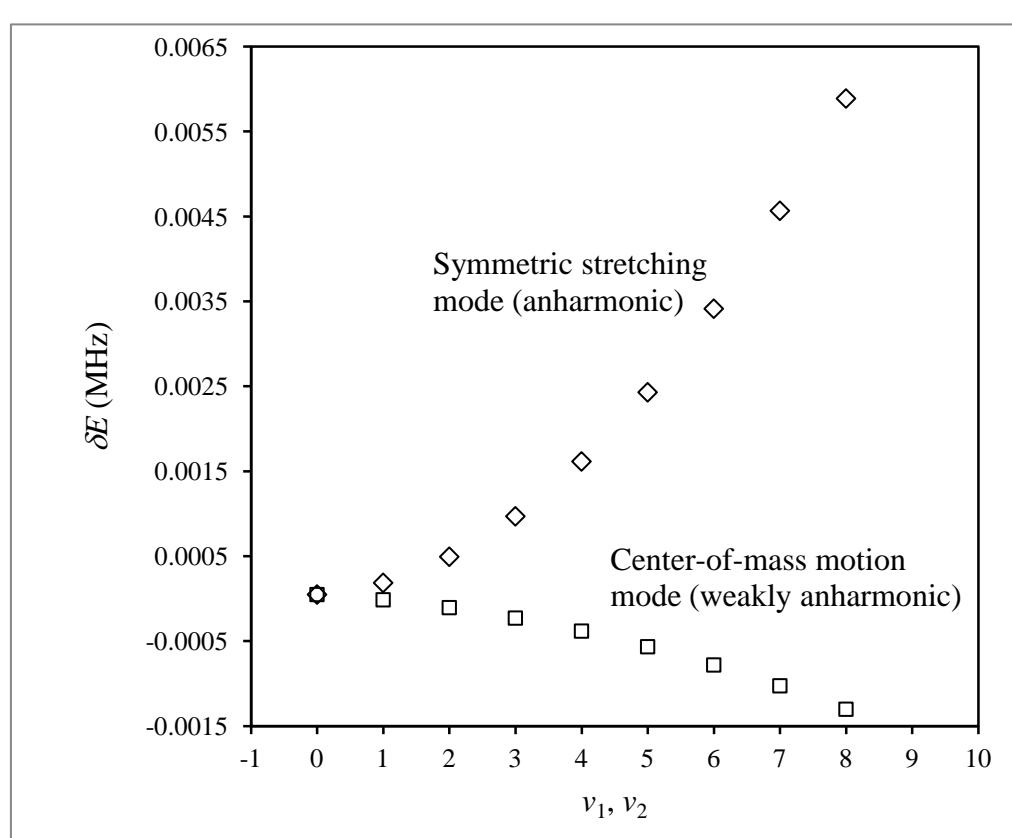


Fig. 4. 16: Effect of anharmonicity for two modes of the vibrational spectrum of two $^{111}\text{Cd}^+$ ions in an anharmonic ($\sim z^4$) potential trap.

Table 4.2 and are also presented in Fig. 4.16 for nine lowest states of each normal mode progression. Figure 4.16 shows very clearly that Mode 1 (center-of-mass motion) is slightly anharmonic and this is different from the case of harmonic trap, illustrated in Fig. 4.9. However this anharmonicity is very weak, despite the fact that a strongly anharmonic trapping potential is used. Mode 2 (symmetric stretching) is anharmonic due to the effect of Coulomb as we expected. Compared to the case of harmonic trap, Mode 2 is only slightly more anharmonic (see Fig. 4.9).

To determine anharmonicities in the $\sim z^4$ potential, the two dimensional Dunham expansion from Eq. (4.1.8.3) was used again to fit 6 lower states, the results are as follows:

$$D/2\pi = 7.371 \times 10^{-6} \text{ MHz},$$

$$\Omega_1/2\pi = 2.577 \text{ MHz},$$

$$\Omega_2/2\pi = 3.326 \text{ MHz},$$

$$\Delta_1/2\pi = 2.435 \times 10^{-6} \text{ MHz},$$

$$\Delta_2/2\pi = -1.346 \times 10^{-5} \text{ MHz},$$

$$\Delta_{12}/2\pi = 9.927 \times 10^{-6} \text{ MHz}.$$

So, the conclusion is that: In the $\sim z^4$ potential Δ_1 is no more zero, which is the result of using the anharmonic trapping potential. The value of Δ_2 is somewhat larger than that in harmonic trapping potential, but overall we do not see any significant

improvement in the case of strongly anharmonic ($\sim z^4$) potential trap. The anharmonicity parameters in this case are $\Delta_1 \sim 10^{-6} \omega_1$, $\Delta_2 \sim 4 \times 10^{-6} \omega_2$. They are still four orders of magnitude smaller than that is needed for the successful control. It is particularly surprising that the Mode 1 does not gain any appreciable anharmonicity. Analysis of this unexpected result is given below.

4.2.2 Analysis of the PES

In order to understand why the normal vibration modes of two ions in a strongly anharmonic potential are still nearly harmonic, we carried out analytic analysis of the PES in the vicinity of the equilibrium position.

Using Eq. (4.2.1.1), the potential energy of the two ions in the anharmonic trapping potential can be expressed as follows (in atomic units):

$$\begin{aligned} V(z_1, z_2) &= V(z_1) + V(z_2) + \frac{1}{|z_2 - z_1|} \\ &= \frac{1}{4!} k' z_1^4 + \frac{1}{4!} k' z_2^4 + \frac{1}{|z_2 - z_1|}, \end{aligned} \quad (4.2.2.1)$$

The equilibrium energy of the system can be written as:

$$V_{eq} = V(z_{e1}, z_{e2}) = \frac{1}{4!} k' z_{e1}^4 + \frac{1}{4!} k' z_{e2}^4 + \frac{1}{|z_{e2} - z_{e1}|}. \quad (4.2.2.2)$$

Again, the procedure of transformation of coordinates was followed as in Sec. 4.1.4 and 4.1.5. We derived the formula in the mass scaled normal mode coordinates and transformed the equation of PES into the mass unscaled normal mode coordinates. We obtained:

$$\begin{aligned}
\hat{V}(\bar{\zeta}_1, \bar{\zeta}_2) &= \frac{1}{4!} k' \left(z_{e1} - \frac{\bar{\zeta}_1 + \bar{\zeta}_2}{\sqrt{2m}} \right)^4 + \frac{1}{4!} k' \left(z_{e2} + \frac{\bar{\zeta}_2 - \bar{\zeta}_1}{\sqrt{2m}} \right)^4 \\
&\quad + \frac{\sqrt{2m}}{|2\bar{\zeta}_2 + \sqrt{2m}(z_{e2} - z_{e1})|} \\
&= \frac{1}{4!} k' \left(z_{e1}^2 - 2z_{e1} \frac{\bar{\zeta}_1 + \bar{\zeta}_2}{\sqrt{2m}} + \frac{\bar{\zeta}_1^2 + \bar{\zeta}_2^2 + 2\bar{\zeta}_1\bar{\zeta}_2}{2m} \right)^2 \\
&\quad + \frac{1}{4!} k' \left(z_{e2}^2 + 2z_{e2} \frac{\bar{\zeta}_2 - \bar{\zeta}_1}{\sqrt{2m}} + \frac{\bar{\zeta}_1^2 + \bar{\zeta}_2^2 - 2\bar{\zeta}_1\bar{\zeta}_2}{2m} \right)^2 \\
&\quad + \frac{\sqrt{2m}}{|2\bar{\zeta}_2 + \sqrt{2m}(z_{e2} - z_{e1})|} \\
&= \frac{1}{4!} k' \left(z_{e1}^4 - 4z_{e1}^3 \frac{\bar{\zeta}_1 + \bar{\zeta}_2}{\sqrt{2m}} + 3z_{e1}^2 \frac{\bar{\zeta}_1^2 + \bar{\zeta}_2^2 + 2\bar{\zeta}_1\bar{\zeta}_2}{m} \right. \\
&\quad \left. - \sqrt{2}z_{e1} \frac{\bar{\zeta}_1^3 + \bar{\zeta}_2^3 + 3\bar{\zeta}_1\bar{\zeta}_2^2 + 3\bar{\zeta}_1^2\bar{\zeta}_2}{m\sqrt{m}} + \frac{\bar{\zeta}_1^4 + \bar{\zeta}_2^4 + 6\bar{\zeta}_1^2\bar{\zeta}_2^2 + 4\bar{\zeta}_1^3\bar{\zeta}_2 + 4\bar{\zeta}_1\bar{\zeta}_2^3}{4m^2} \right) \\
&\quad + \frac{1}{4!} k' \left(z_{e2}^4 + 4z_{e2}^3 \frac{\bar{\zeta}_2 - \bar{\zeta}_1}{\sqrt{2m}} + 3z_{e2}^2 \frac{\bar{\zeta}_1^2 + \bar{\zeta}_2^2 - 2\bar{\zeta}_1\bar{\zeta}_2}{m} \right. \\
&\quad \left. + \sqrt{2}z_{e2} \frac{-\bar{\zeta}_1^3 + \bar{\zeta}_2^3 - 3\bar{\zeta}_1\bar{\zeta}_2^2 + 3\bar{\zeta}_1^2\bar{\zeta}_2}{m\sqrt{m}} + \frac{\bar{\zeta}_1^4 + \bar{\zeta}_2^4 + 6\bar{\zeta}_1^2\bar{\zeta}_2^2 - 4\bar{\zeta}_1^3\bar{\zeta}_2 - 4\bar{\zeta}_1\bar{\zeta}_2^3}{4m^2} \right) \\
&\quad + \frac{\sqrt{2m}}{|2\bar{\zeta}_2 + \sqrt{2m}(z_{e2} - z_{e1})|} \\
&= \frac{1}{4!} k' \left((z_{e1}^4 + z_{e2}^4) + 2 \sqrt{\frac{2}{m}} \bar{\zeta}_2 \left(z_{e2}^3 - z_{e1}^3 \right) + \frac{3}{m} \left(\bar{\zeta}_1^2 + \bar{\zeta}_2^2 \right) (z_{e1}^2 + z_{e2}^2) \right. \\
&\quad \left. + \frac{1}{m} \sqrt{\frac{2}{m}} \left(\bar{\zeta}_2^3 + 3\bar{\zeta}_1^2\bar{\zeta}_2 \right) (z_{e2} - z_{e1}) + \frac{\bar{\zeta}_1^4 + \bar{\zeta}_2^4 + 6\bar{\zeta}_1^2\bar{\zeta}_2^2}{2m^2} \right) \\
&\quad + \frac{\sqrt{2m}}{|2\bar{\zeta}_2 + \sqrt{2m}(z_{e2} - z_{e1})|}. \tag{4.2.2.3}
\end{aligned}$$

Finally,

$$\begin{aligned}
\hat{V}(\zeta_1, \zeta_2) = & \frac{1}{4!} k' \left((z_{e1}^4 + z_{e2}^4) + 2 \sqrt{\frac{6}{5}} \zeta_2 (z_{e2}^3 - z_{e1}^3) \right. \\
& + 3 \left(\zeta_1^2 + \frac{3}{5} \zeta_2^2 \right) (z_{e1}^2 + z_{e2}^2) + 3 \sqrt{\frac{6}{5}} \left(\frac{\zeta_2^3}{5} + \zeta_1^2 \zeta_2 \right) (z_{e2} - z_{e1}) \\
& \left. + \frac{\zeta_1^4 + \frac{9}{25} \zeta_2^4 + \frac{18}{5} \zeta_1^2 \zeta_2^2}{2} \right) + \frac{1}{\left| \sqrt{\frac{6}{5}} \zeta_2 + (z_{e2} - z_{e1}) \right|}. \quad (4.2.2.4)
\end{aligned}$$

As in the case of harmonic trap, the Coulomb interaction term depends on ζ_2 only.

But now, due to the cross terms of $\zeta_1^2 \zeta_2$ and $\zeta_1^2 \zeta_2^2$, the PES is not separable. The equilibrium energy:

$$V_{eq} = V(\zeta_1 = 0, \zeta_2 = 0) = \frac{1}{4!} k' z_{e1}^4 + \frac{1}{4!} k' z_{e2}^4 + \frac{1}{|z_{e2} - z_{e1}|}. \quad (4.2.2.5)$$

Since the equation (4.2.2.4) is non-separable, we will analyze only the slice along ζ_2 , keeping $\zeta_1 = 0$:

$$\begin{aligned}
\hat{V}(\zeta_2, \zeta_1 = 0) = & \frac{1}{4!} k' \left((z_{e1}^4 + z_{e2}^4) + 2 \sqrt{\frac{6}{5}} (z_{e2}^3 - z_{e1}^3) \zeta_2 + \frac{9}{5} (z_{e1}^2 + z_{e2}^2) \zeta_2^2 \right. \\
& \left. + \frac{3}{5} \sqrt{\frac{6}{5}} (z_{e2} - z_{e1}) \zeta_2^3 + \frac{9}{50} \zeta_2^4 \right) + \frac{1}{\left| \sqrt{\frac{6}{5}} \zeta_2 + (z_{e2} - z_{e1}) \right|}. \quad (4.2.2.6)
\end{aligned}$$

This expression is exact. No approximations have been made. It contains the terms

from zero order to fourth order in ζ_2 and the Coulomb term. Subtracting the equilibrium energy Eq. (4.2.2.5) from the Eq. (4.2.2.6), we plot the contribution of

terms with different orders of ζ_2 in Fig. 4. 17. From the figure, we can see that in the

system of two ions in the $\sim z^4$ trapping potential for the symmetric stretching mode: (i)

the quadratic term is much larger than the quartic and third order terms; (ii) the linear (first order) term and the Coulomb term cancel each other! This is beyond our expectation. So the total contribution to the trapping potential of Eq. (4.2.2.6) is mostly from the quadratic term. That means the potential in Eq. (4.2.2.6) is very close to harmonic. This is consistent with results of the fit by Dunham expansion in Sec. 4.2.1. If we keep $\zeta_2 = 0$, the same method can be applied to analyze the slice along ζ_1 .

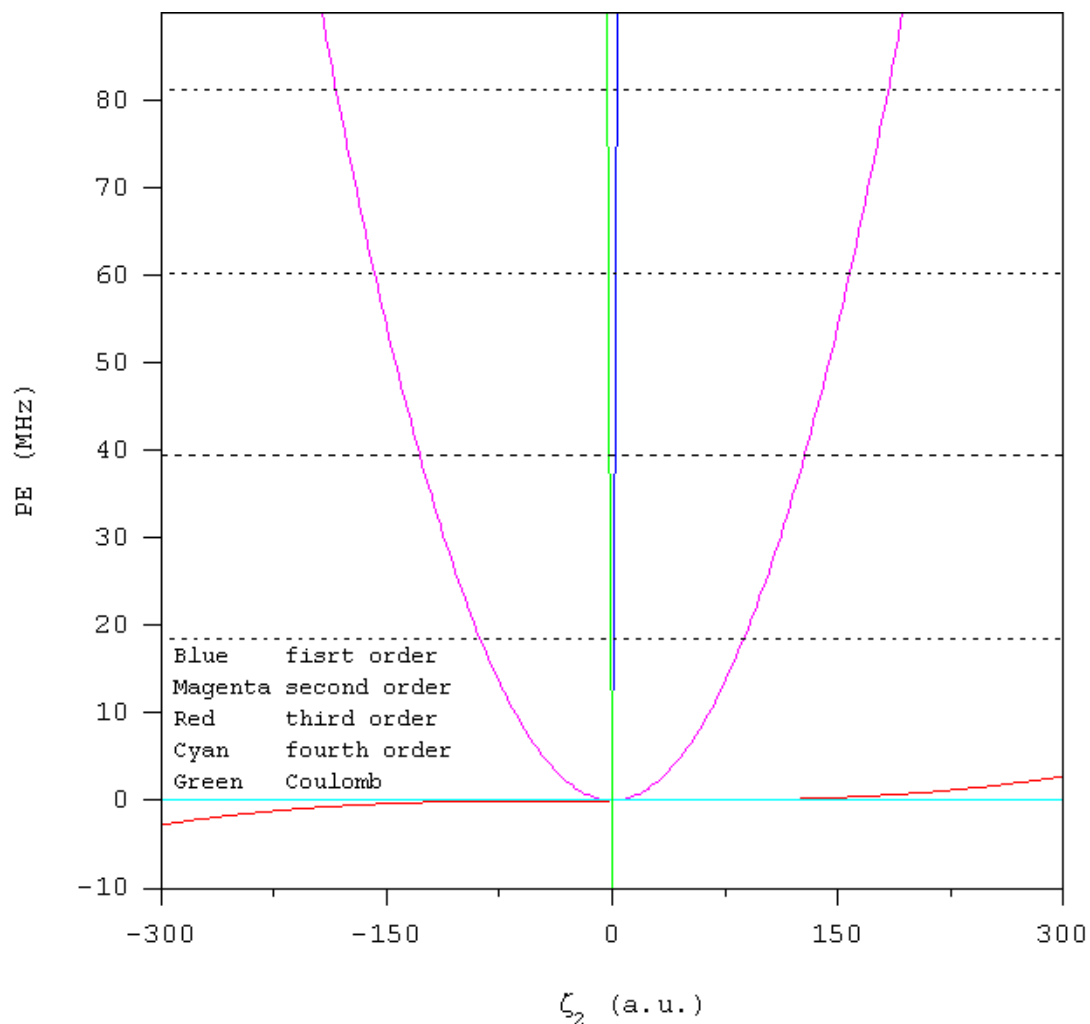


Fig. 4. 17: Components of the potential according to different orders of ζ_2 .

After the correction with equilibrium energy only quadratic and quartic terms are left (no Coulomb for Mode 1). Again, the quadratic term is much larger than the quartic term, which gives a nearly harmonic PES.

4.3 Conclusions

In the system of two $^{111}\text{Cd}^+$ ions in the harmonic trapping potential, the center-of-mass motion mode is exactly harmonic ($\Delta_1 \approx 0$) and cannot be controlled. The Coulomb interaction of two ions introduces weak anharmonicity into the symmetric stretching mode at the level of $\Delta_2 \sim 10^{-6}\Omega_2$. Clearly, this is not sufficient for the control. Furthermore, in this system the symmetric stretching mode is “dark” and cannot be excited by the spatially homogeneous electric field.

In the case of strongly anharmonic trapping potential ($\sim z^4$), the center-of-mass motion mode gains some anharmonicity. But this anharmonicity is very weak, at the level of $\Delta_1 \sim 10^{-6}\Omega_1$. Compared to the harmonic trapping potential, the symmetric stretching mode is only slightly more anharmonic $\Delta_2 \sim 4 \times 10^{-6}\Omega_2$.

So, using two trapped ions does not offer any advantage over the one-ion system. It is even worse. In the two-ion case we cannot even control the center-of-mass motion mode in the strongly anharmonic trap because of the small local anharmonicity of the 2D PES.

Chapter 5: Three-ion system

5.1 Three ions in the harmonic trapping potential

5.1.1 Harmonic trapping potential

In this section, we consider a system of three $^{111}\text{Cd}^+$ ions in the harmonic potential trap of the same form as in Eq. (2.1.1) and restrict the motions of ions to one dimension along the trap axis (z-axis). The force constant k is the same as was used in Chapter 2, 3 and 4 for the one-ion and two-ion systems. In the three-ion system there are three normal vibration modes and we can try to use them to encode qubits. In Fig. 5.1, we show the harmonic trapping potential, the equilibrium positions and several lower lying energy levels of three-ion system. Based on the two-ion case considered in the previous chapter, we expect that here the symmetric stretching mode (Mode 2) is also “dark”. So, we may only be able to employ two modes for encoding qubits: the center of mass motion mode (Mode 1) and the asymmetric stretching mode (Mode 3). The following mapping between the vibrational states of the three-ion-string, labeled by three normal mode quantum numbers (v_1, v_2, v_3), and the four states of the two-qubit system is proposed:

$$\begin{aligned} |00\rangle &\Leftrightarrow (0,0,0); & |01\rangle &\Leftrightarrow (1,0,0); \\ |10\rangle &\Leftrightarrow (0,0,1); & |11\rangle &\Leftrightarrow (1,0,1). \end{aligned} \quad (5.1.1.1)$$

The potential energy of the three ion system can be written as follows (in atomic units):

$$\begin{aligned}
 V(z_1, z_2, z_3) &= V(z_1) + V(z_2) + V(z_3) \\
 &\quad + \frac{1}{|z_2 - z_1|} + \frac{1}{|z_3 - z_1|} + \frac{1}{|z_3 - z_2|} \\
 &= \frac{1}{2} k z_1^2 + \frac{1}{2} k z_2^2 + \frac{1}{2} k z_3^2 \\
 &\quad + \frac{1}{|z_2 - z_1|} + \frac{1}{|z_3 - z_1|} + \frac{1}{|z_3 - z_2|}. \tag{5.1.1.2}
 \end{aligned}$$

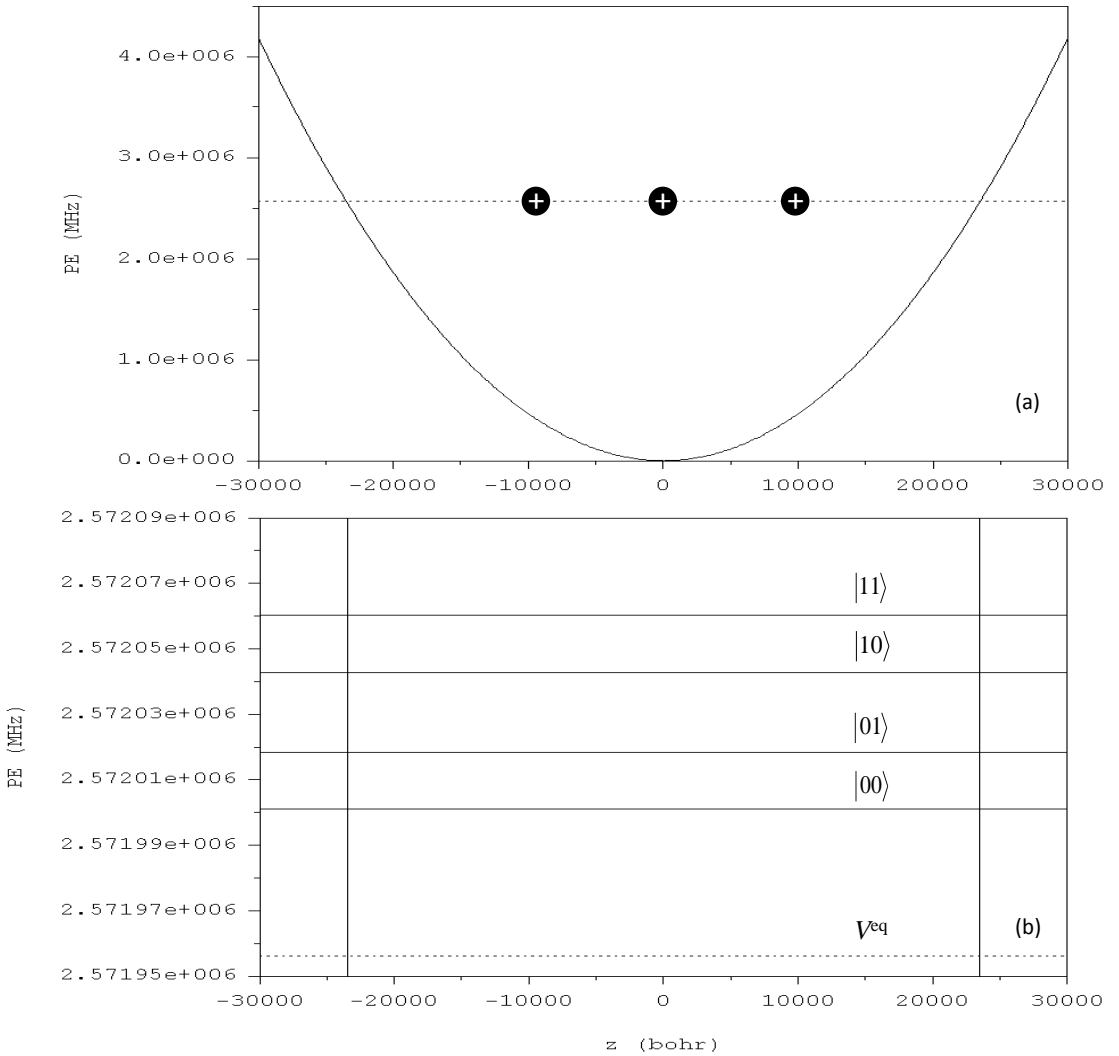


Fig. 5. 1: Three $^{111}\text{Cd}^+$ ions in the harmonic potential trap: (a) Equilibrium positions of ions and minimum energy of the three-ion string; (b) Vibrational spectrum of this system and the encoding of two-qubit states proposed in this work.

where k is the force constant. We use z_1 , z_2 and z_3 to describe the positions of all these three ions and set $z_3 > z_2 > z_1$. Potential energy surface (PES) of three ions in the trap, based on Eq. (5.1.1.2), is shown in Fig. 5.2. When any two ions come close to each other, the potential energy approaches infinity due to Coulomb repulsion (white parts of the Fig. 5.2). Furthermore, although the trapping potential from Eq. (2.1.1) is harmonic, the potential energy of the system is anharmonic due to ion-ion

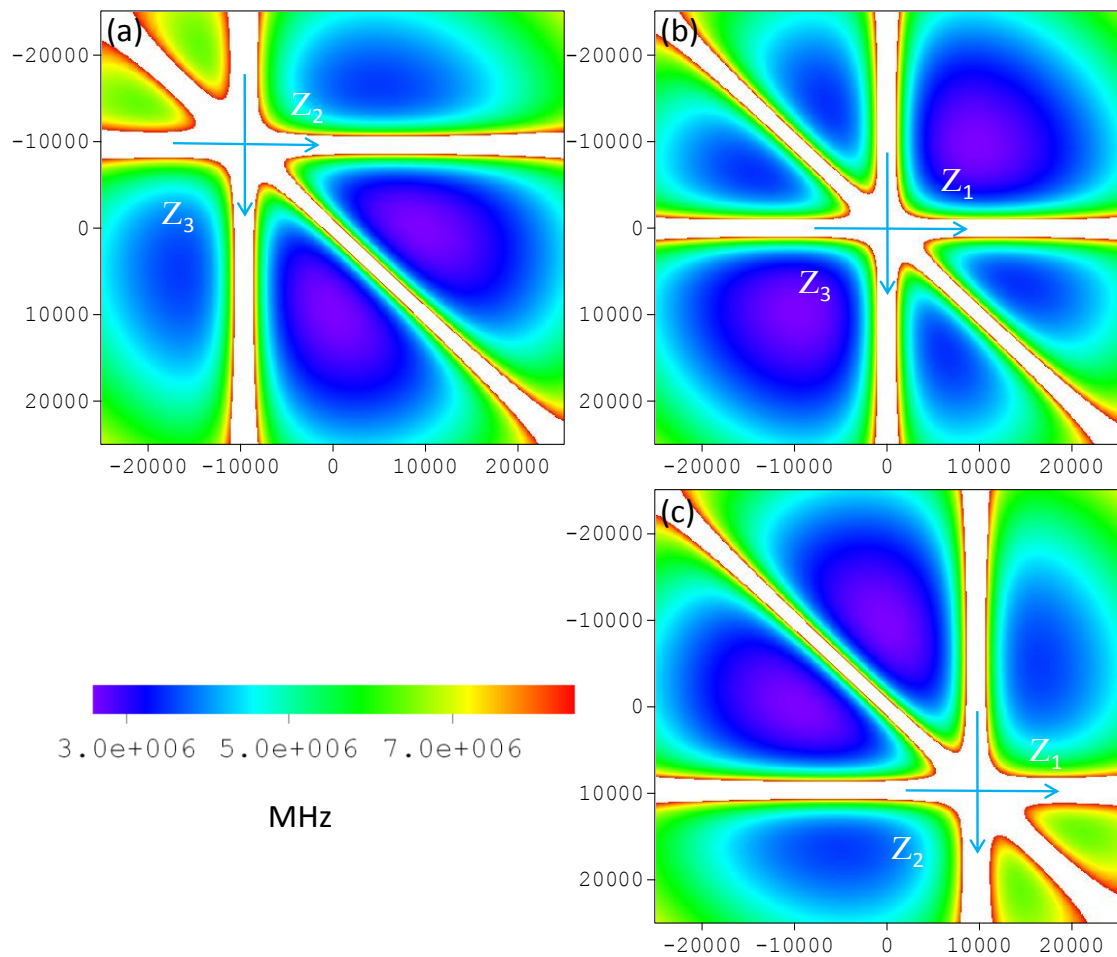


Fig. 5. 2: PES of three $^{111}\text{Cd}^+$ ions in the harmonic potential trap using Cartesian coordinates. Three slices through the 3D-surface are shown: (a) perpendicular to z_1 through $z_1 = 0$, (b) perpendicular to z_2 through $z_2 = 0$ and (c) perpendicular to z_3 through $z_3 = 0$.

Coulomb interaction.

5.1.2 Minimization Method

Again, in order to perform minimization of the potential energy function in 3D and find the equilibrium positions of three ions we use the *Newton-Raphson* (NR) method. It requires calculating the first and second derivatives of the potential energy of the system and these are available analytically:

$$\frac{\partial V(z_1, z_2, z_3)}{\partial z_1} = kz_1 + \frac{1}{(z_2 - z_1)^2} + \frac{1}{(z_3 - z_1)^2}, \quad (5.1.2.1)$$

$$\frac{\partial V(z_1, z_2, z_3)}{\partial z_2} = kz_2 - \frac{1}{(z_2 - z_1)^2} + \frac{1}{(z_3 - z_2)^2}, \quad (5.1.2.2)$$

$$\frac{\partial V(z_1, z_2, z_3)}{\partial z_3} = kz_3 - \frac{1}{(z_3 - z_1)^2} - \frac{1}{(z_3 - z_2)^2}, \quad (5.1.2.3)$$

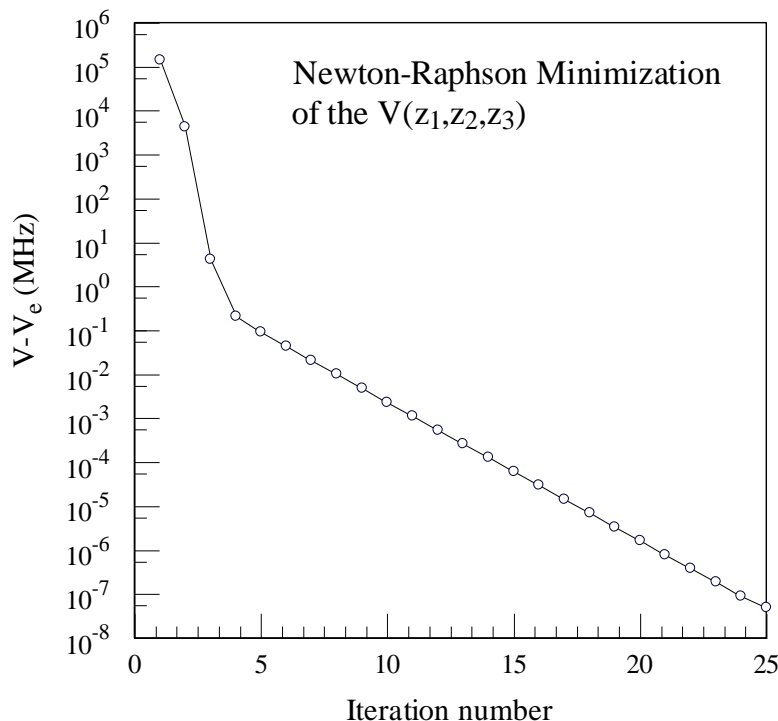


Fig. 5. 3: Potential energy difference between two consequent steps of the system during the minimization.

$$\frac{\partial^2 V(z_1, z_2, z_3)}{\partial z_1^2} = k + \frac{2}{(z_2 - z_1)^3} + \frac{2}{(z_3 - z_1)^3}, \quad (5.1.2.4)$$

$$\frac{\partial^2 V(z_1, z_2, z_3)}{\partial z_2^2} = k + \frac{2}{(z_2 - z_1)^3} + \frac{2}{(z_3 - z_2)^3}, \quad (5.1.2.5)$$

$$\frac{\partial^2 V(z_1, z_2, z_3)}{\partial z_3^2} = k + \frac{2}{(z_3 - z_1)^3} + \frac{2}{(z_3 - z_2)^3}, \quad (5.1.2.6)$$

$$\frac{\partial^2 V(z_1, z_2, z_3)}{\partial z_1 \partial z_2} = \frac{\partial^2 V(z_1, z_2, z_3)}{\partial z_2 \partial z_1} = -\frac{2}{(z_2 - z_1)^3}, \quad (5.1.2.7)$$

$$\frac{\partial^2 V(z_1, z_2, z_3)}{\partial z_1 \partial z_3} = \frac{\partial^2 V(z_1, z_2, z_3)}{\partial z_3 \partial z_1} = -\frac{2}{(z_3 - z_1)^3}, \quad (5.1.2.8)$$

$$\frac{\partial^2 V(z_1, z_2, z_3)}{\partial z_2 \partial z_3} = \frac{\partial^2 V(z_1, z_2, z_3)}{\partial z_3 \partial z_2} = -\frac{2}{(z_3 - z_2)^3}. \quad (5.1.2.9)$$

A computer code 3DMIN was written using FORTRAN language (see Appendix H) to carry out these optimizations for three-ion system numerically. Using the indicated parameters of the trap, we obtained the equilibrium positions of these

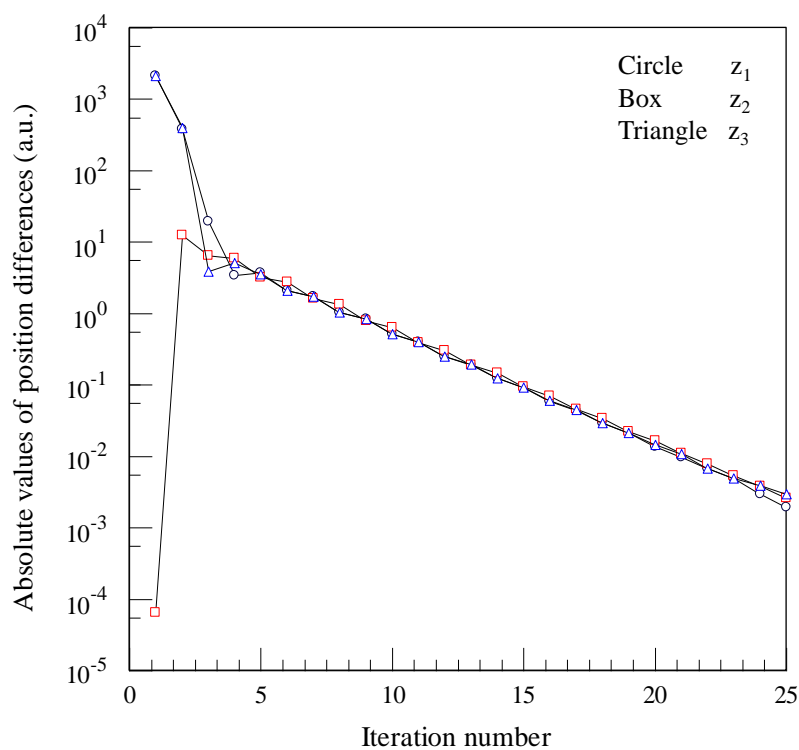


Fig. 5. 4: Absolute values of position difference between two consequent steps during the minimization.

three ions:

$$z_{e1} = -9.5934 \times 10^3 \text{ Bohr},$$

$$z_{e2} = -5.0871 \times 10^{-8} \approx 0 \text{ Bohr},$$

$$z_{e3} = 9.5934 \times 10^3 \text{ Bohr}.$$

The value of potential energy at this point was $V^{eq} = V(z_{e1}, z_{e2}, z_{e3}) = 2.572 \times 10^6$

MHz. To monitor the progress of minimization, we plot potential energy difference

between two consequent steps in Fig. 5.3. It is seen from the graph that the results are

converged very fast and after 25 iterations the energy difference is lower than

1×10^{-7} MHz. In Fig. 5.4, position differences between two subsequent steps during

minimization are presented. The results converge fast, which is consistent with data

from Fig. 5.3. Figures 5.3 and 5.4 show that convergence is exponential in both

energy and positions.

5.1.3 Normal vibration modes

To describe the vibrations of three different modes in the trap, we need to diagonalize Hessian Matrix to find out the different frequencies of three modes.

The Hessian Matrix in mass-weighted coordinates is given as follows:

$$\begin{aligned}
\mathbf{F} &= \begin{vmatrix} m & 0 & 0 \\ 0 & m & 0 \\ 0 & 0 & m \end{vmatrix}^{-1/2} \begin{vmatrix} \frac{\partial^2 V}{\partial z_1^2} & \frac{\partial^2 V}{\partial z_1 \partial z_2} & \frac{\partial^2 V}{\partial z_1 \partial z_3} \\ \frac{\partial^2 V}{\partial z_2 \partial z_1} & \frac{\partial^2 V}{\partial z_2^2} & \frac{\partial^2 V}{\partial z_2 \partial z_3} \\ \frac{\partial^2 V}{\partial z_3 \partial z_1} & \frac{\partial^2 V}{\partial z_3 \partial z_2} & \frac{\partial^2 V}{\partial z_3^2} \end{vmatrix}_{(z_{e1}, z_{e2}, z_{e3})} \begin{vmatrix} m & 0 & 0 \\ 0 & m & 0 \\ 0 & 0 & m \end{vmatrix}^{-1/2} \\
&= \frac{1}{m} \begin{vmatrix} \frac{\partial^2 V}{\partial z_1^2} & \frac{\partial^2 V}{\partial z_1 \partial z_2} & \frac{\partial^2 V}{\partial z_1 \partial z_3} \\ \frac{\partial^2 V}{\partial z_2 \partial z_1} & \frac{\partial^2 V}{\partial z_2^2} & \frac{\partial^2 V}{\partial z_2 \partial z_3} \\ \frac{\partial^2 V}{\partial z_3 \partial z_1} & \frac{\partial^2 V}{\partial z_3 \partial z_2} & \frac{\partial^2 V}{\partial z_3^2} \end{vmatrix}_{(z_{e1}, z_{e2}, z_{e3})} \quad (5.1.3.1)
\end{aligned}$$

Because the system is more complicated than the two-ion case, we did the calculation numerically using program 3DHESSIAN to diagonalize the Hessian matrix in Eq. (5.1.3.1) (see appendix I). We obtained the following eigenvalues of three normal modes:

$$\lambda_1 = 6.997 \times 10^{-18} \text{ a.u.}$$

$$\lambda_2 = 2.099 \times 10^{-17} \text{ a.u.}$$

$$\lambda_3 = 4.058 \times 10^{-17} \text{ a.u.}$$

Using Eq. (4.1.3.4), we calculate frequencies of these three modes and transform to the units of MHz:

$$\omega_1 / 2\pi = 2.770 \text{ MHz}$$

$$\omega_2 / 2\pi = 4.798 \text{ MHz}$$

$$\omega_3 / 2\pi = 6.671 \text{ MHz}$$

The eigenvectors are as follows:

$$\mathbf{A} = \begin{vmatrix} a_{11} & a_{12} & a_{13} \\ a_{21} & a_{22} & a_{23} \\ a_{31} & a_{32} & a_{33} \end{vmatrix} = \begin{vmatrix} 0.57735 & 0.70711 & -0.40825 \\ 0.57735 & 0.00000 & 0.81650 \\ 0.57735 & -0.70711 & -0.40825 \end{vmatrix}$$

These numbers describe three familiar normal modes: the first column describes Mode 1 with $a_{11} = a_{21} = a_{31}$ which is the center-of-mass motion mode, where all three ions move together; the second column describes Mode 2 with $a_{12} = -a_{32}$ and $a_{22} = 0$ which is the symmetric stretching mode, where the central ion stays still while two terminal ions move in the opposite directions; the third column describes Mode 3 with $2a_{13} = -a_{23} = 2a_{33}$ which is the asymmetric stretching mode, where the central ion moves in the direction opposite to the motion of two terminal ions, with twice larger amplitude. These three modes are very well known normal modes.

5.1.4 Hamiltonian and transformation of coordinates

Hamiltonian of three-ion system in Cartesian coordinates is expressed by the following formula:

$$\hat{H}(z_1, z_2, z_3) = -\frac{1}{2m} \frac{\partial^2}{\partial z_1^2} - \frac{1}{2m} \frac{\partial^2}{\partial z_2^2} - \frac{1}{2m} \frac{\partial^2}{\partial z_3^2} + \hat{V}(z_1, z_2, z_3) - V^{eq}, \quad (5.1.4.1)$$

where $\hat{V}(z_1, z_2, z_3)$ is from Eq. (5.1.1.2) and $V^{eq} = V(z_{e1}, z_{e2}, z_{e3})$ is the constant energy shift by the minimum potential energy of the system when three ions are at their classical minimum energy points (z_{e1}, z_{e2}, z_{e3}) .

Second, the mass scaled coordinates are introduced:

$$\bar{z}_1 = \sqrt{m}z_1, \quad \bar{z}_2 = \sqrt{m}z_2, \quad \bar{z}_3 = \sqrt{m}z_3, \quad (5.1.4.2)$$

The Hamiltonian in mass scaled coordinates can be written as follows:

$$\begin{aligned} \hat{H}(\bar{z}_1, \bar{z}_2, \bar{z}_3) &= -\frac{1}{2} \frac{\partial^2}{\partial \bar{z}_1^2} - \frac{1}{2} \frac{\partial^2}{\partial \bar{z}_2^2} - \frac{1}{2} \frac{\partial^2}{\partial \bar{z}_3^2} \\ &\quad + \hat{V}(\bar{z}_1, \bar{z}_2, \bar{z}_3) - V^{eq}, \end{aligned} \quad (5.1.4.3)$$

$$\begin{aligned} \hat{V}(\bar{z}_1, \bar{z}_2, \bar{z}_3) &= \frac{1}{2} \frac{k}{m} \bar{z}_1^2 + \frac{1}{2} \frac{k}{m} \bar{z}_2^2 + \frac{1}{2} \frac{k}{m} \bar{z}_3^2 + \frac{\sqrt{m}}{|\bar{z}_2 - \bar{z}_1|} \\ &\quad + \frac{\sqrt{m}}{|\bar{z}_3 - \bar{z}_1|} + \frac{\sqrt{m}}{|\bar{z}_3 - \bar{z}_2|} \end{aligned} \quad (5.1.4.4)$$

Then, we transform equations above to the mass scaled displacement coordinates:

$$\begin{cases} z_1 - z_{e1} = \Delta z_1 \\ z_2 - z_{e2} = \Delta z_2 \\ z_3 - z_{e3} = \Delta z_3 \end{cases} \Rightarrow \begin{cases} \bar{z}_1 - \sqrt{m}z_{e1} = \Delta \bar{z}_1 \\ \bar{z}_2 - \sqrt{m}z_{e2} = \Delta \bar{z}_2 \\ \bar{z}_3 - \sqrt{m}z_{e3} = \Delta \bar{z}_3 \end{cases}, \quad (5.1.4.5)$$

$$\begin{aligned} \hat{H}(\Delta \bar{z}_1, \Delta \bar{z}_2, \Delta \bar{z}_3) &= -\frac{1}{2} \frac{\partial^2}{\partial \Delta \bar{z}_1^2} - \frac{1}{2} \frac{\partial^2}{\partial \Delta \bar{z}_2^2} - \frac{1}{2} \frac{\partial^2}{\partial \Delta \bar{z}_3^2} \\ &\quad + \hat{V}(\Delta \bar{z}_1, \Delta \bar{z}_2, \Delta \bar{z}_3) - V^{eq}, \end{aligned} \quad (5.1.4.6)$$

$$\begin{aligned} \hat{V}(\Delta \bar{z}_1, \Delta \bar{z}_2, \Delta \bar{z}_3) &= \frac{1}{2} k \left(\frac{\Delta \bar{z}_1}{\sqrt{m}} + z_{e1} \right)^2 + \frac{1}{2} k \left(\frac{\Delta \bar{z}_2}{\sqrt{m}} + z_{e2} \right)^2 + \frac{1}{2} k \left(\frac{\Delta \bar{z}_3}{\sqrt{m}} + z_{e3} \right)^2 \\ &\quad + \frac{\sqrt{m}}{|\Delta \bar{z}_2 - \Delta \bar{z}_1 + \sqrt{m}(z_{e2} - z_{e1})|} + \frac{\sqrt{m}}{|\Delta \bar{z}_3 - \Delta \bar{z}_1 + \sqrt{m}(z_{e3} - z_{e1})|} \\ &\quad + \frac{\sqrt{m}}{|\Delta \bar{z}_3 - \Delta \bar{z}_2 + \sqrt{m}(z_{e3} - z_{e2})|}. \end{aligned} \quad (5.1.4.7)$$

Next we introduce the mass scaled normal mode coordinates $(\bar{\zeta}_1, \bar{\zeta}_2, \bar{\zeta}_3)$,

transformations is as follows:

$$\begin{vmatrix} \Delta \bar{z}_1 \\ \Delta \bar{z}_2 \\ \Delta \bar{z}_3 \end{vmatrix} = \mathbf{A} \begin{vmatrix} \bar{\zeta}_1 \\ \bar{\zeta}_2 \\ \bar{\zeta}_3 \end{vmatrix} = \begin{vmatrix} a_{11} & a_{12} & a_{13} \\ a_{21} & a_{22} & a_{23} \\ a_{31} & a_{32} & a_{33} \end{vmatrix} \begin{vmatrix} \bar{\zeta}_1 \\ \bar{\zeta}_2 \\ \bar{\zeta}_3 \end{vmatrix}, \quad (5.1.4.8)$$

$$\begin{cases} \Delta \bar{z}_1 = a_{11}\bar{\zeta}_1 + a_{12}\bar{\zeta}_2 + a_{13}\bar{\zeta}_3 \\ \Delta \bar{z}_2 = a_{21}\bar{\zeta}_1 + a_{22}\bar{\zeta}_2 + a_{23}\bar{\zeta}_3 \\ \Delta \bar{z}_3 = a_{31}\bar{\zeta}_1 + a_{32}\bar{\zeta}_2 + a_{33}\bar{\zeta}_3 \end{cases}. \quad (5.1.4.9)$$

Here matrix \mathbf{A} in Eq. (5.1.4.8) contains eigenvectors of three modes (from

diagonalization of the Hessian Matrix of the three-ion system in Sec. 5.1.3). Referred to the derivations in Sec. 4.1.4, we obtained the formula of the kinetic energy part of Hamiltonian for the three-ion system:

$$\begin{aligned}\hat{T}(\bar{\zeta}_1, \bar{\zeta}_2, \bar{\zeta}_3) &= -\frac{1}{2} \frac{\partial^2}{\partial \Delta \bar{\zeta}_1^2} - \frac{1}{2} \frac{\partial^2}{\partial \Delta \bar{\zeta}_2^2} - \frac{1}{2} \frac{\partial^2}{\partial \Delta \bar{\zeta}_3^2} \\ &= -\frac{1}{2} \frac{\partial^2}{\partial \bar{\zeta}_1^2} - \frac{1}{2} \frac{\partial^2}{\partial \bar{\zeta}_2^2} - \frac{1}{2} \frac{\partial^2}{\partial \bar{\zeta}_3^2}.\end{aligned}\quad (5.1.4.10)$$

The potential energy part of the system can be rewritten as follows:

$$\begin{aligned}\hat{V}(\bar{\zeta}_1, \bar{\zeta}_2, \bar{\zeta}_3) &= \frac{1}{2} k \left(\frac{a_{11}\bar{\zeta}_1 + a_{12}\bar{\zeta}_2 + a_{13}\bar{\zeta}_3}{\sqrt{m}} + z_{e1} \right)^2 \\ &\quad + \frac{1}{2} k \left(\frac{a_{21}\bar{\zeta}_1 + a_{22}\bar{\zeta}_2 + a_{23}\bar{\zeta}_3}{\sqrt{m}} + z_{e2} \right)^2 + \frac{1}{2} k \left(\frac{a_{31}\bar{\zeta}_1 + a_{32}\bar{\zeta}_2 + a_{33}\bar{\zeta}_3}{\sqrt{m}} + z_{e3} \right)^2 \\ &\quad + \frac{1}{\left| \frac{a_{21}\bar{\zeta}_1 + a_{22}\bar{\zeta}_2 + a_{23}\bar{\zeta}_3}{\sqrt{m}} - \frac{a_{11}\bar{\zeta}_1 + a_{12}\bar{\zeta}_2 + a_{13}\bar{\zeta}_3}{\sqrt{m}} + (z_{e2} - z_{e1}) \right|} \\ &\quad + \frac{1}{\left| \frac{a_{31}\bar{\zeta}_1 + a_{32}\bar{\zeta}_2 + a_{33}\bar{\zeta}_3}{\sqrt{m}} - \frac{a_{11}\bar{\zeta}_1 + a_{12}\bar{\zeta}_2 + a_{13}\bar{\zeta}_3}{\sqrt{m}} + (z_{e3} - z_{e1}) \right|} \\ &\quad + \frac{1}{\left| \frac{a_{31}\bar{\zeta}_1 + a_{32}\bar{\zeta}_2 + a_{33}\bar{\zeta}_3}{\sqrt{m}} - \frac{a_{21}\bar{\zeta}_1 + a_{22}\bar{\zeta}_2 + a_{23}\bar{\zeta}_3}{\sqrt{m}} + (z_{e3} - z_{e2}) \right|}.\end{aligned}\quad (5.1.4.11)$$

Finally, using expressions of the effective masses μ_1 , μ_2 , and μ_3 :

$$\begin{cases} \bar{\zeta}_1 = \sqrt{\mu_1} \zeta_1, \\ \bar{\zeta}_2 = \sqrt{\mu_2} \zeta_2, \\ \bar{\zeta}_3 = \sqrt{\mu_3} \zeta_3. \end{cases}\quad (5.1.4.12)$$

we can introduce the “unscaled” normal mode coordinates $(\zeta_1, \zeta_2, \zeta_3)$ instead of the mass scaled normal mode coordinates:

$$\begin{cases} \mu_1 = m, \\ \mu_2 = m/(\lambda_2/\lambda_1), \\ \mu_3 = m/(\lambda_3/\lambda_1). \end{cases}\quad (5.1.4.13)$$

Using the relationship between ω and λ from Eq. (4.1.3.4), we can rewrite Eq. (5.1.4.13) as follows:

$$\begin{cases} \mu_1 = m, \\ \mu_2 = (\omega_1^2/\omega_2^2)m, \\ \mu_3 = (\omega_1^2/\omega_3^2)m. \end{cases} \quad (5.1.4.14)$$

Finally, the Hamiltonian in the mass unscaled normal mode coordinates can be written as:

$$\hat{H}(\zeta_1, \zeta_2, \zeta_3) = -\frac{1}{2\mu_1} \frac{\partial^2}{\partial \zeta_1^2} - \frac{1}{2\mu_2} \frac{\partial^2}{\partial \zeta_2^2} - \frac{1}{2\mu_3} \frac{\partial^2}{\partial \zeta_3^2} + V(\zeta_1, \zeta_2, \zeta_3) - V^{eq}, \quad (5.1.4.15)$$

$$\begin{aligned} V(\zeta_1, \zeta_2, \zeta_3) = & \frac{k}{2} \omega_1^2 \left(a_{11} \frac{\zeta_1}{\omega_1} + a_{12} \frac{\zeta_2}{\omega_2} + a_{13} \frac{\zeta_3}{\omega_3} + \frac{z_1^{eq}}{\omega_1} \right)^2 \\ & + \frac{k}{2} \omega_1^2 \left(a_{21} \frac{\zeta_1}{\omega_1} + a_{22} \frac{\zeta_2}{\omega_2} + a_{23} \frac{\zeta_3}{\omega_3} + \frac{z_2^{eq}}{\omega_1} \right)^2 \\ & + \frac{k}{2} \omega_1^2 \left(a_{31} \frac{\zeta_1}{\omega_1} + a_{32} \frac{\zeta_2}{\omega_2} + a_{33} \frac{\zeta_3}{\omega_3} + \frac{z_3^{eq}}{\omega_1} \right)^2 \\ & + \frac{1}{\omega_1 \left| (a_{21} - a_{11}) \frac{\zeta_1}{\omega_1} + (a_{22} - a_{12}) \frac{\zeta_2}{\omega_2} + (a_{23} - a_{13}) \frac{\zeta_3}{\omega_3} + \frac{z_2^{eq} - z_1^{eq}}{\omega_1} \right|} \\ & + \frac{1}{\omega_1 \left| (a_{31} - a_{11}) \frac{\zeta_1}{\omega_1} + (a_{32} - a_{12}) \frac{\zeta_2}{\omega_2} + (a_{33} - a_{13}) \frac{\zeta_3}{\omega_3} + \frac{z_3^{eq} - z_1^{eq}}{\omega_1} \right|} \\ & + \frac{1}{\omega_1 \left| (a_{31} - a_{21}) \frac{\zeta_1}{\omega_1} + (a_{32} - a_{22}) \frac{\zeta_2}{\omega_2} + (a_{33} - a_{23}) \frac{\zeta_3}{\omega_3} + \frac{z_3^{eq} - z_2^{eq}}{\omega_1} \right|}. \end{aligned} \quad (5.1.4.16)$$

The potential energy surface in the normal mode coordinates $(\zeta_1, \zeta_2, \zeta_3)$ is shown in Fig. 5.5. Note that white area on the picture goes parallel to the ζ_1 -axis. Recall that in this (white) area of the configuration space the Coulomb repulsion

become very large. Figure 5.5 shows that excitation of Mode 1 does not bring the system closer to the white area, which suggests that Mode 1 is probably harmonic. However, the motion along ζ_2 and/or ζ_3 does bring the system closer to the Coulomb interaction region, which suggests that Modes 2 and 3 are probably anharmonic.

5.1.5 Basis set expansion

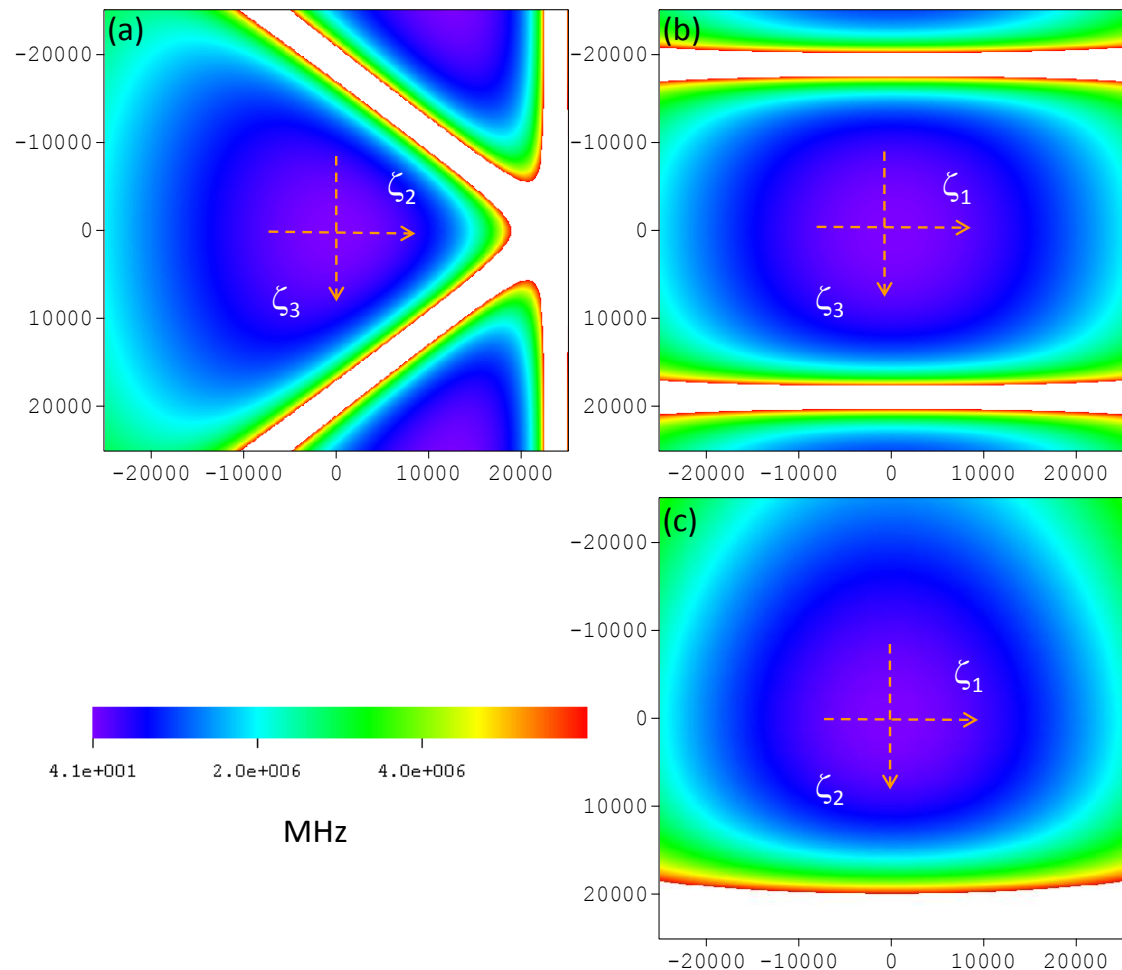


Fig. 5. 5: PES of three $^{111}\text{Cd}^+$ ions in the harmonic potential trap using the normal mode coordinates. Three slices through the 3D-surface are shown: (a) perpendicular to ζ_1 through $\zeta_1 = 0$, (b) perpendicular to ζ_2 through $\zeta_2 = 0$ and (c) perpendicular to ζ_3 through $\zeta_3 = 0$. Note that the Coulomb repulsion part (white) goes parallel to ζ_1 everywhere.

Three-dimensional wavefunctions of the system and the corresponding energy eigenvalues are calculated using the direct product basis set expansion method in the normal mode coordinates:

$$\Psi_v(\zeta_1, \zeta_2, \zeta_3) = \sum_{i,j,k}^N C_{v,i,j,k} \varphi_i(\zeta_1) \varphi_j(\zeta_2) \varphi_k(\zeta_3), \quad (5.1.5.1)$$

here $\varphi_i(\zeta_1)$, $\varphi_j(\zeta_2)$ and $\varphi_k(\zeta_3)$ in the same form of Eq. (2.2.4) are used as basis functions of three different vibrational modes of the system. Index i , j and k lable basis functions and range from 1 to N . Index v lables eigenstates in the three-ion system and ranges from 1 to N^3 . $C_{v,i,j,k}$ are the coefficients of linear combination and in the matrix form it can be written as \mathbf{C}_{N^3, N^3} .

Based on the formalism above, a FORTRAN code named 3DIONTRAP was written. The code is presented in detail (see Appendix J).

5.1.6 Results and analysis

In order to make the three-ion case numerically manageable we used the Message Passing Interface (MPI) to parallelize the calculations (see appendix K) and employed the Gaussian quadrature to calculate the matrix elements of the potential energy operator more efficiently (see appendix L). The calculations for three ions were run using 16 processors of Franklin computer at NERCS [96], the run time for an average job was about 6 wall-clock hours. In the numerical calculations the size of

Table 5. 1: Eigenvalues, assignments and deviations (from the harmonic model) of the vibrational states of three $^{111}\text{Cd}^+$ ions in a harmonic trap.

# of state	E_v (MHz)	E_h (MHz)	v_1	v_2	v_3	δE (MHz)
1	44.73272	44.73257	0	0	0	0.00015
2	62.13713	62.13698	1	0	0	0.00015
3	74.87813	74.8779	0	1	0	0.00023
4	79.54155	79.5414	2	0	0	0.00015
5	86.64832	86.64795	0	0	1	0.00037
6	92.28254	92.28231	1	1	0	0.00023
7	96.94597	96.94581	3	0	0	0.00016
8	104.05273	104.05236	1	0	1	0.00037
9	105.02356	105.02323	0	2	0	0.00033
10	109.68696	109.68673	2	1	0	0.00023
11	114.35038	114.35023	4	0	0	0.00015
12	116.79381	116.79328	0	1	1	0.00053
13	121.45715	121.45678	2	0	1	0.00037
14	122.42797	122.42764	1	2	0	0.00033
15	127.09137	127.09114	3	1	0	0.00023
16	128.56409	128.56332	0	0	2	0.00077
17	131.75479	131.75464	5	0	0	0.00015
18	134.19823	134.19769	1	1	1	0.00054
19	135.16902	135.16856	0	3	0	0.00046
20	138.86156	138.86119	3	0	1	0.00037
25	149.15921	149.15906	6	0	0	0.00015
34	165.31451	165.31389	0	4	0	0.00062
35	166.56363	166.56348	7	0	0	0.00015
38	170.48003	170.47871	0	0	3	0.00132
47	183.96805	183.9679	8	0	0	0.00015
56	195.46004	195.45923	0	5	0	0.00081
62	201.37245	201.3723	9	0	0	0.00015
72	212.39613	212.3941	0	0	4	0.00203
86	225.60559	225.60455	0	6	0	0.00104
124	254.31241	254.30948	0	0	5	0.00293
126	255.75117	255.74989	0	7	0	0.00128
176	285.89679	285.89523	0	8	0	0.00156
196	296.22885	296.22485	0	0	6	0.00400
237	316.04242	316.04056	0	9	0	0.00186
289	338.14548	338.14026	0	0	7	0.00522
403	380.06223	380.05563	0	0	8	0.00660
538	421.97900	421.97101	0	0	9	0.00799

the Gaussian quadrature was $\mathcal{N}_1 = \mathcal{N}_2 = \mathcal{N}_3 = 21$ and the basis set size was $N_1 \times N_2 \times N_3 = 15 \times 15 \times 15$. With these parameters the accuracy of lowest 420 states was better than 10^{-9} MHz.

To simplify the analysis, we introduce an approximate harmonic spectrum of the system by the following formula:

$$E_h = \omega_1 \left(v_1 + \frac{1}{2} \right) + \omega_2 \left(v_2 + \frac{1}{2} \right) + \omega_3 \left(v_3 + \frac{1}{2} \right), \quad (5.1.6.1)$$

here ω_1 , ω_2 and ω_3 are from diagonalization of Hessian matrix in Sec. 5.1.3. In the following study, we define:

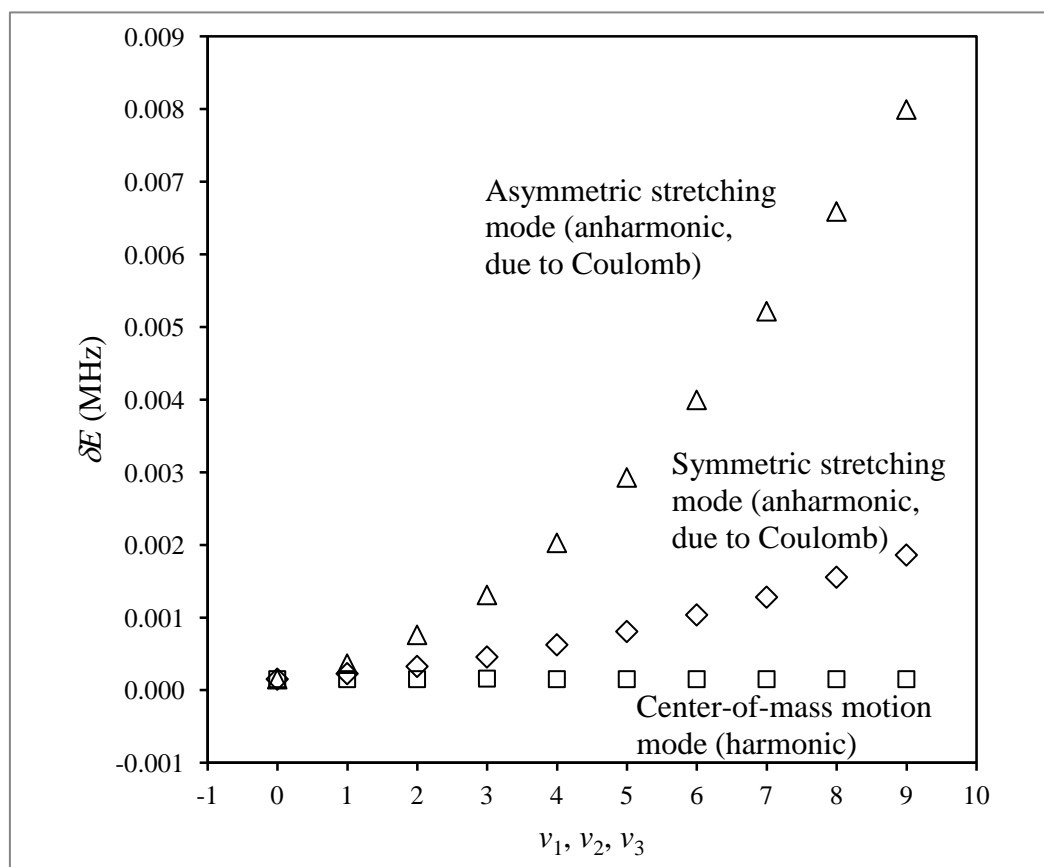


Fig. 5. 6: Effect of anharmonicity on three modes of the vibrational spectrum of three $^{111}\text{Cd}^+$ ions in a harmonic ($\sim z^2$) potential trap.

Table 5. 2: Coefficients of the fit by the Dunham expansion formula, Eq. (5.1.6.3), of the numerically calculated spectrum in Table 5.1 (vibrational states in the harmonic trap). The shift parameter was $D/2\pi = -1.757 \times 10^{-5}$ MHz.

Mode frequency $\Omega_i/2\pi$ ($i = 1,2,3$) (MHz)	Intramode anharmonicity $\Delta_i/2\pi$ ($i = 1,2,3$) (MHz)	Intermode anharmonicity $\Delta_{ij}/2\pi$ (MHz)
2.770	~ 0	$\Delta_{12} \sim 0$
4.798	-2.343×10^{-6}	$\Delta_{13} \sim 0$
6.671	-1.358×10^{-5}	$\Delta_{23}/2\pi = -1.393 \times 10^{-5}$

$$\delta E = E_v - E_h, \quad (5.1.6.2)$$

in order to characterize the deviation of spectrum from the harmonic model. Table 5.1 gives several eigenvalues computed numerically, E_h from Eq. (5.1.6.1), their assignments and deviations δE . From Table 5.1, one sees that our numerical results are a little higher than the analytic spectrum from harmonic approximation. Figure 5.6 shows deviations δE for the three normal mode progressions. These data for Mode 1 show a straight line, which means that Mode 1 is indeed harmonic in agreement with the arguments given above. In contrast, the data for Modes 2 and 3 look more like a parabola, which means that the spectra for these modes are slightly anharmonic, due to Coulomb interaction.

At the next step, we used three dimensional Dunham expansion, described by the following expression, to calculate parameters of the system:

$$\begin{aligned} E_{v_1, v_2, v_3} = & D + \Omega_1 \left(v_1 + \frac{1}{2} \right) - \Delta_1 \left(v_1 + \frac{1}{2} \right)^2 + \Omega_2 \left(v_2 + \frac{1}{2} \right) \\ & - \Delta_2 \left(v_2 + \frac{1}{2} \right)^2 + \Omega_3 \left(v_3 + \frac{1}{2} \right) - \Delta_3 \left(v_3 + \frac{1}{2} \right)^2 - \Delta_{12} \left(v_1 + \frac{1}{2} \right) \left(v_2 + \frac{1}{2} \right) \\ & - \Delta_{13} \left(v_1 + \frac{1}{2} \right) \left(v_3 + \frac{1}{2} \right) - \Delta_{23} \left(v_2 + \frac{1}{2} \right) \left(v_3 + \frac{1}{2} \right). \end{aligned} \quad (5.1.6.3)$$

This equation contains 10 parameters. By fitting ten lower states, we obtain the results of frequencies and anharmonicities, presented in Table 5.2. From the data above, we see that the first mode is purely harmonic ($\Delta_1 \approx 0$). We also see that $\Delta_2 \sim 10^{-6} \Omega_2$ and $\Delta_3 \sim 10^{-5} \Omega_3$, which means that the asymmetric stretching mode is more anharmonic (by about an order of magnitude) than the symmetric stretching mode. Still this anharmonicity (due to Coulomb) is very low and is insufficient for the control.

5.1.7 Three dimensional wavefunctions and transition matrix

After diagonalization of the Hamiltonian matrix, wavefunctions of the system can be obtained from the basis functions and eigenvectors using Eq. (2.2.7). The wavefunctions of the lower 40 states are shown in Fig. 5.7. Based on the shapes of wavefunctions we can assign the normal mode quantum number to these states.

In the three-ion system, the elements of transition matrix are written as follows:

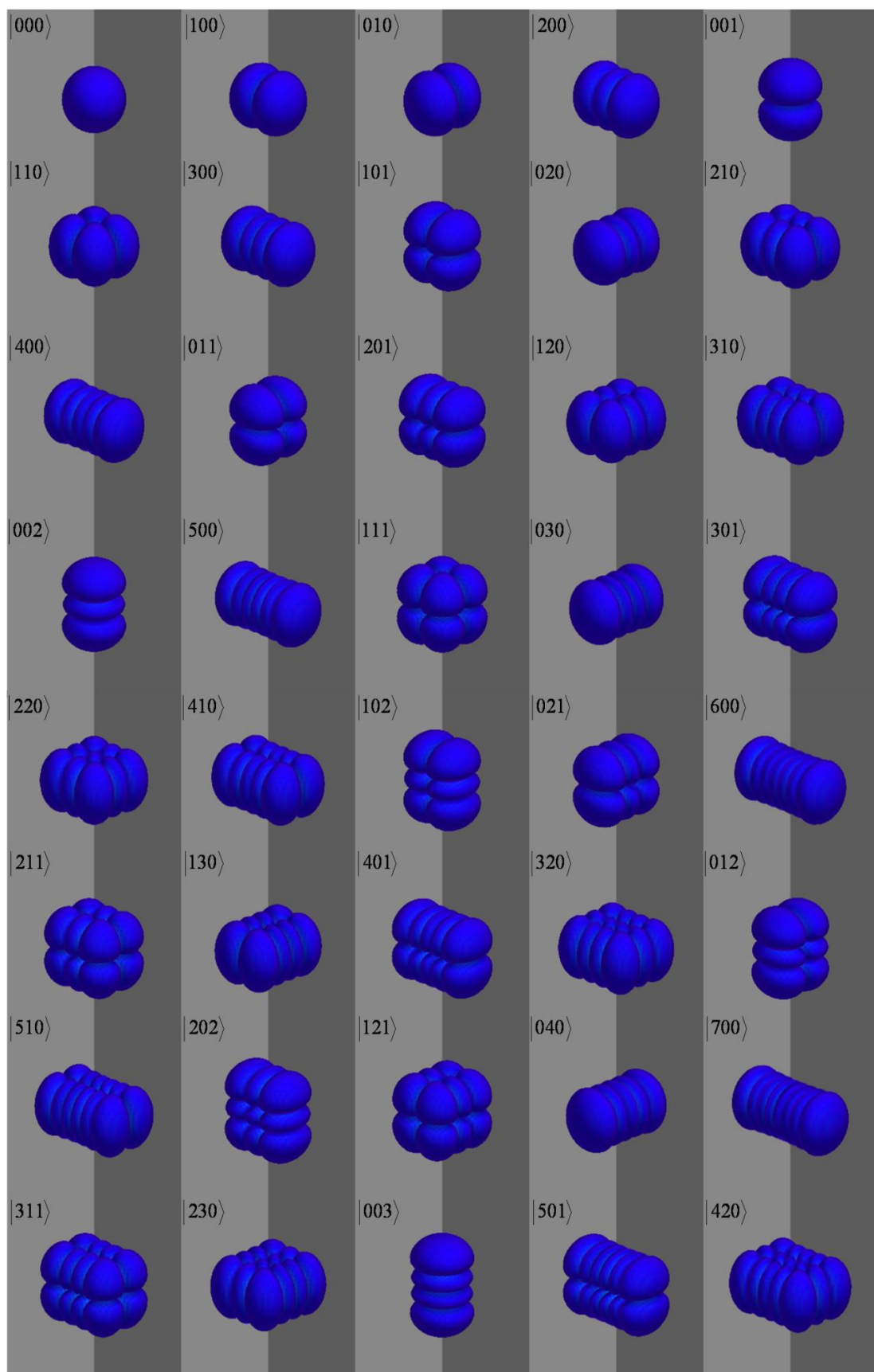


Fig. 5. 7: Wavefunctions of the lower 40 states of three $^{111}\text{Cd}^+$ ions in the harmonic trapping potential.

$$M_{v,v'} = \langle \Psi_v | d(z_1, z_2, z_3) | \Psi_{v'} \rangle. \quad (5.1.7.1)$$

Where the dipole moment function of three ions is

$$d(z_1, z_2, z_3) = q \cdot (z_1 + z_2 + z_3). \quad (5.1.7.2)$$

Note that wavefunctions are obtained in the normal mode coordinates, while the dipole moment function in Eq. (5.1.7.2) is in Cartesian coordinates. In order to carry out the integration in Eq. (5.1.7.1), we have to transform the dipole moment function into the normal mode coordinates using Eqs. (5.1.4.5), (5.1.4.9), (5.1.4.13) and (5.1.4.14). We start with the following equation:

$$M_{v,v'} = q \langle \Psi_v(\zeta_1, \zeta_2, \zeta_3) | z_1 + z_2 + z_3 | \Psi_{v'}(\zeta_1, \zeta_2, \zeta_3) \rangle, \quad (5.1.7.3)$$

and substitute

$$\begin{cases} z_1 = a_{11}\zeta_1 + a_{12}(\omega_1/\omega_2)\zeta_2 + a_{13}(\omega_1/\omega_3)\zeta_3 + z_{e1} \\ z_2 = a_{21}\zeta_1 + a_{22}(\omega_1/\omega_2)\zeta_2 + a_{23}(\omega_1/\omega_3)\zeta_3 + z_{e2}, \\ z_3 = a_{31}\zeta_1 + a_{32}(\omega_1/\omega_2)\zeta_2 + a_{33}(\omega_1/\omega_3)\zeta_3 + z_{e3} \end{cases} \quad (5.1.7.4)$$

$$\begin{aligned} z_1 + z_2 + z_3 &= (a_{11} + a_{21} + a_{31})\zeta_1 + (\omega_1/\omega_2)(a_{12} + a_{22} + a_{32})\zeta_2 \\ &\quad + (\omega_1/\omega_3)(a_{13} + a_{23} + a_{33})\zeta_3 + (z_{e1} + z_{e2} + z_{e3}). \end{aligned} \quad (5.1.7.5)$$

Finally, we use Eq. (5.1.7.5) to rewrite the expression for the of dipole moment in the following form:

$$\begin{aligned} d(z_1, z_2, z_3) &= q \cdot (z_1 + z_2 + z_3) = q \frac{\omega_1}{\omega_1} (a_{11} + a_{21} + a_{31})\zeta_1 + q \frac{\omega_1}{\omega_2} (a_{12} + a_{22} + a_{32})\zeta_2 \\ &\quad + q \frac{\omega_1}{\omega_3} (a_{13} + a_{23} + a_{33})\zeta_3 + q(z_{e1} + z_{e2} + z_{e3}). \end{aligned} \quad (5.1.7.6)$$

The dipole moment function of Eq. (5.1.7.6) and the wave functions of Eq. (5.1.5.1) are substituted into Eq. (5.1.7.3). Using properties of the basis set functions

[81], the integration in Eq. (5.1.7.3) is carried out analytically and elements of the dipole moment matrix are expressed through coefficients $C_{v_{ijk}}$ of the basis set expansion:

$$\begin{aligned}
 M_{v,v'} = & (a_{11} + a_{21} + a_{31}) q \sum_{ijk} C_{v_{ijk}}^* \sum_{i'j'k'} C_{v'_{i'j'k'}} \frac{(\sqrt{i}\delta_{i,i'+1} + \sqrt{i+1}\delta_{i,i'-1})}{\sqrt{2\mu_1\omega_1}} \delta_{j,j'} \delta_{k,k'} \\
 & + \frac{\omega_1}{\omega_2} (a_{12} + a_{22} + a_{32}) q \sum_{ijk} C_{v_{ijk}}^* \sum_{i'j'k'} C_{v'_{i'j'k'}} \frac{(\sqrt{j}\delta_{j,j'+1} + \sqrt{j+1}\delta_{j,j'-1})}{\sqrt{2\mu_2\omega_2}} \delta_{i,i'} \delta_{k,k'} \\
 & + \frac{\omega_1}{\omega_3} (a_{13} + a_{23} + a_{33}) q \sum_{ijk} C_{v_{ijk}}^* \sum_{i'j'k'} C_{v'_{i'j'k'}} \frac{(\sqrt{k}\delta_{k,k'+1} + \sqrt{k+1}\delta_{k,k'-1})}{\sqrt{2\mu_3\omega_3}} \delta_{i,i'} \delta_{j,j'} \\
 & + (z_1^{eq} + z_2^{eq} + z_3^{eq}) q \sum_{ijk} C_{v_{ijk}}^* \sum_{i'j'k'} C_{v'_{i'j'k'}} \delta_{i,i'} \delta_{j,j'} \delta_{k,k'}. \tag{5.1.7.7}
 \end{aligned}$$

Here $(\omega_1, \omega_2, \omega_3)$ are frequencies and (μ_1, μ_2, μ_3) are effective masses of the basis set functions, i.e., normal modes of the trap.

For the system studied in this harmonic trapping potential the second, third and last terms of this sum vanish exactly and are given here only for the purpose of generality. Indeed, from the values of eigenvectors of Hessian matrix, it is found that:

$$a_{11} + a_{21} + a_{31} = 1.73205, \tag{5.1.7.8}$$

$$a_{12} + a_{22} + a_{32} = 0, \tag{5.1.7.9}$$

$$a_{13} + a_{23} + a_{33} = 0. \tag{5.1.7.10}$$

Note that for the system of three equivalent ions the last constant term in Eq. (5.1.7.6) vanishes simply because $z_1^{eq} = -z_3^{eq}$ and $z_2^{eq} = 0$. The symmetric stretching mode,

Mode 2, is characterized by $a_{12} = -a_{32}$ and $a_{22} = 0$, which means that the second term in Eq. (5.1.7.6) vanishes exactly. Similarly, the asymmetric stretching mode, Mode 3, is characterized by $2a_{13} = -a_{23} = 2a_{33}$, which means that the third term in Eq. (5.1.7.6) also vanishes exactly. Thus, the dipole moment function does not depend on ζ_2 and ζ_3 at all, which means that Mode 2 and Mode 3 are both “dark”. To better understand these results, we plot the motion of ions in these three modes in Fig. 5.8.

For the center-of-mass motion mode (Mode 1), all three ions move together with the

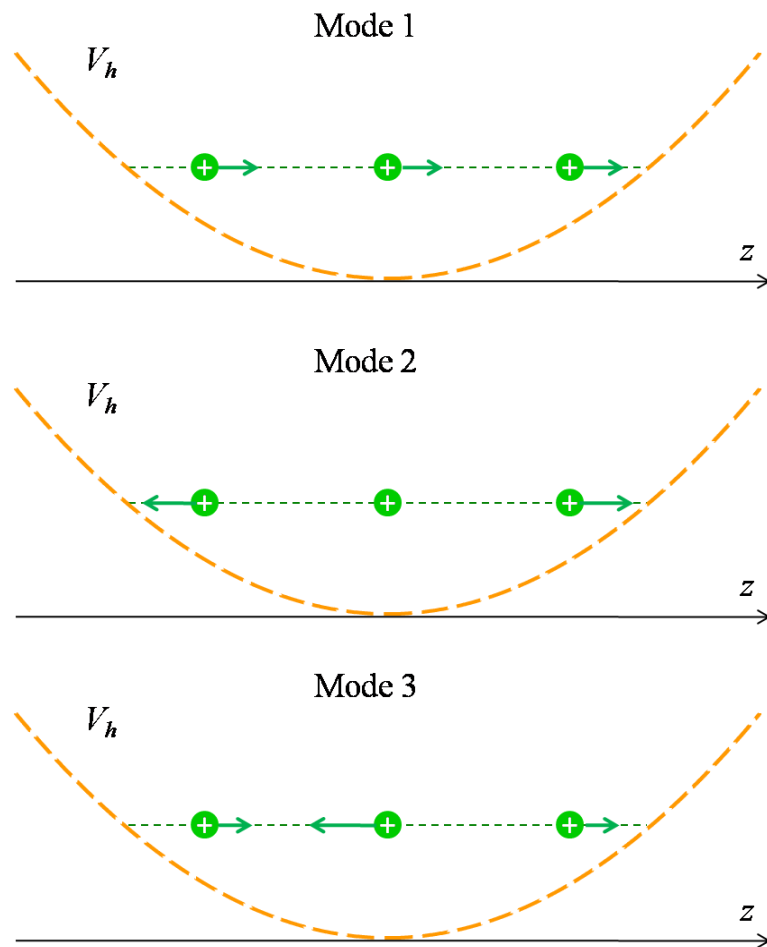


Fig. 5.8: Description of the motions of ions for three vibrational modes in the harmonic trapping potential. Length of the arrows indicates the vibrational motion amplitude of each ion.

same amplitude, just like one ion with triple mass in the harmonic potential trap. In this case the dipole moment is non-zero. For the symmetric stretching mode (Mode 2), the central ion doesn't move while the other two ions move in the opposite position with the same amplitude. As a result, their contributions to the dipole moment cancel each other. In the asymmetric stretching mode the central ion moves in the opposite direction of the other two ions. Because the amplitude of its motion is twice larger than that of the other two ions, the total contribution to the dipole

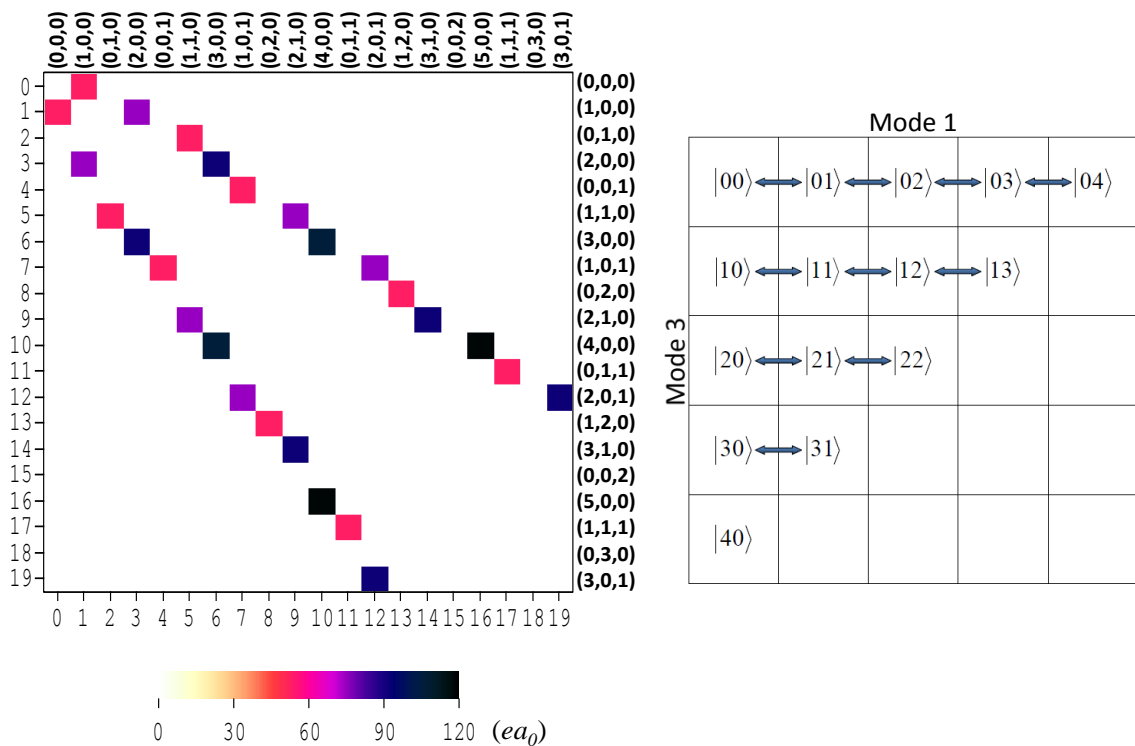


Fig. 5.9: Transition matrix of three $^{111}\text{Cd}^+$ ions in the harmonic potential trap and the diagram of allowed state-to-state transitions in this system. (black corresponds $\mu_{4,5} = 1.18 \times 10^2 \text{ } ea_0$ ($\sim 3.00 \times 10^2 \text{ D}$) and pink corresponds $\mu_{0,1} = 52.94 \text{ } ea_0$ ($\sim 1.35 \times 10^2 \text{ D}$) between states of mode 1).

moment is still zero. These features lead to the result that in the harmonic trapping potential only transitions between states of the first mode are possible. This mode is active. The second and third modes are “dark”.

In Fig. 5.9, the elements of transition matrix obtained from the harmonic potential trap are shown. In this picture we can only see the transitions between states of the first mode, while the other two modes are dark. That means they cannot be controlled by the spatially homogeneous fields.

5.1.8 Effect of Coulomb interaction

In Section 5.1.6, we showed that the symmetric stretching mode and the asymmetric stretching mode are only slightly anharmonic due to Coulomb interaction. This puts forward some questions for us: can we increase the value of anharmonicity by bringing ions close together (which increases Coulomb interaction) and would such anharmonicity be large enough for accurate control? In order to answer these questions, we carried out a series of calculations with different values of the force constant k in Eq. (2.1.1).

The results are summarized in the Fig. 5.10, where we plot equilibrium positions and anharmonicities vs. axial frequencies. When we increase the value of k , the shape of the trapping potential becomes sharper. The equilibrium positions of the terminal atoms become smaller, while frequencies of vibration increase. It is found

that the frequencies of three vibrational modes increase very fast with the increase of k , while the inter-ion distances decrease. When the value of k is increased 50 times, the value of $z_{e3} \approx 2500$ Bohr is observed and the values of frequencies are about 7 times larger (see Fig. 5.10 (a)). The values of Δ_1 stay zero independently of k , while values of Δ_2 and Δ_3 both increase as expected (see Fig. 5.10 (b)). The value of Δ_3 increases much faster than Δ_2 , it reaches about -1.2×10^{-3} MHz when $\Omega_3 \approx 300$ MHz. The intermode anharmonicities, Δ_{12} and Δ_{13} stay at low values even when the

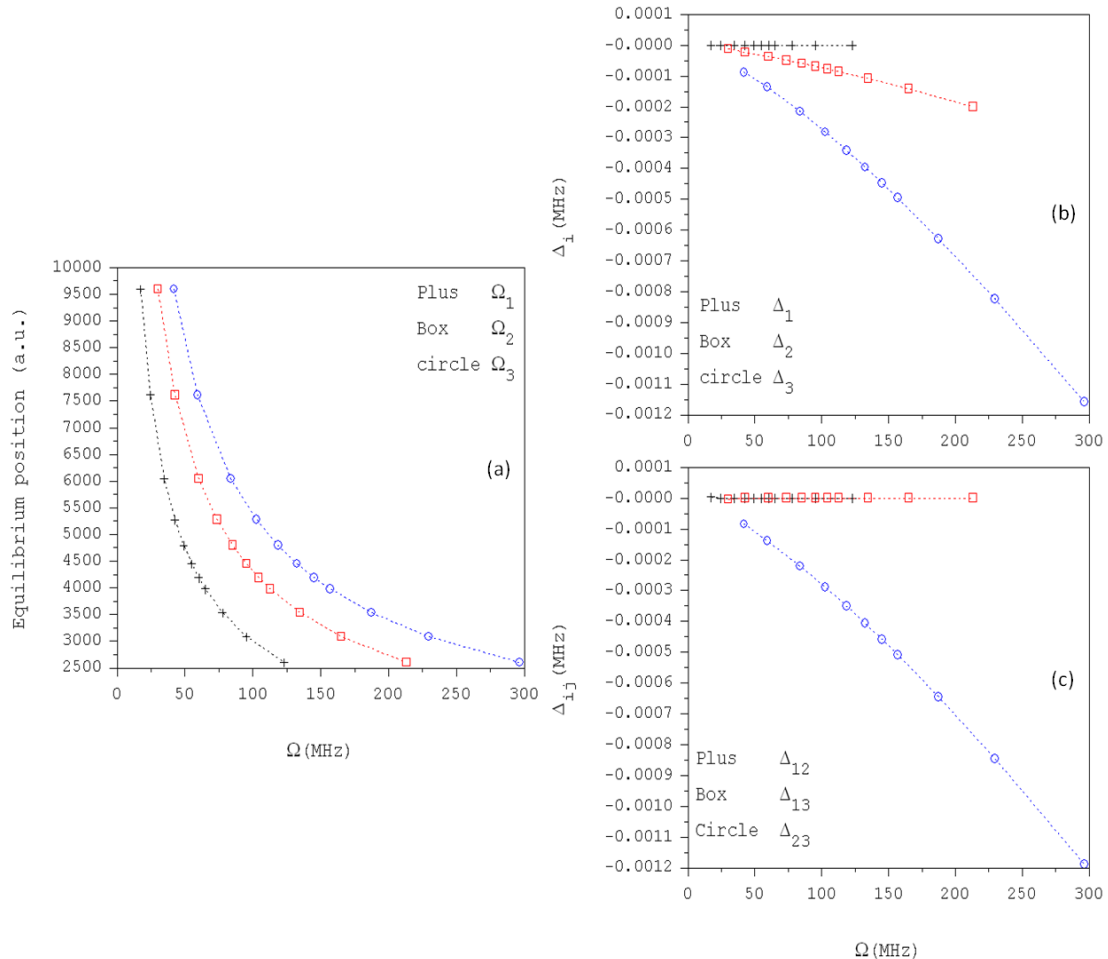


Fig. 5. 10: Relations between the equilibrium distances, normal mode frequencies and vibrational anharmonicities for three $^{111}\text{Cd}^+$ ions in the harmonic potential trap.

mode frequencies increase to large values. At the same time, Δ_{23} goes up faster and reaches about -1.2×10^{-3} MHz when $\Omega_3 \approx 300$ MHz.

The conclusion here is following: by bringing ions closer together we can slightly increase anharmonicity of the symmetric and asymmetric stretching modes. However, the frequencies of the modes increase at the same time so that the ratio of intramode anharmonicity over vibrational frequency is still much lower than the required $\sim 1\%$. The center-of-mass motion mode remains exactly harmonic ($\Delta_1 = 0$). Anharmonicities of the symmetric and asymmetric stretching modes are both small ($\Delta_2 \sim 10^{-6}\Omega_2$, $\Delta_3 \sim 4 \times 10^{-6}\Omega_3$). This means that bringing ions closer together cannot provide large enough anharmonicity for the optimal control. We need to seek some other sources of anharmonicity for our system.

5.2 Three ions in the anharmonic trapping potential

5.2.1 Anharmonic trapping potential

Here we explore a possibility of using an anharmonic trapping potential for a three-ion system. As in the two-ion case, we consider the simplest form of the trap given by:

$$V_a(z) = \frac{1}{4!} k' z^4, \quad (5.2.1.1)$$

where k' is a parameter which controls trap frequency. Here, we present the results of

calculations with $k'/2\pi = 1.494 \times 10^{-7}$ MHz/ a_0^4 . In Fig. 5.11, we show the anharmonic trapping potential, the equilibrium positions and several lower lying energy levels of the three-ion system.

Again, NR method was used to carry out minimization. Results for equilibrium positions are found as follows:

$$z_{e1} = -2.2086 \times 10^3 \text{ Bohr},$$

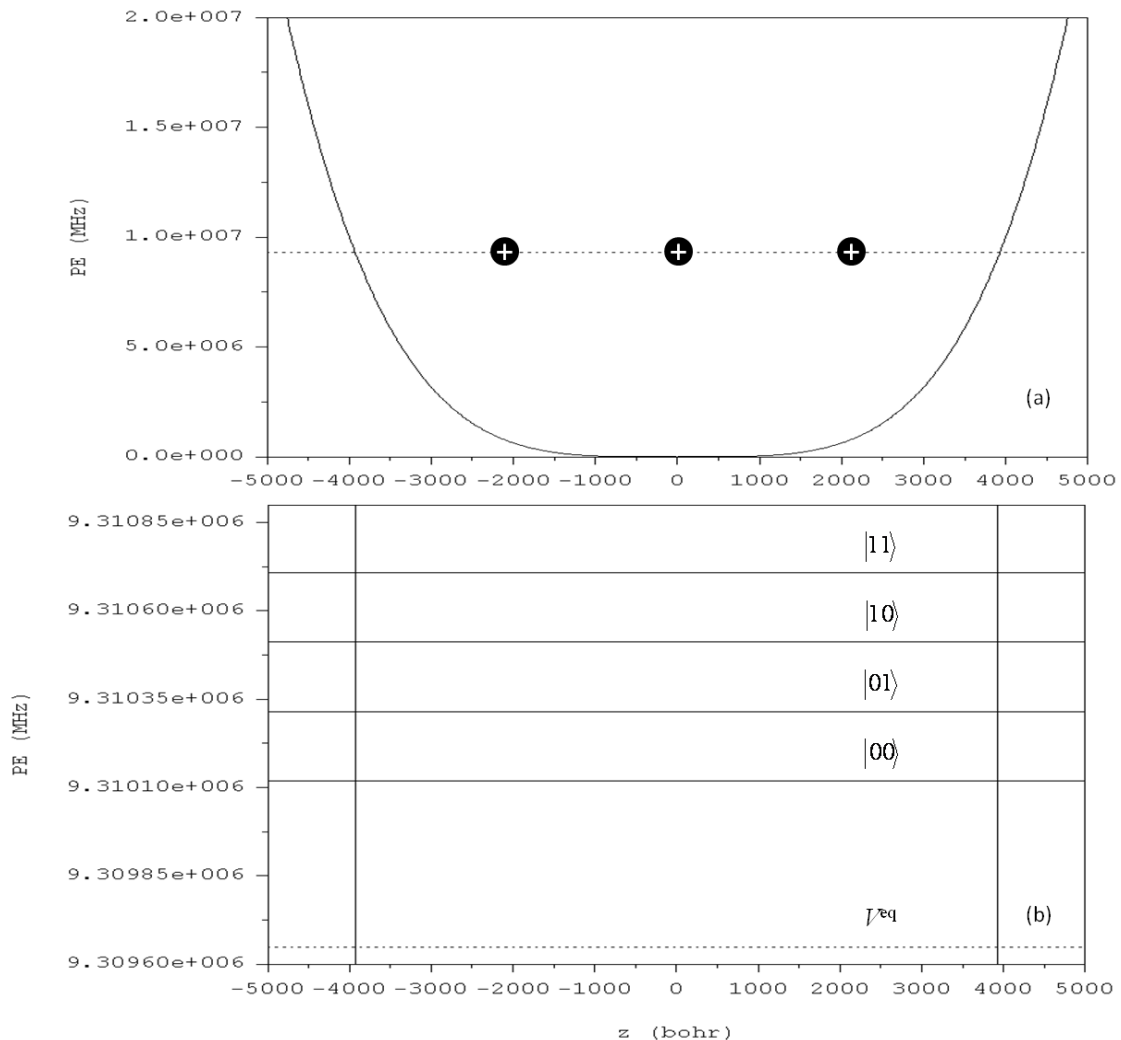


Fig. 5. 11: Three $^{111}\text{Cd}^+$ ions in the $\sim z^4$ potential trap: (a) Equilibrium positions of ions and minimum energy of the three-ion string. (b) Vibrational spectrum of this system and the encoding of two-qubit states proposed in this work.

$$z_{e2} = -2.9187 \times 10^{-8} \approx 0 \text{ Bohr},$$

$$z_{e3} = 2.2086 \times 10^3 \text{ Bohr}.$$

The value of potential energy at this point was $V^{eq} = V(z_{e1}, z_{e2}, z_{e3}) = 9.310 \times 10^6$

MHz.

Diagonalization of the Hessian matrix gave the following eigenvalues:

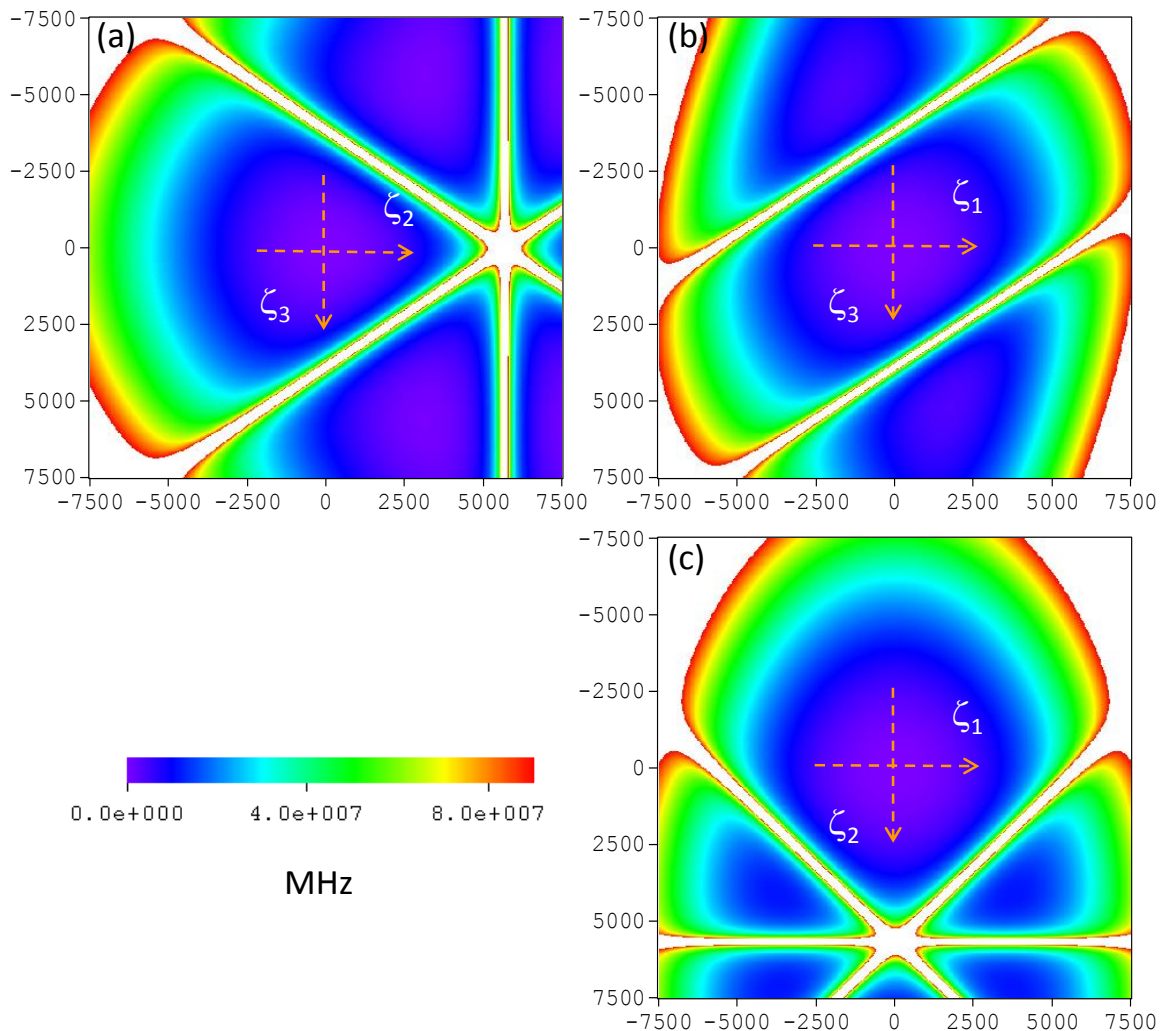


Fig. 5.12: PES of three $^{111}\text{Cd}^+$ ions in the strongly anharmonic potential trap ($\sim z^4$) using the normal mode coordinates. Three slices through the 3D-surface are shown: (a) perpendicular to ζ_1 through $\zeta_1 = 0$, (b) perpendicular to ζ_2 through $\zeta_2 = 0$ and (c) perpendicular to ζ_3 through $\zeta_3 = 0$.

$$\lambda_1 = 8.781 \times 10^{-16} \text{ a.u.}$$

$$\lambda_2 = 2.867 \times 10^{-15} \text{ a.u.}$$

$$\lambda_3 = 3.594 \times 10^{-15} \text{ a.u.}$$

Using Eq. (4.1.3.4), we calculate the frequencies of these three modes and transform to the units of MHz:

$$\omega_1/2\pi = 31.032 \text{ MHz}$$

$$\omega_2/2\pi = 56.071 \text{ MHz}$$

$$\omega_3/2\pi = 62.783 \text{ MHz}$$

Meanwhile, the eigenvectors are obtained:

$$\mathbf{A} = \begin{vmatrix} a_{11} & a_{12} & a_{13} \\ a_{21} & a_{22} & a_{23} \\ a_{31} & a_{32} & a_{33} \end{vmatrix} = \begin{vmatrix} 0.41966 & 0.70711 & -0.56911 \\ 0.80484 & 0.00000 & 0.59349 \\ 0.41966 & -0.70711 & -0.56911 \end{vmatrix}.$$

From the values of eigenvectors we can see that in the $\sim z^4$ trapping potential the first mode (center-of-mass motion mode) represents a different kind of motion, compared to the well known $\sim z^2$ case. Now the central ion moves almost twice further than the terminal ions. One can explain this feature by flattening of the $\sim z^4$ potential near location of the central ion. The central ion can move further because the potential is flatter in its vicinity.

The PES in the normal mode coordinates is presented in Fig. 5.12. It is seen that the motion along any normal mode axis (ζ_1 , ζ_2 , or ζ_3) brings the system closer to the white part (strong Coulomb repulsion) and results in appearance of the Coulomb

Table 5. 3: Eigenvalues, assignments and deviations (from the harmonic model) of the vibrational states of three $^{111}\text{Cd}^+$ ions in a strongly anharmonic trap.

# of state	E_v (MHz)	E_h (MHz)	v_1	v_2	v_3	δE (MHz)
1	470.8868	470.8802	0	0	0	0.0066
2	665.8705	665.8593	1	0	0	0.0112
3	823.1980	823.1868	0	1	0	0.0112
4	860.8562	860.8384	2	0	0	0.0178
5	865.3718	865.3549	0	0	1	0.0169
6	1018.1835	1018.1660	1	1	0	0.0175
7	1055.8441	1055.8176	3	0	0	0.0265
8	1060.3585	1060.3340	1	0	1	0.0245
9	1175.5116	1175.4935	0	2	0	0.0181
10	1213.1710	1213.1451	2	1	0	0.0259
11	1217.6852	1217.6615	0	1	1	0.0237
12	1250.8340	1250.7968	4	0	0	0.0372
13	1255.3473	1255.3131	2	0	1	0.0342
14	1259.8645	1259.8296	0	0	2	0.0349
15	1370.4989	1370.4727	1	2	0	0.0262
16	1408.1606	1408.1243	3	1	0	0.0364
17	1412.6737	1412.6406	1	1	1	0.0331
18	1445.8260	1445.7758	5	0	0	0.0503
19	1450.3383	1450.2922	3	0	1	0.0460
20	1454.8542	1454.8087	1	0	2	0.0455
21	1527.8278	1527.8002	0	3	0	0.0276
22	1565.4883	1565.4518	2	2	0	0.0365
23	1570.0010	1569.9681	0	2	1	0.0328
24	1603.1525	1603.1033	4	1	0	0.0492
25	1607.6643	1607.6198	2	1	1	0.0446
26	1612.1801	1612.1362	0	1	2	0.0438
27	1640.8202	1640.7549	6	0	0	0.0653
28	1645.3312	1645.2714	4	0	1	0.0598
29	1649.8461	1649.7878	2	0	2	0.0582
30	1654.3647	1654.3043	0	0	3	0.0604
31	1722.8169	1722.7793	1	3	0	0.0376
32	1760.4799	1760.4308	3	2	0	0.0491
33	1764.9913	1764.9473	1	2	1	0.0441
34	1798.1464	1798.0824	5	1	0	0.0640
41	1880.1464	1880.1068	0	4	0	0.0396
55	2048.8728	2048.7791	0	0	4	0.0938
68	2232.4675	2232.4133	0	5	0	0.0542
92	2443.3884	2443.2537	0	0	5	0.1348
104	2584.7913	2584.7200	0	6	0	0.0713
148	2837.9119	2837.7285	0	0	6	0.1833

anharmonicity. This means we can expect that the PES is anharmonic along all the three normal mode coordinates.

In numeric calculations the size of the Gaussian quadrature was $\mathcal{N}_1 = \mathcal{N}_2 = \mathcal{N}_3 = 21$ and the basis set size was $N_1 \times N_2 \times N_3 = 15 \times 15 \times 15$. This provided accuracy better than 10^{-9} MHz to the lower 250 vibrational states. The spectrum of states is given in Table 5.3. Deviations of the normal mode progressions from the harmonic model are presented in Fig. 5.13. Figure 5.13 shows very clearly that in the anharmonic trap all three normal modes are slightly anharmonic (contrast to Fig. 5.6).

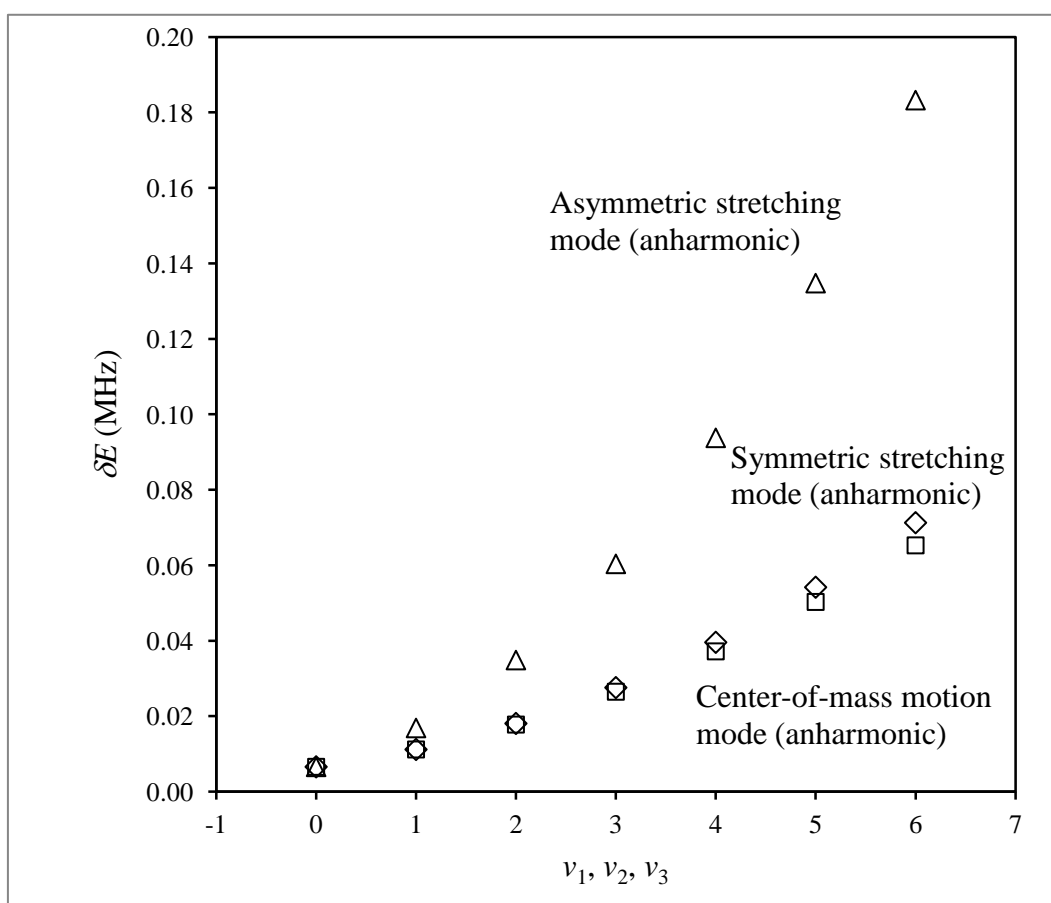


Fig. 5.13: Effect of anharmonicity on three modes of the vibrational spectrum of three $^{111}\text{Cd}^+$ ions in a strongly anharmonic ($\sim z^4$) potential trap.

Anharmonicities of the Modes 1 and 2 are very similar. Mode 3 is the most anharmonic mode.

To determine anharmonicity in the $\sim z^4$ potential, the three dimensional Dunham expansion from Eq. (5.1.6.3) was used to fit 10 lower states, the results for frequencies and anharmonicities are shown in Table 5.4. It was quite surprising to find that the spectrum of three ions in the *highly* anharmonic trap is only *slightly* anharmonic. It was especially unexpected to see that the center-of-mass motion mode (Mode 1) is the less anharmonic mode: $\Delta_1 \sim 5 \times 10^{-6} \Omega_1$. Based on general arguments one might expect that the center-of-mass motion mode of three ions in an anharmonic trap describes the motion similar to vibration of one ion in an anharmonic trap. Since anharmonicity of the one-ion spectrum was very pronounced (see Chapter 2), we expected to see the effect of similar magnitude in the three-ion case. It appears, however, that the Mode 1 in the anharmonic trap is special; it is different from the center-of-mass mode in the harmonic trap. Namely, in the anharmonic potential the terminal ions are allowed to move less than the central atom, which compensates for anharmonicity of the trapping potential and makes the Mode 1 less anharmonic. Put another way, for Mode 1 in the anharmonic trap the arrangement of three ions is not rigid and adjusts to the changes of the potential, minimizing the effect of anharmonicity. The positive outcome of this effect is that all three modes become

Table 5. 4: Coefficients of the fit by the Dunham expansion formula, Eq. (5.1.6.3), of the numerically calculated spectrum in Table 5.3 (vibrational states in the strongly anharmonic trap). The shift parameter was $D/2\pi = -5.269 \times 10^{-4}$ MHz.

Mode frequency $\Omega_i/2\pi$ ($i = 1,2,3$) (MHz)	Intramode anharmonicity $\Delta_i/2\pi$ ($i = 1,2,3$) (MHz)	Intermode anharmonicity $\Delta_{ij}/2\pi$ (MHz)
31.032	-1.667×10^{-4}	$\Delta_{12}/2\pi = -2.916 \times 10^{-4}$
56.071	-1.989×10^{-4}	$\Delta_{13}/2\pi = -4.859 \times 10^{-4}$
62.783	-6.103×10^{-4}	$\Delta_{23}/2\pi = -3.517 \times 10^{-4}$

anharmonic. The negative outcome is that the values of anharmonicity parameters remain small. The magnitude of anharmonicity for Mode 2 is similar to that of Mode 1, $\Delta_2 \sim 4 \times 10^{-6} \Omega_2$. These data show that for the most anharmonic Mode 3 (asymmetric stretching mode) the parameter of anharmonicity reaches only $\Delta_3 \sim 10^{-5} \Omega_3$, insufficient for the control. This means that in a three-ion case a strongly anharmonic trap offers no improvements over the purely harmonic trap.

5.2.2 Three-dimensional wavefunctions and transition matrix

Using the basis functions and eigenvectors from diagonalization of the Hamiltonian matrix in Eq. (2.2.7), wavefunctions of the system can be obtained. The

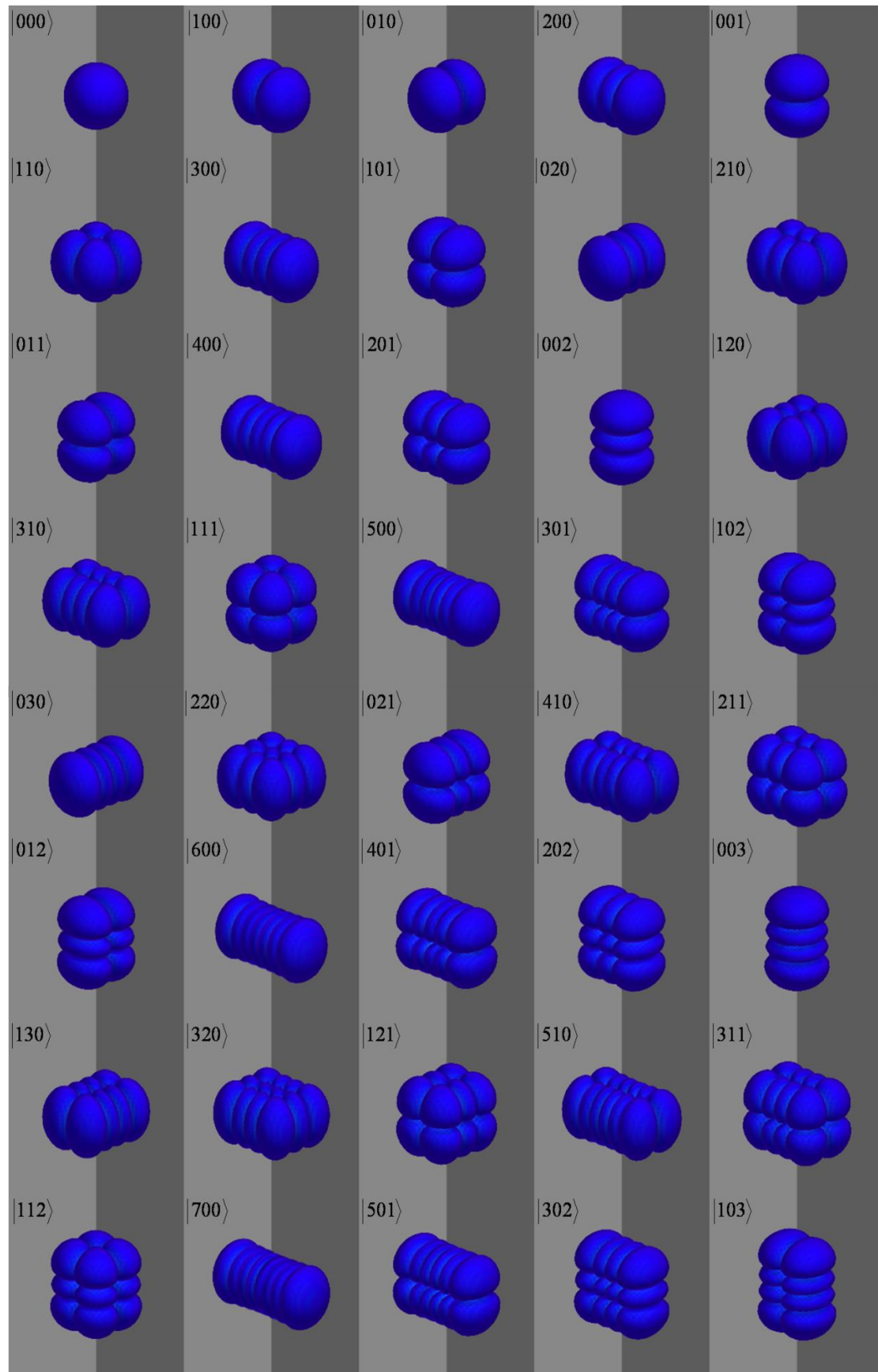


Fig. 5. 14: Wavefunctions of the lower 40 states of three $^{111}\text{Cd}^+$ ions in the $\sim z^4$ trapping potential.

wavefunctions of lower 40 states are shown in Fig. 5.14. Based on shapes of the wavefunctions we can assign the normal mode quantum numbers to these states.

The transition matrix can be calculated using the Eqs (5.1.7.3) and (5.1.7.6).

The coefficients of three vibration modes in Eq. (5.1.7.6) are shown here:

$$a_{11} + a_{21} + a_{31} = 1.64416, \quad (5.2.2.1)$$

$$a_{12} + a_{22} + a_{32} = 0, \quad (5.2.2.2)$$

$$a_{13} + a_{23} + a_{33} = -0.54473. \quad (5.2.2.3)$$

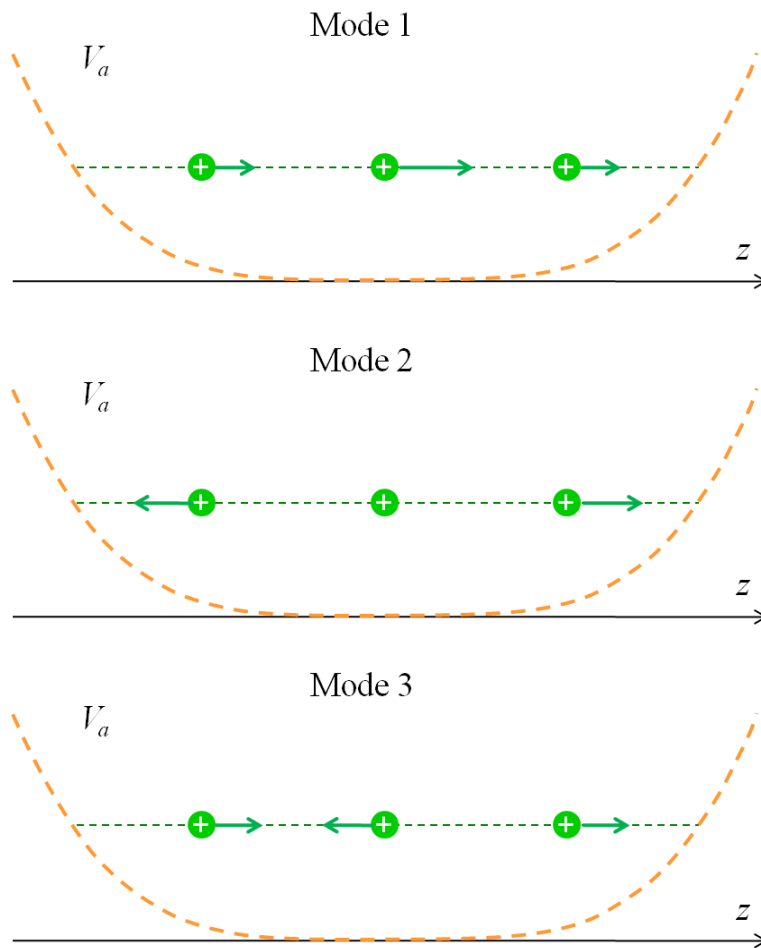


Fig. 5. 15: Description of the motions of ions for three vibrational motion modes in the $\sim z^4$ trapping potential. Length of the arrows indicates the vibrational motion amplitude of each ion.

The motions of three vibration modes are plotted in Fig. 5.15 in order to help us understand this system better. Note that the Modes 1 and 3 of the anharmonic trap are different from those of the harmonic trap. We see that in the eigenvector matrix of anharmonic trapping potential: $a_{21} > a_{11} = a_{31}$ and $|a_{23}| > |a_{13}| = |a_{33}|$. This happens because the $\sim z^4$ potential is flatter in the center and is sharper near the turning points, compared to the harmonic case. As a result, the amplitude of motion of the central ion is larger than the amplitudes of motion of the terminal ions.

These features lead to the following result: The third mode (asymmetric

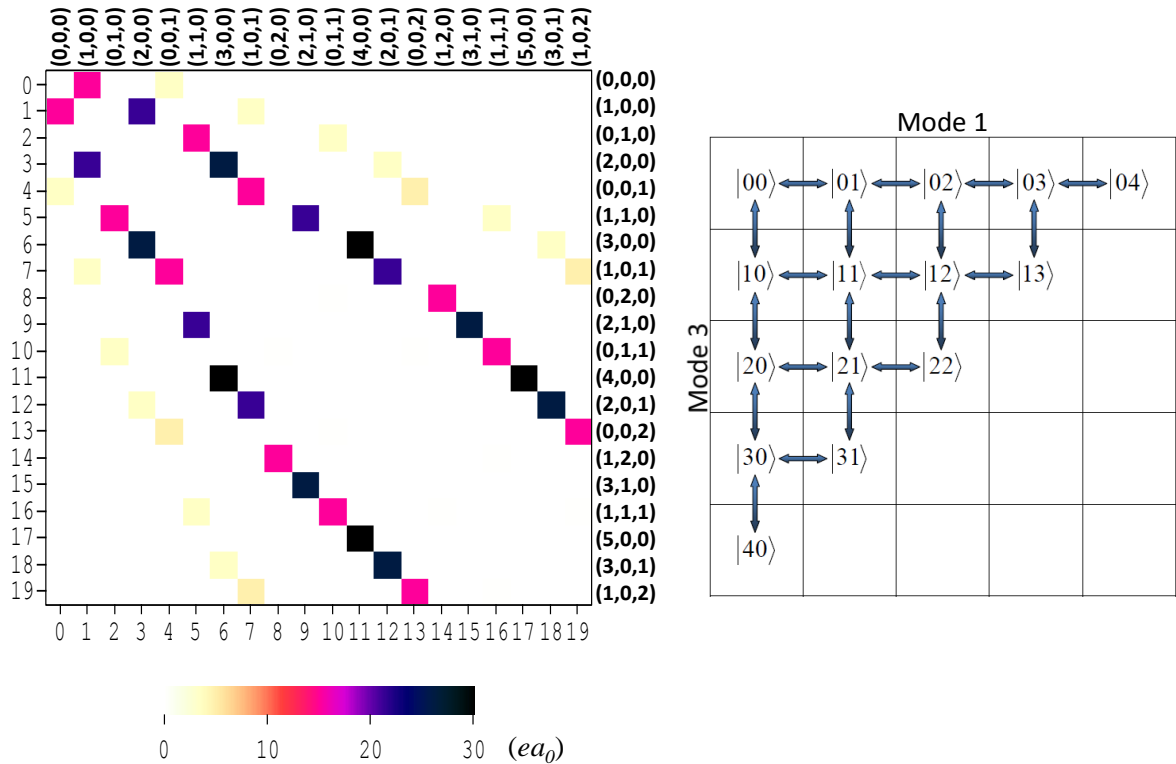


Fig. 5.16: Transition matrix of three $^{111}\text{Cd}^+$ ions in the $\sim z^4$ potential trap and the diagram of allowed state-to-state transitions in this system. (black corresponds $\mu_{4,5} = 33.57 \text{ } ea_0$ ($\sim 85.33 \text{ D}$) between states of mode 1 and light yellow corresponds $\mu_{0,1} = 3.50 \text{ } ea_0$ ($\sim 8.90 \text{ D}$) between states of mode 3).

stretching) becomes active and can be excited in principle. The first mode is also active, while the second mode (symmetric stretching) stays dark in the $\sim z^4$ potential. The transition matrix of two ions in the anharmonic trapping potential is shown in Fig. 5.16. From this picture, it is seen that the second mode is “dark”, while the transitions between the states of the first and third modes are possible.

5.2.3 Effect of Coulomb anharmonicity

We hoped to increase the values of anharmonicity parameters in this system by raising the value of force constant k' . A number of computational experiments were carried out. Their results are presented in Fig. 5.17. As one might expect, the frequencies of three vibrational modes increase as k' is raised, while the eqilibrium internuclear distances decrease (see Fig. 5.17 (a)). Frequencies of Modes 2 and 3 remain close to each other and are about twice higher than the frequency of Mode 1. As k' is raised all three intramode anharmonicity parameters (see Fig. 5.17 (b)) and all three intermode anharmonicity parameters (see Fig. 5.17 (c)) grow about linearly. The Mode 3 remains most anharmonic. When k' is raised by a factor of 525, anharmonicity of this mode reaches almost $\Delta_3/2\pi = -6.4 \times 10^{-4}$ MHz. However, the frequency of this mode grows at the same time and reaches almost $\Omega_3/2\pi = 64$ MHz, leading to about the same relative effect of anharmonicity: $\Delta_3 \sim 10^{-5} \Omega_3$. Indeed, the linear dependencies in Figs. 5.17 (b, c) here and in Figs. 5.10 (b, c) above

demonstrate very clearly that raising force constant has negligible effect on the Δ_i / ω_i ratios in both harmonic and strongly anharmonic traps.

The conclusion here is following: by bringing ions closer together we can slightly increase anharmonicity of all three vibration modes. However, the frequencies of the modes increase at the same time so that the ratio of intramode anharmonicity over vibrational frequency is still much lower than the required $\sim 1\%$. Anharmonicities of the center-of-mass motion mode and the symmemetric stretching mode are

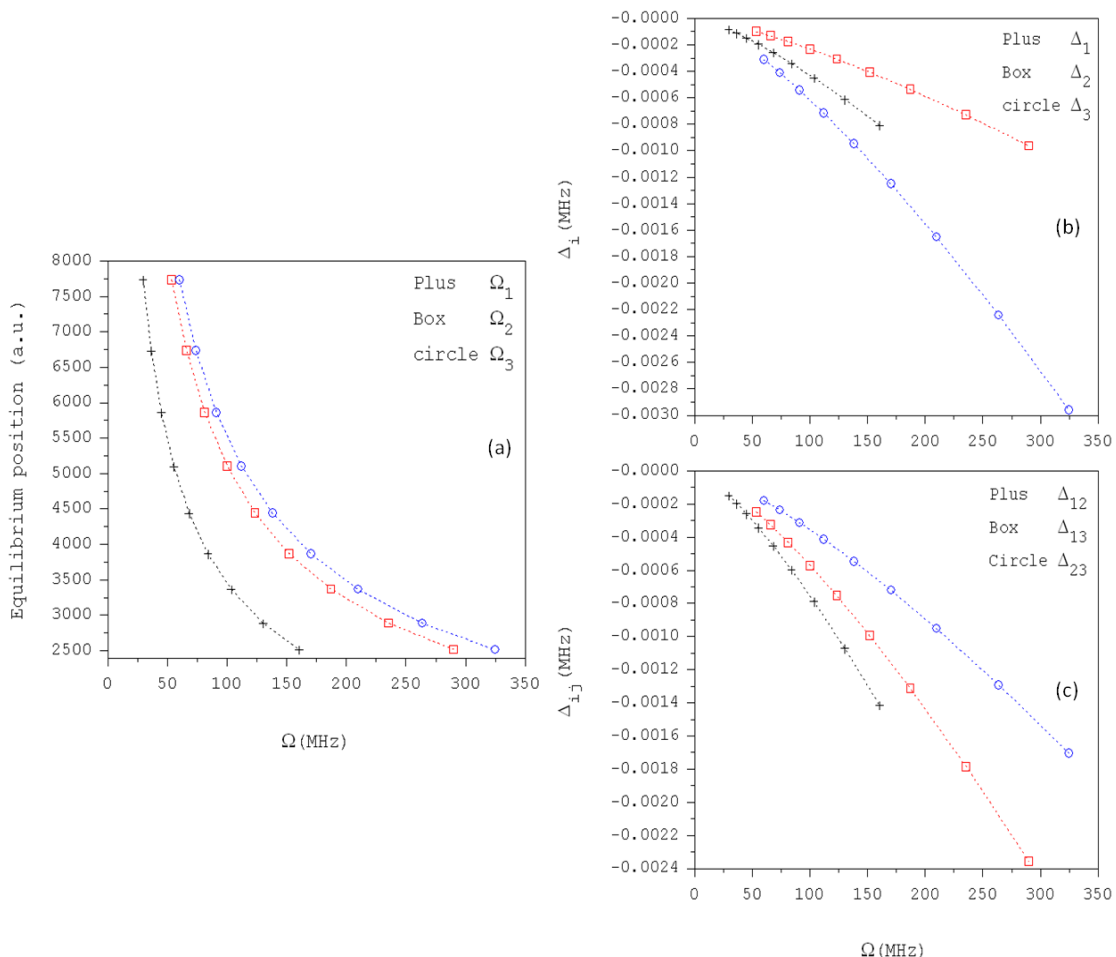


Fig. 5.17: Relations between the equilibrium distances, normal mode frequencies and vibrational anharmonicities for three $^{111}\text{Cd}^+$ ions in the strongly ($\sim z^4$) anharmonic potential trap.

comparable ($\Delta_1 \sim 5 \times 10^{-6} \Omega_1$, $\Delta_2 \sim 3 \times 10^{-6} \Omega_2$). The most anharmonic mode is the asymmetric stretching mode, $\Delta_3 \sim 10^{-5} \Omega_3$. This means that bringing ions closer together cannot provide large enough anharmonicity for the optimal control in the $\sim z^4$ trapping potential.

5.3 Conclusions

In the system of three $^{111}\text{Cd}^+$ ions in the harmonic trapping potential, the first mode (center-of-mass motion mode) is exactly harmonic ($\Delta_1 \approx 0$) and cannot be controlled. The second mode (symmetric stretching mode) and the third mode (asymmetric stretching mode) are anharmonic even in the harmonic trapping potential due to Coulomb interaction ($\Delta_2 \sim 10^{-6} \Omega_2$, $\Delta_3 \sim 4 \times 10^{-6} \Omega_3$), but this anharmonicity is very weak. Clearly, this is not sufficient for the control.

In the case of strongly anharmonic trapping potential ($\sim z^4$), the center-of-mass motion mode gains some anharmonicity. But this anharmonicity is very weak, at the level of $\Delta_1 \sim 5 \times 10^{-6} \Omega_1$. Anharmonicities of symmetric and asymmetric stretching mode are not improved a lot ($\Delta_2 \sim 3 \times 10^{-6} \Omega_2$, $\Delta_3 \sim 10^{-5} \Omega_3$). This is only about 3 times larger than in the harmonic trap and is much smaller than required for accurate control. So, using three trapped ions does not offer any advantage over the one-ion system. It is even worse. In this three-ion case we cannot even control the center-of-mass motion mode in the strongly anharmonic trap because of the small

local anharmonicity of the 3D PES.

Furthermore, in this system the symmetric stretching mode is “dark” and cannot be excited by the spatially homogeneous electric field.

Chapter 6: Three ions in the combined potential traps with applications to adiabatic and optimal control of three ions in the trap

6.1 Combined anharmonic potential

In Chapter 5, we found that for the system of three ions in the purely harmonic ($\sim z^2$) or purely anharmonic ($\sim z^4$) potential traps, we could not obtain enough anharmonicity for the optimal control. One possibility is to check whether some kind of combination potentials is better. Here we will use the trapping potential in general form:

$$V_a(z) = \alpha \frac{1}{2} kz^2 + \beta \frac{1}{4!} k' z^4, \quad (6.1.1)$$

where k and k' are two force constants. The axial frequency is $\omega/2\pi = 2.77$ MHz, related to the force constant through $k = m\omega^2$, with $k/2\pi = 1.483 \times 10^{-3}$ MHz/ a_0^2 , as it was used in Chapters 2 to 5. The value $k'/2\pi = 1.494 \times 10^{-7}$ MHz/ a_0^4 was chosen again, like in Sec. 5.2. We can control the shape of the trap by changing the unitless parameters α and β in Eq. (6.1.1). We will determine anharmonicity of the system as a function of the β/α ratio.

We carried out calculations of the spectra for twelve values of this ratio in the range $7.1 \times 10^{-6} \leq \beta/\alpha \leq 7.1 \times 10^{-3}$. In each case we did the Dunham expansion fit to determine the frequencies, intramode and intermode anharmonicities of three vibration modes. All the results are summarized in the Fig. 6.1. From the picture, it is

seen that although the intramode and intermode anharmonicities increase as we raise the β/α ratio, the frequencies of three normal vibration modes increase at the same time. It means that even if we keep on increasing the value of ratio β/α , we will never reach the situation when the anharmonicity would approach 1% of the frequency.

As for the transition matrix, we saw that transitions between states of the first

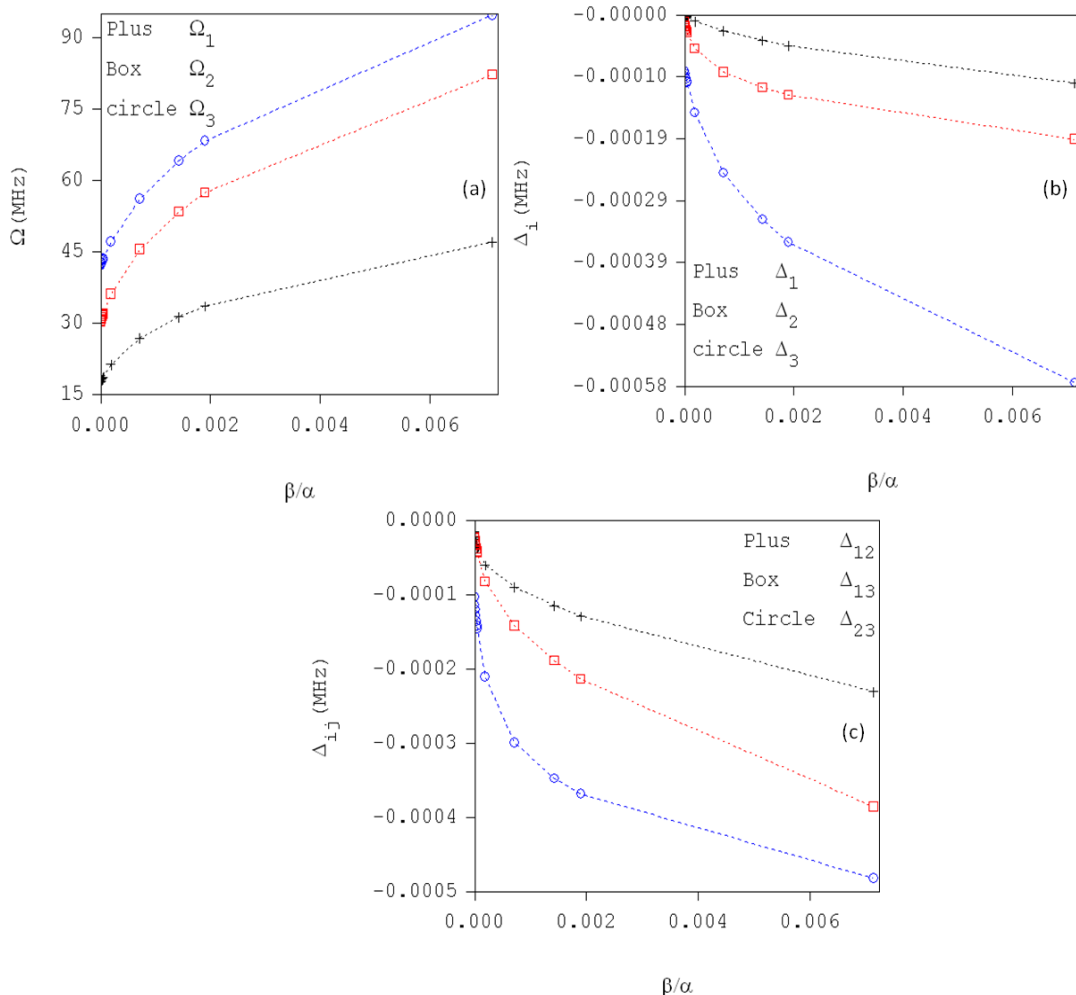


Fig. 6. 1: Relations between the equilibrium distances, normal mode frequencies and vibrational anharmonicities for three $^{111}\text{Cd}^+$ ions in the anharmonic combined

potential trap ($\alpha \frac{1}{2} k z^2 + \beta \frac{1}{4!} k' z^4, \alpha > 0, \beta > 0$).

mode in this system are possible. The second mode (symmetric stretching mode) always stays “dark”. The third mode (asymmetric stretching mode) becomes active due to introduction of the quartic term, and in principle can be excited.

Conclusion for this combined anharmonic potential is following: the spectrum of three ions is only *slightly* anharmonic. The most anharmonic mode is Mode 3 (the asymmetric stretching mode), where the parameter of anharmonicity reaches $\Delta_3 \sim 6 \times 10^{-6} \Omega_3$. Anharmonicities of the center-of-mass motion mode and the symmetric stretching mode are comparable ($\Delta_1 \sim 2 \times 10^{-6} \Omega_1$, $\Delta_2 \sim 2 \times 10^{-6} \Omega_2$). Clearly, this is insufficient for the control. In the combined potential anharmonicity is always lower than in the $\sim z^4$ potential, which makes sense. This means that the anharmonic potential with $\alpha > 0$ and $\beta > 0$ carries no improvement. So, in the combined trapping potential increasing the value of ratio β/α cannot provide large enough anharmonicity for the optimal control.

6.2 Inverted combined potential ($\alpha < 0$, $\beta > 0$)

Here we consider the case of inverted combined potential trap, where β is positive, but α is a *negative* number [32, 71, 72]. When the $-\alpha/\beta$ ratio is very large this expression describes a double well potential with two (separated, almost independent) wells, but we are far from that limit. In the cases considered here the first term of Eq. (6.1.1) lifts, just slightly, the potential in the middle of the z^4 well,

creating a wide, strongly anharmonic trap, with the vibrational zero-point energy well above the top of the barrier at $z = 0$. The shape of this kind of potential trap is shown in Fig. 6.2, where $k/2\pi = 1.483 \times 10^{-3}$ MHz/ a_0^2 , same as in the harmonic case. The value of $k'/2\pi = 1.494 \times 10^{-7}$ MHz/ a_0^4 is the same as in Chapters 5 and 6. Parameters $\alpha = -100$ and $\beta/\alpha = -0.01$ are chosen for this example.

Again, the NR method was used to carry out minimization. The results of

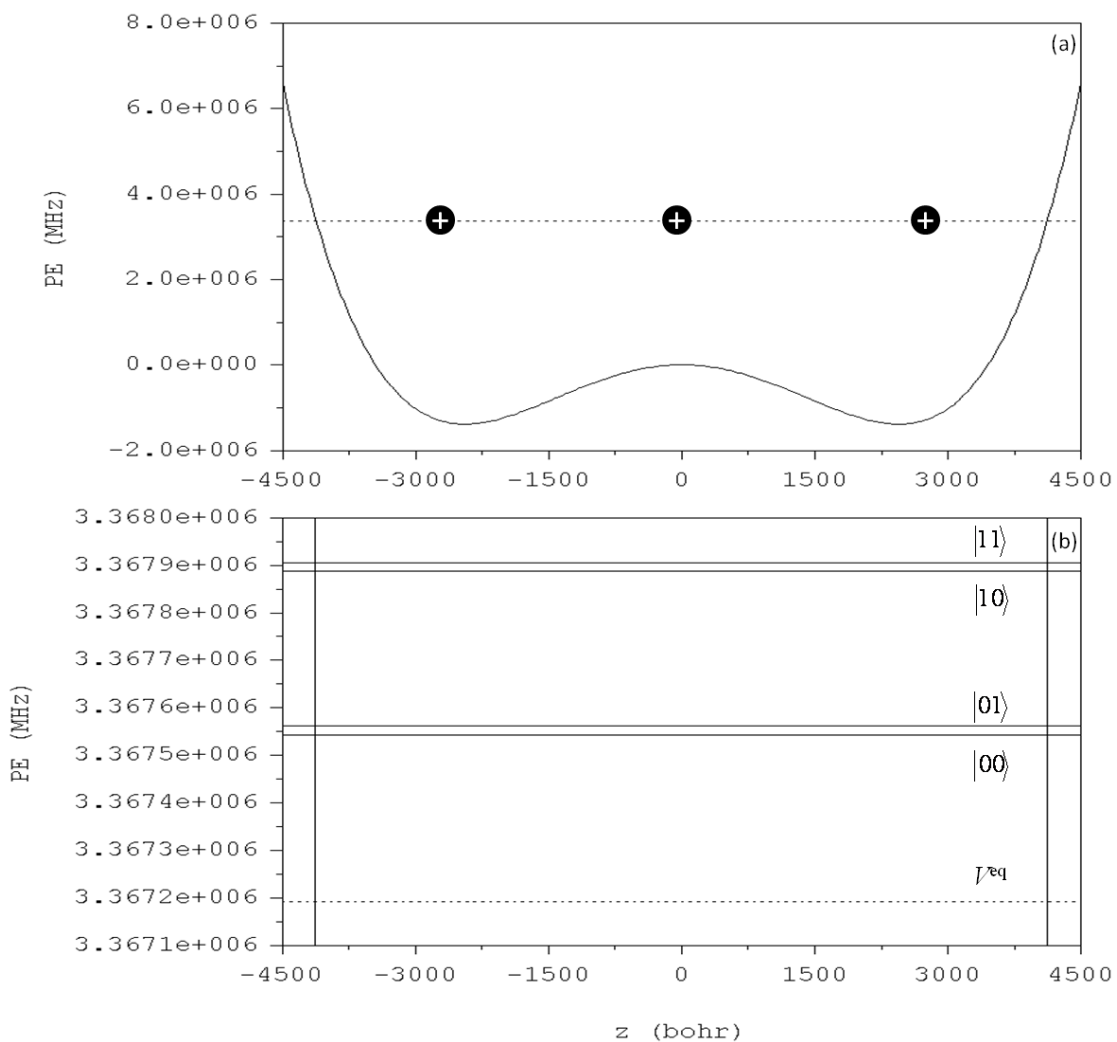


Fig. 6. 2: (a) Equilibrium positions of $^{111}\text{Cd}^+$ ions and minimum energy of a three-ion string trapped in a flat anharmonic potential of the form $\alpha \frac{1}{2} k z^2 + \beta \frac{1}{4!} k' z^4$. (b) Vibrational spectrum of this system and the encoding of two-qubit states proposed in this work.

equilibrium positions are:

$$z_{e1} = -2.8624 \times 10^3 \text{ Bohr},$$

$$z_{e2} = -8.3218 \times 10^{-6} \approx 0 \text{ Bohr},$$

$$z_{e3} = 2.8624 \times 10^3 \text{ Bohr}.$$

The value of potential energy at this point is $V^{eq} = V(z_{e1}, z_{e2}, z_{e3}) = 3.367 \times 10^6 \text{ MHz}$.

Next, the diagonalization of Hessian matrix was done and the following eigenvalues were found:

$$\lambda_1 = 6.817 \times 10^{-18} \text{ a.u.}$$

$$\lambda_2 = 2.716 \times 10^{-15} \text{ a.u.}$$

$$\lambda_3 = 2.748 \times 10^{-15} \text{ a.u.}$$

Using Eq. (4.1.3.4), we calculate the frequencies of these three vibration in the units of MHz:

$$\omega_1/2\pi = 2.734 \text{ MHz},$$

$$\omega_2/2\pi = 54.579 \text{ MHz},$$

$$\omega_3/2\pi = 54.890 \text{ MHz}.$$

Note that the frequencies of Mode 2 and 3 are very close to each other. They are nearly degenerate.

Meanwhile, the eigenvectors of the system are obtained:

$$\mathbf{A} = \begin{vmatrix} a_{11} & a_{12} & a_{13} \\ a_{21} & a_{22} & a_{23} \\ a_{31} & a_{32} & a_{33} \end{vmatrix} = \begin{vmatrix} 0.15776 & 0.70711 & -0.68928 \\ 0.97480 & 0.00000 & 0.22310 \\ 0.15776 & -0.70711 & -0.68928 \end{vmatrix}.$$

The PES of this system, transformed into the normal mode coordinates is shown in Fig. 6.3. From analysis of Fig. 6.3 one can expect that in this system Mode 1 is the most anharmonic. Somewhat less obvious but still possible to derive from Fig.

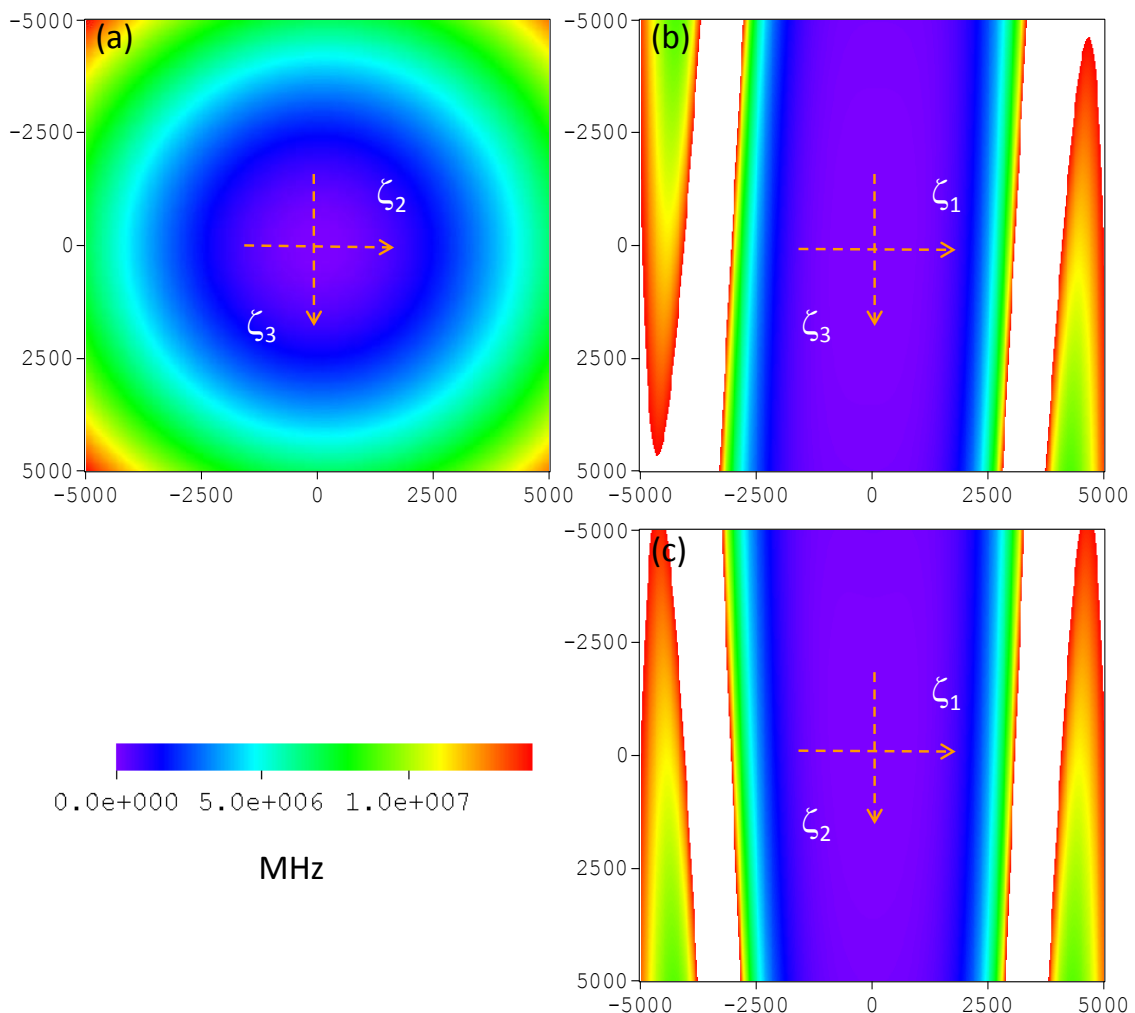


Fig. 6.3: PES of three $^{111}\text{Cd}^+$ ions in the inverted combined potential trap using the normal mode coordinates. Three slices through the 3D-surface are shown: (a) perpendicular to ζ_1 through $\zeta_1 = 0$, (b) perpendicular to ζ_2 through $\zeta_2 = 0$ and (c) perpendicular to ζ_3 through $\zeta_3 = 0$.

6.3 is that the Modes 2 and 3 are also somewhat anharmonic.

Referring to the matrix \mathbf{A} we can see that: The normal Modes 1 and 3 are very unusual. Mode 1 describes motion where amplitude of the central ion is almost an order of magnitude larger than amplitudes of the terminal ions: $a_{21} \gg a_{11} = a_{31}$. Mode 3 shows just opposite: $|a_{23}| \ll |a_{13}| = |a_{33}|$. The behavior of Mode 1 is easy to explain. The central atom sits on the top of a small “hill” so that its deviation from the equilibrium point reduces the potential energy, compensating for increase of potential energy due to the motion of terminal atoms. As a result, the PES is very flat along ζ_1 and is very anharmonic. The behavior of Mode 3 is less intuitive, or even somewhat counterintuitive. We think that the Mode 3 is as it is simply because it must be orthogonal to the Modes 1 and 2. Overall, the Mode 1 (low frequency mode) describes mostly the motion of central ion, while the Modes 2 and 3 (high frequency, nearly degenerate modes) describe mostly the motion of two terminal ions.

In numerical calculations, due to very different frequencies of the modes, we used the following parameters: $N_1 = 21$, $N_2 = N_3 = 17$ for the Gaussian quadratures in ζ_1 , ζ_2 and ζ_3 , respectively, and $N_1 \times N_2 \times N_3 = 15 \times 10 \times 10$ for the basis set size. Accuracy was comparable to or better than in the calculations presented above (10^{-9} MHz for the lower 364 vibrational states). The spectrum of numerical eigenvalues is given in Table 6.1, along with the state assignments and deviations of their energies

Table 6. 1: Eigenvalues, assignments and deviations (from the harmonic model) of the vibrational states of three $^{111}\text{Cd}^+$ ions in a combined inverted trap with $\alpha = -100$ and $\beta = 1$. See text for details.

# of state	E (MHz)	E_h (MHz)	v_1	v_2	v_3	δE (MHz)
1	352.6682	352.4980	0	0	0	0.1702
2	370.4720	369.6774	1	0	0	0.7945
3	388.8237	386.8568	2	0	0	1.9669
4	407.6818	404.0362	3	0	0	3.6457
5	427.0121	421.2155	4	0	0	5.7965
6	446.7856	438.3949	5	0	0	8.3907
7	466.9779	455.5743	6	0	0	11.4036
16	695.5058	695.4293	0	1	0	0.0765
17	697.4395	697.3835	0	0	1	0.0560
46	1038.3293	1038.3605	0	2	0	-0.0311
48	1042.2279	1042.2690	0	0	2	-0.0411
89	1381.1338	1381.2917	0	3	0	-0.1580
94	1387.0280	1387.1545	0	0	3	-0.1266
149	1723.9099	1724.2229	0	4	0	-0.3130
153	1731.8368	1732.0400	0	0	4	-0.2032
222	2066.6421	2067.1541	0	5	0	-0.5120
229	2076.6531	2076.9255	0	0	5	-0.2725
311	2409.3013	2410.0854	0	6	0	-0.7842
318	2421.4751	2421.8110	0	0	6	-0.3359

from the analytic harmonic model. Figure 6.4 shows deviations from the harmonic model for the three normal mode progressions. From this picture we see that all three normal modes are strongly anharmonic, with the Mode 1 being the most anharmonic. Anharmonicities of the Modes 2 and 3 seem to be comparable.

To determine anharmonicity in the inverted combined potential, the three dimensional Dunham expansion from Eq. (5.1.6.3) was used to fit 10 lower states, the results of frequencies and anharmonicities are shown in Table 6.2.

Table 6. 2: Coefficients of the fit by the Dunham expansion formula, Eq. (5.1.6.3), of the numerically calculated spectrum in Table 6.1 (vibrational states in the combined inverted trap). The shift parameter was $D/2\pi = -2.115 \times 10^{-2}$ MHz.

Mode frequency $\Omega_i/2\pi$ ($i = 1,2,3$) (MHz)	Intramode anharmonicity $\Delta_i/2\pi$ ($i = 1,2,3$) (MHz)	Intermode anharmonicity $\Delta_{ij}/2\pi$ (MHz)
2.738	-4.361×10^{-2}	$\Delta_{12}/2\pi = -1.102 \times 10^{-2}$
54.580	1.106×10^{-3}	$\Delta_{13}/2\pi = -4.871 \times 10^{-3}$
54.886	-1.371×10^{-3}	$\Delta_{23}/2\pi = 3.872 \times 10^{-2}$

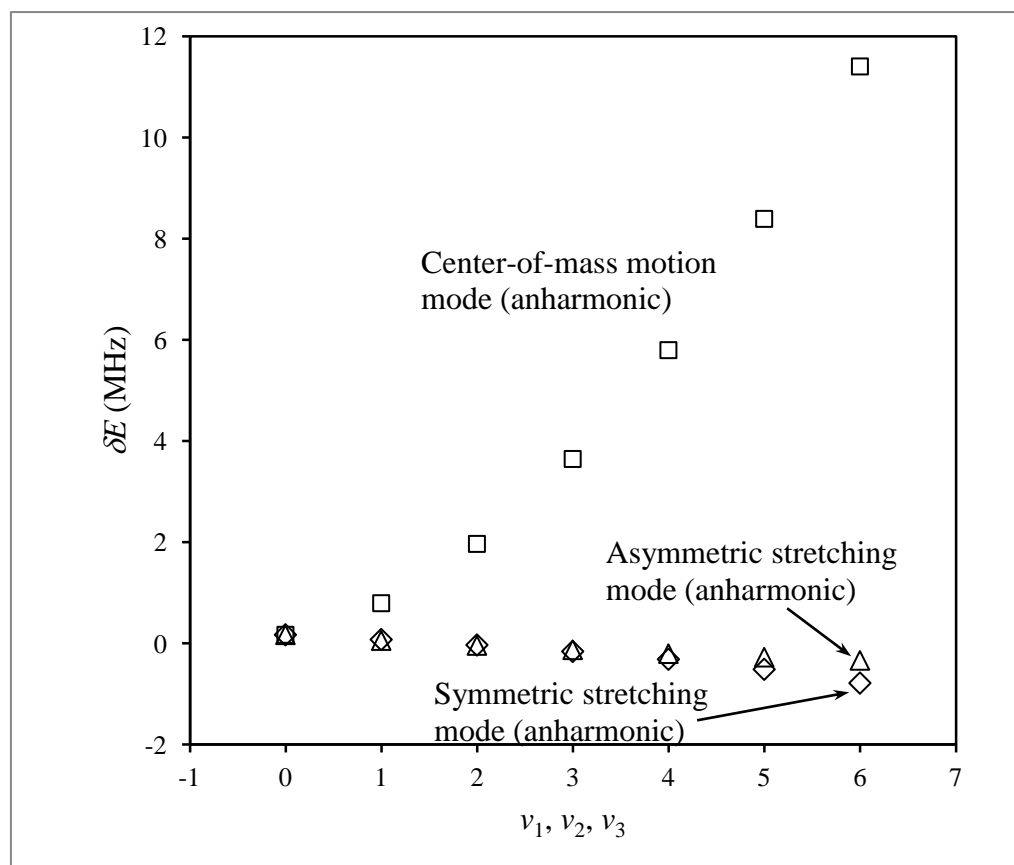


Fig. 6. 4: Effect of anharmonicity on three modes of the vibrational spectrum of three $^{111}\text{Cd}^+$ ions in an inverted combined potential trap (with $\alpha = -100$ and $\beta = 1$).

In the inverted combined potential, frequencies of the second and third mode are very close to each other and are much larger than the frequency of Mode 1. Anharmonicity parameters in this system show dramatic improvement compared to all cases studied above. We see that $\Delta_1 \sim 10^{-2} \Omega_1$, which is well sufficient for the successful control. Mode 2 and 3 are less anharmonic: $\Delta_2 \sim 2 \times 10^{-5} \Omega_2$ and $\Delta_3 \sim 3 \times 10^{-5} \Omega_3$. Still, they are more anharmonic than any mode in the $\sim z^2$ or $\sim z^4$ potentials studied in Chapters 4 and 5.

6.3 Three-dimensional wavefunctions and the transition matrix

Using the basis functions and eigenvectors from diagonalization of Hamiltonian matrix in Eq. (2.2.7), the wavefunctions of the system can be obtained. The wavefunctions of some useful states without excitation of mode 2 (which is anyway “dark” and cannot be controlled) are shown in Fig. 6.5. The normal mode quantum numbers can be assigned based on shapes of the wavefunctions.

From the matrix of eigenvectors, one can obtain:

$$a_{11} + a_{21} + a_{31} = 1.29032, \quad (6.3.1)$$

$$a_{12} + a_{22} + a_{32} = 0, \quad (6.3.2)$$

$$a_{13} + a_{23} + a_{33} = -1.15546. \quad (6.3.3)$$

The motions of ions in these three vibrational modes are plotted in Fig. 6.6. The normal Modes 1 and 3 are very unusual. Mode 1 describes motion where amplitude of

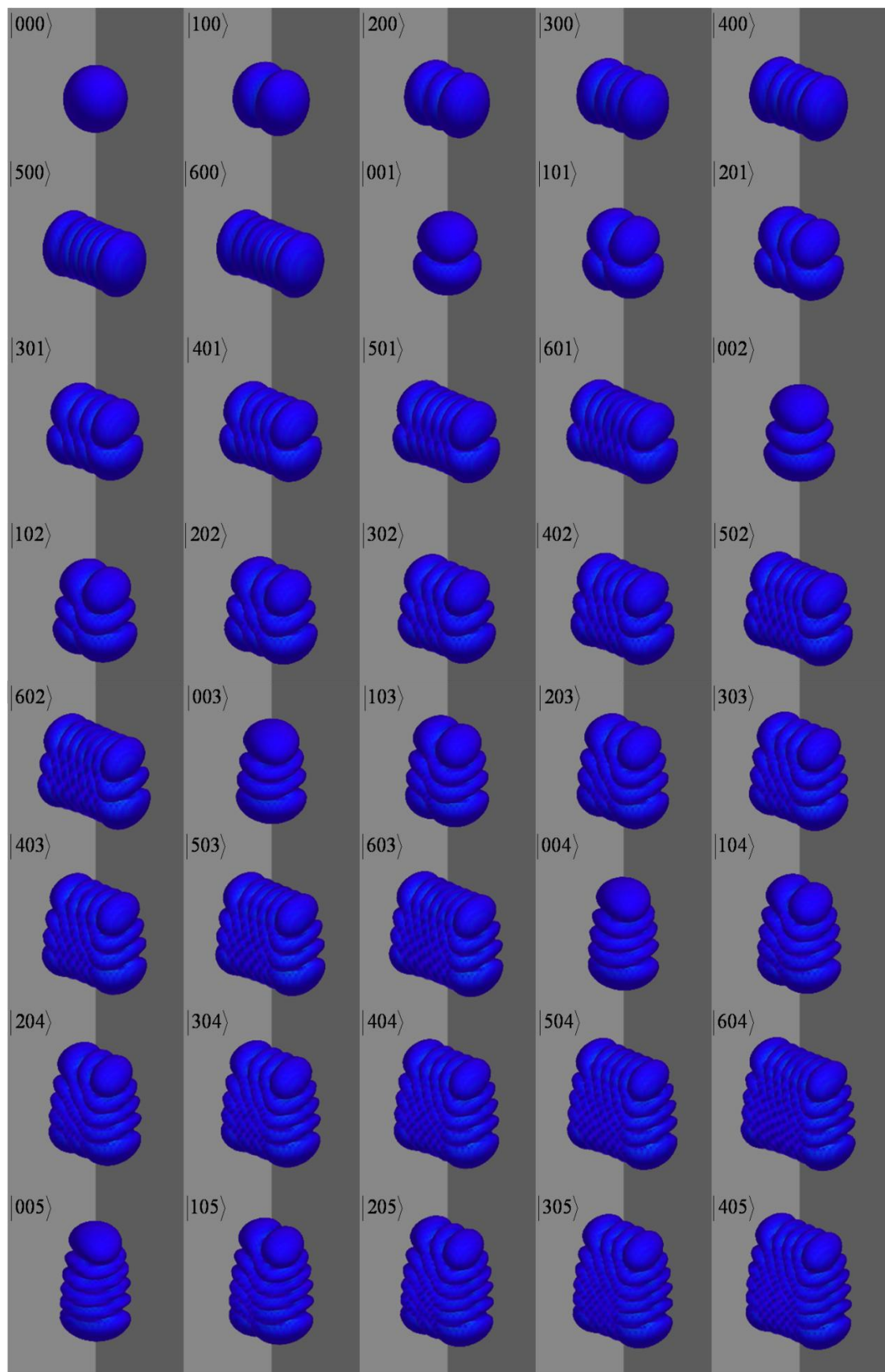


Fig. 6. 5: Wavefunctions of 40 states with excitation to the first and the third modes of three $^{111}\text{Cd}^+$ ions in the inverted combined trapping potential.

the central ion is almost an order of magnitude larger than amplitudes of the terminal ions: $a_{21} \gg a_{11} = a_{31}$. The symmetric stretching mode (Mode 2) remains the same as in harmonic case due to symmetry. Mode 3 shows some opposite attribute to Mode 1: $|a_{23}| \ll |a_{13}| = |a_{33}|$, the amplitudes of motion of the terminal ions are about 3 times larger than the amplitude of motion of the central ion.

As a result, the second mode (symmetric stretching mode) stays “dark” in inverted combined potential, while the third mode (asymmetric stretching mode)

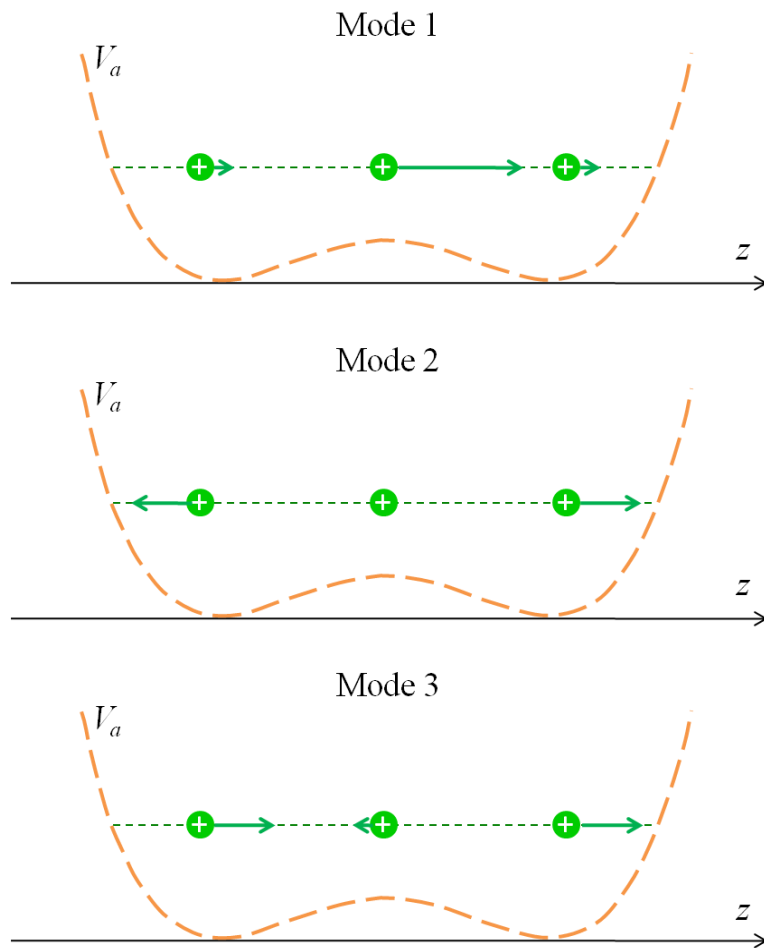


Fig. 6.6: Description of the motions of ions for three vibrational motion modes in inverted combined trapping potential with $\alpha = -100$ and $\beta = 1$. Length of the arrows indicates the vibrational motion amplitude of each ion.

becomes active and in principle can be excited. Using Eqs. (5.1.7.3) and (5.1.7.6), the transition matrix for three ions in the inverted combined potential was calculated in the normal mode coordinates. The results are shown in the Fig. 6.7. Because the second mode is always dark, we picked up only the states with $v_2 = 0$. For the first mode the $\Delta v_1 = \pm 1$ selection rule is lifted, because this mode is highly anharmonic. Thus, the transitions with $\Delta v_1 = \pm 3, \pm 5 \dots$ are allowed. Transitions between the states of the third mode are also allowed. Since Mode 3 is much less anharmonic (compared to the Mode 1), we see mostly the $\Delta v_3 = \pm 1$ transitions.

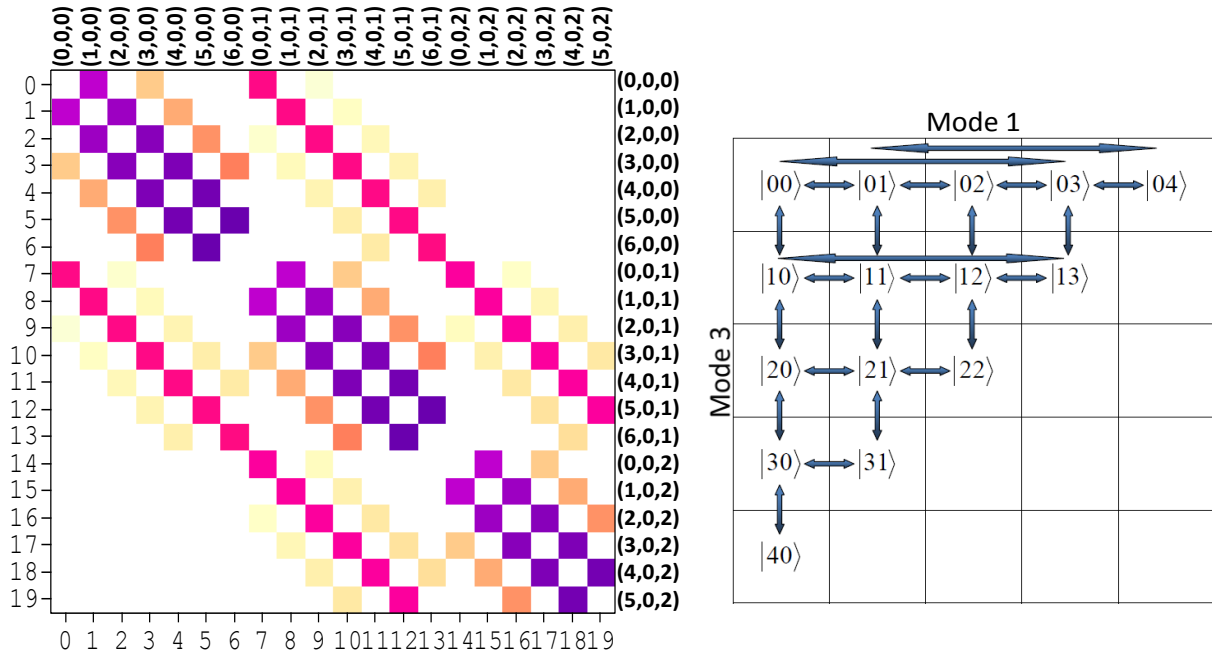


Fig. 6.7: Transition matrix of three $^{111}\text{Cd}^+$ ions in inverted combined potential trap with $\alpha = -100$ and $\beta = 1$ and the diagram of allowed state-to-state transitions in this system. Color indicates magnitudes of matrix elements in the logarithmic scale (dark purple corresponds $\mu_{4,5} = 82.77 \text{ } ea_0$ ($\sim 2.10 \times 10^2 \text{ D}$) between states of mode 1 and light pink corresponds $\mu_{0,1} = 7.90 \text{ } ea_0$ ($\sim 20.08 \text{ D}$) between states of mode 3).

6.4 Study of anharmonicity

We also studied how the anharmonicity of the three-ion system in the inverted combined potential changes as the ratio of β/α is changed. The value of α was

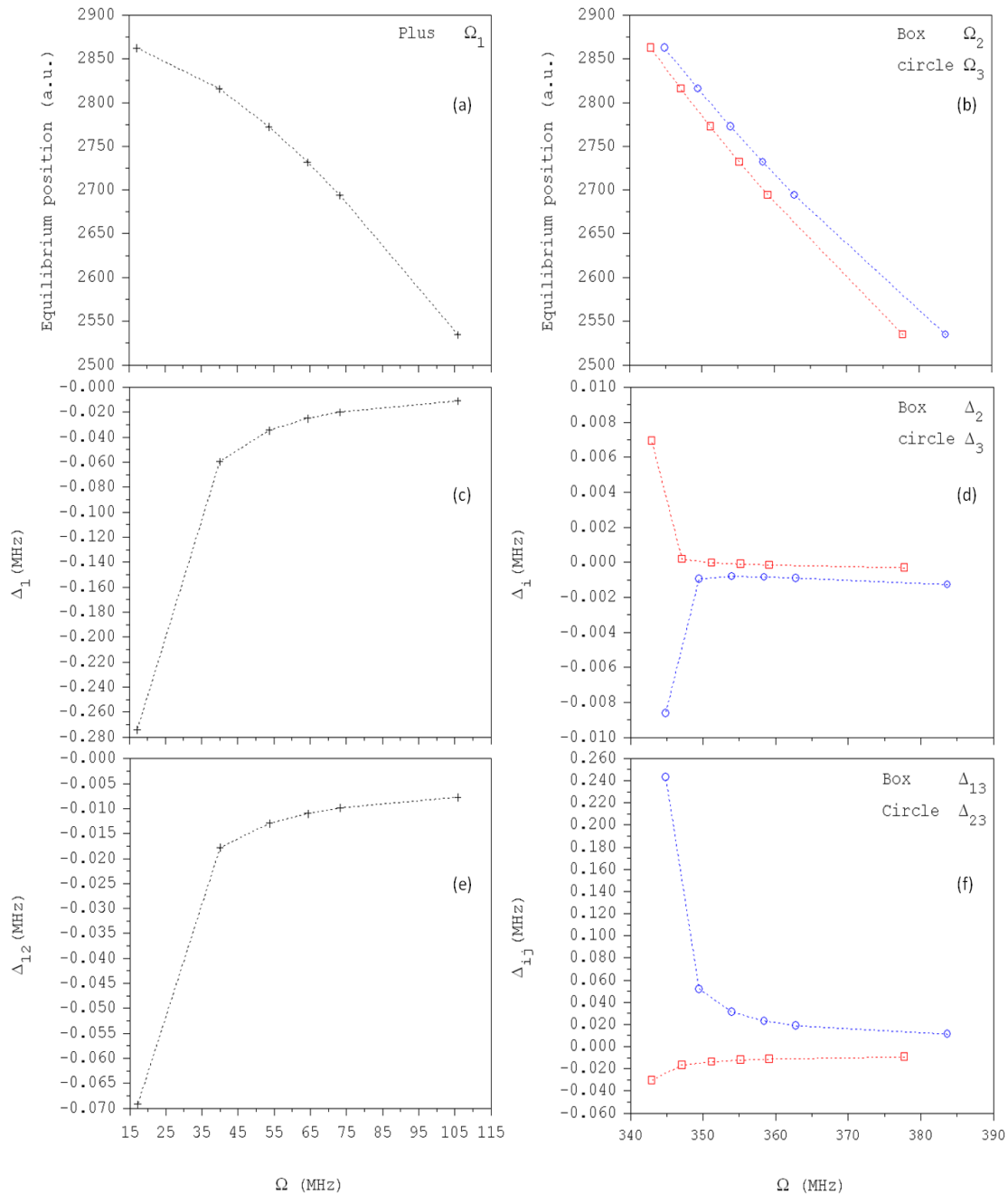


Fig. 6.8: Relations between the equilibrium distances, normal mode frequencies and vibrational anharmonicities for three $^{111}\text{Cd}^+$ ions in the inverted combined potential trap.

chosen fixed at $\alpha = -100$, while the value of β was varied. In Fig. 6.8, we show the

values of frequencies and anharmonicities of this system versus β , when $\alpha = -100$.

The following values were studied: $\beta = 1.43, 1.19, 1.14, 1.10, 1.05, 1$. Different

values of β correspond to different equilibrium positions. For example, $\beta = 1$

corresponds $z_{e3} = 2862$ Bohr and $\beta = 1.43$ corresponds $z_{e3} = 2534$ Bohr.

Variations of β reveal an important and interesting property of this system.

When β is raised (from $\beta = 1$ to $\beta = 1.43$ in Fig. 6.8) the frequencies of all modes

increase (see Fig. 6.8 (a, b)) while the values of anharmonicity parameters all drop

(see Fig. 6.8 (c-f)). This behavior is exactly opposite to that seen in the $\sim z^2$ and $\sim z^4$

traps studied above. It appears that in the case of inverted combined potential there is

no reason to raise β . When $\alpha = -100$, small values of $\beta \leq 1$ are appropriate. The

dependence of anharmonicity vs. frequency in Fig. 6.8 is quite dramatic. Note that the

case we presented here in detail ($\alpha = -100$, $\beta = 1$) is, in fact, just on the edge of the

region where anharmonicity increases very sharply. If we move further into the region

of small β or, alternatively, increase the value of α , even more anharmonic system

is obtained. For example, we tried several smaller values of β and found that for

$\beta = 0.989$ the Dunham parameters are even more attractive. The results of

frequencies and anharmonicities are shown in Table 6.3. We conclude that the low

frequency/high anharmonicity system can be readily created by the appropriate choice

Table 6. 3: Coefficients of the fit by the Dunham expansion formula, Eq. (5.1.6.3), of the numerically calculated spectrum (vibrational states in the strongly anharmonic combined inverted trap). The shift parameter was $D/2\pi = -0.331$ MHz.

Mode frequency $\Omega_i/2\pi$ ($i = 1,2,3$) (MHz)	Intramode anharmonicity $\Delta_i/2\pi$ ($i = 1,2,3$) (MHz)	Intermode anharmonicity $\Delta_{ij}/2\pi$ (MHz)
7.210×10^{-2}	-0.562	$\Delta_{12}/2\pi = -0.128$
54.425	2.372×10^{-2}	$\Delta_{13}/2\pi = -8.610 \times 10^{-2}$
54.583	-3.677×10^{-2}	$\Delta_{23}/2\pi = 0.177$

of the two force constants in the combined potential of Eq. (6.1.1).

6.5 Optimal control of three-ion system

We propose to create a purely vibrational two-qubit system by encoding the first (control) qubit into the states of less anharmonic asymmetric stretching vibration mode, while the second qubit is encoded into the states of a more anharmonic center-of-mass motion mode. The third mode of this system, symmetric stretching, appears to be dark and should not interfere. Using tools of the optimal control theory, we carry out modeling of this two-qubit system and derive RF fields for direct adiabatic control of state-to-state transitions. Pulses for the major quantum gates are obtained and

properties of the qubit transformations in this system are explored.

a) One qubit control and the gate NOT

Here we focus on the gate NOT on second qubit in the two-qubit system:

$$\text{NOT}|00\rangle \rightarrow |01\rangle, \quad (6.5.1)$$

$$\text{NOT}|01\rangle \rightarrow |00\rangle, \quad (6.5.2)$$

$$\text{NOT}|10\rangle \rightarrow |11\rangle, \quad (6.5.3)$$

$$\text{NOT}|11\rangle \rightarrow |10\rangle. \quad (6.5.4)$$

Recall that in our approach the qubits are encoded into *collective* vibration modes, not into individual ions, and the control field is applied to the entire system, not to the individual qubits. For this reason, the state of the first qubit should also be reflected in the training set of transitions, even if we are trying to optimize the pulse for controlling the second qubit only. In this sense our gates are global. First two transitions of the training set describe action of gate NOT on first qubit with the second qubit being in state $|0\rangle$. Next two transitions of the training set describe gate NOT on second qubit with the first qubit being in state $|1\rangle$. Due to anharmonicities, the frequencies of corresponding $|00\rangle \leftrightarrow |01\rangle$ and $|10\rangle \leftrightarrow |11\rangle$ transitions are slightly different.

The optimization procedure is not fully automated. The pulse duration and the maximum allowed field amplitude should be tuned “by hand”. A number of

independent computational experiments were carried out with different values of the target time in the range between 2 μs and 20 μs and different values of the penalty factor between 10^{11} and 10^{13} . The following values led to the simplest pulse shape and were finally adopted for the gate NOT on the second qubit: $T = 4 \mu\text{s}$ and $\alpha_0 = 2.0 \times 10^{12}$. A very large number of iterations, 4000 forward-backward loops, were needed in order to converge the pulse shape. The length of time-step in the wave packet propagation was on the order of 0.5 nanosecond (9000 time steps total).

The 4 μs pulse derived for the gate NOT on the second qubit is presented in Fig. 6.9. The pulse is quite symmetric and its shape is simple, the maximum field is achieved in the middle of the pulse. This shape reflects the envelope function (see Sec. 2.7) used to switch the pulse on and off smoothly. Amplitude of the electric field does not exceed 5.7 mV/cm. Such pulses should be relatively easy to produce in the experiment.

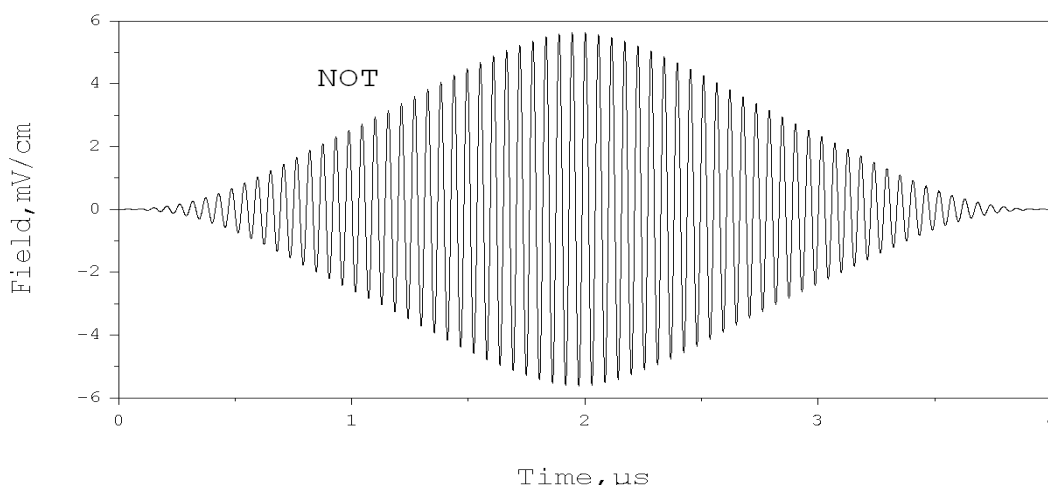


Fig. 6.9: Optimally shaped electric field of the gate NOT in the $^{111}\text{Cd}^+$ ion trap with inverted combined potential optimized with four transitions. ($\alpha_0 = 2.0 \times 10^{12}$)

Figure 6.10 shows evolution of state populations during the pulse. Four frames of this picture correspond to four optimized transitions of the training set. We see that, overall, the population transfer is quite direct, in a sense that population of the initial state(s) is monotonically transferred to the final state(s), without any reverse transfer.

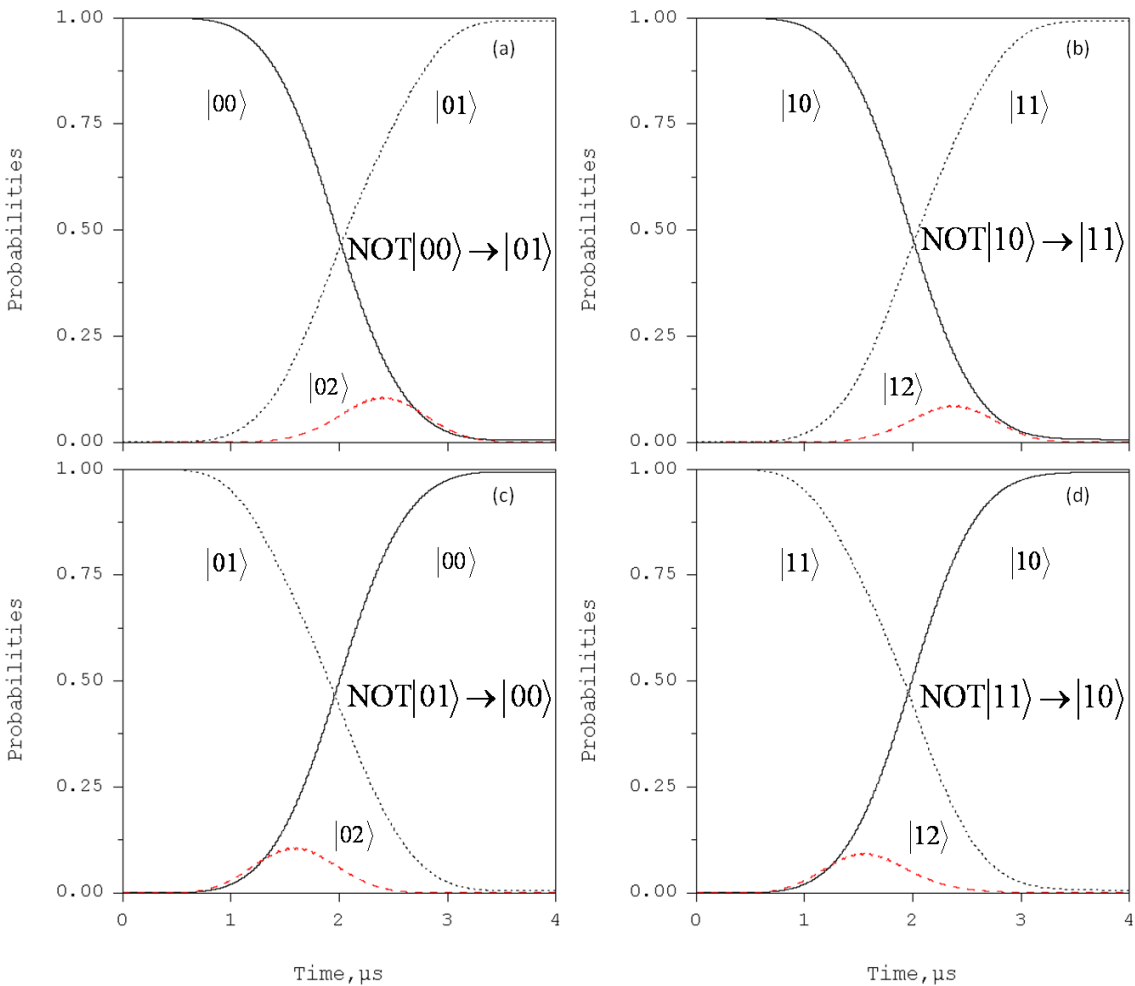


Fig. 6. 10: The gate NOT on second qubit in the $^{111}\text{Cd}^+$ ion trap with inverted combined potential. (a) Switching of population between the qubit states during the $\text{NOT}|00\rangle \rightarrow |01\rangle$. (b) Switching of population between the qubit states during the $\text{NOT}|10\rangle \rightarrow |11\rangle$. (c) The same during $\text{NOT}|01\rangle \rightarrow |00\rangle$ transformation. (d) The same during $\text{NOT}|11\rangle \rightarrow |10\rangle$ transformation.

Note, however, that the system does not behave as an isolated four-state system of two qubits. The upper states of the normal mode progressions gain some population during the pulse. Here, the states $|02\rangle$ and $|12\rangle$ are excited most significantly (populations exceeds 0.1), which can be seen in Fig. 6.10 without any magnification. However, the system is well controlled – by the end of the pulse all population is dumped into the target state(s) of two qubits. The value of cumulative transition probability, as defined in Eq. (2.7.7), reaches $P = 0.996$.

In Fig. 6.11, the Fourier analysis of the pulse in Fig. 6.9 is carried out and it is shown that the spectrum is dominated by structure in the $\omega/2\pi = 2.7$ -to- 3.2 MHz region, which corresponds to excitation of one quantum of vibration in the first qubit. The structure is asymmetric. Its most intense peak corresponds to frequency of $|0\rangle \leftrightarrow |1\rangle$ transition in the second qubit. A wing, composed of series of less intense peaks, extends into the blue part of spectrum and covers $|1\rangle \leftrightarrow |2\rangle$, $|3\rangle \leftrightarrow |4\rangle$ and $|4\rangle \leftrightarrow |5\rangle$ transitions in the second qubit, which means that this pulse is trying to control *selectively* the ladder of transitions (an anharmonic oscillator). Note that all these transitions are well resolved by the pulse – the widths of peaks in the spectrum are narrower than frequency differences. However, the transitions $|00\rangle \leftrightarrow |01\rangle$ and $|10\rangle \leftrightarrow |11\rangle$ etc., are not resolved. Frequencies of these transitions are very close to each other because anharmonicity of first qubit is very small. Widths of peaks in the

spectrum are much broader than this frequency difference, which means that the $|00\rangle \leftrightarrow |01\rangle$ and $|10\rangle \leftrightarrow |11\rangle$ transitions are controlled *together*, but not selectively. Intensity of the signal near the frequency of $|2\rangle \leftrightarrow |3\rangle$ transition is suppressed, relative to others, which explains why the population of state $|3\rangle$ remains low during the pulse. Fourier analysis shows no frequency components near 2ω for the second qubit (consistent with selection rules described in Section 6.3) and only small intensity near $3\omega/2\pi = 8.8$ MHz region, $|0\rangle \leftrightarrow |3\rangle$ transition in the second qubit, consistent with low population of state $|3\rangle$. Nothing in the spectrum corresponds to transitions between states of the first qubit.

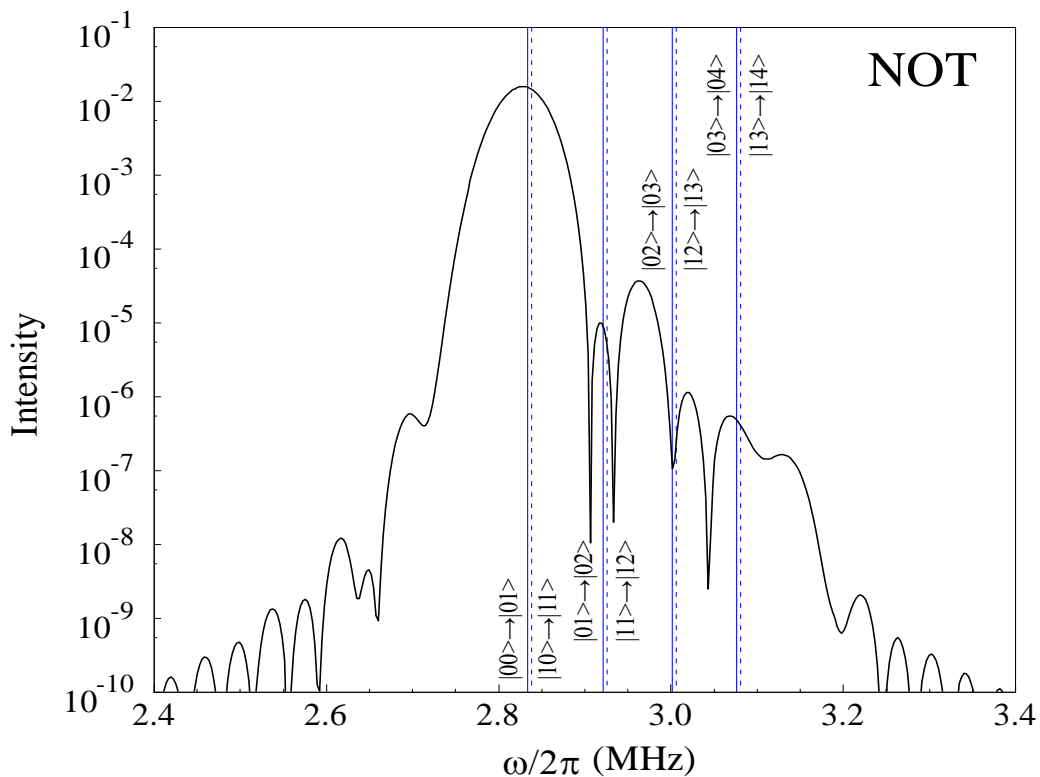


Fig. 6. 11: Fourier analysis of the pulse in Fig 6.9 for the gate NOT.

Results obtained with longer pulses ($T > 4 \mu\text{s}$) indicate that increase of the pulse duration leads to decrease of the field amplitude and decrease of population of the interfering upper states. For example, we found that during the pulse optimized with $T = 20 \mu\text{s}$ the field does not exceed 2.5 mV/cm, the populations of states $|02\rangle$ and $|12\rangle$ do not exceed 0.02, while the cumulative transition probability reaches $P = 0.9998$.

b) Two-qubit control and the Conditional NOT Gate (CNOT)

For the gate CNOT, we need to control the following four transitions:

$$\text{CNOT}|00\rangle \rightarrow |00\rangle, \quad (6.5.5)$$

$$\text{CNOT}|01\rangle \rightarrow |01\rangle, \quad (6.5.6)$$

$$\text{CNOT}|10\rangle \rightarrow |11\rangle, \quad (6.5.7)$$

$$\text{CNOT}|11\rangle \rightarrow |10\rangle. \quad (6.5.8)$$

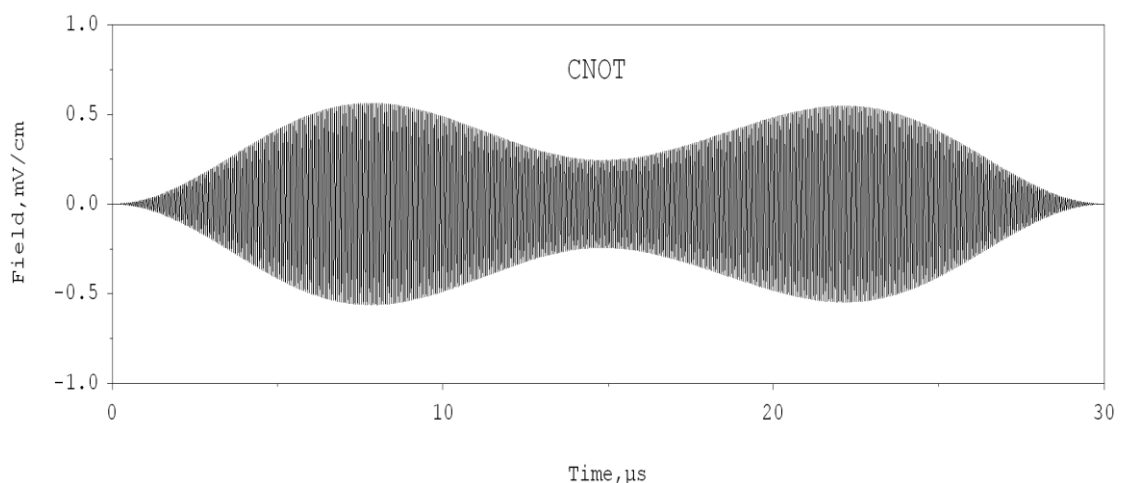


Fig. 6.12: Optimally shaped electric field of the gate CNOT for the two-qubit system in the $^{111}\text{Cd}^+$ ion trap with inverted combined potential. Large penalty factor $\alpha_0 = 6.0 \times 10^{12}$.

Here when the control (first) qubit is in state $|0\rangle$, the target (second) qubit stays

unchanged. But if the control qubit is in state $|1\rangle$, the target qubit flips.

Experimentation with pulse duration showed that CNOT gate requires much longer

pulses than NOT gate. In order to obtain accurate CNOT gate, we had to

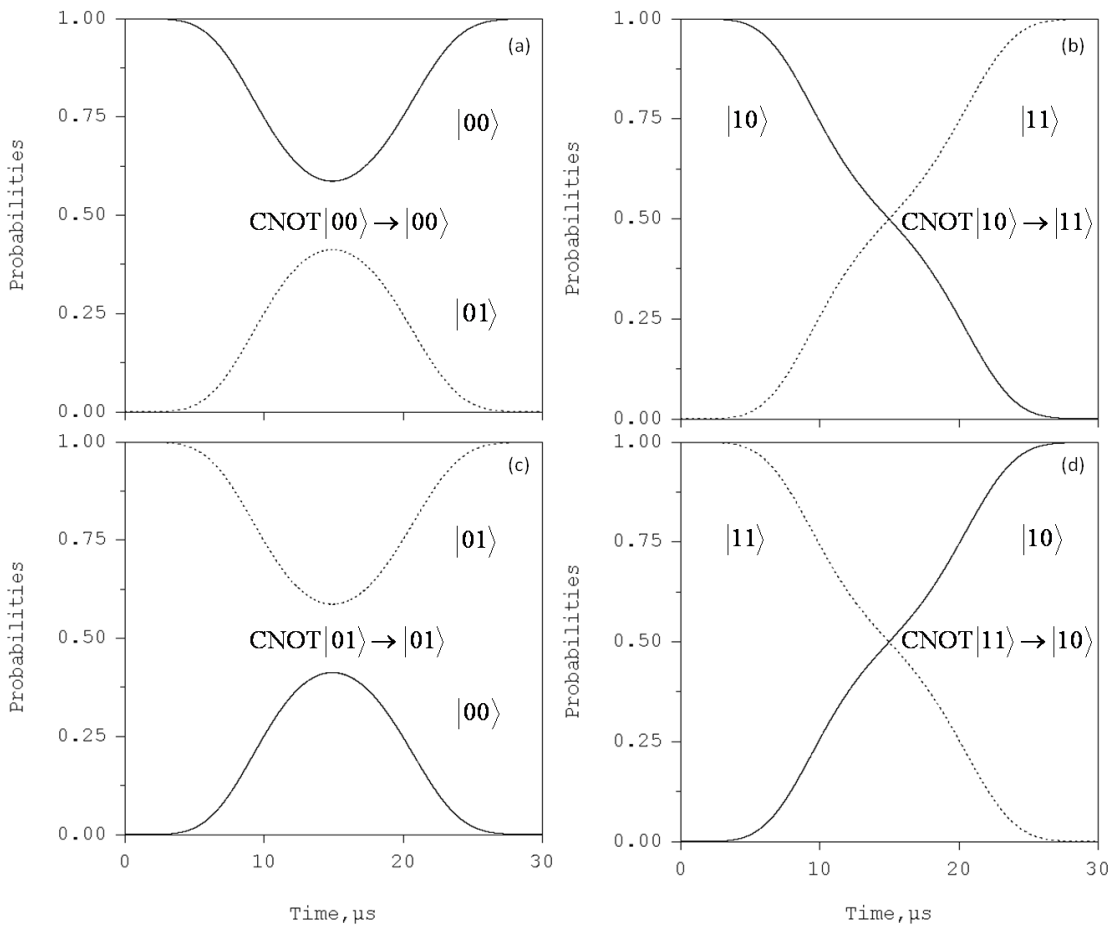


Fig. 6.13: The gate CNOT for the two-qubit control in the $^{111}\text{Cd}^+$ ion trap optimized with four transitions. Large penalty factor $\alpha_0 = 6.0 \times 10^{12}$. (a) Switching of population between the qubit states during the $\text{CNOT}|00\rangle \rightarrow |00\rangle$. (b) Switching of population between the qubit states during the $\text{CNOT}|10\rangle \rightarrow |11\rangle$. (c) The same during

between the qubit states during the $\text{CNOT}|01\rangle \rightarrow |01\rangle$ transformation. (d) The same during $\text{CNOT}|11\rangle \rightarrow |10\rangle$ transformation.

increase the pulse duration to $T = 30 \mu\text{s}$. The number of time steps for wave packet propagation was increased to 18,000. Variation of the penalty factor revealed an interesting feature. This feature is demonstrated below using results for two pulses, one with $\alpha = 6.0 \times 10^{12}$ and second with $\alpha_0 = 8.0 \times 10^{11}$.

The pulse optimized with larger penalty factor, $\alpha_0 = 6.0 \times 10^{12}$, is shown in Fig. 6.12. This pulse is simply shaped, symmetric, and consists of two time-delayed sub-pulses. The maximum field amplitude of about 0.6 mV/cm is achieved at approximately $t = 7.5$ and $22.5 \mu\text{s}$. The state-to-state transitions driven by this pulse are shown in Fig. 6.13. Four frames correspond to four optimized transitions of the training set. When the control qubit is in state $|1\rangle$ the population transfer is monotonic

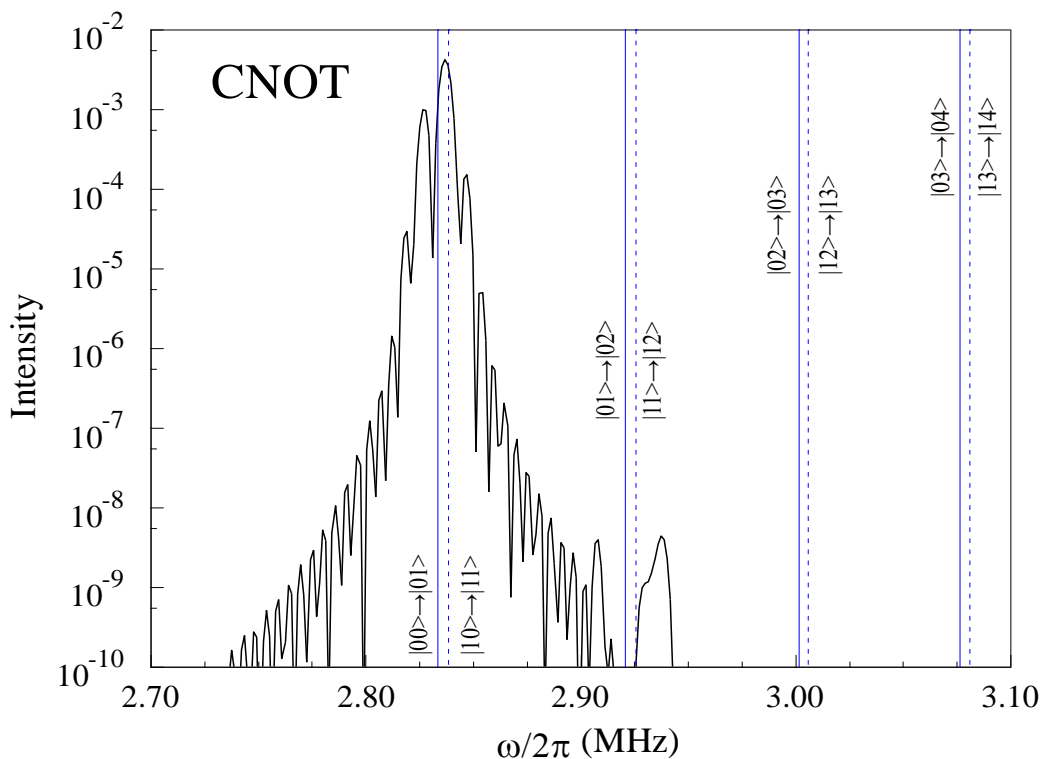


Fig. 6. 14: Fourier analysis of the pulse in Fig 6.12 for the gate CNOT.

and is very much direct, see Figs. 6.13 (b) and (d). Only two states of the system are involved and those are states $|10\rangle$ and $|11\rangle$ of the qubit. Transitions to any upper states of the system are suppressed. When the control qubit is in state $|0\rangle$ the population transfer is not monotonic: The first sub-pulse creates a superposition state of $|00\rangle$ and $|01\rangle$, while the second sub-pulse returns population back to the initial state(s), as required by this gate, see Figs. 6.13 (a) and (c). Cumulative accuracy of the qubit transformation is very high, $P \sim 0.9995$. Fourier analysis of the optimized pulse in Fig. 6.14 shows that the $|10\rangle \leftrightarrow |11\rangle$ transition is induced, while the frequency of the $|00\rangle \leftrightarrow |01\rangle$ transition is somewhat reduced. This is different from the unconditional gate NOT. The frequencies of all other transitions are completely suppressed. Even the frequency of $|1\rangle \leftrightarrow |2\rangle$ transition in the second qubit is entirely suppressed, which explains why population is restricted to only states $|0\rangle$ and $|1\rangle$ of

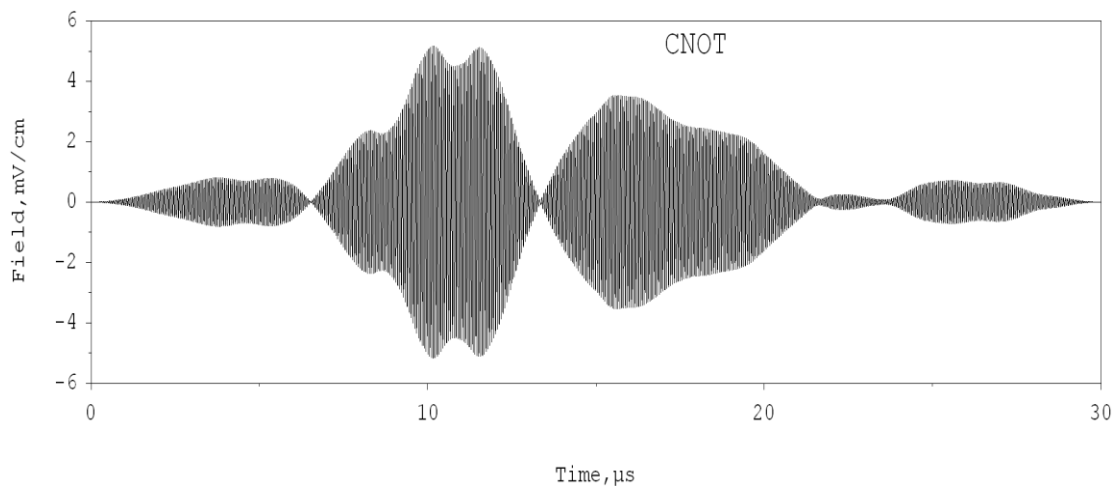


Fig. 6. 15: Optimally shaped electric field of the gate CNOT for the two-qubit control in the $^{111}\text{Cd}^+$ ion trap with inverted combined potential. Small penalty factor $\alpha_0 = 8.0 \times 10^{11}$.

the second qubit.

The fact that transitions to the upper states of the system can be suppressed and population is restricted to only four states of the 2×2 qubit space is very interesting. We believe that such high selectivity is made possible by the relatively

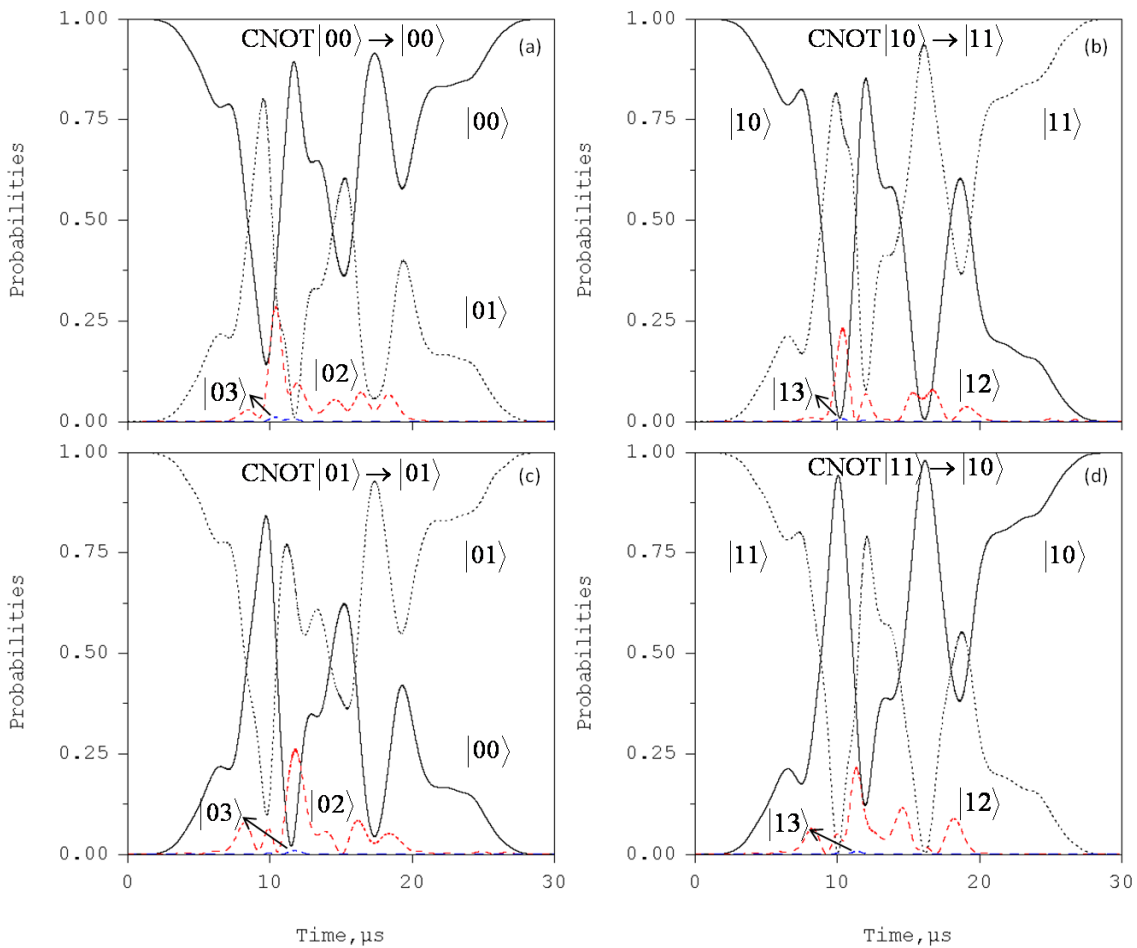


Fig. 6.16: The gate CNOT for the two-qubit control in the $^{111}\text{Cd}^+$ ion trap optimized with four transitions. Small penalty factor $\alpha_0 = 8.0 \times 10^{11}$. (a) Switching of population between the qubit states during the CNOT $|00\rangle \rightarrow |00\rangle$. (b) Switching of population between the qubit states during the CNOT $|10\rangle \rightarrow |11\rangle$. (c) The same during CNOT $|01\rangle \rightarrow |01\rangle$ transformation. (d) The same during CNOT $|11\rangle \rightarrow |10\rangle$ transformation.

low amplitude of field of the pulse in Fig. 6.12, leading to very delicate control of vibrational excitations.

In order to support this hypothesis we present results for another pulse, optimized with lower penalty factor $\alpha_0 = 8.0 \times 10^{11}$. In general, lowering the penalty factor allows raising amplitude of the field during the optimization procedure. The optimized pulse shape for this case is presented in Fig. 6.15. The maximum field amplitude of this pulse is roughly 5.1 mV/cm, about an order of magnitude higher compared to the previous case. The pulse shape is much more complicated, asymmetric, containing multiple sub-pulses of different amplitudes. This shape reflects complicated evolution of state populations presented in Fig. 6.16. During the

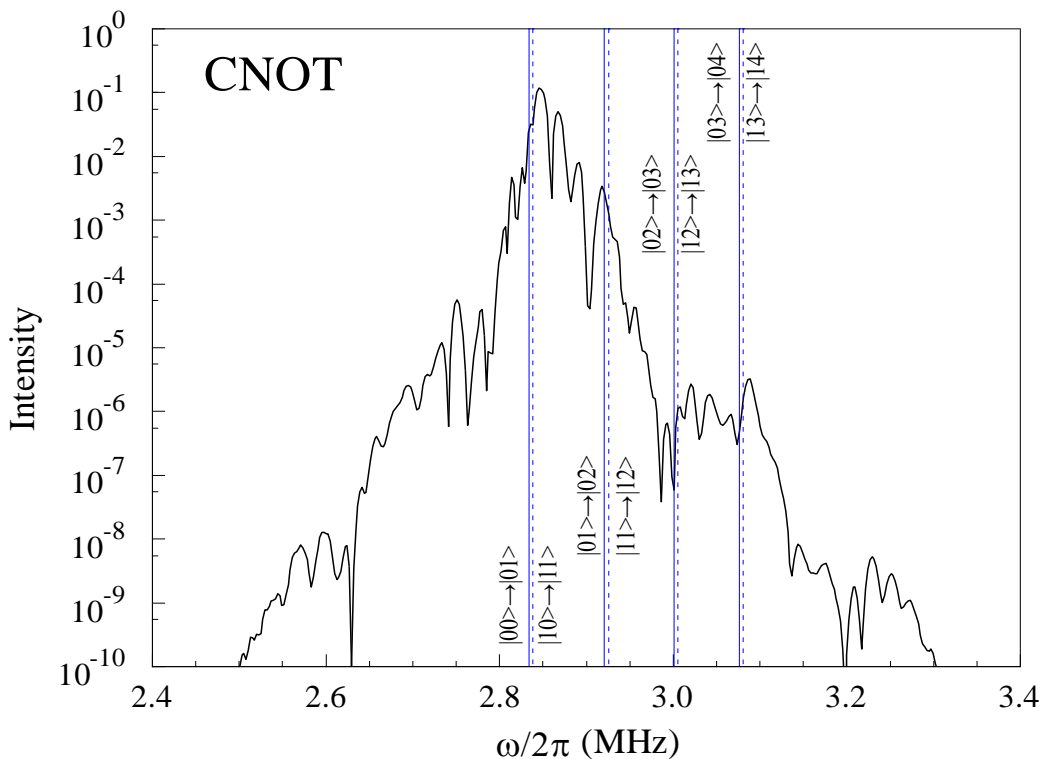


Fig. 6. 17: Fourier analysis of the pulse in Fig 6.15 for the gate CNOT.

pulse, the populations are exchanged back and forth between the initial and the final states of the qubit, and are also transferred to the excited states of the system, $|02\rangle$ and $|12\rangle$. Despite complicated evolution during the pulse, at time $t = T$ the population is directed towards the target states, leading to high accuracy of qubit transformation, $P \sim 0.9996$. Fourier analysis of this optimized pulse in Fig. 6.17 shows a spectral structure that covers $|0\rangle \leftrightarrow |1\rangle$, $|1\rangle \leftrightarrow |2\rangle$ and $|3\rangle \leftrightarrow |4\rangle$ transitions in the second qubit, which clearly corresponds to control of the ladder. The frequency of $|2\rangle \leftrightarrow |3\rangle$ transition in the second qubit is, again, somewhat suppressed.

Two examples of CNOT gate presented above suggest that a careful choice of constraints on the control field, such as pulse duration and field amplitude, may be necessary in order to obtain the control pulses of desirable accuracy and simplicity.

c) Phase control and the Hadamard Gate

For the Hadamard gate, to achieve the phase control, we need to optimize five transitions at the same time and the training set of transitions for the Hadamard transformation of the second qubit is:

$$\text{HAD}|00\rangle \rightarrow \frac{1}{\sqrt{2}}(|00\rangle + |01\rangle)e^{i\varphi_1}, \quad (6.5.9)$$

$$\text{HAD}|01\rangle \rightarrow \frac{1}{\sqrt{2}}(|00\rangle - |01\rangle)e^{i\varphi_2}, \quad (6.5.10)$$

$$\text{HAD}|10\rangle \rightarrow \frac{1}{\sqrt{2}}(|10\rangle + |11\rangle)e^{i\varphi_3}, \quad (6.5.11)$$

$$\text{HAD}|\psi\rangle \rightarrow \frac{1}{\sqrt{2}}(|10\rangle - |11\rangle)e^{i\varphi_4}, \quad (6.5.12)$$

$$\text{HAD} \frac{1}{2}(|00\rangle + |01\rangle + |10\rangle + |11\rangle) \rightarrow \frac{1}{\sqrt{2}}(|00\rangle + |10\rangle)e^{i\varphi_5}, \quad (6.5.13)$$

The fifth transition here is the sum of the first four transitions and is included in order to achieve control over phases, which is essential for this gate: $\varphi_1 = \varphi_2 = \varphi_3 = \varphi_4$. Note that the cumulative probability of Eq. (2.7.7) neglects phases of transitions, since moduli squared of overlaps are used. However, the accuracy of gates like Hadamard should be measured by a phase-sensitive moiety, like the fidelity F defined on page 57 and 58 [35, 37]. One solution is to replace P by F in the functional of Eq. (2.7.6) and re-derive the equations [35, 37], but this approach was not followed here. A simpler fix to the standard procedure is to include, in addition to four transitions of the training set, one more transition that represents sum of the previous four [85, 92]. In order to ensure that the phase is indeed controlled, the fidelity rather

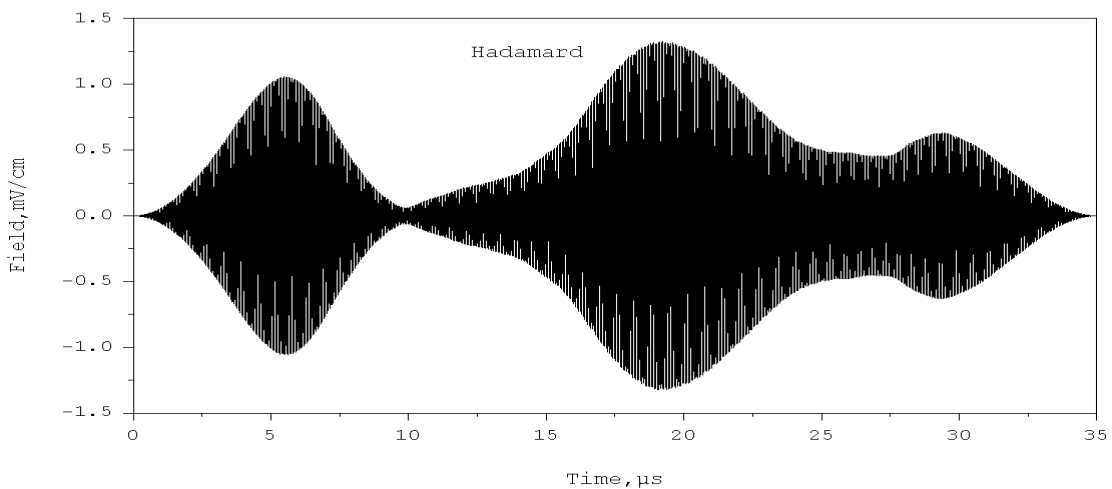


Fig. 6. 18: Optimally shaped electric field of the gate Hadamard on the second qubit in the $^{111}\text{Cd}^+$ ion trap with inverted combined potential optimized with five transitions. ($\alpha_0 = 1.0 \times 10^{12}$)

than probability of Eq. (2.7.7), should be monitored as convergence criterion.

Different values of pulse duration and penalty factor were tried and the following parameters were finally adopted: $\alpha_0 = 1.0 \times 10^{12}$ and $T = 35 \mu\text{s}$. The number of time steps was also adjusted to 55,000.

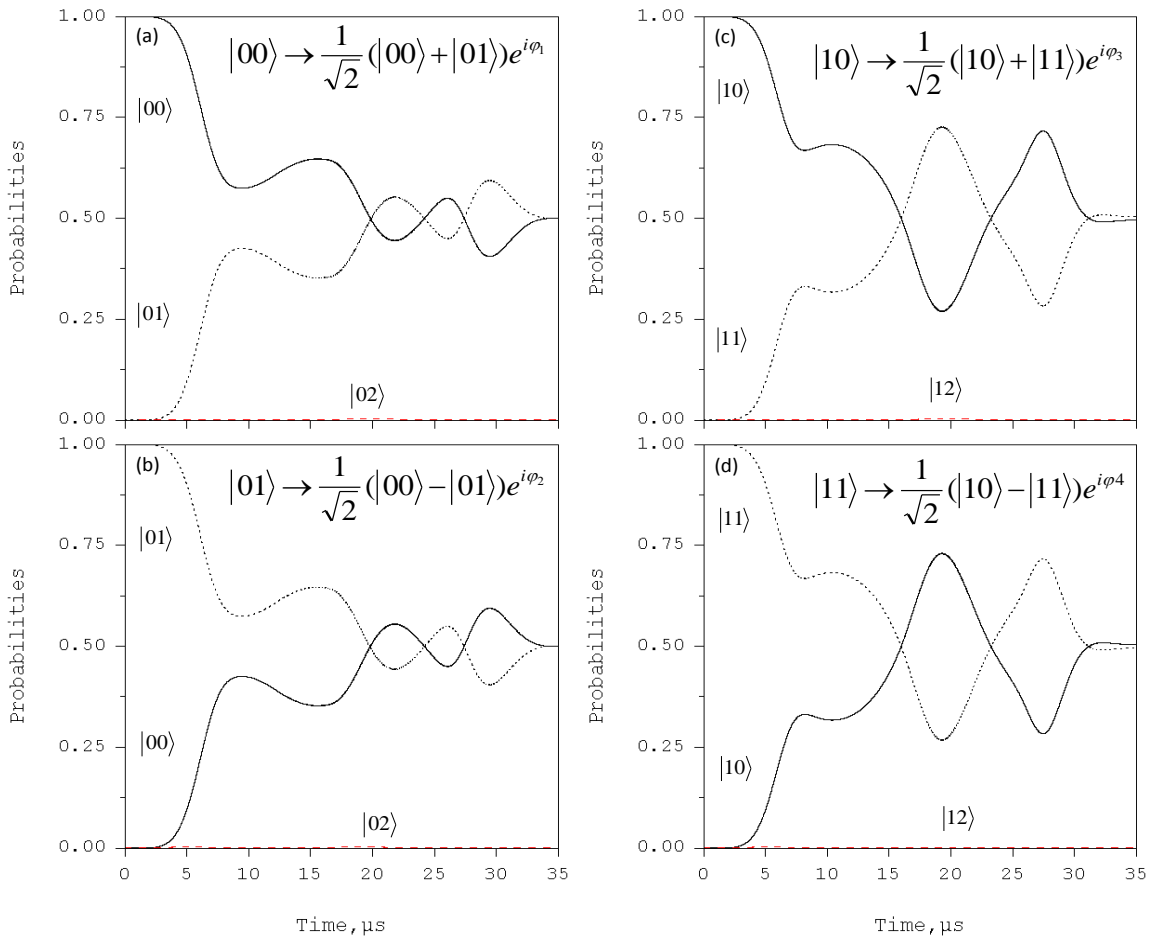


Fig. 6.19: The gate Hadamard on the second qubit in the $^{111}\text{Cd}^+$ ion trap optimized with five transitions. (a) Switching of population between the qubit states during the HAD $|00\rangle \rightarrow \frac{1}{\sqrt{2}}(|00\rangle + |01\rangle)e^{i\varphi_1}$. (b) Switching of population between the qubit states during the HAD $|01\rangle \rightarrow \frac{1}{\sqrt{2}}(|00\rangle - |01\rangle)e^{i\varphi_2}$. (c) The same during HAD $|10\rangle \rightarrow \frac{1}{\sqrt{2}}(|10\rangle + |11\rangle)e^{i\varphi_3}$ transformation. (d) The same during HAD $|11\rangle \rightarrow \frac{1}{\sqrt{2}}(|10\rangle - |11\rangle)e^{i\varphi_4}$ transformation.

The optimized pulse is presented in Fig. 6.18. The pulse is asymmetric and consists of three sub-pulses of slightly different amplitudes. Maximum amplitude of the field is about 1.3 mV/cm. Roles of these sub-pulses are revealed by analysis of state populations presented in Fig. 6.19. The first sub-pulse achieves a significant transfer of populations, creating a superposition state with probabilities close to the needed 50/50, while the second sub-pulse manipulates phases of the optimized transitions

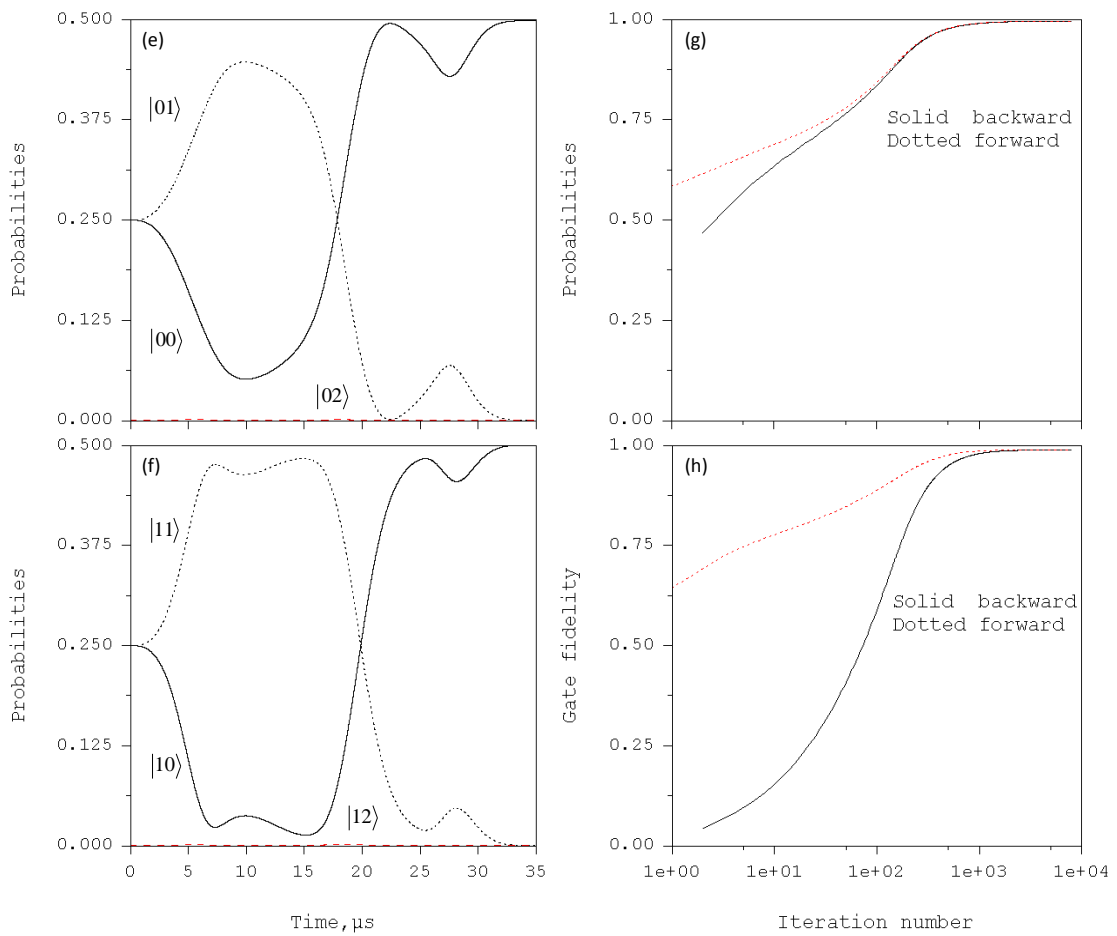


Fig. 6. 20: The gate Hadamard on the second qubit in the $^{111}\text{Cd}^+$ ion trap. Frames (e) and (f): Switching of population of states $|00\rangle$ and $|01\rangle$ during the

$$\text{HAD} \frac{1}{2} (|00\rangle + |01\rangle + |10\rangle + |11\rangle) \rightarrow \frac{1}{\sqrt{2}} (|00\rangle + |10\rangle) e^{i\varphi_5}$$

probability. (g) Gate fidelity as functions of number of iterations.

(with only minor population transfer). Third sub-pulse finalizes the entire transformation by minor transfer of remaining populations and fine phase correction. Analysis of phase angle of the optimized transitions supports this conclusion: During the first sub-pulse phases are not controlled at all. Second sub-pulse reduces phase differences monotonically to only $\sim 30\text{-}50^\circ$. Third sub-pulse reduces phase differences to less than 4° at the end of the pulse.

Fourier analysis of the optimized pulse shows two spectral structures. First structure in Fig 6.21 is in the $\omega/2\pi = 2.7\text{-}3.0$ MHz region (excitation of one quantum in the second qubit). Here the $|0\rangle \leftrightarrow |1\rangle$ transition is clearly dominant, while

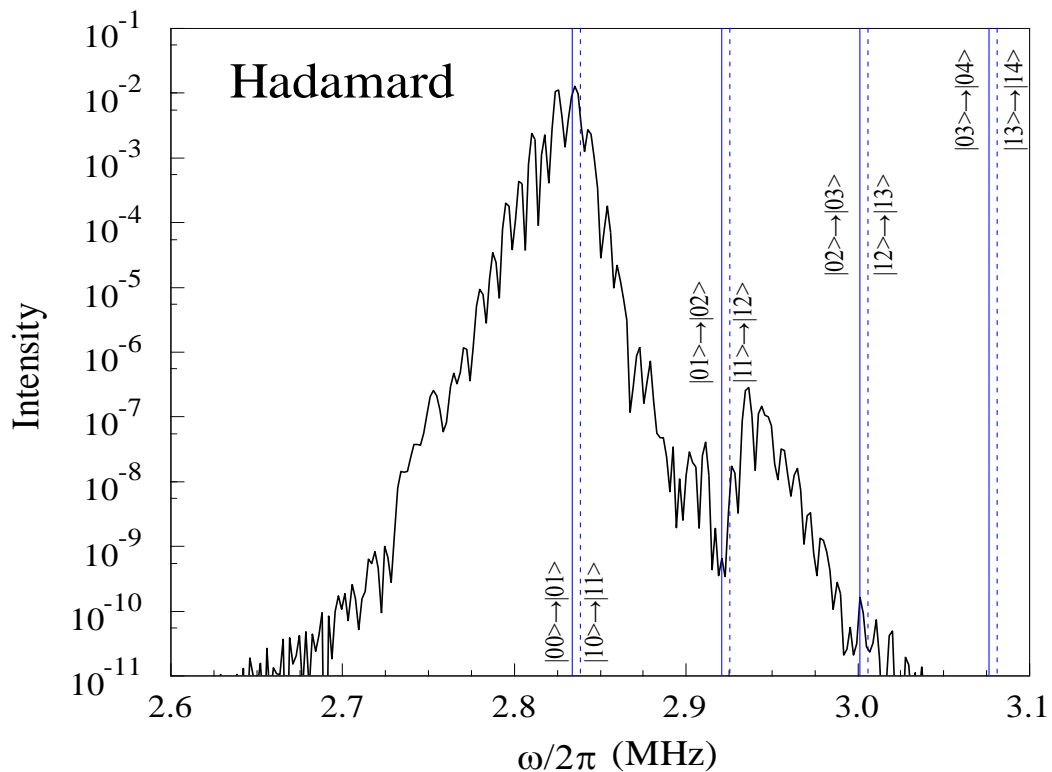


Fig. 6. 21: Fourier analysis of the pulse in Fig 6.18 for the gate Hadamard (lower frequency part).

the $|1\rangle \leftrightarrow |2\rangle$ transition is significantly suppressed, consistent with low population of states $|02\rangle$ and $|12\rangle$ in Fig. 6.19. The second spectral structure in Fig. 6.22 is in the $\omega/2\pi = 54.8$ -to- 54.9 MHz region, which corresponds to excitation of one quantum of the first qubit. Transitions between $|0\rangle \leftrightarrow |1\rangle$, $|1\rangle \leftrightarrow |2\rangle$, $|3\rangle \leftrightarrow |4\rangle$ and $|4\rangle \leftrightarrow |5\rangle$ states of the first qubit are covered by the blue-side wing of this spectral structure. We tend to state that these transitions are *partially* resolved because they all have different intensities, due to slope of the wing and some minor oscillations of intensity.

Note that frequency components that control first qubit have not been observed in the optimized NOT and CNOT pulses discussed above. We found that

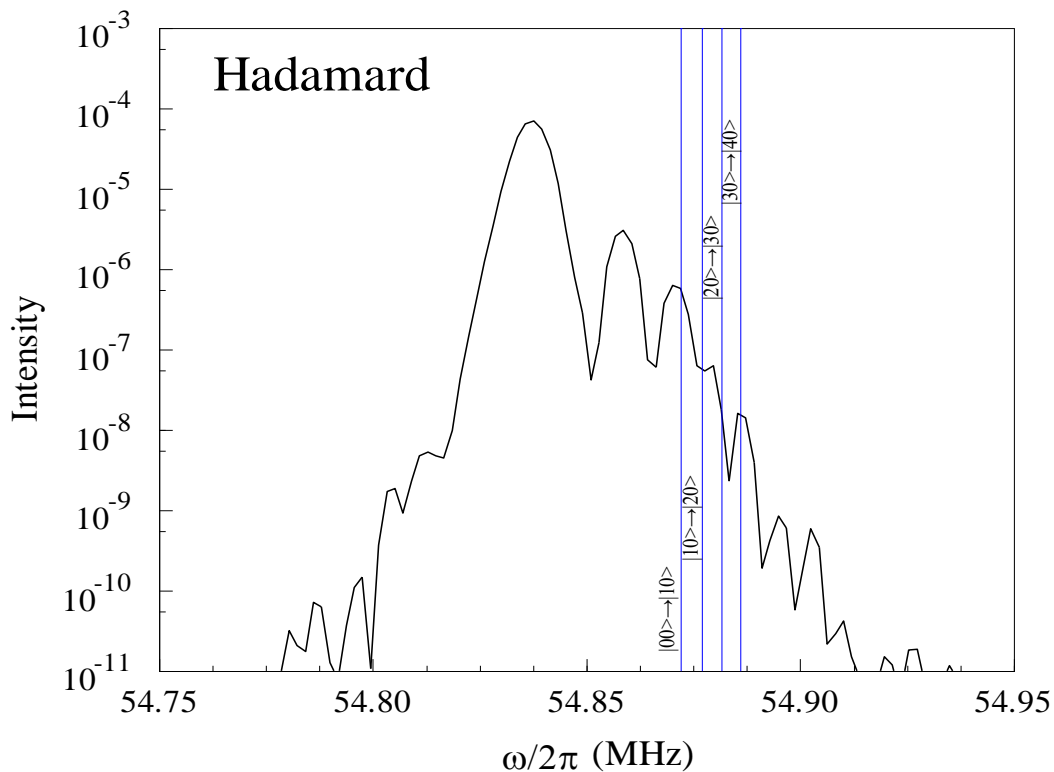


Fig. 6. 22: Fourier analysis of the pulse in Fig 6.18 for the gate Hadamard (higher frequency part).

these frequencies appear only when we include fifth transition into the training set (e.g., Eq. (6.5.13)) in order to control phases of the optimized transitions. The pulses optimized for such truly coherent manipulations of the qubit states always contain frequency components for control of both qubits of the two-qubit system.

In Fig. 6.20 we can see that average probability P converges much faster than the fidelity F . After about one hundred iterations, probability in the backward and forward propagations already converge, while it takes almost one thousand iterations for the convergence of the fidelity. This is evidence that controlling the phase is more difficult than controlling only the state populations. The cumulative transition probability for this Hadamard gate is $P \sim 0.998$. Its fidelity is slightly lower, $F \sim 0.990$, due to small residual difference of phases ($\sim 4^\circ$).

6.6 Conclusions

In this chapter we carried out the first optimal control study of a system of multiple ions in an anharmonic linear trap. The method of encoding qubits into the quantized collective motional/vibrational states of the linear ion-string was proposed and explored computationally. The time-varying microwave fields were used to achieve adiabatic control over these states.

Although all ions are identical, the vibration modes of the ion-string are different and the qubits, encoded into these modes, are also different. Numerical

analysis of frequencies and anharmonicities of the vibration modes was used to identify modes most suitable for encoding qubits. It was shown that in a strongly anharmonic trap, obtained by combining a repulsive quadratic with an attractive quartic potentials, the center-of-mass motion mode is the most anharmonic. It is most suitable for encoding states of the target qubit. The control qubit can be encoded into a less anharmonic asymmetric stretching mode. The symmetric stretching mode remains dark.

Optimal control theory was used to derive pulses for a set of universal quantum gates. It was shown that if parameters of the pulse, such as pulse duration and maximum field amplitude, are carefully chosen the qubit transformations (gates) are accurate and the pulses are simple. Durations of the pulses obtained were in the 4 μ s to 40 μ s range. Amplitudes of the control fields were on the order of few mV/cm.

Only one set of parameters for the shape of the trap was considered in this paper. It seems feasible, however, to further increase anharmonicity of the vibrational spectrum of the system by changing parameters of the trapping potential. Higher anharmonicities, in turn, should simplify the control and allow deriving more accurate and shorter gate pulses. Exploring a system of more than three ions offers more opportunities. There may be more than one anharmonic mode that can be efficiently controlled and used for encoding qubits.

Chapter 7: Future research directions

In this dissertation, we studied two scaling methods for the adiabatic optimal control scheme and its applications in quantum computation. First method of scaling is to use more than one excited vibrational state (Chapter 3). But only if the anharmonicity is large enough, we may be able to access and control multiple excited vibrational states: $|0\rangle, |1\rangle, |2\rangle, |3\rangle, \dots$. It would be interesting to repeat such optimization calculations for an even more anharmonic system with more than 16 states. For example, the 6-qubit system requires 2^6 states. Can we control such a system? It seems that the limit in this approach is due to complexity of the pulse. Thus, incorporation of the experimental constraints onto the pulse optimization instrumentation is desirable.

Note that the quantum circuit diagram shown in Fig. 3.3 represents a standard implementation of Shor's algorithm, in which it is assumed from the beginning that registers of information are represented by qubits – the physically distinct two-state quantum objects. In our physical system (vibrational states of trapped ion) the two-state qubits do not really exist. Physically, we operate with information registers of arbitrary length: q-words rather than q-bits. It would be very interesting to employ a better use of q-words, than simply splitting them onto a number of two-state qubits. There may be a better way of formulating Shor's algorithm using the language of q-

words. In particular, the inconveniences brought by the near-diagonal structure of the dipole-moment matrix could be minimized which, hopefully, could lead to simpler shaped and more accurate pulses. This interesting opportunity will be explored in the future.

The second method of scaling is to employ more than one ion. In Chapter 6, we presented an architecture for the two-qubit system based on a linear chain of three trapped ions in the inverted combined trap. If we want to control more than two qubits, four or more ions should be trapped and different qubits should be encoded into different normal vibration modes of the system. Bad news is that the symmetric stretching modes will always be dark (using the spatially homogeneous control field), but there will be more than one asymmetric stretching mode in the four-ion case. Also, the system of four trapped ions is totally different from the three-ion system. For three ions in the inverted combined trapping potential, the central ion sits on top of the hill

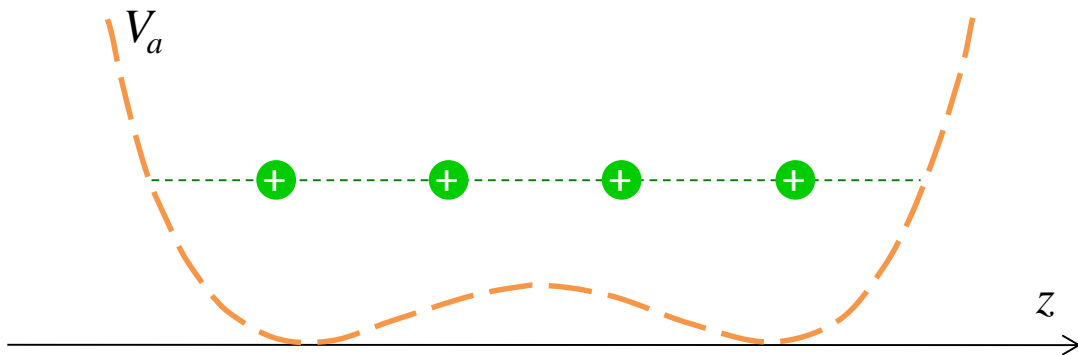


Fig. 7. 1: A four-ion string trapped in a flat anharmonic potential of the form

$$\alpha \frac{1}{2} k z^2 + \beta \frac{1}{4!} k' z^4 .$$

(see Fig. 6.2). In the four-ion system: four ions sit over two wells symmetrically (see Fig. 7.1). One can expect that this system carries more anharmonicity, because no ions are located near the hill, where the PES is flat. Thus, it would be very interesting to study the four-ion system in the inverted combined potential in the future.

Note that the symmetric stretching mode is dark only in the case when a spatially homogeneous field is used, as assumed in this work. Creating a quadrupole potential would allow controlling the symmetric stretching mode too. This opportunity will be studied theoretically and computationally in the future work.

We have done some preliminary investigation related to trapping molecular ions, such as H_3O^+ . In this case we could encode the quantum information into the motional energy levels like in this dissertation, but also into the inversion-rotation energy levels of each ion. It was found that the frequency of transitions between the inversions-rotation energy levels is four orders of magnitude higher than the frequency of transitions between the motional modes. It may be not straightforward to implement transitions within these two kinds of energy levels with single control pulse. But two or more consequent pulses may work, which gives us another interesting possibility for the future research.

BIBLIOGRAPHY

- [1] Feynman, R, *Int. J. Theor. Phys.* **1982**, 21, 467-488.
- [2] Johnson, G, *A Shortcut Through Time : The Path to the Quantum Computer.* **2003**.
- [3] Holzscheiter, M. H. *Los Alamos Science,* **2002**, 27, 264-283.
- [4] Cirac, J. I.; Zoller, P., *Phys. Rev. Lett.* **1995**, 74, 4091-4094.
- [5] Peirce, A. P.; Dahleh, M.A.; Rabitz, H, *Phys. Rev. A.* **1988**, 37, 4950-4964.
- [6] Judson, R. S.; Rabitz, H., *Phys. Rev. Lett.* **1992**, 98, 1500-1503.
- [7] Warren, W. S.; Rabitz, H. S.; Dahleh, M., *Science,* **1993**, 1581-1589.
- [8] Zhu, W.; Botina, J.; Rabitz, H., *J. Chem. Phys.* **1998**, 108, 1953-1963.
- [9] Ren, Q.; Balint-Kurti, G. G.; Manby, F. R.; Artamonov, M.; Ho, T. S.; Rabitz, H., *J. Chem. Phys.* **2006**, 125, 021104.
- [10] Rabitz, H; Turinici, G., *Phys. Rev. A.* **2007**, 75, 043409.
- [11] Toth, G. J.; Lorincz, A.; Rabitz, H., *J. Chem. Phys.* **1994**, 101, 3715-3722.
- [12] Cheng, T.; Brown, A., *J. Chem. Phys.* **2006**, 124, 144109.
- [13] Lozovoy, V. V.; Dantus, M., *ChemPhysChem.* **2005**, 6, 1970-2000.
- [14] Dela Cruz, J. M.; Lozovoy, V. V.; Dantus, M., *J. Phys. Chem. A.* **2005**, 109, 8447-8450.
- [15] Lozovoy, V. V.; Gunaratne, T. C.; Shane, J. C.; Dantus, M., *ChemPhysChem.* **2006**, 7, 2471-2473.
- [16] Lozovoy, V. V.; Xu, B. W.; T. C.; Shane, J. C.; Dantus, M., *Phys. Rev. A.* **2006**, 74, 041805.
- [17] Monroe, C.; Meedhof, D. M.; King, B. E.; Itano, W. M.; Wineland, D. J., *Phys. Rev. Lett.* **1995**, 75, 4714-4718.

- [18] Meekhoff, D. M.; Monroe, C.; King, B. E.; Itano, W. M.; Wineland, D. J., *Phys. Rev. Lett.* **1996**, *76*, 1796-1799.
- [19] Sackett, C. A.; Kielpinski, D.; King, B. E.; Langer, C.; Meyer, V.; Myatt, C. J.; Rowe, M.; Turchette, Q. A.; Itano, W. M.; Wineland, D. J.; Monroe, C., *Nature*. **2000**, *404*, 256-259.
- [20] Garcia-Ripoll, J. J.; Zoller, P.; Cirac, J. I., *Phys. Rev. Lett.* **2003**, *91*, 157901.
- [21] Schmidt-Kaler, F.; Haeffner, H.; Riebe, M.; Gulde, S.; Lancaster, G. P. T.; Deuschle, T.; Becher, C.; Roos, C. F.; Eschner, J.; Blatt, R., *Nature*. **2003**, *422*, 408-411.
- [22] Haeffner, H.; Haensel, W.; Roos, C. F.; Benhelm, J.; Chek-al-kar, D.; Chwalla, M.; Korber, T.; Rapol, U. D.; Riebe, M.; Schmidt, P. O.; Becher, C.; Guhne, O.; Dur, W.; Blatt, R., *Nature*. **2005**, *438*, 643-646.
- [23] Leibfried, D.; Knill, E.; Seidelin, S.; Britton, J.; Blakestad, R. B.; Chiaverini, J.; Hume, D. B.; Itano, W. M.; Jost, J. D.; Langer, C.; Ozeri, R.; Reichle, R.; Wineland, D. J., *Nature*. **2005**, *438*, 639-642.
- [24] Schmidt-Kaler, F.; Häffner, H.; Gulde, S.; Riebe, M.; Lancaster, G.P.T.; Deuschle, T.; Becher, C.; Hänsel, W.; Eschner, J.; Roos, C. F.; Blatt, R., *Appl. Phys. B*. **2003**, *77*, 789-796.
- [25] Bushev, P.; Rotter, D.; Wilson, A.; Dubin, F.; Becher, C.; Eschner, J.; Blatt, R.; Steixner, V.; Rabl, P.; Zoller, P., *Phys. Rev. Lett.* **2006**, *96*, 043003.
- [26] Monroe, C.; Wineland, D., *Scientific American*. **2008**, 64-71.
- [27] Leibfried, D.; Blatt, R.; Monroe, C.; Wineland, D., *Rev. Mod. Phys.* **2003**, *75*, 281-324.
- [28] Blatt, R.; Wineland, D., *Nature*. **2008**, *453*, 1008-1015.
- [29] Kim, K.; Chang, M. S.; Islam, R.; Korenblit, S.; Duan, L. M.; Monroe, C., *Phys. Rev. Lett.* **2009**, *103*, 120502.
- [30] Kim, K.; Chang, M. S.; Korenblit, S.; Islam, R.; Edwards, E. E.; Freericks, J. K.; Lin, G. D.; Duan, L. M.; Monroe, C., *Nature*. **2010**, *465*, 590-593.

- [31] Duan, L. M.; Monroe, C., *Rev. Mod. Phys.* **2010**, 82, 1209-1224.
- [32] Lin, G. D.; Zhu, S. L.; Islam, R.; Kim, K.; Chang, M. S.; Korenblit, S.; Monroe, C.; Duan, L. M.; *Europhysics Lett.* **2009**, 86, 60004.
- [33] Weidinger, D.; Gruebele, M., *Mol. Phys.* **2007**, 105, 1999-2008.
- [34] Weidinger, D.; Gruebele, M., *Chem. Phys.* **2008**, 350, 139-144.
- [35] Palao, J. P.; Kosloff, R., *Phys. Rev. Lett.* **2002**, 89, 188301.
- [36] Vala, J.; Amitay, Z.; Zhang, B.; Leone, S. R.; Kosloff, R., *Phys. Rev. A.* **2002**, 66, 062316.
- [37] Palao, J. P.; Kosloff, R., *Phys. Rev. A.* **2003**, 68, 062308.
- [38] Menzel-Jones, C.; Shapiro, M., *Phys. Rev. A.* **2007**, 75, 052308.
- [39] Suzuki, S.; Mishima, K.; Yamashita, K., *Chem. Phys. Lett.* **2005**, 410, 358-364.
- [40] Shioya, K.; Mishima, K.; Yamashita, K., *Mol. Phys.* **2007**, 105, 1283-1295.
- [41] Mishima, K.; Yamashita, K., *Chem. Phys.* **2009**, 361, 106-117.
- [42] Mishima, K.; Yamashita, K., *J. Chem. Phys.* **2009**, 130, 034108.
- [43] Tesch, C. M.; Kurtz, L.; Vivie-Riedle, R. De., *Chem. Phys. Lett.* **2001**, 343, 633-641.
- [44] Tesch, C. M.; Vivie-Riedle, R. De., *Phys. Rev. Lett.* **2002**, 89, 157901.
- [45] Tesch, C. M.; Vivie-Riedle, R. De., *Chem. Phys.* **2004**, 121, 12158-12168.
- [46] Korff, B. M. R.; Troppmann, U.; Kompa, K. L.; Vivie-Riedle, R. De., *J. Chem. Phys.* **2005**, 123, 244509.
- [47] Troppmann, U.; Vivie-Riedle, R. De., *J. Chem. Phys.* **2005**, 122, 154105.
- [48] Gollub, C.; Troppmann, U.; Vivie-Riedle, R. De., *New J. Phys.* **2006**, 8, 48.
- [49] Troppmann, U.; Gollub, C.; Vivie-Riedle, R. De., *New J. Phys.* **2006**, 8, 100.

- [50] Sugny, D.; Kontz, C.; Ndong, M.; Justum, Y.; Dive, G.; Desouter-Lecomte, M., *Phys. Rev. A.* **2006**, 74, 043419.
- [51] Sugny, D.; Ndong, M.; Lauvergnat, D.; Justum, Y.; Desouter-Lecomte, M., *J. Photochem. Photobiol. A.* **2007**, 190, 359-371.
- [52] Teranishi, Y.; Ohtsuki, Y.; Hosaka, K.; Chiba, H.; Katsuki, H.; Ohmori, K., *J. Chem. Phys.* **2006**, 124, 114110.
- [53] Nielsen, M. A.; Chuang, I. L., *Quantum Computation and Quantum Information* (Cambridge University Press, Cambridge), **2000**.
- [54] Nielsen, M. A.; Dowling, M. R.; Gu, M.; Doherty, A. C., *Phys. Rev. A.* **2006**, 73, 062323.
- [55] Cheng, T.; Brown, A., *J. Chem. Phys.* **2006**, 124, 034111.
- [56] Ndong, M.; Lauvergnat, D.; Chapuisat, X.; Desouter-Lecomte, M., *J. Chem. Phys.* **2007**, 126, 244505.
- [57] Bomble, L.; Lauvergnat, D.; Remacle, F.; Desouter-Lecomte, M., *J. Chem. Phys.* **2008**, 128, 064110.
- [58] Grace, M.; Brif, C.; Rabitz, H.; Walmsley, I.; Kosut, R.; Lidar, D., *New J. Phys.* **2006**, 8, 35.
- [59] Lozovoy, V. V.; Dantus, M., *Chem. Phys. Lett.* **2002**, 351, 213-221.
- [60] Babikov, D.; Mozhayskiy, V. A.; Krylov, A. I., *J. Chem. Phys.* **2006**, 125, 84306.
- [61] www.quantumoptics.at
- [62] Ostendorf, A.; Roth, B.; Lammerzahl, C.; Schiller, S., Poster : “*Preparation and Storage of Ultracold Complex Molecules*” in Cold Molecules(CM), **2002**.
- [63] Zhao, M.; Babikov, D., *Phys. Rev. A.* **2008**, 77, 012338.
- [64] Kielpinski, D.; Monroe, C.; Wineland, D. J., *Nature.* **2002**, 417, 709-711.
- [65] Schulz, S.; Poschinger, U.; Singer, K.; Schmidt-Kaler, F., *Fortschr. Phys.* **2006**, 54, 648-665.

- [66] Stick, D.; Hensinger, W. K.; Olmschenk, S.; Madsen, M. J.; Schwab, K.; Monroe, C., *Nature Physics*. **2006**, 2, 36-37.
- [67] Hensinger, W. K.; Olmschenk, S.; Stick, D.; Hucul, D.; Yeo, M.; Acton, M.; Deslauriers, L.; Monroe, C., *Appl. Phys. Lett.* **2006**, 88, 034101.
- [68] Beckman, D.; Chari, A. N.; Devabhaktuni, S.; Preskill, J., *Phys. Rev. A*. **1996**, 54, 1034.
- [69] Meyrath, T. P.; James, D. F. V., *Phys. Lett. A*. **1998**, 240, 37-42.
- [70] James, D. F. V., *Appl. Phys. B*. **1998**, 66, 181-190.
- [71] Wang, L.; Babikov, D., *Phys. Rev. A*. **2011**, 83, 022305.
- [72] Wang, L.; Babikov, D., *Phys. Rev. A*. **2011**, 83, 052319.
- [73] Blinov, B. B.; Moehring, D. L.; Duan, L.-M.; Monroe, C., *Nature*. **2004**, 428, 153-157.
- [74] Deslauriers, L.; Olmschenk, S.; Stick, D.; Hensinger, W. K.; Sterk, J.; Monroe, C., *Phys. Rev. Lett.* **2006**, 97, 103007.
- [75] Deslauriers, L.; Acton, M.; Blinov, B. B.; Brickman, K. A.; Haljan, P. C.; Hensinger, W. K.; Hucul, D.; Katnik, S.; Kohn, R. N.; Lee, Jr. P. J.; Madsen, M. J.; Maunz, P.; Olmschenk, S.; Moehring, D. L.; Stick, D.; Sterk, J.; Yeo, M.; Younge, K. C.; Monroe, C., *Phys. Rev. A*. **2006**, 74, 063421.
- [76] James, D. F. V., *Phys. Rev. Lett.* **1998**, 81, 317-320.
- [77] Milburn, G. J.; Schneider, S.; James, D. F. V., *Fortschritte der Physik*. **2000**, 48, 801-810.
- [78] Schneider, S.; James, D.; Milburn, G. J., *J. Mod. Opt.* **2000**, 47, 499-505.
- [79] Shankar, R., *Principles of Quantum Mechanics (Second edition)*. **1994**.
- [80] Press, W. H.; Flannery, B. P.; Teukolsky, S. A.; Vetterling, W. T., *Numerical recipes*. **1989**.
- [81] Bransden, B. H.; Joachain, C. J., *Introduction to Quantum Mechanics*. **1989**.

- [82] Zhang, S.; Jin, J., *Computation of Special Functions*. **1996**.
- [83] Demtröder, W., *Molecular Physics*. **2005**.
- [84] Zhao, M.; Babikov, D., *J. Chem. Phys.* **2007**, 126, 204102.
- [85] Zhao, M.; Babikov, D., *J. Chem. Phys.* **2006**, 125, 024105.
- [86] Ho, T. S.; Rabitz, H., *J. Photochem. Photobiol. A*. **2006**, 180, 226-240.
- [87] Rabitz, H.; Zhu, W. S., *Acc. Chem. Res.* **2000**, 33, 572-578.
- [88] Ren, Q.; Balint-Kurti, G. G.; Manby, F. R.; Artamonov, M.; Ho, T. S.; Rabitz, H., *J. Chem. Phys.* **2006**, 124, 014111.
- [89] Sundermann, K.; Vivie-Riedle, R. de, *J. Chem. Phys.* **1999**, 110, 1896-1904.
- [90] Babikov, D, *J. Chem. Phys.* **2004**, 121, 7577-7585.
- [91] Gu, Y. Y.; Babikov, D, *J. Chem. Phys.* **2009**, 131, 034306.
- [92] Tesch, C. M.; Vivie-Riedle, R. de, *J. Chem. Phys.* **2004**, 121, 12158.
- [93] Zaari, R. R.; Brown, A., *J. Chem. Phys.* **2011**, 135, 044317.
- [94] www.mhpcc.edu/training/workshop/mpi/MAIN.html. **2003**.
- [95] hpcf.nerc.gov/training/tutorials/mpi/intro/. **2002**.
- [96] National Energy Research Scientific Computing Center (www.nerc.gov).
- [97] Leach, A. R., *Molecular Modelling-Principles and Applications (Second edition)*. **2001**.
- [98] Jensen, F., *Introduction to Computational Chemistry*. **1999**.
- [99] Wineland, D.J.; Monroe, C.; Itano, W.M.; Leibfried, D.; King, B.; Meekhof, D.M., *Journal of Research of the National Institute of Standards and Technology*. **1998**, 103, 259-328.
- [100] Press, W. H.; Teukolsky, S. A.; Vetterling, W. T.; Flannery, B. P., *Numerical Recipes (Third edition)*. **2007**.

[101] DSYEV from LAPACK is a software package provided by Univ. of Tennessee,
Univ. of California Berkeley, Univ. of Colorado Denver and NAG Ltd, **2006**.

Appendix A

This code is written to diagonalize the Hamiltonian matrix of one $^{111}\text{Cd}^+$ ion in the anharmonic potential trap to obtain its eigenvalues (energies) and the eigenvectors (parameter matrix \mathbf{C} in Sec. 2.2). Lines 1-24 of this code contain the definition of variables; Lines 26-59 are the input data and step size definition; Lines 61-149 describe the basis set expansion; Lines 151-166 define kinetic energy matrix and lines 168-185 are definition of potential energy matrix; Hamiltonian matrix is constructed in lines 187-210; DSYEV subroutine from ACML library is used in lines 212-226 for matrix diagonalization [101]; Lines 228-262 are the construction of wavefunctions of the system; Transition matrix is calculated in lines 264-286; Lines 288-300 are the subroutine NVJ which is used to calculate $j!$ of Eq. (2.2.5) and the subroutine OTHPL in lines 302-361 describe calculation of Hermite polynomials and their first derivatives [82]. In this program, during the numerical calculations for the spectrum of vibrational states, I used atomic units. It was transformed into the units of MHz at the end.

```

Program 1DIONTRAP
implicit real*8 (a-h,o-z)
integer mv,nz
real*8 towpi,autonm
parameter(mv=20,max=60)
parameter(nz=501)
parameter(twopi=6.28318530717959d0)
parameter(autonm=0.05291772d0)
character*1 UPLO, JOBZ
parameter(JOBZ ='V',UPLO ='U')
integer INFO
double precision EV(mv), WORK(3*mv-1),Hamil(mv,mv)
real*8 energy1,energy2,delta1,delta2
real*8 mass1,mu,n1,beta1,y1,sum
double precision
z(nz),psi1(max,nz),psi2(max,nz),h(max),dh(max)
double precision psi(max,nz),psir(max,nz),psii(max,nz)
double precision
norm1(max,max),norm2(max,max),norm3(max,max)
double precision
norm(max,max),wavef(max,nz),dipole(max,max)
dimension v1(nz),v2(nz),p2s2m(nz)
real*8 dp,n,b
pi=acos(-1.d0)

ccc Parameters for Cd ion from experiment(in a.u.):
mass1=111.d0
mass1=mass1*1822.8885d0
mu=1.d0
w=2770.0*2*pi
delta=27.7*2*pi      !(unit=KHz=3.33*10^-8cm^-1)
delta1=15.0*2*pi
delta2=30.0*2*pi

w=w*3.33564d-8/219474.63d0
delta=delta*3.33564d-8/219474.63d0
delta1=delta1*3.33564d-8/219474.63d0
delta2=delta2*3.33564d-8/219474.63d0

ccc Definition of distance step:
zi=-650.d0
zf=650.d0
dz=(zf-zi)/(nz-1)
write(8,*) zi*autonm,zf*autonm,dz*autonm

do iz=1,nz
  z(iz)=zi+(iz-1)*dz
end do

open(100,file='uneigen.dat',status='unknown')
do i=0,mv-1
  energy1=w*(i+0.5d0)-delta1*(i+0.5d0)*(i+0.5d0)
  energy2=w*(i+0.5d0)-delta2*(i+0.5d0)*(i+0.5d0)
  energy1=energy1*219474.63*2.997924d4
  energy2=energy2*219474.63*2.997924d4
  write(100,*) energy1,energy2
end do
close(100)

ccc Harmonic parameters for mode 1 (in a.u.):
w01=w
dk1=dsqrt(mass1)*w01           !dk=dsqrt(k)
beta1=dsqrt(mass1)*dk1

ccc Basis functions for mode 1:
do iz=1,nz
  y1=dsqrt(beta1)*z(iz)

```

```

iv=0
psi1(iv+1,iz)=(beta1/pi)**0.25d0*dexp(-1*y1**2/2.d0)
ccc Call the subroutine which will give the value of
Hermite:
call othpl(4,mv,y1,h,dh)
do iv=1,mv-1,1
  n=iv
  call nvj(n,b)
  n1=dsqrt(dsqrt(beta1/pi)/(2**n)/b)
  psi1(iv+1,iz)=n1*h(iv+1)*exp(-1*y1**2/2.d0)
end do
end do

ccc Normalization of wavefunctions for mode 1:
open(9,file='gp.dat',status='unknown')
do iv=1,mv
  sum=0.d0
  do iz=1,nz
    sum=sum+psi1(iv,iz)**2
  end do
  sum=sum*dz
  write(9,10) sum
  do iz=1,nz
    psi1(iv,iz)=psi1(iv,iz)/dsqrt(sum)
  end do
end do
close(9)

ccc Output of basis functions:
open(10,file='basisset.dat',status='unknown')
do iz=1,nz
  write(10,10) z(iz),(psi1(iv,iz),iv=1,mv)
end do
close(10)

ccc Test of orthonormality:
do iv=1,mv
  do jv=1,mv
    sum=0.d0
    do iz=1,nz
      sum=sum+psi1(iv,iz)*psi1(jv,iz)
    end do
    norm3(iv,jv)=sum*dz
  end do
end do

open(20,file='matrix.dat',status='unknown')
do iv=1,mv
  write(20,20) (norm3(iv,jv),jv=1,mv)
end do
close(20)

ccc Calculation of second derivative of kinetic part:
do iz=1,nz
  y1=dsqrt(beta1)*z(iz)
  call othpl(4,mv,y1,h,dh)
  G=exp(-1*y1**2/2.d0)
  G1=-1*beta1*z(iz)*exp(-1*y1**2/2.d0)
  G2=beta1*exp(-1*y1**2/2.d0)*(y1**2-1)
  iv=0
  psi(iv+1,iz)=dsqrt(dsqrt(beta1/pi))*G2
  do iv=1,mv-1
    n=iv
    call nvj(n,b)
    n1=dsqrt(dsqrt(beta1/pi)/(2**n)/b)
    H1=dsqrt(beta1)*dh(iv+1)
    H2=2*iv*dh(iv)*beta1
    psi(iv+1,iz)=n1*(G2*h(iv+1)+2*G1*H1+G*H2)
  end do
end do

```

```

    end do
end do
do iv=1,mv
  do iz=1,nz
    psir(iv,iz)=-psi(iv,iz)/(2*mass1)
  end do
end do

open(30,file='secwavr.dat',status='unknown')
do iz=1,nz
  write(30,30) z(iz), (psir(iv,iz),iv=1,mv)
end do
close(30)

ccc Kinetic part for Hamiltonian:
do iv=1,mv
  do jv=1,mv
    sum=0.d0
    do iz=1,nz
      sum=sum+psil(iv,iz)*psir(jv,iz)
    end do
    norm1(iv,jv)=sum*dz
  end do
end do

open(35,file='kinetic.dat',status='unknown')
do iv=1,mv
  write(35,50) (norm1(iv,jv),jv=1,mv)
end do
close(35)

ccc Potential part for Hamiltonian:
do iv=1,mv
  do jv=1,mv
    sum=0.d0
    do iz=1,nz
      v1(iz)=0.5d0*dk1**2*z(iz)**2+3.0d-6*dk1**2*z(iz)**4
      sum=sum+psil(iv,iz)*v1(iz)*psil(jv,iz)
    end do
    norm2(iv,jv)=sum*dz
  end do
end do

open(40,file='potential.dat',status='unknown')
do iv=1,mv
  write(40,50) (norm2(iv,jv),jv=1,mv)
end do
close(40)

ccc Hamiltonian matrix:
do iv=1,mv
  do jv=1,mv
    norm(iv,jv)=norm1(iv,jv)+norm2(iv,jv)
  end do
end do

open(50,file='Hamiltonian.dat',status='unknown')
do iv=1,mv
  write(50,50) (norm(iv,jv),jv=1,mv)
end do
close(50)

do iv=1,mv
  do jv=1,mv
    Hamil(iv,jv)=0
  end do
end do

```

```

do iv=1,mv
  do jv=iv,mv
    Hamil(mv+iv-jv,jv)=norm(iv,jv)
  end do
end do

ccc Diagonalization of Hamiltonian Matrix:
call DSYEV( JOBZ, UPLO, mv, Hamil, mv, EV, WORK,
$           3*(mv)-1, INFO )

open(60,file='Eigenvalue.dat',status='unknown')
do iv=1,mv
  write(60,50) EV(iv)*219474.63*2.997924d4
end do
close(60)

open(70,file='Eigenvector.dat',status='unknown')
do iv=1,mv
  write(70,50) (Hamil(iv,jv),jv=1,mv)
end do
close(70)

ccc Wavefunctions of the system:
do iz=1,nz
  do jv=1,mv
    wavef(jv,iz)=0.d0
    do iv=1,mv
      wavef(jv,iz)=wavef(jv,iz)+Hamil(iv,jv)*psi1(iv,iz)
    end do
  end do
end do

open(80,file='wavef1.dat',status='unknown')
do iz=1,nz
  write(80,10) z(iz), (wavef(jv,iz),jv=1,mv)
end do
close(80)

do iz=1,nz
  do jv=1,mv
    if(jv.eq.2) then
      wavef(jv,iz)=-wavef(jv,iz)
    else if(jv.eq.12) then
      wavef(jv,iz)=-wavef(jv,iz)
    else if(jv.eq.16) then
      wavef(jv,iz)=-wavef(jv,iz)
    else
      wavef(jv,iz)=wavef(jv,iz)
    end if
  end do
end do

open(90,file='wavefunction.dat',status='unknown')
do iz=1,nz
  write(90,10) z(iz), (wavef(jv,iz),jv=1,mv)
end do
close(90)

ccc Transition Matrix:
do iv=1,mv
  do jv=1,mv
    sum=0.d0
    do iz=1,nz
      sum=sum+wavef(iv,iz)*mu*z(iz)*wavef(jv,iz)
    end do
    dipole(iv,jv)=sum*dz
  end do
end do

```

```

open(100,file='transitiondipole.dat',status='unknown')
do iv=1,mv
  write(100,20) (dipole(iv,jv),jv=1,mv)
end do
close(100)

10   format(e24.16,150(x,f24.16))
20   format(150(x,e30.16))
30   format(e24.16,150(x,f24.14))
40   format(150(x,f24.16))
50   format(150(x,e30.16))
End
C-----
CCC FACTORIAL OF N
SUBROUTINE NVJ(M,A)
REAL*8 I,M,A

IF(M.EQ.0) THEN
  A=1.0
ELSE
  A=1.0
  DO I=1,M
    A=A*I
  END DO
END IF
END
C-----
SUBROUTINE OTHPL(KF,N,X,PL,DPL)
C =====
C PURPOSE: COMPUTE ORTHOGONAL POLYNOMIALS: TN(X) OR
UN(X),
C          OR LN(X) OR HN(X), AND THEIR DERIVATIVES
C INPUT : KF --- FUNCTION CODE
C
C           KF=1 FOR CHEBYSHEV POLYNOMIAL TN(X)
C           KF=2 FOR CHEBYSHEV POLYNOMIAL UN(X)
C           KF=3 FOR LAGUERRE POLYNOMIAL LN(X)
C           KF=4 FOR HERMITE POLYNOMIAL HN(X)
C
C   N --- ORDER OF ORTHOGONAL POLYNOMIALS
C   X --- ARGUMENT OF ORTHOGONAL POLYNOMIALS
C   OUTPUT: PL(N) --- TN(X) OR UN(X) OR LN(X) OR HN(X)
C           DPL(N) --- TN'(X) OR UN'(X) OR LN'(X) OR
HN'(X)
C =====
C
IMPLICIT DOUBLE PRECISION (A-H,O-Z)
DIMENSION PL(0:N),DPL(0:N)
A=2.0D0
B=0.0D0
C=1.0D0
Y0=1.0D0
Y1=2.0D0*X
DY0=0.0D0
DY1=2.0D0
PL(0)=1.0D0
PL(1)=2.D0*X
DPL(0)=0.0D0
DPL(1)=2.0D0
IF (KF.EQ.1) THEN
  Y1=X
  DY1=1.0D0
  PL(1)=X
  DPL(1)=1.0D0
ELSE IF (KF.EQ.3) THEN
  Y1=1.D0-X
  DY1=-1.0D0
  PL(1)=1.0D0-X
  DPL(1)=-1.0D0

```

```
END IF
DO 10 K=2,N
  IF (KF.EQ.3) THEN
    A=-1.0D0/K
    B=2.0D0+A
    C=1.0D0+A
  ELSE IF (KF.EQ.4) THEN
    C=2.0D0*(K-1.0D0)
  END IF
  YN=(A*X+B)*Y1-C*Y0
  DYN=A*Y1+(A*X+B)*DY1-C*DY0
  PL(K)=YN
  DPL(K)=DYN
  Y0=Y1
  Y1=YN
  DY0=DY1
10      DY1=DYN
RETURN
END
```

Appendix B

This code is written to calculate the optimized control pulse, transition probability and fidelity during the control of quantum gates. Lines 1-42 of this code contain the definition of variables; Lines 43-55 are used to initialize Message Passing Interface (MPI) calculation; Lines 57-110 are the step size definition and input data; Lines 112-206 are used to restart this code; Lines 208-264 are the names of output files; Lines 266-291 are used to calculate the phase term during the propagation of the time-dependent wavefunction; Lines 293-333 are used to propagate the backward wavefunction; Lines 335-387 are used to calculate the probability and fidelity versus time for the last but one iteration (backward); Lines 389-432 are used to output backward probability and fidelity; Lines 434-572 are used for forward propagation; Lines 574-587 are used to create the file for restarting the code; Lines 589-694 are used to output the optimized control pulse, state-to-state transition probability and finalize MPI; Lines 696-708 define the guess field and lines 710-809 are used to calculate the control pulse; Coefficients of the time-dependent wavefunctions are calculated in lines 811-876; RK4 subroutine is used in lines 878-915 [80]. Note that the optimization code is parallelized using MPI to carry out N propagations of the Schrödinger equations using N different processors of the parallel computer.

```

program main
c this code was extracted from timeprop.f. (1-
dimension) (09/22/05)
c this code can be used for restart, which means when the
code was running, the power was off,
c then the code can be restarted from the checkpoint of
restart file (refer to the Parameter file).

implicit real*8 (a-h,o-z)
include 'parameter.h'
c-----
real*8 mij(nv,nv),e(nv),tt
common/hamiltonian/mij,e,amp,omega,tpulse,pi
common/iteration/iter,idir,it

dimension c0(2*nv,nt+1),c1(2*nv,nt+1)
dimension c0Re(2*nv,nt+1),c0Im(2*nv,nt+1)
!real and imaginary part of the backward wavefuncition
including the phase.
dimension c1Re(2*nv,nt+1),c1Im(2*nv,nt+1)
!real and imaginary part of the forward wavefuncition
including the phase.
common /wavefunct/c0,c1
dimension field0(nt+1),field1(nt+1)
common /field/ field0,field1
dimension fbsinij(nv,nv,2*nt+1),fbcosij(nv,nv,2*nt+1)
common/phase/fbsinij,fbcosij
c-----
dimension cre(nv),cim(nv),dcdt(2*nv)
dimension time(nt+1),time1(nt+1),time2(2*nt+1)
dimension strtre(mv),strtim(mv),targre(mv),targim(mv)
dimension FRE(mv),FIM(mv),fidelity1(nt+1),fidelity2(nt+1)
dimension probability1(nt+1),probability2(nt+1)
dimension back_re(mv,nt+1),back_im(mv,nt+1)

```

```

dimension back_cos(mv,nt+1),back_sin(mv,nt+1)
dimension forw_re(mv,nt+1),forw_im(mv,nt+1)
dimension forw_cos(mv,nt+1),forw_sin(mv,nt+1)
character*13 fileout
character*19 filepop

external derivs,field_gess,field_iter
!----- MPI STAFF -----
include 'mpif.h'
integer rc,comm
common/pedat/mype,npe,comm
!-----
c MPI start:
call MPI_INIT(ierr)
comm=MPI_COMM_WORLD
call MPI_COMM_RANK(comm,mype,ierr)
call MPI_COMM_SIZE(comm,npe,ierr)
write(6,*) 'mype=',mype,' npe=',npe
call MPI_BARRIER(comm,ierr)
call mysecond(ts)

c Pulse parameters:
tpulse=tt/automisec ! (unit: atomic)

dt=tpulse/nt

do it=1,nt+1
  time(it)=(it-1)*dt      !(unit: atomic)
  time1(it)=(it-1)*dt*automisec   !(unit: microsec)
end do

do it=1,2*nt+1

```

```

      time2(it)=(it-1)*dt/2.d0      !(unit: atomic, for sin
and cos function)
end do

pi=acos(-1.d0)
c Open and read in eigenvalues:

open(20,file='eigen.dat',status='old')
read(20,*) n_read
if(n_read.lt.nv) then
  print*, 'ERROR: Problem reading eigenvalues.dat'
  stop
end if

do iv=1,nv
  read(20,*) e(iv)
end do
close(20)

c Open and read in transition moments matrix:

open(30,file='dipol.dat',status='old')
read(30,*) n_read
if(n_read.lt.nv) then
  print *, 'ERROR: Problem reading matrix.dat'
  stop
end if

do iv=1,nv
  read(30,*) (mij(iv,jv),jv=1,nv)
end do
close(30)

c Open and read in starting and target qubit states:

```

```

fileout='transition_ '
write (fileout(12:13),'(i2.2)') mype+1
open(40, file=fileout,status='old')
do l=1,mv
  read(40,*) strtre(l),strtim(l),targre(l),targim(l)
end do
close(40)

c RESTART:

if (restart) theN
  filepop= 'restart_.dat'
  write (filepop(9:10),'(i2.2)') mype+1
  open(16,file=filepop,status='old', form='unformatted')
  read (16) iter
  read (16) (field1(it),it=1,nt+1)
  read (16) ((c1(j,it),j=1,2*nv),it=1,nt+1)
  close(16)

  fileout='iter_back_ '
  write(fileout(11:12),'(i2.2)') mype+1
  open(19,file=fileout,status='unknown')

  fileout='iter_forw_ '
  write(fileout(11:12),'(i2.2)') mype+1
  open(20,file=fileout,status='unknown')

  fileout='re_back_ '
  write(fileout(9:10),'(i2.2)') mype+1
  open(21,file=fileout,status='unknown')

  fileout='im_back_ '
  write(fileout(9:10),'(i2.2)') mype+1

```

```

open(22,file=fileout,status='unknown')
fileout='re_forw_ '
write(fileout(9:10),'(i2.2)') mype+1
open(25,file=fileout,status='unknown')

fileout='im_forw_ '
write(fileout(9:10),'(i2.2)') mype+1
open(26,file=fileout,status='unknown')

fileout='back_fidel_ '
write(fileout(12:13),'(i2.2)') mype+1
open(23,file=fileout,status='unknown')

fileout='forw_fidel_ '
write(fileout(12:13),'(i2.2)') mype+1
open(24,file=fileout,status='unknown')

fileout='back_aprob_ '
write(fileout(12:13),'(i2.2)') mype+1
open(29,file=fileout,status='unknown')

fileout='forw_aprob_ '
write(fileout(12:13),'(i2.2)') mype+1
open(31,file=fileout,status='unknown')

do j=0,(iter-1)/2
  read (23,*) iter, prob1
  read (24,*) iter, probab2
  read (29,*) iter, prob2
  read (31,*) iter, probab4
  read (19,*) iter, probab
  read (20,*) iter, probab
  read (21,*) iter, sum1

read (22,*) iter, sum2
read (25,*) iter, sum3
read (26,*) iter, sum4
end do

print *, "restart info obtained."

c Sin and Cos of (Ei-Ej)*t, for Interaction Representation
only (phase term in subroutine):

do it=1,2*nt+1
  do i=1,nv
    fbsinij(i,i,it)=0.d0
    fbcosij(i,i,it)=1.d0
  end do

  do j=1,nv-1
    do i=j+1,nv
      det=(e(i)-e(j))*time2(it)
      fbsinij(i,j,it)=sin(det)
      fbcosij(i,j,it)=cos(det)
    end do
  end do

  do j=2,nv
    do i=1,j-1
      fbsinij(i,j,it)=-fbsinij(j,i,it)
      fbcosij(i,j,it)= fbcosij(j,i,it)
    end do
  end do

end do

goto 10

```

```

end if

c First start:

fileout='iter_back_ '
write(fileout(11:12),'(i2.2)') mype+1
open(19,file=fileout,status='unknown')

fileout='iter_forw_ '
write(fileout(11:12),'(i2.2)') mype+1
open(20,file=fileout,status='unknown')

fileout='re_back_ '
write(fileout(9:10),'(i2.2)') mype+1
open(21,file=fileout,status='unknown')

fileout='im_back_ '
write(fileout(9:10),'(i2.2)') mype+1
open(22,file=fileout,status='unknown')

fileout='re_forw_ '
write(fileout(9:10),'(i2.2)') mype+1
open(25,file=fileout,status='unknown')

fileout='im_forw_ '
write(fileout(9:10),'(i2.2)') mype+1
open(26,file=fileout,status='unknown')

fileout='ini_state_ '
write(fileout(11:12),'(i2.2)') mype+1
open(27,file=fileout,status='unknown')

fileout='fin_state_ '
write(fileout(11:12),'(i2.2)') mype+1

open(28,file=fileout,status='unknown')

fileout='back_fidel_ '
write(fileout(12:13),'(i2.2)') mype+1
open(23,file=fileout,status='unknown')

fileout='forw_fidel_ '
write(fileout(12:13),'(i2.2)') mype+1
open(24,file=fileout,status='unknown')

fileout='back_aprob_ '
write(fileout(12:13),'(i2.2)') mype+1
open(29,file=fileout,status='unknown')

fileout='forw_aprob_ '
write(fileout(12:13),'(i2.2)') mype+1
open(31,file=fileout,status='unknown')

do l=1,mv
  write(27,*) strtre(l),strtim(l)
end do

do l=1,mv
  write(28,*) targre(l),targim(l)
end do

c Sin and Cos of (Ei-Ej)*t, for Interaction Representation
only (phase term in subroutine):

do it=1,2*nt+1

  do i=1,nv
    fbsinij(i,i,it)=0.d0
    fbcosij(i,i,it)=1.d0

```

```

end do

do j=1,nv-1
  do i=j+1,nv
    det=(e(i)-e(j))*time2(it)
    fbsinij(i,j,it)=sin(det)
    fbcosij(i,j,it)=cos(det)
  end do
end do

do j=2,nv
  do i=1,j-1
    fbsinij(i,j,it)=-fbsinij(j,i,it)
    fbcosij(i,j,it)= fbcosij(j,i,it)
  end do
end do

end do

c ITERATIONS

iter=-1

10  continue
call MPI_BARRIER(comm,ierror)

c Iteration number:

iter=iter+1

c Set up target wavefunction:

do l=1,nv
  cre(l)=0.d0
end do

do l=1,mv
  cre(l)=targre(l)
  cim(l)=targim(l)
end do

c Set up real vector out of Cre & Cim:

do l=1,nv
  c0(  l,nt+1)=cre(l)*cos(e(l)*tpulse)
  $           -cim(l)*sin(e(l)*tpulse)
  c0(nv+l,nt+1)=cre(l)*sin(e(l)*tpulse)
  $           +cim(l)*cos(e(l)*tpulse)
end do

c Backward propagation:

idir=-1

do it=nt+1,2,-1
  call derivs(time(it),c0(1,it),dcdt,0)
  call rk4(c0(1,it),dcdt,2*nv,time(it),-dt,
  $      c0(1,it-1),derivs)
end do

c -----prob and fidelity etc. versus time for the last
but one iteration

if(iter.eq.(niter-1)) then

  do it=1,nt+1
    sum1=0.d0

```

```

sum2=0.d0
do l=1,mv
sum1=sum1+strtre(l)*(c0(    l,it)*cos(e(l)*time(it))
$                  +c0(nv+l,it)*sin(e(l)*time(it)))
$                  +strtim(l)*(c0(nv+l,it)*cos(e(l)*time(it))
$                  -c0(    l,it)*sin(e(l)*time(it)))
sum2=sum2-strtim(l)*(c0(    l,it)*cos(e(l)*time(it))
$                  +c0(nv+l,it)*sin(e(l)*time(it)))
$                  +strtre(l)*(c0(nv+l,it)*cos(e(l)*time(it))
$                  -c0(    l,it)*sin(e(l)*time(it)))
back_re(l,it)=c0(l,it)*cos(e(l)*time(nt+2-it))
$                  -c0(nv+l,it)*sin(e(l)*time(nt+2-it))
!real part of backward wavefunction for state 1
back_im(l,it)=c0(nv+l,it)*cos(e(l)*time(nt+2-it))
$                  +c0(l,it)*sin(e(l)*time(nt+2-it))
!imaginary part of backward wavefuntion for state 1
end do

probab5=sum1**2+sum2**2

ccc Consider the fidelity.

call MPI_ALLREDUCE(sum1,sum5,1,MPI_DOUBLE_PRECISION,
$   MPI_SUM,comm,ierror)
call MPI_ALLREDUCE(sum2,sum6,1,MPI_DOUBLE_PRECISION,
$   MPI_SUM,comm,ierror)
call
MPI_ALLREDUCE(probab5,probab6,1,MPI_DOUBLE_PRECISION,
$   MPI_SUM,comm,ierror)

fidelity1(it)=(sum5**2+sum6**2)/N**2
probability1(it)=probab6/N
end do

filepop='      _backfidprb_ '
write(filepop(1:5),'(i5.5)') iter
write(filepop(18:19),'(i2.2)') mype+1
open(130,file=filepop,status='unknown')

do it=1,nt+1,printstep
  write(130,100)
  time1(it),fidelity1(it),probability1(it),
  & (back_re(i,it),i=1,mv),(back_im(i,it),i=1,mv)
end do
close(130)
end if

c Output final overlap and energy of the field:

sum1=0.d0
sum2=0.d0

do l=1,mv
sum1=sum1+strtre(l)*(c0(    l,1)*cos(e(l)*time(1))
$                  +c0(nv+l,1)*sin(e(l)*time(1)))
$                  +strtim(l)*(c0(nv+l,1)*cos(e(l)*time(1))
$                  -c0(    l,1)*sin(e(l)*time(1)))
sum2=sum2-strtim(l)*(c0(    l,1)*cos(e(l)*time(1))
$                  +c0(nv+l,1)*sin(e(l)*time(1)))
$                  +strtre(l)*(c0(nv+l,1)*cos(e(l)*time(1))
$                  -c0(    l,1)*sin(e(l)*time(1)))
end do

probab=sum1**2+sum2**2

write(19,50) iter, probab
write(21,50) iter,sum1
write(22,50) iter,sum2

```

```

call myflush(19)
call myflush(21)
call myflush(22)

print*, 'pe #',mype,' Iteration',iter,' Transfer:',probab
call MPI_BARRIER(comm,ierror)

call MPI_ALLREDUCE(sum1,sum5,1,MPI_DOUBLE_PRECISION,
$      MPI_SUM,comm,ierror)
call MPI_ALLREDUCE(sum2,sum6,1,MPI_DOUBLE_PRECISION,
$      MPI_SUM,comm,ierror)
Call MPI_ALLREDUCE(probab,probabl,1,
$      MPI_DOUBLE_PRECISION,MPI_SUM,comm,ierror)

prob1=(sum5**2+sum6**2)/N**2
!backward fidelity
probab2=probabl/N
!backward average prob
write(23,50) iter,prob1
write(29,50) iter,probab2
call myflush(23)
call myflush(29)

c Iteration number:

iter=iter+1

c Set up initial wavefunction:

do l=1,nv
  cre(l)=0.d0
  cim(l)=0.d0
end do

do l=1,mv
  cre(l)=strtre(l)
  cim(l)=strtim(l)
end do

c Set up real vector(size ntot) out of Cre & Cim:

do l=1,nv
  c1(    l,1)=cre(l)
  c1(nv+l,1)=cim(l)
end do

c Forward propagation:

idir=1

do it=1,nt
  call derivs(time(it),c1(1,it),dcdt,0)
  call rk4(c1(1,it),dcdt,2*nv,time(it),dt,
$        c1(1,it+1),derivs)
end do

c-----prob and fidelity etc. versus time for the
last iteration

if(iter.eq.niter) then

  do it=1,nt+1
    sum3=0.d0
    sum4=0.d0
    do l=1,mv
      sum3=sum3+targre(l)*(c1(    l,it)*cos(e(l)*time(it))
$                           +c1(nv+l,it)*sin(e(l)*time(it)))
$                           +targim(l)*(c1(nv+l,it)*cos(e(l)*time(it)))
    end do
  end if
end if

```

```

$           -c1( l,it)*sin(e(l)*time(it)))
sum4=sum4-targim(l)*(c1( l,it)*cos(e(l)*time(it))
$           +c1(nv+l,it)*sin(e(l)*time(it)))
$     +targre(l)*(c1(nv+l,it)*cos(e(l)*time(it))
$           -c1( l,it)*sin(e(l)*time(it)))
forw_re(l,it)=c1(l,it)*cos(e(l)*time(it))
$           +c1(nv+l,it)*sin(e(l)*time(it))
!real part of forward wavefunction for state l
  forw_im(l,it)=c1(nv+l,it)*cos(e(l)*time(it))
  $           -c1(l,it)*sin(e(l)*time(it))
!imaginary part of forward wavefunction for state l
end do

probab7=sum3**2+sum4**2

ccc Consider the fidelity.

call MPI_ALLREDUCE(sum3,sum7,1,MPI_DOUBLE_PRECISION,
$   MPI_SUM,comm,ierror)
call MPI_ALLREDUCE(sum4,sum8,1,MPI_DOUBLE_PRECISION,
$   MPI_SUM,comm,ierror)
call MPI_ALLREDUCE(probab7,probab8,1,
$   MPI_DOUBLE_PRECISION,MPI_SUM,comm,ierror)

fidelity2(it)=(sum7**2+sum8**2)/N**2
probability2(it)=probab8/N
end do

filepop=' _forwfidprb_ '
write(filepop(1:5),'(i5.5)') iter
write(filepop(18:19),'(i2.2)') mype+1
open(140,file=filepop,status='unknown')

do it=1,nt+1,printstep
               write(140,100)
               timel(it),fidelity2(it),probability2(it),
               & (forw_re(i,it),i=1,mv),(forw_im(i,it),i=1,mv)
end do
close(140)
end if

c Output overlap and energy of the field:

sum3=0.d0
sum4=0.d0

do l=1,mv
  sum3=sum3+targre(l)*(c1( l,nt+1)*cos(e(l)*time(nt+1))
$           +c1(nv+l,nt+1)*sin(e(l)*time(nt+1)))
$     +targim(l)*(c1(nv+l,nt+1)*cos(e(l)*time(nt+1))
$           -c1( l,nt+1)*sin(e(l)*time(nt+1)))
  sum4=sum4-targim(l)*(c1( l,nt+1)*cos(e(l)*time(nt+1))
$           +c1(nv+l,nt+1)*sin(e(l)*time(nt+1)))
$     +targre(l)*(c1(nv+l,nt+1)*cos(e(l)*time(nt+1))
$           -c1( l,nt+1)*sin(e(l)*time(nt+1)))
  FRE(l)=c1(l,nt+1)*cos(e(l)*time(nt+1))
  $           +c1(nv+l,nt+1)*sin(e(l)*time(nt+1))
!real part of forward function at time T, which can be
output with iter vs. real value.
  FIM(l)=c1(nv+l,nt+1)*cos(e(l)*time(nt+1))
  $           -c1(l,nt+1)*sin(e(l)*time(nt+1))
!imaginary part of forward funciton at time T, it was used
for checking the phase during coding.
end do

probab=sum3**2+sum4**2
               write(20,50) iter,probab

```

```

write(25,50) iter,sum3
write(26,50) iter,sum4

call myflush(20)
call myflush(25)
call myflush(26)
print*, 'pe #',mype,' Iteration',iter,'Transfer:',probab

ccc Consider the fidelity.

call MPI_ALLREDUCE(sum3,sum7,1,MPI_DOUBLE_PRECISION,
$      MPI_SUM,comm,ierror)
call MPI_ALLREDUCE(sum4,sum8,1,MPI_DOUBLE_PRECISION,
$      MPI_SUM,comm,ierror)
call MPI_ALLREDUCE(probab,probab3,1,
$      MPI_DOUBLE_PRECISION,MPI_SUM,comm,ierror)

prob2=(sum7**2+sum8**2)/N**2           !forward
fidelity
probab4=probab3/N                       !forward
average probability
write(24,50) iter,prob2
write(31,50) iter,probab4
call myflush(24)
call myflush(31)
call MPI_BARRIER(comm,ierror)

c Restart file:

if (chkflag.gt.0) then
  if (MOD(iter,nchkpt) .EQ. 1) then
    filepop= 'restart_.dat'
    write (filepop(9:10),'(i2.2)') mype+1

```

```

      open(16,file=filepop,status='unknown',form='unformatted')
      write (16) iter
      write (16) (field1(it),it=1,nt+1)
      write (16) ((c1(j,it),j=1,2*nv),it=1,nt+1)
      close(16)
      end if
    end if

c Output field and states populations during the run:

if(iter.eq.niter) then

c By one processor only:

  if(mype.eq.0) then
    fileout=' _fields'
    write(fileout(1:5),'(i5.5)') iter
    open(16,file=fileout,status='unknown')

    do it=1,nt+1,nprint
      field0(it)=field0(it)*automvc
      field1(it)=field1(it)*automvc
      write(16,100) timel(it),field0(it),field1(it)
    end do
    close(16)

  end if
  call MPI_BARRIER(comm,ierror)

c By each processor:

  filepop=' _transf_ '
  write(filepop(1:5),'(i5.5)') iter

```

```

write(filepop(14:15),'(i2.2)') mype+1
open(17,file=filepop,status='unknown')

do it=1,nt+1,printstep
  sum3=0.d0
  sum4=0.d0
  do l=1,mv
    sum3=sum3+targre(l)*(c1( l,it)*cos(e(l)*time(it))
    $           +c1(nv+l,it)*sin(e(l)*time(it)))
    $           +targim(l)*(c1(nv+l,it)*cos(e(l)*time(it))
    $           -c1( l,it)*sin(e(l)*time(it)))
    sum4=sum4-targim(l)*(c1( l,it)*cos(e(l)*time(it))
    $           +c1(nv+l,it)*sin(e(l)*time(it)))
    $           +targre(l)*(c1(nv+l,it)*cos(e(l)*time(it))
    $           -c1( l,it)*sin(e(l)*time(it)))
  end do
  write(17,100) time1(it),sum3**2+sum4**2
end do
close(17)

filepop=' _populs_ '
write(filepop(1:5),'(i5.5)') iter
write(filepop(14:15),'(i2.2)') mype+1
open(18,file=filepop,status='unknown')

do it=1,nt+1,printstep
  sum9=0.d0
  sum10=0.d0
  do i=1,nv
    sum9=sum9+c0(i,it)**2+c0(nv+i,it)**2
    sum10=sum10+c1(i,it)**2+c1(nv+i,it)**2
    c0Re(i,it)=c0( i,it)*cos(e(i)*time(it))
    $           +c0(nv+i,it)*sin(e(i)*time(it))
    c0Im(i,it)=c0(nv+i,it)*cos(e(i)*time(it))
    $           -c0( i,it)*sin(e(i)*time(it))
    c1Re(i,it)=c1( i,it)*cos(e(i)*time(it))
    $           +c1(nv+i,it)*sin(e(i)*time(it))
    c1Im(i,it)=c1(nv+i,it)*cos(e(i)*time(it))
    $           -c1( i,it)*sin(e(i)*time(it))
  end do
  write(18,100) time1(it),
  & (c0(i,it)**2+c0(nv+i,it)**2,i=1,nv),
  & (c1(i,it)**2+c1(nv+i,it)**2,i=1,nv),
  & (c0Re(i,it),c0Im(nv+i,it),i=1,nv),
  & (c1Re(i,it),c1Im(nv+i,it),i=1,nv),sum9,sum10
end do
close(18)

call MPI_BARRIER(comm,ierror)
end if

c Iterations:
if(iter.lt.niter) goto 10

close(19)
close(20)
close(21)
close(22)
close(23)
close(24)
close(25)
close(26)
close(27)
close(28)
close(29)
close(31)

50      format(i4,5(x,e18.12))

```

```

100  format(e16.8,300(x,e24.12))
200  format(10(x,e24.16))
800  format(g16.11,5x,g16.10)
807  format(a25,f7.2,2x,a8)

call mysecond(tf)
write(6,*) 'PE: ',mype,' Exiting...to Barrier'
write(6,807) 'Final CPU Time= ',(tF-tS)/60.0d0,' (min)'

call MPI_BARRIER(comm,ierror)
call MPI_FINALIZE(rc)

end
c-----
function field_gess(t)
implicit real*8 (a-h,o-z)
include 'parameter.h'

real*8 mij(nv,nv),e(nv),guessf
common /hamiltonian/mij,e,amp,omega,tpulse,pi

amp=guessf/automvc
omega=abs(e(2)-e(1))
field_gess=amp*sin(omega*t)

return
end
c-----
function field_iter(c,t,point)
implicit real*8 (a-h,o-z)

include 'parameter.h'

real*8 mij(nv,nv),e(nv)
common /hamiltonian/mij,e,amp,omega,tpulse,pi
dimension fbsinij(nv,nv,2*nt+1),fbcosij(nv,nv,2*nt+1)
common/phase/fbsinij,fbcosij
common /iteration/iter,idir,it
dimension c0(2*nv,nt+1),c1(2*nv,nt+1),c(2*nv),cpr(2*nv)
common /wavefunct/ c0,c1
real*8 Im0,Re0,ReCC,ImCC,ReM,ImM
integer point

c Coefficients from previous iteration:

select case(idir)
case(1)

    select case(point)
    case(0)
        do l=1,2*nv
            cpr(l)=c0(l,it)
        end do
    case(1)
        do l=1,2*nv
            cpr(l)=(c0(l,it)+c0(l,it+1))/2.d0
            if((it.gt.1).and.(it.lt.(nt-1))) then
                cpr(l)=cpr(l)-(c0(l,it-1)-c0(l,it)
                -c0(l,it+1)+c0(l,it+2))/16.d0
            end if
        end do
    case(2)
        do l=1,2*nv
            cpr(l)=c0(l,it+1)
        end do
    end select
end function

```

```

jt=2*it-1+point           !forward segment number of fbsin
and fbcos

case(-1)

select case(point)
case(0)
  do l=1,2*nv
    cpr(l)=c1(l,it)
  end do
case(1)
  do l=1,2*nv
    cpr(l)=(c1(l,it)+c1(l,it-1))/2.d0
    if((it.gt.2).and.(it.lt.(nt+1))) then
      cpr(l)=cpr(l)-(c1(l,it+1)-c1(l,it)
$          -c1(l,it-1)+c1(l,it-2))/16.d0
    end if
  end do
case(2)
  do l=1,2*nv
    cpr(l)=c1(l,it-1)
  end do
end select

jt=2*it-1-point           !backward segment number of
fbsin and fbcos

end select

c Overlap <psi_pr|mu|psi>:

ReM=0.d0
ImM=0.d0

do i=1,nv
  do j=1,nv
    ReCC=c(i)*cpr(j)+c(nv+i)*cpr(nv+j)
    ImCC=c(nv+i)*cpr(j)-c(i)*cpr(nv+j)
    ReM=ReM+(ReCC*fbcosij(j,i,jt)-
    ImCC*fbsinij(j,i,jt))*mij(i,j)
    ImM=ImM+(ImCC*fbcosij(j,i,jt)+ReCC*fbsinij(j,i,jt))*mij
    (i,j)
  end do
end do

c Overlap <psi|psi_pr>:
Re0=0.d0
Im0=0.d0

do i=1,nv
  Re0=Re0+(c(i)*cpr(i)+c(nv+i)*cpr(nv+i))
  Im0=Im0+(c(i)*cpr(nv+i)-c(nv+i)*cpr(i))
end do

c Field Im(<psi|psi_pr><psi_pr|mu|psi>):idir is used to
modify the equation for backward propagation,because
c cpr is now backward wavefunciton in this case.

field_iter=-idir*(Im0*ReM+Re0*ImM)
return
end
-----
subroutine derivs(t,c,dcdt,point)
implicit real*8 (a-h,o-z)

include 'parameter.h'

real*8 mij(nv,nv),e(nv),alpha

```

```

common /hamiltonian/ mij,e,amp,omega,tpulse,pi
dimension fbsinij(nv,nv,2*nt+1),fbcosij(nv,nv,2*nt+1)
common/phase/fbsinij,fbcosij
common /iteration/iter,idir,it
dimension field0(nt+1),field1(nt+1)
common /field/field0,field1
dimension c(2*nv),dcdt(2*nv)
integer point
!----- MPI STAFF-----
include 'mpif.h'
integer comm
common/pedat/mype,npe,comm
!-----
c Remember the field:
if(iter.eq.0) then
  field=field_gess(t)*(sin(pi*t/Tpulse))**2
else
  field2=field_iter(c,t,point)*(sin(pi*t/Tpulse))**2/alpha
  call MPI_BARRIER(comm,ierror)
  call MPI_ALLREDUCE(field2,field,1,MPI_DOUBLE_PRECISION,
    $      MPI_SUM,comm,ierror)
end if

c Remember the field:

if(point.eq.0) then
  select case (idir)
  case(1)
    field1(it)=field
  case(-1)
    field0(it)=field
  end select
end if

c Laser field action (interaction representation):
select case (idir)
case(1)
  jt=2*it-1+point
case(-1)
  jt=2*it-1-point
end select
do j=1,nv
  sum_re=0.d0
  sum_im=0.d0

  do i=1,nv
    sum_re=sum_re+(c( i)*fbsinij(i,j,jt)
      $           -c(nv+i)*fbcosij(i,j,jt))*mij(i,j)
    sum_im=sum_im+(c( i)*fbcosij(i,j,jt)
      $           +c(nv+i)*fbsinij(i,j,jt))*mij(i,j)
  end do

  dcdt( j)=field*sum_re
  dcdt(nv+j)=field*sum_im
end do

return
end
c-----
subroutine rk4(y,dydx,n,x,h,yout,derivs)
implicit real*8 (a-h,o-z)

dimension dydx(n),y(n),yout(n)
external derivs
parameter(nmax=80)      !should be larger than 2*nv.
dimension dym(nmax),dxt(nmax),yt(nmax)
integer comm

```

```

hh=h*0.5d0
h6=h/6.d0
xh=x+hh

do i=1,n
    yt(i)=y(i)+hh*dydx(i)
end do

call derivs(xh,yt,dyt,1)           !!! First step

do i=1,n
    yt(i)=y(i)+hh*dyt(i)
end do

call derivs(xh,yt,dym,1)           !!! Second step

do i=1,n
    yt(i)=y(i)+h*dym(i)
    dym(i)=dyt(i)+dym(i)
end do

call derivs(x+h,yt,dyt,2)           !!! Third step.

do i=1,n
    yout(i)=y(i)+h6*(dydx(i)+dyt(i)+2.d0*dym(i))
end do

return
end
c-----
subroutine mysecond(t)

real*8 t
include 'mpif.h'

t=MPI_WTIME()

return
end
c-----
subroutine myflush(iout)

integer iout

flush(iout)

return
end
c-----

```

Appendix C

This code is written to carry out 1D FFT. Lines 1-17 of this code contain the definition of variables; Lines 19-34 are the input data and step size definition; Lines 36-64 describe the process of FFT; Lines 66-75 are used to output final data.

```

Program 1DFFT
implicit real*8 (a-h,o-z)
integer nt,nj,n,mj
real*8 towpi,pi,deltat,maxw,dw
parameter(nm=600001,mm=1,nt=(nm-1)/mm+1,nj=2)
parameter(mj=81,n=mj*nt,automhz=6579682606.6812d0)
parameter(pi=3.1415926535897932384d0,twopi=6.2831853071795
9d0)
Parameter(automvcn=5.14221d12,automisec=0.0242d-
9,st=100,stp=5)
integer INFO
double precision COMM(3*n+100),X(n,nj),time(nt),tim(nt)
double precision
field0(nt),field1(nt),field2(nm),field3(nm)
double precision w((n-1)/2),amp((n-1)/2,nj),phi((n-
1)/2,nj)
common /field/ amp,phi,X,w

open(5,file='04001fields',status='old')
do it=1,nm
  read(5,*) tim(it),field2(it),field3(it)
end do
close(5)

do it=1,nt
  time(it)=tim((it-1)*mm+1)
  field0(it)=field2((it-1)*mm+1)
  field1(it)=field3((it-1)*mm+1)
end do

deltat=time(2)-time(1)
maxw=0.5d0/deltat/twopi
dw=maxw/(((n-1)/2)-1.d0)
write(12,*) maxw

open(6,file='fields.dat',status='unknown')
do it=1,nt
  write(6,100) time(it),field0(it),field1(it)
end do
close(6)

do i=1,nj
  do it=1,n
    X(it,i)=0.d0
  end do
end do

do it=((mj-1)/2)*nt+1,((mj+1)/2)*nt
  X(it,1)=field0(it-nt*((mj-1)/2))
  X(it,2)=field1(it-nt*((mj-1)/2))
end do

do it=1,(n-1)/2
  w(it)=(it-1)*dw
end do

call DZFFTM( nj, n, X, COMM, INFO )

do i=1,nj
  do it=1,(n-1)/2
    amp(it,i)=dsqrt(X(it+1,i)**2+X(n-it+1,i)**2)
    phi(it,i)=atan(X(n-it+1,i)/X(it+1,i))
  end do
end do

open(10,file='FastFourier.dat',status='unknown')
do it=1,2*nt,stp
  write(10,40) w(it),(amp(it,i),phi(it,i),i=1,nj)
end do

```

```
end do  
close(10)  
  
40      format(150(x,e24.16))  
100     format(e16.8,100(x,e24.12))  
End
```

Appendix D

This code is written to carry out 2D Fourier analysis. Lines 1-23 of this code contain the definition of variables; Lines 25-64 are the input data and step size definition; Lines 66-91 describe the process of 2D Fourier transform; Lines 93-123 are used to output final data.

```

Program 2DFT
implicit real*8 (a-h,o-z)
integer nt,nj,n,mj,ntst,nted,lgwd,alpha,cs,step,st,nop
real*8 towpi,pi,deltat,maxw,dw,dt
parameter(nm=600001,mm=200,nt=(nm-1)/mm+1,
nj=501,mj=85,n=mj*nt)
Parameter(alpha=100,cs=80,st=200,stl=20,nop=1001)
parameter(pi=3.1415926535897932384d0,twopi=6.2831853071795
9d0)
Parameter(automvcn=5.14221d12,automisec=0.0242d-9)
Parameter(automhz=6579682606.6812d0)
integer INFO
double precision tim(nm),field2(nm),field3(nm)
double precision COMM(3*n+100),X(n,nj),t(nop),gauss(nop)
double precision field0(nt),field1(nt),time(nt),time1(nj)
double precision w((n-1)/2),amp((n-1)/2,nj),
phi((n-1)/2,nj)
common /field/ amp,phi,X

character*8 filedat
character*14 fileout

open(5,file='04001fields',status='old')
do it=1,nt
  read(5,*) tim(it),field2(it),field3(it)
end do
close(5)

do it=1,nt
  time(it)=tim((it-1)*mm+1)
  field0(it)=field2((it-1)*mm+1)
  field1(it)=field3((it-1)*mm+1)
end do

open(6,file='fieldsa.dat',status='unknown')
do it=1,nt
  write(6,100) time(it),field0(it),field1(it)
end do
close(6)

dt=cs/(nop-1)
do i=1,nop
  t(i)=(i-1)*dt
  gauss(i)=alpha*exp(-(t(i)-cs/2.d0)**2.d0/2/cs**2)
end do

open(7,file='gaussian.dat',status='unknown')
do i=1,nop
  write(7,100) t(i),gauss(i)
end do
close(7)

deltat=time(2)-time(1)
maxw=0.5d0/deltat/twopi
dw=maxw/(((n-1)/2)-1.d0)
write(13,*) maxw

do it=1,(n-1)/2
  w(it)=(it-1)*dw
end do

step=(nt-1)/(nj-1)

do i=1,nj
  time1(i)=time((i-1)*step+1)
end do

do it=1,n

```

```

X(it,i)=0.d0
end do

do it=((mj-1)/2)*nt+1,((mj+1)/2)*nt
  X(it,i)=field1(it-nt*((mj-1)/2))
end do

ntst=((mj-1)/2)*nt+(i-1)*step+1
do it=1,n
  X(it,i)=X(it,i)*alpha*exp(-(it-ntst)**2.d0/2/cs**2)
end do

call DZFFT( i, n, X, COMM, INFO )

do it=1,(n-1)/2
  amp(it,i)=dsqrt(X(it+1,i)**2+X(n-it+1,i)**2)
  phi(it,i)=atan(X(n-it+1,i)/X(it+1,i))
end do

end do

open(17,file='FFT2Da.dat',status='unknown')
write(17,50) (time1(i),i=1,nj)
do it=nt*23,nt*31,stl
  write(17,50) w(it),(amp(it,i),i=1,nj)
end do
close(17)

open(18,file='FFT2D1a.dat',status='unknown')
write(18,50) (time1(i),i=1,nj)
do it=1,(n-1)/2,st
  write(18,50) w(it),(amp(it,i),i=1,nj)
end do

close(18)

open(19,file='FFT2D2a.dat',status='unknown')
write(19,50) (time1(i),i=1,nj)
  do it=nt*23,nt*31,stl
    write(19,50) w(it),(log(amp(it,i)),i=1,nj)
  close(19)

open(20,file='FFT2D3a.dat',status='unknown')
write(20,50) (time1(i),i=1,nj)
do it=1,(n-1)/2,st
  write(20,50) w(it),(log(amp(it,i)),i=1,nj)
end do
close(20)

50      format(1000(x,e21.13))
100     format(e16.8,100(x,e24.12))

End

```

Appendix E

This code is written to carry out minimization for two-ion system. Lines 1-6 of this code contain the definition of variables; Lines 8-29 are the definition of potential energy of the system; Lines 33-58 describe the process of minimization; Lines 60-63 are used to output final data.

```

Program 2DMIN
parameter(nz=2,niter=2000,z1g=-15000,z2g=15000)
Parameter(automhz=6579682606.6812d0,std=1.0d-8)
real*8 mass1,mu,w,w01,dk1,beta1,V,V1,zd
double precision z(nz),sdz(nz),fdz(nz),minz(nz)
pi=acos(-1.d0)

c harmonic parameters for Cd ion(in a.u.):
mass1=111.d0
mass1=mass1*1822.8885d0
mu=1.d0
w=2770.0*2*pi
w=w*3.33564d-8/219474.63d0

c Hamonic parameters for mode 1 (in a.u.)
w01=w
dk1=dsqrt(mass1)*w01           ! dk=dsqrt(k)
beta1=dsqrt(mass1)*dk1

c potential
z(1)=z1g
z(nz)=z2g
iter=0
V1=0.5*dk1**2*z(1)**2+0.5*dk1**2*z(nz)**2
$                               +1/abs(z(nz)-z(1))
write(10,20) iter,V1,z(1),z(nz)

10      continue

iter=iter+1

do iz=1,nz
  sdz(iz)=dk1**2+2/(z(nz)-z(1))**3
  write(20,*) sdz(iz)
end do

do iz=1,nz
  fdz(iz)=dk1**2*z(iz)+(-1)**(iz-1)/(z(nz)-z(1))**2
  write(30,*) fdz(iz)
end do

do iz=1,nz
  minz(iz)=z(iz)-fdz(iz)/sdz(iz)
  write(40,*) minz(iz)
end do

V=0.5*dk1**2*minz(1)**2+0.5*dk1**2*minz(nz)**2
$                               +1/abs(minz(nz)-minz(1))

write(60,20) iter,V,minz(1),minz(nz)
Zd=abs(minz(2)-z(2))
z(1)=minz(1)
z(nz)=minz(nz)

if(std.lt.zd) goto 10

write(50,20) iter,V,minz(1),minz(nz)
20      format(i6,10(x,e25.16))
end

```

Appendix F

This code is written to dianonalize the Hessian matrix for two-ion system.

Lines 1-10 of this code contain the definition of variables; Lines 12-35 are the input

data; Lines 37-83 describe the construction of Hessian matrix; Lines 85-101 are used

to diaganalize the Hessian matrix and output final data.

```

Program 2DHESSIAN
parameter(nz=2)
real*8 mass1,mu,w,w01,dk1,betal
double precision
z(nz),m(nz,nz),V(nz,nz),F(nz,nz),sqrtm(nz,nz)
character*1 UPLO, JOBZ
parameter(JOBZ ='V',UPLO ='U')
double precision Eigenv(nz),WORK(3*nz-1)
integer INFO
pi=acos(-1.d0)

c harmonic parameters for Cd ion(in a.u.):
mass1=111.d0
mass1=mass1*1822.8885d0
mu=1.d0
w=2770.0*2*pi
w=w*3.33564d-8/219474.63d0

c Hamonic parameters for mode 1 (in a.u.)
w01=w
dk1=dsqrt(mass1)*w01           !dk=dsqrt(k)
betal=dsqrt(mass1)*dk1

c potential
open(100,file='equilibrium.dat',status='old')
read(100,*) (z(iz),iz=1,nz)
close(100)

open(30,file='position.dat',status='unknown')
do iz=1,nz
  write(30,20) z(iz)
end do

close(30)

do iz=1,nz
  do ix=1, nz
    if(ix.eq.iz) then
      m(iz,ix)=mass1
    else
      m(iz,ix)=0
    end if
  end do
end do

do iz=1,nz
  do ix=1, nz
    if(ix.eq.iz) then
      sqrtm(iz,ix)=m(iz,ix)**(-0.5)
    else
      sqrtm(iz,ix)=0
    end if
  end do
end do

open(40,file='mass.dat',status='unknown')
do iz=1,nz
  write(40,20) (sqrtm(iz,ix),ix=1,nz)
end do
close(40)

do iz=1,nz
  do ix=1,nz
    if(ix.eq.iz) then
      V(iz,ix)=dk1**2+2/(z(nz)-z(1))**3
    else
      V(iz,ix)=-2/(z(nz)-z(1))**3
    end if
  end do
end do

```

```
    end if
    end do
end do

do iz=1,nz
  do ix=1,nz
    F(iz,ix)=V(iz,ix)/mass1
  end do
end do

open(50,file='function.dat',status='unknown')
do iz=1,nz
  write(50,20) (F(iz,ix),ix=1,nz)
end do
close(50)

call DSYEV( JOBZ, UPLO, nz, F, nz, Eigenv, WORK, 3*nz-1,
INFO )

open(10,file='Eigenvalue.dat',status='unknown')
do iz=1,nz
  write(10,20) Eigenv(iz)
end do
close(10)

open(20,file='Eigenvector.dat',status='unknown')
do iz=1,nz
  write(20,20) (F(iz,ix),ix=1,nz)
end do
close(20)

20      format(10(x,e25.16))
end
```

Appendix G

This code is written to diagonalize the Hamiltonian matrix of two $^{111}\text{Cd}^+$ ions in the harmonic potential trap to obtain its eigenvalues (energies) and the eigenvectors (parameter matrix \mathbf{C} in Sec. 2.2). Lines 1-32 of this code contain the definition of variables; Lines 34-78 are the input data and step size definition; Lines 80-299 describe the basis set expansion based on two normal vibration modes; Lines 300-348 define kinetic energy matrix and lines 350-387 are definition of potential energy matrix; Hamiltonian matrix is constructed in lines 389-413; DSYEV subroutine from ACML library is used in lines 415-428 for matrix diagonalization [101]; Lines 430-539 are the construction of wavefunctions of the system; Transition matrix is calculated in lines 541-667; Lines 670-683 are the subroutine NVJ which is used to calculate $j!$ of Eq. (2.2.5) and the subroutine OTHPL in lines 684-741 describe calculation of Hermite polynomials and their first derivatives [82]. In this program, during the numerical calculations for the spectrum of vibrational states, I used atomic units. It was transformed into the units of MHz at the end.

```

Program 2DIONTRAP
implicit real*8 (a-h,o-z)
integer mv,nz,mz,ciz1,ciz2,dz1,dz2
real*8 towpi,autonm
parameter(mv=15,max=60)
parameter(nz=101,mz=2,dz1=10,dz2=10)
parameter(twopi=6.28318530717959d0)
parameter(autonm=0.05291772d0)
Parameter(automhz=6579682606.6812d0)
character*1 UPLO, JOBZ
parameter(JOBZ ='V',UPLO ='U')
integer INFO
double precision EV(mv*mv),EZ (mv*mv,mv*mv),WORK(3*(mv*mv)-
1)

real*8
mass1,mu,n,n1,n2,y1,y2,sum1,sum2,sum3,sum4,sum,G,G1,G2
real*8 alphal,alpha2,dk1,w,w1,w2
double precision ek(mz),cz(mz), z1(nz),z2(nz)
double precision psil1(mv,nz),psi2(mv,nz),h(max),dh(max)
double precision psil1r(mv,nz),psi2r(mv,nz),V(nz,nz)
double precision norm1(mv,mv),norm2(mv,mv)
double precision psill1(mv,nz),psi22(mv,nz)
double precision bs1(mv*mv,nz,nz),bs2(mv*mv,nz,nz)
double precision bs3(mv*mv,nz,nz),wavef(mv*mv,nz,nz)
double precision hk1(mv*mv,mv*mv),hk2(mv*mv,mv*mv)
double precision KE(mv*mv,mv*mv),PE (mv*mv,mv*mv)
double precision Hamil(mv*mv,mv*mv),Hamil1(mv*mv,mv*mv)
double precision KE1(mv*mv,mv*mv),PE1(mv*mv,mv*mv)
double precision
AEV(mv,mv),Evaluate(mv,mv),dipole(mv*mv,mv*mv)
pi=acos(-1.d0)

c harmonic parameters for Cd ion(in a.u.):
mass1=111.d0
mass1=mass1*1822.8885d0
mu=1.d0
w=2770.0*2*pi
w=w*3.33564d-8/219474.63d0
dk1=dsqrt (mass1)*w           !dk=dsqrt(k)

open(5,file='Eigenvalue.dat',status='old')
do iz=1,mz
  read(5,*) ek(iz)
end do
close(5)

open(3,file='position.dat',status='old')
do iz=1,mz
  read(3,*) cz(iz)
end do
close(3)

do i=1,mv
  do j=1,mv
    AEV(i,j)=(i-0.5d0)*dsqrt(ek(1))+(j-0.5d0)*dsqrt(ek(mz))
    AEV(i,j)=AEV(i,j)*automhz
  end do
end do

open(2,file='ApproEigen.dat',status='unknown')
do i=1,mv
  write(2,50) (AEV(i,j),j=1,mv)
end do
close(2)

Zmax=dz1*(nz-1)

```

```

zi=-Zmax/2
zf=Zmax/2

do iz1=1,nz
  z1(iz1)=zi+(iz1-1)*dz1
end do

do iz2=1,nz
  z2(iz2)=zi+(iz2-1)*dz2
end do

c Basis functions for mode 1 (in a.u.)
w1=dsqrt(ek(1))
alpha1=dsqrt(mass1*w1)
do iz1=1,nz
  y1=alpha1*z1(iz1)
  iv1=0
  psil(iv1+1,iz1)=dsqrt(alpha1)/(pi**0.25d0)*dexp(-
y1**2/2.d0)

!!!!!! call the subroutine which will give the value
of Hermite.
call othpl(4,mv,y1,h,dh)
do iv1=1,mv-1,1
  n=iv1
  call nvj(n,b)
  n1=dsqrt(alpha1/dsqrt(pi)/(2**n)/b)
  psil(iv1+1,iz1)=n1*h(iv1+1)*dexp(-y1**2/2.d0)
end do
end do

cc Normalization of wavefunctions for mode 1.
do iv1=1,mv
  suml=0.d0
  do iz1=1,nz
    suml=suml+psil(iv1,iz1)**2
  end do
  suml=suml*dz1
  do iz1=1,nz
    psil(iv1,iz1)=psil(iv1,iz1)/dsqrt(suml)
  end do
end do

c Test of wavefunction

open(10,file='basisset1.dat',status='unknown')
do iz1=1,nz
  write(10,10) z1(iz1),(psil(iv1,iz1),iv1=1,mv)
end do
close(10)

c Test of orthonormality:

do iv1=1,mv
  do jv1=1,mv
    suml=0.d0
    do iz1=1,nz
      suml=suml+psil(iv1,iz1)*psil(jv1,iz1)
    end do
    norml(iv1,jv1)=suml*dz1
  end do
end do

open(20,file='matrix1.dat',status='unknown')
do iv1=1,mv
  write(20,20) (norml(iv1,jv1),jv1=1,mv)
end do
close(20)

```

```

c Basis functions for mode 2 (in a.u.)

w2=dsqrt(ek(mz))
alpha2=dsqrt(mass1*w2*ek(1)/ek(mz))
c Harmonic wavefunctions for ion 2
do iz2=1,nz
  y2=alpha2*z2(iz2)
  iv2=0
  psi2(iv2+1,iz2)=dsqrt(alpha2) / (pi**0.25d0) *dexp(-
y2**2/2.d0)

!!!!!! call the subroutine which will give the value
of Hermite.
call othpl(4,mv,y2,h,dh)
do iv2=1,mv-1,1
  n=iv2
  call nvj(n,b)
  n2=dsqrt(alpha2/dsqrt(pi)/(2**n)/b)
  psi2(iv2+1,iz2)=n2*h(iv2+1)*dexp(-y2**2/2.d0)
end do
end do

cc Normalization of wavefunctions for mode 2.
do iv2=1,mv
  sum2=0.d0
  do iz2=1,nz
    sum2=sum2+psi2(iv2,iz2)**2
  end do
  sum2=sum2*dz2
  do iz2=1,nz
    psi2(iv2,iz2)=psi2(iv2,iz2)/dsqrt(sum2)
  end do
end do

c Test of wavefunction

open(30,file='basisset2.dat',status='unknown')
do iz2=1,nz
  write(30,10) z2(iz2), (psi2(iv2,iz2),iv2=1,mv)
end do
close(30)

c Test of orthonormality:

do iv2=1,mv
  do jv2=1,mv
    sum2=0.d0
    do iz2=1,nz
      sum2=sum2+psi2(iv2,iz2)*psi2(jv2,iz2)
    end do
    norm2(iv2,jv2)=sum2*dz2
  end do
end do

open(40,file='matrix2.dat',status='unknown')
do iv2=1,mv
  write(40,20) (norm2(iv2,jv2),jv2=1,mv)
end do
close(40)

c calculate Hamitonian

c second direvative of kinetic energy part for mode 1

do iz1=1,nz
  y1=alpha1*z1(iz1)
  call othpl(4,mv,y1,h,dh)

```

```

G=exp (-1*y1**2/2.d0)
G1=-1*alpha1**2*z1(iz1)*exp (-1*y1**2/2.d0)
G2=alpha1**2*exp (-1*y1**2/2.d0)*(y1**2-1)
iv1=0
psi11(iv1+1,iz1)=dsqrt(alpha1/dsqrt(pi))*G2
do iv1=1,mv-1
  n=iv1
  call nvj(n,b)
  n1=dsqrt(alpha1/dsqrt(pi)/(2**n)/b)
  H1=alpha1*dh(iv1+1)
  H2=2*iv1*dh(iv1)*alpha1**2
  psi11(iv1+1,iz1)=n1*(G2*h(iv1+1)+2*G1*H1+G*H2)
end do
end do

do iv1=1,mv
  do iz1=1,nz
    psi1r(iv1,iz1)=-psi11(iv1,iz1)/2.d0/mass1
  end do
end do

c second derivative of first mode

open(50,file='secwavr1.dat',status='unknown')
do iz1=1,nz
  write(50,30) z1(iz1),(psi1r(iv1,iz1),iv1=1,mv)
end do
close(50)

c second direvative of kinetic energy part for mode 2

do iz2=1,nz
  y2=alpha2*z2(iz2)
  call othpl(4,mv,y2,h,dh)
  G=exp (-1*y2**2/2.d0)
  G1=-1*alpha2**2*z2(iz2)*exp (-1*y2**2/2.d0)
  G2=alpha2**2*exp (-1*y2**2/2.d0)*(y2**2-1)
  iv2=0
  psi22(iv2+1,iz2)=dsqrt(alpha2/dsqrt(pi))*G2
  do iv2=1,mv-1
    n=iv2
    call nvj(n,b)
    n2=dsqrt(alpha2/dsqrt(pi)/(2**n)/b)
    H1=alpha2*dh(iv2+1)
    H2=2*iv2*dh(iv2)*alpha2**2
    psi22(iv2+1,iz2)=n2*(G2*h(iv2+1)+2*G1*H1+G*H2)
  end do
  end do

do iv2=1,mv
  do iz2=1,nz
    psi2r(iv2,iz2)=-psi22(iv2,iz2)*ek(mz)/ek(1)/2.d0/mass1
  end do
end do

c second derivative of second mode

open(60,file='secwavr2.dat',status='unknown')
do iz2=1,nz
  write(60,30) z2(iz2),(psi2r(iv2,iz2),iv2=1,mv)
end do
close(60)

c basis set of the system

do iv=1,mv
  do jv =1,mv
    do iz1=1,nz

```

```

do iz2=1,nz                                sum3=sum3+bs1(i,iz1,iz2)*bs2(j,iz1,iz2)
bs1((jv-1)*mv+iv,iz1,iz2)=psi1(iv,iz1)*psi2(jv,iz2)      end do
end do                                         end do
end do                                         hk1(i,j)=sum3*dz1*dz2
end do                                         end do
end do                                         end do

do iv=1,mv
do jv =1,mv
do iz1=1,nz
do iz2=1,nz
bs2((jv-1)*mv+iv,iz1,iz2)=psi1r(iv,iz1)*psi2(jv,iz2)
end do
end do
end do
end do

do iv=1,mv
do jv =1,mv
do iz1=1,nz
do iz2=1,nz
bs3((jv-1)*mv+iv,iz1,iz2)=psi2r(jv,iz2)*psi1(iv,iz1)
end do
end do
end do
end do

c kinetic energy matrix

do i=1,mv*mv
do j=1,mv*mv
sum3=0.d0
do iz1=1,nz
do iz2=1,nz
sum3=sum3+bs1(i,iz1,iz2)*bs2(j,iz1,iz2)
end do
end do
hk1(i,j)=sum3*dz1*dz2
end do
end do

do i=1,mv*mv
do j=1,mv*mv
sum3=0.d0
do iz1=1,nz
do iz2=1,nz
sum3=sum3+bs1(i,iz1,iz2)*bs3(j,iz1,iz2)
end do
end do
hk2(i,j)=sum3*dz1*dz2
end do
end do

do i=1,mv*mv
do j=1,mv*mv
KE(i,j)=hk1(i,j)+hk2(i,j)
end do
end do

open(70,file='kinetic.dat',status='unknown')
do i=1,mv*mv
write(70,50) (KE(i,j),j=1,mv*mv)
end do
close(70)

do i=1,mv*mv
do j=1,mv*mv
KE1(i,j)=KE(i,j)*automhz
end do
end do

```

```

end do
end do

open(700,file='kinetic1.dat',status='unknown')
do i=1,mv*mv
  write(700,50) (KE1(i,j),j=1,mv*mv)
end do
close(700)

c potential energy matrix
do i=1,mv*mv
  do j=1,mv*mv
    sum4=0.d0
    do iz1=1,nz
      do iz2=1,nz
        V(iz1,iz2)=0.5d0*dk1**2*z1(iz1)**2
$       +0.5d0*dk1**2*z2(iz2)**2*ek(1)/ek(mz)
$       +dk1**2*z2(iz2)*(cz(mz)-
$       cz(1))*dsqrt(ek(1)/ek(mz)/2.d0)
$       +1/abs(dsqrt(2.d0*ek(1)/ek(mz)))
$       *z2(iz2)+cz(mz)-cz(1))
$       +dk1**2*cz(mz)**2-0.5d0*dk1**2*cz(1)**2
$       -0.5d0*dk1**2*cz(mz)**2-1/abs(cz(mz)-cz(1))
sum4=sum4+bs1(i,iz1,iz2)*V(iz1,iz2)*bs1(j,iz1,iz2)
      end do
    end do
    PE(i,j)=sum4*dz1*dz2
  end do
end do

open(80,file='potential.dat',status='unknown')
do i=1,mv*mv
  write(80,50) (PE(i,j),j=1,mv*mv)
end do

close(80)
do i=1,mv*mv
  do j=1,mv*mv
    PE1(i,j)=PE(i,j)*automhz
  end do
end do

open(800,file='potential1.dat',status='unknown')
do i=1,mv*mv
  write(800,50) (PE1(i,j),j=1,mv*mv)
end do
close(800)

c Hamiltonian matrix
do i=1,mv*mv
  do j=1,mv*mv
    Hamil(i,j)=KE(i,j)+PE(i,j)
  end do
end do

open(90,file='Hamiltonian.dat',status='unknown')
do i=1,mv*mv
  write(90,50) (Hamil(i,j),j=1,mv*mv)
end do
close(90)

do i=1,mv*mv
  do j=1,mv*mv
    Hamill(i,j)=Hamil(i,j)*automhz
  end do
end do

```

```

open(900,file='Hamiltonian1.dat',status='unknown')
do i=1,mv*mv
  write(900,50) (Hamill(i,j),j=1,mv*mv)
end do
close(900)

call DSYEV( JOBZ, UPLO, mv*mv, Hamil, mv*mv, EV, WORK,
$           3*(mv*mv)-1, INFO )

open(100,file='Eigen.dat',status='unknown')
do i=1,mv*mv
  write(100,50) EV(i)*automhz
end do
close(100)

open(110,file='Eigenvector.dat',status='unknown')
do i=1,mv*mv
  write(110,50) (Hamil(i,j),j=1,mv*mv)
end do
close(110)

do iz1=1,nz
  do iz2=1,nz
    do j=1,mv*mv
      sum=0.d0
      do i=1,mv*mv
        sum=sum+Hamil(i,j)*bs1(i,iz1,iz2)
      end do
      wavef(j,iz1,iz2)=sum
    end do
  end do
end do

c Output of wavefunctions

open(120,file='wavefunction00.dat',status='unknown')
write(120,50) (z1(iz1),iz1=1,nz)
do i=1,1
  do iz2=1,nz
    write(120,50) z2(iz2),(wavef(i,iz1,iz2),iz1=1,nz)
  end do
end do
close(120)

open(121,file='wavefunction10.dat',status='unknown')
write(121,50) (z1(iz1),iz1=1,nz)
do i=2,2
  do iz2=1,nz
    write(121,50) z2(iz2),(wavef(i,iz1,iz2),iz1=1,nz)
  end do
end do
close(121)

open(122,file='wavefunction01.dat',status='unknown')
write(122,50) (z1(iz1),iz1=1,nz)
do i=3,3
  do iz2=1,nz
    write(122,50) z2(iz2),(wavef(i,iz1,iz2),iz1=1,nz)
  end do
end do
close(122)

open(123,file='wavefunction20.dat',status='unknown')
write(123,50) (z1(iz1),iz1=1,nz)
do i=4,4
  do iz2=1,nz
    write(123,50) z2(iz2),(wavef(i,iz1,iz2),iz1=1,nz)
  end do
end do

```

```

close(123)

open(124,file='wavefunction30.dat',status='unknown')
write(124,50) (z1(iz1),iz1=1,nz)
do i=6,6
  do iz2=1,nz
    write(124,50) z2(iz2), (wavef(i,iz1,iz2),iz1=1,nz)
  end do
end do
close(124)

open(125,file='wavefunction02.dat',status='unknown')
write(125,50) (z1(iz1),iz1=1,nz)
do iz2=1,nz
  do i=7,7
    write(125,50) z2(iz2), (wavef(i,iz1,iz2),iz1=1,nz)
  end do
end do
close(125)

open(126,file='wavefunction40.dat',status='unknown')
write(126,50) (z1(iz1),iz1=1,nz)
do iz2=1,nz
  do i=9,9
    write(126,50) z2(iz2), (wavef(i,iz1,iz2),iz1=1,nz)
  end do
end do
close(126)

open(127,file='wavefunction50.dat',status='unknown')
write(127,50) (z1(iz1),iz1=1,nz)
do iz2=1,nz
  do i=12,12
    write(127,50) z2(iz2), (wavef(i,iz1,iz2),iz1=1,nz)
  end do
end do
close(127)

open(128,file='wavefunction03.dat',status='unknown')
write(128,50) (z1(iz1),iz1=1,nz)
do iz2=1,nz
  do i=13,13
    write(128,50) z2(iz2), (wavef(i,iz1,iz2),iz1=1,nz)
  end do
end do
close(128)

open(129,file='wavefunction60.dat',status='unknown')
write(129,50) (z1(iz1),iz1=1,nz)
do iz2=1,nz
  do i=16,16
    write(129,50) z2(iz2), (wavef(i,iz1,iz2),iz1=1,nz)
  end do
end do
close(129)

open(130,file='wavefunction04.dat',status='unknown')
write(130,50) (z1(iz1),iz1=1,nz)
do iz2=1,nz
  do i=20,20
    write(130,50) z2(iz2), (wavef(i,iz1,iz2),iz1=1,nz)
  end do
end do
close(130)

open(131,file='wavefunction05.dat',status='unknown')
write(131,50) (z1(iz1),iz1=1,nz)
do iz2=1,nz

```

```

do i=29,29
  write(131,50) z2(iz2), (wavef(i,iz1,iz2),iz1=1,nz)
end do
end do
close(131)

open(132,file='wavefunction06.dat',status='unknown')
write(132,50) (z1(iz1),iz1=1,nz)
do iz2=1,nz
  do i=40,40
    write(132,50) z2(iz2), (wavef(i,iz1,iz2),iz1=1,nz)
  end do
end do
close(132)

open(133,file='wavefunction11.dat',status='unknown')
write(133,50) (z1(iz1),iz1=1,nz)
do iz2=1,nz
  do i=5,5
    write(133,50) z2(iz2), (wavef(i,iz1,iz2),iz1=1,nz)
  end do
end do
close(133)

open(134,file='wavefunction12.dat',status='unknown')
write(134,50) (z1(iz1),iz1=1,nz)
do iz2=1,nz
  do i=10,10
    write(134,50) z2(iz2), (wavef(i,iz1,iz2),iz1=1,nz)
  end do
end do
close(134)

open(135,file='wavefunction13.dat',status='unknown')
write(135,50) (z1(iz1),iz1=1,nz)
do iz2=1,nz
  do i=17,17
    write(135,50) z2(iz2), (wavef(i,iz1,iz2),iz1=1,nz)
  end do
end do
close(135)

open(136,file='wavefunction21.dat',status='unknown')
write(136,50) (z1(iz1),iz1=1,nz)
do iz2=1,nz
  do i=8,8
    write(136,50) z2(iz2), (wavef(i,iz1,iz2),iz1=1,nz)
  end do
end do
close(136)

open(137,file='wavefunction22.dat',status='unknown')
write(137,50) (z1(iz1),iz1=1,nz)
do iz2=1,nz
  do i=14,14
    write(137,50) z2(iz2), (wavef(i,iz1,iz2),iz1=1,nz)
  end do
end do
close(137)

open(138,file='wavefunction23.dat',status='unknown')
write(138,50) (z1(iz1),iz1=1,nz)
do iz2=1,nz
  do i=22,22
    write(138,50) z2(iz2), (wavef(i,iz1,iz2),iz1=1,nz)
  end do
end do
close(138)

```

```

open(139,file='wavefunction31.dat',status='unknown')
write(139,50) (z1(iz1),iz1=1,nz)
do iz2=1,nz
  do i=11,11
    write(139,50) z2(iz2),(wavef(i,iz1,iz2),iz1=1,nz)
  end do
end do
close(139)

open(140,file='wavefunction32.dat',status='unknown')
write(140,50) (z1(iz1),iz1=1,nz)
do iz2=1,nz
  do i=18,18
    write(140,50) z2(iz2),(wavef(i,iz1,iz2),iz1=1,nz)
  end do
end do
close(140)

open(141,file='wavefunction33.dat',status='unknown')
write(141,50) (z1(iz1),iz1=1,nz)
do iz2=1,nz
  do i=27,27
    write(141,50) z2(iz2),(wavef(i,iz1,iz2),iz1=1,nz)
  end do
end do
close(141)

c Transition matrix:

do i=1,mv*mv
  do j=1,mv*mv
    sum=0.d0
    do iz1=1,nz
      do iz2=1,nz
        sum=sum+wavef(i,iz1,iz2)*mu*(-
          dsqrt(2/mass1)*z1(iz1))
        $           *wavef(j,iz1,iz2)
      end do
    end do
    dipole(i,j)=sum*dz1*dz2
  end do
end do

open(200,file='transitiondipole.dat',status='unknown')
do i=1,mv*mv
  write(200,20) (dipole(i,j),j=1,mv*mv)
end do
close(200)

10   format(e24.16,150(x,f24.16))
20   format(150(x,e24.16))
30   format(e24.16,150(x,f24.16))
40   format(150(x,e24.16))
50   format(550(x,e24.16))
End

c-----
SUBROUTINE NVJ(M,A)
REAL*8 I,M,A

IF(M.EQ.0) THEN
  A=1.0
ELSE
  A=1.0
  DO I=1,M
    A=A*I
  END DO

```

```

END IF

C      WRITE(200,*) A
END
C-----
SUBROUTINE OTHPL(KF,N,X,PL,DPL)
C =====
C PURPOSE: COMPUTE ORTHOGONAL POLYNOMIALS: TN(X) OR
UN(X),
C           OR LN(X) OR HN(X), AND THEIR DERIVATIVES
C INPUT : KF --- FUNCTION CODE
C          KF=1 FOR CHEBYSHEV POLYNOMIAL TN(X)
C          KF=2 FOR CHEBYSHEV POLYNOMIAL UN(X)
C          KF=3 FOR LAGUERRE POLYNOMIAL LN(X)
C          KF=4 FOR HERMITE POLYNOMIAL HN(X)
C N --- ORDER OF ORTHOGONAL POLYNOMIALS
C X --- ARGUMENT OF ORTHOGONAL POLYNOMIALS
C OUTPUT: PL(N) --- TN(X) OR UN(X) OR LN(X) OR HN(X)
C          DPL(N)--- TN'(X) OR UN'(X) OR LN'(X) OR
HN'(X)
C =====
C
IMPLICIT DOUBLE PRECISION (A-H,O-Z)
DIMENSION PL(0:N),DPL(0:N)
A=2.0D0
B=0.0D0
C=1.0D0
Y0=1.0D0
Y1=2.0D0*X
DY0=0.0D0
DY1=2.0D0
PL(0)=1.0D0
PL(1)=2.D0*X
DPL(0)=0.0D0

```

```

DPL(1)=2.0D0
IF (KF.EQ.1) THEN
  Y1=X
  DY1=1.0D0
  PL(1)=X
  DPL(1)=1.0D0
ELSE IF (KF.EQ.3) THEN
  Y1=1.D0-X
  DY1=-1.0D0
  PL(1)=1.0D0-X
  DPL(1)=-1.0D0
END IF
DO 10 K=2,N
  IF (KF.EQ.3) THEN
    A=-1.0D0/K
    B=2.0D0+A
    C=1.0D0+A
  ELSE IF (KF.EQ.4) THEN
    C=2.0D0*(K-1.0D0)
  END IF
  YN=(A*X+B)*Y1-C*Y0
  DYN=A*Y1+(A*X+B)*DY1-C*DY0
  PL(K)=YN
  DPL(K)=DYN
  Y0=Y1
  Y1=YN
  DY0=DY1
10      DY1=DYN
RETURN
END
C=====

```

Appendix H

This code is written to carry out minimization for three-ion system. Lines 1-7 of this code contain the definition of variables; Lines 9-34 are the definition of potential energy of the system; Lines 36-80 describe the process of minimization; Lines 82-93 are used to output final data.

```

Program 3DMIN
Real*8 automhz,std
parameter(nz=3,z1g=-15000,z2g=-20,z3g=15000)
Parameter(automhz=6579682606.6812d0,std=2.4d-8)
real*8 mass1,mu,w,w01,dk1, Vi,Zd
double precision z(nz),sdz(nz),fdz(nz),minz(nz),V,V1
pi=acos(-1.d0)

c harmonic parameters for Cd ion(in a.u.):
mass1=111.d0
mass1=mass1*1822.8885d0
mu=1.d0
w=2770.0*2*pi
w=w*3.33564d-8/219474.63d0
w01=w
dk1=dsqrt(mass1)*w01           !dk=dsqrt(k)

dl=(1/mass1/(w01**2))**(1.d0/3.d0)
x1=(-1)*(5.d0/4.d0)**(1.d0/3.d0)*dl
x2=0.d0*dl
x3=(5.d0/4.d0)**(1.d0/3.d0)*dl

c potential
z(1)=z1g
z(2)=z2g
z(nz)=z3g
iter=0
Vi=0.5*dk1**2*z(1)**2+0.5*dk1**2*z(2)**2
$ +0.5*dk1**2*z(nz)**2
$ +1/abs(z(2)-z(1))+1/abs(z(nz)-z(1))+1/abs(z(nz)-z(2))
write(10,20) iter,Vi,z(1),z(2),z(nz)

open(60,file='potential.dat',status='unknown')
10      continue
iter=iter+1

sdz(1)=dk1**2+2/(z(2)-z(1))**3+2/(z(nz)-z(1))**3
sdz(2)=dk1**2+2/(z(2)-z(1))**3+2/(z(nz)-z(2))**3
sdz(nz)=dk1**2+2/(z(nz)-z(1))**3+2/(z(nz)-z(2))**3
do iz=1,nz
    write(20,*) sdz(iz)
end do

fdz(1)=dk1**2*z(1)+1/(z(2)-z(1))**2+1/(z(nz)-z(1))**2
fdz(2)=dk1**2*z(2)-1/(z(2)-z(1))**2+1/(z(nz)-z(2))**2
fdz(nz)=dk1**2*z(nz)-1/(z(nz)-z(1))**2-1/(z(nz)-z(2))**2
do iz=1,nz
    write(30,*) fdz(iz)
end do

do iz=1,nz
    minz(iz)=z(iz)-fdz(iz)/sdz(iz)
    write(40,*) minz(iz)
end do

V1=0.5*dk1**2*minz(1)**2+0.5*dk1**2*minz(2)**2
$ +0.5*dk1**2*minz(nz)**2+1/abs(minz(2)-minz(1))
$ +1/abs(minz(nz)-minz(1))+1/abs(minz(nz)-minz(2))

write(60,20) iter,V1,V1*automhz,minz(1),minz(2),minz(nz)

V=0.5*dk1**2*z(1)**2+0.5*dk1**2*z(2)**2
$ +0.5*dk1**2*z(nz)**2
$ +1/abs(z(2)-z(1))+1/abs(z(nz)-z(1))+1/abs(z(nz)-z(2))

```

```
Zd=abs(minz(2)-z(2))
z(1)=minz(1)
z(2)=minz(2)
z(nz)=minz(nz)

if(Zd.gt.std) goto 10
close(60)

write(50,20) iter,V,minz(1),minz(2),minz(nz)

open(70,file='equilibrium.dat',status='unknown')
do iz=1,nz
    write(70,30) z(iz)
end do
close(70)

write(80,30) x1,x2,x3
20      format(i6,10(x,e25.16))
30      format(10(x,e25.16))
end
```

Appendix I

This code is written to dianonalize the Hessian matrix for three-ion system.

Lines 1-10 of this code contain the definition of variables; Lines 12-26 are the input data; Lines 28-80 describe the construction of Hessian matrix; Lines 82-98 are used to diaganalize the Hessian matrix and output final data.

```

Program 3DHESSIAN
parameter(nz=3)
real*8 mass1,mu,w,w01,dk1
double precision
z(nz),m(nz,nz),V(nz,nz),F(nz,nz),sqrtm(nz,nz)
character*1 UPLO, JOBZ
parameter(JOBZ = 'V', UPLO = 'U')
double precision Eigenv(nz),WORK(3*nz-1)
integer INFO
pi=acos(-1.d0)

c harmonic parameters for Cd ion(in a.u.):
mass1=111.d0
mass1=mass1*1822.8885d0
mu=1.d0
w=2770.0*2*pi
w=w*3.33564d-8/219474.63d0
w01=w
dk1=dsqrt(mass1)*w01           ! dk=dsqrt(k)

c potential
open(100,file='equilibrium.dat',status='old')
do iz=1,nz
  read(100,20) z(iz)
end do
close(100)

do iz=1,nz
  do ix=1,nz
    if(ix.eq.iz) then
      m(iz,ix)=mass1
    else
      m(iz,ix)=0
    end if
  end do
end do

do iz=1,nz
  do ix=1,nz
    if(ix.eq.iz) then
      sqrtm(iz,ix)=m(iz,ix)**(-0.5)
    else
      sqrtm(iz,ix)=0
    end if
  end do
end do

open(40,file='mass.dat',status='unknown')
do iz=1,nz
  write(40,20) (sqrtm(iz,ix),ix=1,nz)
end do
close(40)

do iz=1,nz-1
  do ix=iz+1,nz
    V(iz,ix)=-2/(z(ix)-z(iz))**3
  end do
end do

do iz=nz,2,-1
  do ix=nz-1,1,-1
    V(iz,ix)=-2/(z(iz)-z(ix))**3
  end do
end do

V(1,1)=dk1**2+2/(z(2)-z(1))**3+2/(z(nz)-z(1))**3
V(2,2)=dk1**2+2/(z(2)-z(1))**3+2/(z(nz)-z(2))**3
V(nz,nz)=dk1**2+2/(z(nz)-z(1))**3+2/(z(nz)-z(2))**3

```

```
do iz=1,nz
  do ix=1,nz
    F(iz,ix)=V(iz,ix)/mass1
  end do
end do

open(50,file='function.dat',status='unknown')
do iz=1,nz
  write(50,20) (F(iz,ix),ix=1,nz)
end do
close(50)

call DSYEV( JOBZ, UPLO, nz, F, nz, Eigenv, WORK, 3*nz-1,
INFO )

open(10,file='Eigenvalue.dat',status='unknown')
do iz=1,nz
  write(10,20) Eigenv(iz)
end do
close(10)

open(20,file='Eigenvector.dat',status='unknown')
do iz=1,nz
  write(20,20) (F(iz,ix),ix=1,nz)
end do
close(20)

20      format(10(x,e25.16))
end
```

Appendix J

This code is written to diagonalize the Hamiltonian matrix of three $^{111}\text{Cd}^+$ ions in the harmonic potential trap to obtain its eigenvalues (energies) and the eigenvectors (parameter matrix \mathbf{C} in Sec. 2.2). Lines 1-35 of this code contain the definition of variables; Lines 37-98 are the input data and step size definition; Lines 100-322 describe the basis set expansion based on three normal vibration modes; Lines 324-447 are used to construct kinetic energy matrix, potential energy matrix and Hamiltonian matrix; DSYEV subroutine from ACML library is used in lines 449-473 for matrix diagonalization [101]; Lines 475-486 are the subroutine NVJ which is used to calculate $j!$ of Eq. (2.2.5) and the subroutine OTHPL in lines 488-544 describe calculation of Hermite polynomials and their first derivatives [82]. In this program, during the numerical calculations for the spectrum of vibrational states, I used atomic units. It was transformed into the units of MHz at the end.

```

Program 3DIONTRAP
implicit real*8 (a-h,o-z)
integer mv,nz,mz,dz1,dz2,dz3
real*8 towpi,autonm
parameter(mv=15,max=60)
parameter(nz=121,mz=3,dz1=10,dz2=10,dz3=10)
parameter(twopi=6.28318530717959d0)
parameter(autonm=0.05291772d0)
Parameter(automhz=6579682606.6812d0)
character*1 UPLO, JOBZ
parameter(JOBZ ='V',UPLO ='U')
integer INFO
double precision EV(mv**3),EZ(mv**3,mv**3),WORK(3*(mv**3)-
1)

real*8 mass1,mu,dk1,b,n,n1,n2,n3,y1,y2,y3
real*8 commt1,commt2,commte1,commte2,commter2
real*8 dd,comm1,comm2,comm3
real*8 alpha1,alpha2,alpha3,sum1,sum2,sum3,sum4,sum5,sum
real*8
w,w1,w2,w3,deter,deter1,deter2,deter3,G,G1,G2,za1,za2,za3
double precision ek(mz),cz(mz),z1(nz),z2(nz),z3(nz)
double precision psi1(mv,nz),psi2(mv,nz),psi3(mv,nz)
double precision h(max),dh(max)
double precision psi1r(mv,nz),psi2r(mv,nz),psi3r(mv,nz)
double precision psi11(mv,nz),psi12(mv,nz),psi13(mv,nz)
double precision
KE(mv*mv*mv,mv*mv*mv),PE(mv*mv*mv,mv*mv*mv)
double precision Hamil(mv**3,mv**3)
double precision AEV(mv,mv,mv),V(nz,nz,nz)
double precision am(mz,mz)

pi=acos(-1.d0)

c harmonic parameters for Cd ion(in a.u.):
call mysecond(ts)

mass1=111.d0
mass1=mass1*1822.8885d0
mu=1.d0
w=2770.0*2*pi
w=w*3.33564d-8/219474.63d0

dk1=dsqrt(mass1)*w           !dk=dsqrt(k)
open(5,file='Eigenvalue.dat',status='old')
do iz=1,mz
  read(5,*) ek(iz)
end do
close(5)

open(4,file='Eigenvector.dat',status='old')
do iz1=1,mz
  read(4,*) (am(iz1,iz2),iz2=1,mz)
end do
close(4)

open(3,file='position.dat',status='old')
do iz=1,mz
  read(3,*) cz(iz)
end do
close(3)

do i=1,mv
  do j=1,mv
    do k=1,mv
      AEV(i,j,k)=(i-0.5d0)*dsqrt(ek(1))
$      +(j-0.5d0)*dsqrt(ek(2))
$      +(k-0.5d0)*dsqrt(ek(mz))
    end do
  end do
end do

```

```

      AEV(i,j,k)=AEV(i,j,k)*automhz
    end do
  end do
end do

open(2,file='ApproEigen.dat',status='unknown')
do i=1,mv
  do j=1,mv
    write(2,50) (AEV(i,j,k),k=1,mv)
  end do
end do
close(2)

Zmax=dz1*(nz-1)
zi=-Zmax/2
zf=Zmax/2

do iz1=1,nz
  z1(iz1)=zi+(iz1-1)*dz1
end do

do iz2=1,nz
  z2(iz2)=zi+(iz2-1)*dz2
end do

do iz3=1,nz
  z3(iz3)=zi+(iz3-1)*dz3
end do

c Basis functions for mode 1 (in a.u.)
w1=dsqrt(ek(1))
alpha1=dsqrt(mass1*w1)
c Harmonic wavefunctions for ion 1

      do iz1=1,nz
        y1=alpha1*z1(iz1)
        iv1=0
        psi1(iv1+1,iz1)=dsqrt(alpha1)/(pi**0.25d0)
        $           *dexp(-y1**2/2.d0)
        !!!!!!! call the subroutine which will give the value
        of Hermite.
        call othpl(4,mv,y1,h,dh)
        do iv1=1,mv-1,1
          n=iv1
          call nvj(n,b)
          n1=dsqrt(alpha1/dsqrt(pi)/(2**n)/b)
          psi1(iv1+1,iz1)=n1*h(iv1+1)*dexp(-y1**2/2.d0)
        end do
      end do

      cc Normalization of wavefunctions for mode 1.
      do iv1=1,mv
        sum1=0.d0
        do iz1=1,nz
          sum1=sum1+psi1(iv1,iz1)**2
        end do
        sum1=sum1*dz1
        do iz1=1,nz
          psi1(iv1,iz1)=psi1(iv1,iz1)/dsqrt(sum1)
        end do
      end do

      c Test of wavefunction

      open(10,file='basisset1.dat',status='unknown')
      do iz1=1,nz
        write(10,10) z1(iz1),(psi1(iv1,iz1),iv1=1,mv)
      end do

```

```

close(10)

c Basis functions for mode 2 (in a.u.)

w2=dsqrt(ek(2))
alpha2=dsqrt(mass1*w2*ek(1)/ek(2))
do iz2=1,nz
  y2=alpha2*z2(iz2)
  iv2=0
  psi2(iv2+1,iz2)=dsqrt(alpha2)/(pi**0.25d0)
$          *dexp(-y2**2/2.d0)
  !!!!!!! call the subroutine which will give the value
of Hermite.
  call othpl(4,mv,y2,h,dh)
  do iv2=1,mv-1,1
    n=iv2
    call nvj(n,b)
    n2=dsqrt(alpha2/dsqrt(pi)/(2**n)/b)
    psi2(iv2+1,iz2)=n2*h(iv2+1)*dexp(-y2**2/2.d0)
  end do
end do

cc Normalization of wavefunctions for mode 2.
do iv2=1,mv
  sum2=0.d0
  do iz2=1,nz
    sum2=sum2+psi2(iv2,iz2)**2
  end do
  sum2=sum2*dz2
  do iz2=1,nz
    psi2(iv2,iz2)=psi2(iv2,iz2)/dsqrt(sum2)
  end do
end do

c Test of wavefunction

open(30,file='basisset2.dat',status='unknown')
do iz2=1,nz
  write(30,10) z2(iz2),(psi2(iv2,iz2),iv2=1,mv)
end do
close(30)

c Basis functions for mode 3 (in a.u.)

w3=dsqrt(ek(mz))
alpha3=dsqrt(mass1*w3*ek(1)/ek(mz))
c Hamonic wavefunctions for ion 3
do iz3=1,nz
  y3=alpha3*z3(iz3)
  iv3=0
  psi3(iv3+1,iz3)=dsqrt(alpha3)/(pi**0.25d0)
$          *dexp(-y3**2/2.d0)
  !!!!!!! call the subroutine which will give the value
of Hermite.
  call othpl(4,mv,y3,h,dh)
  do iv3=1,mv-1,1
    n=iv3
    call nvj(n,b)
    n3=dsqrt(alpha3/dsqrt(pi)/(2**n)/b)
    psi3(iv3+1,iz3)=n3*h(iv3+1)*dexp(-y3**2/2.d0)
  end do
end do

cc Normalization of wavefunctions for mode 3.
do iv3=1,mv
  sum3=0.d0
  do iz3=1,nz
    sum3=sum3+psi3(iv3,iz3)**2
  end do
end do

```

```

end do
sum3=sum3*dz3
do iz3=1,nz
  psi3(iv3,iz3)=psi3(iv3,iz3)/dsqrt(sum3)
end do
end do

c Test of wavefunction

open(50,file='basisset3.dat',status='unknown')
do iz3=1,nz
  write(50,10) z3(iz3), (psi3(iv3,iz3),iv3=1,mv)
end do
close(50)

c calculation of Hamitonian
c Second direvative of kinetic energy part for mode 1

do iz1=1,nz
  y1=alpha1*z1(iz1)
  call othpl(4,mv,y1,h,dh)
  G=exp(-1*y1**2/2.d0)
  G1=-1*alpha1**2*z1(iz1)*exp(-1*y1**2/2.d0)
  G2=alpha1**2*exp(-1*y1**2/2.d0)*(y1**2-1)
  iv1=0
  psill(iv1+1,iz1)=dsqrt(alpha1/dsqrt(pi))*G2
  do iv1=1,mv-1
    n=iv1
    call nvj(n,b)
    n1=dsqrt(alpha1/dsqrt(pi)/(2**n)/b)
    H1=alpha1*dh(iv1+1)
    H2=2*iv1*dh(iv1)*alpha1**2
    psill(iv1+1,iz1)=n1*(G2*h(iv1+1)+2*G1*H1+G*H2)
  end do
end do

end do
do iv1=1,mv
  do iz1=1,nz
    psilr(iv1,iz1)=-psill(iv1,iz1)/2.d0/mass1
  end do
end do

c second derivative of first mode
open(70,file='secwavr1.dat',status='unknown')
do iz1=1,nz
  write(70,30) z1(iz1), (psilr(iv1,iz1),iv1=1,mv)
end do
close(70)

c Second direvative of kinetic energy part for mode 2

do iz2=1,nz
  y2=alpha2*z2(iz2)
  call othpl(4,mv,y2,h,dh)
  G=exp(-1*y2**2/2.d0)
  G1=-1*alpha2**2*z2(iz2)*exp(-1*y2**2/2.d0)
  G2=alpha2**2*exp(-1*y2**2/2.d0)*(y2**2-1)
  iv2=0
  psizz(iv2+1,iz2)=dsqrt(alpha2/dsqrt(pi))*G2
  do iv2=1,mv-1
    n=iv2
    call nvj(n,b)
    n2=dsqrt(alpha2/dsqrt(pi)/(2**n)/b)
    H1=alpha2*dh(iv2+1)
    H2=2*iv2*dh(iv2)*alpha2**2
    psizz(iv2+1,iz2)=n2*(G2*h(iv2+1)+2*G1*H1+G*H2)
  end do
end do

```

```

do iv2=1,mv
  do iz2=1,nz
    psi2r(iv2,iz2)=-psi22(iv2,iz2)*ek(2)/ek(1)/2.d0/mass1
  end do
end do

c second derivative of second mode
open(80,file='secwavr2.dat',status='unknown')
do iz2=1,nz
  write(80,30) z2(iz2),(psi2r(iv2,iz2),iv2=1,mv)
end do
close(80)

c Second derivative of kinetic energy part for mode 3

do iz3=1,nz
  y3=alpha3*z3(iz3)
  call othpl(4,mv,y3,h,dh)
  G=exp(-1*y3**2/2.d0)
  G1=-1*alpha3**2*z3(iz3)*exp(-1*y3**2/2.d0)
  G2=alpha3**2*exp(-1*y3**2/2.d0)*(y3**2-1)
  iv3=0
  psi33(iv3+1,iz3)=dsqrt(alpha3/dsqrt(pi))*G2
  do iv3=1,mv-1
    n=iv3
    call nvj(n,b)
    n3=dsqrt(alpha3/dsqrt(pi)/(2**n)/b)
    H1=alpha3*dh(iv3+1)
    H2=2*iv3*dh(iv3)*alpha3**2
    psi33(iv3+1,iz3)=n3*(G2*h(iv3+1)+2*G1*H1+G*H2)
  end do
end do

do iv3=1,mv
  do iz3=1,nz
    psi3r(iv3,iz3)=-psi33(iv3,iz3)*ek(mz)/ek(1)/2.d0/mass1
  end do
end do

c second derivative of third mode
open(90,file='secwavr3.dat',status='unknown')
do iz3=1,nz
  write(90,30) z3(iz3),(psi3r(iv3,iz3),iv3=1,mv)
end do
close(90)

c Calculation for elements of Hamiltonian matrix

do iz1=1,nz
  do iz2=1,nz
    do iz3=1,nz
      za1=am(1,1)*z1(iz1)+am(1,2)*z2(iz2)*dsqrt(ek(1)/ek(2))
      $ +am(1,3)*z3(iz3)*dsqrt(ek(1)/ek(mz))
      za2=am(2,1)*z1(iz1)+am(2,2)*z2(iz2)*dsqrt(ek(1)/ek(2))
      $ +am(2,3)*z3(iz3)*dsqrt(ek(1)/ek(mz))
      za3=am(3,1)*z1(iz1)+am(3,2)*z2(iz2)*dsqrt(ek(1)/ek(2))
      $ +am(3,3)*z3(iz3)*dsqrt(ek(1)/ek(mz))
      V(iz1,iz2,iz3)=
      $ 0.5d0*dk1**2*(za1+cz(1))**2
      $ +0.5d0*dk1**2*(za2+cz(2))**2
      $ +0.5d0*dk1**2*(za3+cz(mz))**2
      $ +1/abs((za2-za1)+(cz(2)-cz(1)))
      $ +1/abs((za3-za1)+(cz(mz)-cz(1)))
      $ +1/abs((za3-za2)+(cz(mz)-cz(2)))
      $ -0.5d0*dk1**2*cz(1)**2
      $ -0.5d0*dk1**2*cz(2)**2
      $ -0.5d0*dk1**2*cz(mz)**2-1/abs(cz(2)-cz(1))
    end do
  end do
end do

```

```

$      -1/abs(cz(mz)-cz(1))-1/abs(cz(mz)-cz(2))           sum5=sum5+comm3*V(iz1,iz2,iz3)
end do                                         $      *commt2*psi3(kv1,iz3)
end do                                         end do
end do                                         end do
end do                                         end do
dd=dz1*dz2*dz3

do iv=1,mv
call mysecond(tf)
open(6,file='cputime.dat',status='unknown')
write(6,807) 'CPU Time= ',(tF-tS)/3600.0d0,' (hour)'
do jv=1,mv
do kv=1,mv
write(200,70) iv,jv,kv
call flush(200)
do iv1=1,mv
do jv1=1,mv
do kv1=1,mv
sum4=0.d0
sum5=0.d0
do iz1=1,nz
comm1=psi1(iv,iz1)
comm1t=psi1(iv1,iz1)
commte1=psi1r(iv1,iz1)
do iz2=1,nz
comm2=comm1*psi2(jv,iz2)
comm2t=comm1t*psi2(jv1,iz2)
commte2=commte1*psi2(jv1,iz2)
commter2=comm1t*psi2r(jv1,iz2)
do iz3=1,nz
comm3=comm2*psi3(kv,iz3)
sum4=sum4+comm3*(commte2*psi3(kv1,iz3)
$      +commter2*psi3(kv1,iz3)
$      +commt2*psi3r(kv1,iz3))

sum5=sum5+comm3*V(iz1,iz2,iz3)
$      *commt2*psi3(kv1,iz3)
end do
end do
end do
KE((kv-1)*mv**2+(jv-1)*mv+iv,(kv1-1)*mv**2+(jv1-
1)*mv+iv1)=sum4*dd

PE((kv-1)*mv**2+(jv-1)*mv+iv,(kv1-1)*mv**2+(jv1-
1)*mv+iv1)=sum5*dd
end do
end do
end do
end do
close(6)

c kinetic part for Hamitonian

open(100,file='kinetic.dat',status='unknown',recl=74250)
do i=1,mv**3
write(100,50) (KE(i,j),j=1,mv**3)
end do
close(100)

open(101,file='kinetic1.dat',status='unknown',recl=74250)
do i=1,mv**3
write(101,50) (KE(i,j)*automhz,j=1,mv**3)
end do
close(101)

c potential part for Hamitonian
open(110,file='potential.dat',status='unknown',recl=74250)

```

```

do i=1,mv**3
  write(110,50) (PE(i,j),j=1,mv**3)
end do
close(110)

open(111,file='potential1.dat',status='unknown',recl=74250
)
do i=1,mv**3
  write(111,50) (PE(i,j)*automhz,j=1,mv**3)
end do
close(111)

c Hamiltonian matrix
do i=1,mv**3
  do j=1,mv**3
    Hamil(i,j)=KE(i,j)+PE(i,j)
  end do
end do

open(120,file='Hamiltonian.dat',status='unknown',recl=74250
)
do i=1,mv**3
  write(120,50) (Hamil(i,j),j=1,mv**3)
end do
close(120)

open(121,file='Hamiltonian1.dat',status='unknown',recl=7425
0)
do i=1,mv**3
  write(121,50) (Hamil(i,j)*automhz,j=1,mv**3)
end do
close(121)

call DSYEV( JOBZ, UPLO, mv**3, Hamil, mv**3, EV, WORK,
$           3*(mv**3)-1, INFO )

open(130,file='Eigen.dat',status='unknown')
do i=1,mv**3
  write(130,60) EV(i)*automhz
end do
close(130)

open(140,file='EigenvectorOfHami.dat',status='unknown',rec
l=74250)
do i=1,mv**3
  write(140,50) (Hamil(i,j),j=1,mv**3)
end do
close(140)

10   format(e24.16,150(x,f24.16))
20   format(150(x,e24.16))
30   format(e24.16,150(x,f24.16))
40   format(150(x,e24.16))
50   format(3375(x,e21.13))
60   format(400(x,e24.16))
70   format(200(x,i4))
807  format(a20,f7.2,2x,a8)
End
C-----
SUBROUTINE NVJ(M,A)
REAL*8 I,M,A

IF(M.EQ.0) THEN
  A=1.0
ELSE
  A=1.0
  DO I=1,M
    A=A*I
  End DO
End IF

```

```

END DO
END IF
END
C-----
SUBROUTINE OTHPL(KF,N,X,PL,DPL)
C =====
C PURPOSE: COMPUTE ORTHOGONAL POLYNOMIALS: TN(X) OR
UN(X),
C OR LN(X) OR HN(X), AND THEIR DERIVATIVES
C INPUT : KF --- FUNCTION CODE
C KF=1 FOR CHEBYSHEV POLYNOMIAL TN(X)
C KF=2 FOR CHEBYSHEV POLYNOMIAL UN(X)
C KF=3 FOR LAGUERRE POLYNOMIAL LN(X)
C KF=4 FOR HERMITE POLYNOMIAL HN(X)
C N --- ORDER OF ORTHOGONAL POLYNOMIALS
C X --- ARGUMENT OF ORTHOGONAL POLYNOMIALS
C OUTPUT:PL(N) --- TN(X) OR UN(X) OR LN(X) OR HN(X)
C DPL(N)--- TN'(X) OR UN'(X) OR LN'(X) OR HN'(X)
C =====
IMPLICIT DOUBLE PRECISION (A-H,O-Z)
DIMENSION PL(0:N),DPL(0:N)
A=2.0D0
B=0.0D0
C=1.0D0
Y0=1.0D0
Y1=2.0D0*X
DY0=0.0D0
DY1=2.0D0
PL(0)=1.0D0
PL(1)=2.D0*X
DPL(0)=0.0D0
DPL(1)=2.0D0
IF (KF.EQ.1) THEN
  Y1=X

```

```

DY1=1.0D0
PL(1)=X
DPL(1)=1.0D0
ELSE IF (KF.EQ.3) THEN
  Y1=1.D0-X
  DY1=-1.0D0
  PL(1)=1.0D0-X
  DPL(1)=-1.0D0
END IF
DO 10 K=2,N
  IF (KF.EQ.3) THEN
    A=-1.0D0/K
    B=2.0D0+A
    C=1.0D0+A
  ELSE IF (KF.EQ.4) THEN
    C=2.0D0*(K-1.0D0)
  END IF
  YN=(A*X+B)*Y1-C*Y0
  DYN=A*Y1+(A*X+B)*DY1-C*DY0
  PL(K)=YN
  DPL(K)=DYN
  Y0=Y1
  Y1=YN
  DY0=DY1
10      DY1=DYN
RETURN
END
C=====
SUBROUTINE MYSECOND(TIME)
REAL*8 TIME
TIME=MPI_WTIME()
RETURN
END

```

Appendix K

During our work, the main difficulty that we faced was the increase in the computer time for the calculation of the eigenvalues and eigenvectors of the system. For example, when we do calculation in one ion system with 15 basis functions, we need to diagonalize a 15×15 matrix and it takes only about 1 minute for calculation. If we come to the three ion system with $N = 15$, we have to deal with a very large matrix with the size $15^3 \times 15^3$. Now it takes more than 48 hours to finish the calculation, which exceeds the limit of computational time for one processor in Jacquard from NERSC. So it is necessary for us to find out a way to optimize our program and save the computer time.

Here, we try to parallelize our code (in Appendix I) with Message Passing Interface (MPI) method [94, 95]. In the MPI programming, we split our original serial code into several parallel parts which are arranged to different processors from the computer system for calculation. Different processors will run their own calculation separately and finally all the results from different processors are collected and transferred to the processor 0 (the first processor, we can transfer the final data to any processor we like) for the finial data output. If $N = 15$ in our work, we need to request for 16 processors from Jacquard Linux System. One processor is for the calculation of kinetic energy matrix and the other 15 processors are used to calculate

potential energy matrix. During the calculation of potential energy matrix, because the matrix is symmetric, we only need to calculate the upper triangular matrix. To make sure the time consuming of every processor are almost the same, we arrange these 15 processors to do the calculation like this: processor 1 calculate matrix elements of columns 1, 16, 31, ..., processor 2 for columns 2, 17, 32, ..., data from all these 15 processors are added up with the internal command of MPI program in NERSC to finalize the potential energy matrix. After the MPI programming is applied, it reduces about 90% extra computational time.

This code is written to diagonalize the Hamiltonian matrix of three $^{111}\text{Cd}^+$ ions in the harmonic potential trap to obtain its eigenvalues (energies) and the eigenvectors (parameter matrix \mathbf{C} in Sec. 2.2), where MPI programming is applied. Lines 1-39 of this code contain the definition of variables; Lines 41-58 are used to initialize Message Passing Interface (MPI) calculation; Lines 60-120 are the input data and step size definition; Lines 122-348 describe the basis set expansion based on three normal vibration modes; Lines 350-467 are used to construct kinetic energy matrix, potential energy matrix and Hamiltonian matrix; DSYEV subroutine from ACML library is used in lines 469-493 for matrix diagonalization and MPI finalization [101]; Lines 495-504 are the subroutine NVJ which is used to calculate $j!$ of Eq. (2.2.5) and the subroutine OTHPL in lines 506-579 describe calculation of Hermite polynomials and

their first derivatives [82]. In this program, during the numerical calculations for the spectrum of vibrational states, I used atomic units. It was transformed into the units of MHz at the end.

```

Program MPI3DIONTRAP
implicit real*8 (a-h,o-z)
integer mv,nz,mz,dz1,dz2,dz3
real*8 towpi,autonm,pi
parameter(mv=15,max=60)
parameter(nz=121,mz=3,dz1=10,dz2=10,dz3=10)
parameter(pi=3.1415926535897932384d0,twopi=6.283185307179
59d0)
parameter(autonm=0.05291772d0)
Parameter(automhz=6579682606.6812d0)
character*1 UPL0, JOBZ
character*10 filetime
parameter(JOBZ ='V',UPL0 ='U')
integer INFO
double precision
EV(mv**3),EZ(mv**3,mv**3),WORK(3*(mv**3)-1)

real*8 mass1,mu,dk1,b,n,n1,n2,n3,y1,y2,y3
real*8 commt1,commt2,commte1,commte2,commter2
real*8 dd,comm1,comm2,comm3
real*8
alpha1,alpha2,alpha3,sum1,sum2,sum3,sum4,sum5,sum6,sum
real*8
w,w1,w2,w3,deter,deter1,deter2,deter3,G,G1,G2,za1,za2,za3
double precision ek(mz),cz(mz),z1(nz),z2(nz),z3(nz)
double precision psil(mv,nz),psi2(mv,nz),psi3(mv,nz)
double precision h(max),dh(max)
double precision psilr(mv,nz),psi2r(mv,nz),psi3r(mv,nz)
double precision psil1(mv,nz),psi22(mv,nz),psi33(mv,nz)
double precision
KE(mv*mv*mv,mv*mv*mv),PE(mv*mv*mv,mv*mv*mv)
double precision
KE1(mv*mv*mv,mv*mv*mv),PE1(mv*mv*mv,mv*mv*mv)
double precision Hamil(mv**3,mv**3)

double precision AEV(mv,mv,mv),V(nz,nz,nz)
double precision am(mz,mz)

!----- MPI STAFF -----
include 'mpif.h'
integer ierror,comm,rc
common/pedat/mype,npe,comm
!-----
c MPI start:
call MPI_INIT(ierror)
comm=MPI_COMM_WORLD
call MPI_COMM_RANK(comm,mype,ierror)
call MPI_COMM_SIZE(comm,npe,ierror)

print *, 'mype=',mype,' npe=',npe

if (npe.ne.mv+1) then
  print *, 'processor # is wrong'
  print *, npe,mv
  stop
end if

c harmonic parameters for Cd ion(in a.u.):
call mysecond(ts)
mass1=111.d0
mass1=mass1*1822.8885d0
mu=1.d0
w=2770.0*2*pi
w=w*3.33564d-8/219474.63d0
dk1=dsqrt(mass1)*w           !dk=dsqrt(k)

open(5,file='Eigenvalue.dat',status='old')
do iz=1,mz
  read(5,*) ek(iz)

```

```

end do
close(5)

open(4,file='Eigenvector.dat',status='old')
do iz1=1,mz
  read(4,*) (am(iz1,iz2),iz2=1,mz)
end do
close(4)

open(3,file='position.dat',status='old')
do iz=1,mz
  read(3,*) cz(iz)
end do
close(3)

do i=1,mv
  do j=1,mv
    do k=1,mv
      AEV(i,j,k)=(i-0.5d0)*dsqrt(ek(1))
      $ +(j-0.5d0)*dsqrt(ek(2))
      $ +(k-0.5d0)*dsqrt(ek(mz))
      AEV(i,j,k)=AEV(i,j,k)*automhz
    end do
  end do
end do

open(2,file='ApproEigen.dat',status='unknown')
do i=1,mv
  do j=1,mv
    write(2,50) (AEV(i,j,k),k=1,mv)
  end do
end do
close(2)

      zmax=dz1*(nz-1)
      zi=-zmax/2
      zf=zmax/2

      do iz1=1,nz
        z1(iz1)=zi+(iz1-1)*dz1
      end do

      do iz2=1,nz
        z2(iz2)=zi+(iz2-1)*dz2
      end do

      do iz3=1,nz
        z3(iz3)=zi+(iz3-1)*dz3
      end do

c Hamonic parameters for ion 1 (in a.u.)
w1=dsqrt(ek(1))
alpha1=dsqrt(mass1*w1)
c Hamonic wavefunctions for ion 1
do iz1=1,nz
  y1=alpha1*z1(iz1)
  iv1=0
  psil(iv1+1,iz1)=dsqrt(alpha1)/(pi**0.25d0)*dexp(-
y1**2/2.d0)
  !!!!!!! call the subroutine which will give the value
of Hermite.
  call othpl(4,mv,y1,h,dh)
  do iv1=1,mv-1,1
    n=iv1
    call nvj(n,b)
    n1=dsqrt(alpha1/dsqrt(pi)/(2**n)/b)
    psil(iv1+1,iz1)=n1*h(iv1+1)*dexp(-y1**2/2.d0)

```

```

end do
end do

cc Normalization of wavefunctions for ion 1.
do iv1=1,mv
sum1=0.d0
do iz1=1,nz
  sum1=sum1+psi1(iv1,iz1)**2
end do
sum1=sum1*dz1
do iz1=1,nz
  psi1(iv1,iz1)=psi1(iv1,iz1)/dsqrt(sum1)
end do
end do

c Hamonic parameters for ion 2 (in a.u.)

w2=dsqrt(ek(2))
alpha2=dsqrt(mass1*w2*ek(1)/ek(2))
c Hamonic wavefunctions for ion 2
do iz2=1,nz
  y2=alpha2*z2(iz2)
  iv2=0
  psi2(iv2+1,iz2)=dsqrt(alpha2)/(pi**0.25d0)*dexp(-
y2**2/2.d0)
  !!!!!!! call the subroutine which will give the value
of Hermite.
  call othpl(4,mv,y2,h,dh)
  do iv2=1,mv-1,1
    n=iv2
    call nvj(n,b)
    n2=dsqrt(alpha2/dsqrt(pi)/(2**n)/b)
    psi2(iv2+1,iz2)=n2*h(iv2+1)*dexp(-y2**2/2.d0)
  end do

end do

cc Normalization of wavefunctions for ion 2.
do iv2=1,mv
sum2=0.d0
do iz2=1,nz
  sum2=sum2+psi2(iv2,iz2)**2
end do
sum2=sum2*dz2
do iz2=1,nz
  psi2(iv2,iz2)=psi2(iv2,iz2)/dsqrt(sum2)
end do
end do

c Hamonic parameters for ion 3 (in a.u.)

w3=dsqrt(ek(mz))
alpha3=dsqrt(mass1*w3*ek(1)/ek(mz))
c Hamonic wavefunctions for ion 3
do iz3=1,nz
  y3=alpha3*z3(iz3)
  iv3=0
  psi3(iv3+1,iz3)=dsqrt(alpha3)/(pi**0.25d0)*dexp(-
y3**2/2.d0)
  !!!!!!! call the subroutine which will give the value
of Hermite.
  call othpl(4,mv,y3,h,dh)
  do iv3=1,mv-1,1
    n=iv3
    call nvj(n,b)
    n3=dsqrt(alpha3/dsqrt(pi)/(2**n)/b)
    psi3(iv3+1,iz3)=n3*h(iv3+1)*dexp(-y3**2/2.d0)
  end do
end do

```

```

cc Normalization of wavefunctions for ion 3.
do iv3=1,mv
  sum3=0.d0
  do iz3=1,nz
    sum3=sum3+psi3(iv3,iz3)**2
  end do
  sum3=sum3*dz3
  do iz3=1,nz
    psi3(iv3,iz3)=psi3(iv3,iz3)/dsqrt(sum3)
  end do
end do

c Test of wavefunction
if(mype.eq.0) then

  open(10,file='basisset1.dat',status='unknown')
  do iz1=1,nz
    write(10,10) z1(iz1),(psi1(iv1,iz1),iv1=1,mv)
  end do
  close(10)

  open(30,file='basisset2.dat',status='unknown')
  do iz2=1,nz
    write(30,10) z2(iz2),(psi2(iv2,iz2),iv2=1,mv)
  end do
  close(30)

  open(50,file='basisset3.dat',status='unknown')
  do iz3=1,nz
    write(50,10) z3(iz3),(psi3(iv3,iz3),iv3=1,mv)
  end do
  close(50)

end if

call MPI_BARRIER(comm,ierror)

c calculate Hamitonian
c kinetic energy for ion 1

do iz1=1,nz
  y1=alpha1*z1(iz1)
  call othpl(4,mv,y1,h,dh)
  G=exp(-1*y1**2/2.d0)
  G1=-1*alpha1**2*z1(iz1)*exp(-1*y1**2/2.d0)
  G2=alpha1**2*exp(-1*y1**2/2.d0)*(y1**2-1)
  iv1=0
  psi11(iv1+1,iz1)=dsqrt(alpha1/dsqrt(pi))*G2
  do iv1=1,mv-1
    n=iv1
    call nvj(n,b)
    n1=dsqrt(alpha1/dsqrt(pi))/(2**n)/b
    H1=alpha1*dh(iv1+1)
    H2=2*iv1*dh(iv1)*alpha1**2
    psi11(iv1+1,iz1)=n1*(G2*h(iv1+1)+2*G1*H1+G*H2)
  end do
  end do

do iv1=1,mv
  do iz1=1,nz
    psi1r(iv1,iz1)=-psi11(iv1,iz1)/2.d0/mass1
  end do
end do

c kinetic energy for ion 2

do iz2=1,nz
  y2=alpha2*z2(iz2)
  call othpl(4,mv,y2,h,dh)

```

```

G=exp(-1*y2**2/2.d0)
G1=-1*alpha2**2*z2(iv2)*exp(-1*y2**2/2.d0)
G2=alpha2**2*exp(-1*y2**2/2.d0)*(y2**2-1)
iv2=0
psi22(iv2+1,iz2)=dsqrt(alpha2/dsqrt(pi))*G2
do iv2=1,mv-1
  n=iv2
  call nvj(n,b)
  n2=dsqrt(alpha2/dsqrt(pi)/(2**n)/b)
  H1=alpha2*dh(iv2+1)
  H2=2*iv2*dh(iv2)*alpha2**2
  psi22(iv2+1,iz2)=n2*(G2*h(iv2+1)+2*G1*H1+G*H2)
end do
end do

do iv2=1,mv
  do iz2=1,nz
    psi2r(iv2,iz2)=-psi22(iv2,iz2)*ek(2)/ek(1)/2.d0/mass1
  end do
end do

c kinetic energy for ion 3

do iz3=1,nz
  y3=alpha3*z3(iz3)
  call othpl(4,mv,y3,h,dh)
  G=exp(-1*y3**2/2.d0)
  G1=-1*alpha3**2*z3(iz3)*exp(-1*y3**2/2.d0)
  G2=alpha3**2*exp(-1*y3**2/2.d0)*(y3**2-1)
  iv3=0
  psi33(iv3+1,iz3)=dsqrt(alpha3/dsqrt(pi))*G2
  do iv3=1,mv-1
    n=iv3
    call nvj(n,b)
    n3=dsqrt(alpha3/dsqrt(pi)/(2**n)/b)
    H1=alpha3*dh(iv3+1)
    H2=2*iv3*dh(iv3)*alpha3**2
    psi33(iv3+1,iz3)=n3*(G2*h(iv3+1)+2*G1*H1+G*H2)
  end do
  end do

  do iv3=1,mv
    do iz3=1,nz
      psi3r(iv3,iz3)=-psi33(iv3,iz3)*ek(mz)/ek(1)/2.d0/mass1
    end do
  end do

  c second derivative of first ion wavefunction
  if(mype.eq.0) then
    open(20,file='secwavr1.dat',status='unknown')
    do iz1=1,nz
      write(20,30) z1(iz1),(psilr(iv1,iz1),iv1=1,mv)
    end do
    close(20)

    open(40,file='secwavr2.dat',status='unknown')
    do iz2=1,nz
      write(40,30) z2(iz2),(psi2r(iv2,iz2),iv2=1,mv)
    end do
    close(40)

    open(60,file='secwavr3.dat',status='unknown')
    do iz3=1,nz
      write(60,30) z3(iz3),(psi3r(iv3,iz3),iv3=1,mv)
    end do
    close(60)
  end if
end if

```

```

end if

call MPI_BARRIER(comm,ierror)

c basis set
do iz1=1,nz
  do iz2=1,nz
    do iz3=1,nz
      za1=am(1,1)*z1(iz1)+am(1,2)*z2(iz2)*dsqrt(ek(1)/ek(2))
      $ +am(1,3)*z3(iz3)*dsqrt(ek(1)/ek(mz))
      za2=am(2,1)*z1(iz1)+am(2,2)*z2(iz2)*dsqrt(ek(1)/ek(2))
      $ +am(2,3)*z3(iz3)*dsqrt(ek(1)/ek(mz))
      za3=am(3,1)*z1(iz1)+am(3,2)*z2(iz2)*dsqrt(ek(1)/ek(2))
      $ +am(3,3)*z3(iz3)*dsqrt(ek(1)/ek(mz))
      V(iz1,iz2,iz3)=
        $ 0.5d0*dk1**2*(za1+cz(1))**2
        $ +0.5d0*dk1**2*(za2+cz(2))**2
        $ +0.5d0*dk1**2*(za3+cz(mz))**2
        $ +1/abs((za2-za1)+(cz(2)-cz(1)))
        $ +1/abs((za3-za1)+(cz(mz)-cz(1)))
        $ +1/abs((za3-za2)+(cz(mz)-cz(2)))
        $ -0.5d0*dk1**2*cz(1)**2
        $ -0.5d0*dk1**2*cz(2)**2
        $ -0.5d0*dk1**2*cz(mz)**2-1/abs(cz(2)-cz(1))
        $ -1/abs(cz(mz)-cz(1))-1/abs(cz(mz)-cz(2))
    end do
  end do
end do

dd=dz1*dz2*dz3

if(mype.eq.mv) then
  do iv=1,mv
    do jv=1,mv

```

```

open(6,file=filetime,status='unknown')
write(6,807) 'CPU Time= ',(tF-ts)/3600.0d0,' (hour)'
do kv=1,mv
  do iv1=1,mv
    do jv1=1,mv
      do kv1=kv,mv
        sum=0.d0
        do iz1=1,nz
          comm1=psi1(iv,iz1)
          commt1=psi1(iv1,iz1)
          do iz2=1,nz
            comm2=comm1*psi2(jv,iz2)
            commt2=commt1*psi2(jv1,iz2)
            do iz3=1,nz
              comm3=comm2*psi3(kv,iz3)
            sum=sum+comm3*V(iz1,iz2,iz3)*commt2*psi3(kv1,iz3)
            end do
          end do
        end do
      PE1((kv-1)*mv**2+(jv-1)*mv+iv,(kv1-1)*mv**2+(jv1-
      1)*mv+iv1)=sum*dd
      end do
    end do
  end do
end do
close(6)
end if

call MPI_BARRIER(comm,ierror)

do i=1,mv**3
  do j=1,mv**3
    call MPI_ALLREDUCE(PE1(i,j),PE(i,j),
$           1,MPI_DOUBLE_PRECISION,MPI_SUM,comm,ierror)
    end do
  end do

if(mype.eq.mv) then

do i=1,mv**3
  do j=i,mv**3
    PE(j,i)=PE(i,j)
  end do
end do

c Hamiltonian
do i=1,mv**3
  do j=1,mv**3
    Hamil(i,j)=KE(i,j)+PE(i,j)
  end do
end do

call DSYEV( JOBZ, UPLO, mv**3, Hamil, mv**3, EV, WORK,
$           3*(mv**3)-1, INFO )

open(130,file='Eigen.dat',status='unknown')
do i=1,mv**3
  write(130,60) EV(i)*automhz
end do
close(130)

end if
call MPI_BARRIER(comm,ierror)

10   format(e24.16,150(x,f24.16))
20   format(150(x,e24.16))

```

```

30      format(e24.16,150(x,f24.16))
40      format(150(x,e24.16))
50      format(3375(x,e24.16))
60      format(400(x,e24.16))
70      format(200(x,i4))
807     format(a20,f7.2,2x,a8)

call MPI_BARRIER(comm,ierror)
call MPI_FINALIZE(ierror)

End
c-----
subroutine delta(ii,ji,deltav)
integer ii,ji
real*8 deltav

deltav=0.d0
if(ii.eq.ji) then
  deltav=1.d0
end if

end
c-----
subroutine nvj(m,A)
real*8 i,m,A

if(m.eq.0) then
  A=1.0
else
  A=1.0
  do i=1,m
    A=A*i
  end do
end if

      end
c-----
SUBROUTINE OTHPL(KF,N,X,PL,DPL)
C
C =====
C   Purpose: Compute orthogonal polynomials: Tn(x) or
C   Un(x),
C           or Ln(x) or Hn(x), and their derivatives
C   Input : KF --- Function code
C           KF=1 for Chebyshev polynomial Tn(x)
C           KF=2 for Chebyshev polynomial Un(x)
C           KF=3 for Laguerre polynomial Ln(x)
C           KF=4 for Hermite polynomial Hn(x)
C           n --- Order of orthogonal polynomials
C           x --- Argument of orthogonal polynomials
C   Output: PL(n) --- Tn(x) or Un(x) or Ln(x) or Hn(x)
C           DPL(n)--- Tn'(x) or Un'(x) or Ln'(x) or
Hn'(x)
C =====
C
IMPLICIT DOUBLE PRECISION (A-H,O-Z)
DIMENSION PL(0:N),DPL(0:N)
A=2.0D0
B=0.0D0
C=1.0D0
Y0=1.0D0
Y1=2.0D0*X
DY0=0.0D0
DY1=2.0D0
PL(0)=1.0D0
PL(1)=2.D0*X
DPL(0)=0.0D0
DPL(1)=2.0D0
IF (KF.EQ.1) THEN

```

```

Y1=X
DY1=1.0D0
PL(1)=X
DPL(1)=1.0D0
ELSE IF (KF.EQ.3) THEN
  Y1=1.D0-X
  DY1=-1.0D0
  PL(1)=1.0D0-X
  DPL(1)=-1.0D0
END IF
DO 10 K=2,N
  IF (KF.EQ.3) THEN
    A=-1.0D0/K
    B=2.0D0+A
    C=1.0D0+A
  ELSE IF (KF.EQ.4) THEN
    C=2.0D0*(K-1.0D0)
  END IF
  YN=(A*X+B)*Y1-C*Y0
  DYN=A*Y1+(A*X+B)*DY1-C*DY0
  PL(K)=YN
  DPL(K)=DYN
  Y0=Y1
  Y1=YN
  DY0=DY1
10      DY1=DYN
RETURN
END
C=====
subroutine mysecond(time)

real*8 time

time=MPI_WTIME()

```

Appendix L

To optimize our code (in Appendix K) further and save more computer time, we use Gaussian Quadrature Method instead of the Equally-Spaced Abscissas method for the calculation of 3D integrals in our code. In Gaussian Quadrature Method [100], we could choose not only the weighting coefficients, but also the location of the abscissas at which the function is to be evaluated. Then we can calculate the integral exactly for a class of integrands: polynomials times some known function $W(z)$. In other words, if the integration number (N) is known, we can find a set of weights w_j and abscissas z_j to make the approximation:

$$\int_a^b W(z)f(z)dz \approx \sum_{j=0}^{N-1} w_j f(z_j), \quad (1)$$

which is exact if $f(z)$ is a polynomial.

In our work, we are dealing with the integral of Gauss-Hermite type with the following weight functions, intervals and recurrence relations:

$$W(z) = e^{-z^2}, \quad -\infty < z < \infty, \quad (2)$$

$$H_{j+1} = 2zH_j - 2jH_{j-1}. \quad (3)$$

In the code, the orthonormal set of polynomials \tilde{H}_j is used to avoid computations overflow for large N instead of functions from Eqs. (2) and (3) and they are generated as follows:

$$\tilde{H}_{-1} = 0, \quad \tilde{H}_0 = \frac{1}{\pi^{1/4}}, \quad \tilde{H}_{j+1} = z \sqrt{\frac{2}{j+1}} \tilde{H}_j - \sqrt{\frac{j}{j+1}} \tilde{H}_{j-1}. \quad (4)$$

The formula for the weights:

$$w_j = \frac{2}{[\tilde{H}'_N(z_j)]^2} \quad (5)$$

The formula for the derivative with this normalization is:

$$\tilde{H}'_j = \sqrt{2j} \tilde{H}_{j-1} \quad (6)$$

Then the integration formula can be written as follows:

$$\int_{-\infty}^{+\infty} e^{-z^2} f(z) dz = \sum_{j=0}^{N-1} w_j f(z_j), \quad (7)$$

For our problem, because of the introduce of α , we need to make a correction to Eq.

(7).

$$\int_{-\infty}^{+\infty} e^{-\alpha^2 z^2} f(\alpha z) dz = \int_{-\infty}^{+\infty} e^{-(\alpha z)^2} \frac{f(\alpha z)}{\alpha} d\alpha z, \quad (8)$$

Setting:

$$y = \alpha z, \quad -\infty < y < \infty, \quad (9)$$

Then we come to the final formula:

$$\int_{-\infty}^{+\infty} e^{-y^2} \frac{f(y)}{\alpha} dy = \sum_{j=0}^{N-1} w_j \frac{f(y_j)}{\alpha}. \quad (10)$$

All the calculation to produce abscissas and weights is carried out using the subroutine GAUHER [100]. After implementation of the Gaussian Quadrature method, it saves about 90% of computer time as compared to the code.

This code is written to diagonalize the Hamiltonian matrix of three $^{111}\text{Cd}^+$ ions in the anharmonic potential trap to obtain its eigenvalues (energies) and the eigenvectors (parameter matrix \mathbf{C} in Sec. 2.2), where MPI programming and Gaussian Quadrature Method are both applied. Lines 1-62 of this code contain the definition of variables; Lines 64-80 are used to initialize Message Passing Interface (MPI) calculation; Lines 82-130 are the input data, the abscissas and weights of integration points using Gaussian Quadrature Method; Lines 132-384 describe the basis set expansion based on three normal vibration modes; Lines 386-517 are used to construct kinetic energy matrix, potential energy matrix and Hamiltonian matrix; DSYEV subroutine from ACML library is used in lines 519-535 for matrix diagonalization [101]; Lines 537-722 are the construction of wavefunctions of the system; Transition matrix calculation and MPI finalization are carried out in lines 724-788; Subroutine in lines 790-799 is used to calculate the delta function; Lines 801-813 are the subroutine NVJ which is used to calculate $j!$ of Eq. (2.2.5) and the subroutine OTHPL in lines 815-875 describe calculation of Hermite polynomials and their first derivatives [82]. Subroutine GAUHER in lines 886-930 are used to produce abscissas and weights using Gaussian Quadrature Method. In this program, during the numerical calculations for the spectrum of vibrational states, I used atomic units. It was transformed into the units of MHz at the end.

```

Program MPIGAUSS3DIONTRAP
implicit real*8 (a-h,o-z)
integer mv,nz,mz,dz1,dz2,dz3,lm,lp
real*8 towpi,autonm,pi
parameter(mv=15,max=45)
parameter(nz=21,mz=3)
parameter(ns=53,lp=70,lm=30)
parameter(pi=3.1415926535897932384d0,twopi=6.283185307179
59d0)
parameter(autonm=0.05291772d0,alpha=-100.d0,beta=4.2d-6)
Parameter(automhz=6579682606.6812d0)
character*1 UPL0, JOBZ
character*10 filetime
character*10 filewavefp2
character*10 filewavefp1
character*8 filewavef
character*11 fileabswavef
character*13 filebsf
parameter(JOBZ ='V',UPLO ='U')
integer INFO
double precision
EV(mv**3),EZ(mv**3,mv**3),WORK(3*(mv**3)-1)

real*8 mass1,mu,dk1,b,n,n1,n2,n3,y1,y2,y3
real*8 commt1,commt2,commt3
real*8 dd,comm1,comm2,comm3,sa1,sa2,sa3
real*8
alpha1,alpha2,alpha3,sum1,sum2,sum3,sum4,sum5,sum6,sum
real*8
w,w1,w2,w3,deter,deter1,deter2,deter3,G,G1,G2,za1,za2,za3
double precision ek(mz),cz(mz),zf1(ns),zf2(ns),zf3(ns)
double precision
wt1(ns),wt2(ns),wt3(ns),zfx1(ns),zfx2(ns),zfx3(ns)

double precision
z1(nz),z2(nz),z3(nz),zp1(nz),zp2(nz),zp3(nz)
double precision weight1(nz),weight2(nz),weight3(nz)
double precision psi1(mv,nz),psi2(mv,nz),psi3(mv,nz)
double precision ps1(mv,nz),ps2(mv,nz),ps3(mv,nz)
double precision bsi1(mv,ns),bsi2(mv,ns),bsi3(mv,ns)
double precision bs1(mv,ns),bs2(mv,ns),bs3(mv,ns)
double precision h(max),dh(max)
double precision psilr(mv,nz),psi2r(mv,nz),psi3r(mv,nz)
double precision psil1(mv,nz),psi22(mv,nz),psi33(mv,nz)
double precision psilp(mv,nz),psi2p(mv,nz),psi3p(mv,nz)
double precision psils(mv,nz),psi2s(mv,nz),psi3s(mv,nz)
double precision
KE (mv*mv*mv,mv*mv*mv), PE (mv*mv*mv,mv*mv*mv)
double precision
KE1 (mv*mv*mv,mv*mv*mv), PE1 (mv*mv*mv,mv*mv*mv)
double precision Hamil(mv**3,mv**3),dipole(lp,lp)
double precision
AEV(mv,mv,mv),V(nz,nz,nz),wavefp(lp,ns,ns,ns)
double precision am(mz,mz),norm(lp,lp),tdm(ns,ns,ns)
real*8, allocatable, dimension(:,:,:,:) :: wavef_j, wavefp_j
real*8, allocatable, dimension(:) :: bs_j, bsi_j

!----- MPI STAFF -----
include 'mpif.h'
integer ierror,comm,rc
common/pedat/mype,npe,comm
!-----
c MPI start:
call MPI_INIT(ierror)
comm=MPI_COMM_WORLD
call MPI_COMM_RANK(comm,mype,ierror)
call MPI_COMM_SIZE(comm,npe,ierror)
print *, 'mype=' , mype, ' npe=' , npe

```

```

if (npe.ne.mv+1) then
  print *, 'processor # is wrong'
  print *, npe,mv
  stop
end if

c harmonic parameters for Cd ion(in a.u.):
call mysecond(ts)
mass1=111.d0
mass1=mass1*1822.8885d0
mu=1.d0
w=2770.0*2*pi
w=w*3.33564d-8/219474.63d0
dk1=dsqrt(mass1)*w           !dk=dsqrt(k)

open(5,file='Eigenvalue.dat',status='old')
do iz=1,mz
  read(5,*) ek(iz)
end do
close(5)

open(4,file='Eigenvector.dat',status='old')
do iz1=1,mz
  read(4,*) (am(iz1,iz2),iz2=1,mz)
end do
close(4)

open(3,file='position.dat',status='old')
do iz=1,mz
  read(3,*) cz(iz)
end do
close(3)

do i=1,mv
  do j=1,mv
    do k=1,mv
      AEV(i,j,k)=(i-0.5d0)*dsqrt(ek(1))+(j-
      0.5d0)*dsqrt(ek(2))
      $           +(k-0.5d0)*dsqrt(ek(mz))
      AEV(i,j,k)=AEV(i,j,k)*automhz
    end do
  end do
end do

open(2,file='ApproEigen.dat',status='unknown')
do i=1,mv
  do j=1,mv
    write(2,50) (AEV(i,j,k),k=1,mv)
  end do
end do
close(2)

call gauher(z1,weight1,nz)
call gauher(z2,weight2,nz)
call gauher(z3,weight3,nz)

c Hamonic parameters for ion 1 (in a.u.)
w1=dsqrt(ek(1))
alpha1=dsqrt(mass1*w1)
do iz1=1,nz
  zp1(iz1)=z1(iz1)/alpha1
end do
c Hamonic wavefunctions for ion 1
do iz1=1,nz
  y1=z1(iz1)
  iv1=0

```

```

psi1(iv1+1,iz1)=dsqrt(alpha1)/(pi**0.25d0)*dexp(-
y1**2/2.d0)
ps1(iv1+1,iz1)=dsqrt(alpha1)/(pi**0.25d0)
!!!!!! call the subroutine which will give the value
of Hermite.
call othpl(4,mv,y1,h,dh)
do iv1=1,mv-1,1
  n=iv1
  call nvj(n,b)
  n1=dsqrt(alpha1/dsqrt(pi)/(2**n)/b)
  psi1(iv1+1,iz1)=n1*h(iv1+1)*dexp(-y1**2/2.d0)
  ps1(iv1+1,iz1)=n1*h(iv1+1)
end do
end do

cc Normalization of wavefunctions for ion 1.
do iv1=1,mv
  sum1=0.d0
  do iz1=1,nz
    sum1=sum1+ps1(iv1,iz1)**2*weight1(iz1)/alpha1
  end do
  do iz1=1,nz
    psi1(iv1,iz1)=psi1(iv1,iz1)/dsqrt(sum1)
  end do
end do

c Hamonic parameters for ion 2 (in a.u.)

w2=dsqrt(ek(2))
alpha2=dsqrt(mass1*w2*ek(1)/ek(2))
do iz2=1,nz
  zp2(iz2)=z2(iz2)/alpha2
end do
c Hamonic wavefunctions for ion 2

do iz2=1,nz
  y2=z2(iz2)
  iv2=0
  psi2(iv2+1,iz2)=dsqrt(alpha2)/(pi**0.25d0)*dexp(-
y2**2/2.d0)
  ps2(iv2+1,iz2)=dsqrt(alpha2)/(pi**0.25d0)
!!!!!! call the subroutine which will give the value
of Hermite.
  call othpl(4,mv,y2,h,dh)
  do iv2=1,mv-1,1
    n=iv2
    call nvj(n,b)
    n2=dsqrt(alpha2/dsqrt(pi)/(2**n)/b)
    psi2(iv2+1,iz2)=n2*h(iv2+1)*dexp(-y2**2/2.d0)
    ps2(iv2+1,iz2)=n2*h(iv2+1)
  end do
end do

cc Normalization of wavefunctions for ion 2.
do iv2=1,mv
  sum2=0.d0
  do iz2=1,nz
    sum2=sum2+ps2(iv2,iz2)**2*weight2(iz2)/alpha2
  end do
  do iz2=1,nz
    psi2(iv2,iz2)=psi2(iv2,iz2)/dsqrt(sum2)
  end do
end do

c Hamonic parameters for ion 3 (in a.u.)

w3=dsqrt(ek(mz))
alpha3=dsqrt(mass1*w3*ek(1)/ek(mz))
do iz3=1,nz

```

```

zp3(iz3)=z3(iz3)/alpha3
end do
c Harmonic wavefunctions for ion 3
do iz3=1,nz
  y3=z3(iz3)
  iv3=0
  psi3(iv3+1,iz3)=dsqrt(alpha3) / (pi**0.25d0) *dexp(-
y3**2/2.d0)
  ps3(iv3+1,iz3)=dsqrt(alpha3) / (pi**0.25d0)
  !!!!!!! call the subroutine which will give the value
of Hermite.
  call othpl(4,mv,y3,h,dh)
  do iv3=1,mv-1,1
    n=iv3
    call nvj(n,b)
    n3=dsqrt(alpha3/dsqrt(pi) / (2**n) /b)
    psi3(iv3+1,iz3)=n3*h(iv3+1)*dexp(-y3**2/2.d0)
    ps3(iv3+1,iz3)=n3*h(iv3+1)
  end do
end do

cc Normalization of wavefunctions for ion 3.
do iv3=1,mv
  sum3=0.d0
  do iz3=1,nz
    sum3=sum3+ps3(iv3,iz3)**2*weight3(iz3)/alpha3
  end do
  do iz3=1,nz
    psi3(iv3,iz3)=psi3(iv3,iz3)/dsqrt(sum3)
  end do
end do

c Test of wavefunction
if(mype.eq.0) then
open(10,file='basisset1.dat',status='unknown')
do iz1=1,nz
  write(10,10) zp1(iz1),(psi1(iv1,iz1),iv1=1,mv)
end do
close(10)

open(30,file='basisset2.dat',status='unknown')
do iz2=1,nz
  write(30,10) zp2(iz2),(psi2(iv2,iz2),iv2=1,mv)
end do
close(30)

open(50,file='basisset3.dat',status='unknown')
do iz3=1,nz
  write(50,10) zp3(iz3),(psi3(iv3,iz3),iv3=1,mv)
end do
close(50)

end if

call MPI_BARRIER(comm,ierror)
c calculate Hamitonian

c kinetic energy for ion 1

do iz1=1,nz
  y1=z1(iz1)
  call othpl(4,mv,y1,h,dh)
  G=exp(-1*y1**2/2.d0)
  G1=-1*alpha1*y1*exp(-1*y1**2/2.d0)
  G2=alpha1**2*exp(-1*y1**2/2.d0)*(y1**2-1)
  iv1=0
  ps11(iv1+1,iz1)=dsqrt(alpha1/dsqrt(pi))*G2
end do

```

```

do iv1=1,mv-1
  n=iv1
  call nvj(n,b)
  n1=dsqrt(alpha1/dsqrt(pi)/(2**n)/b)
  H1=alpha1*dh(iv1+1)
  H2=2*iv1*dh(iv1)*alpha1**2
  psi11(iv1+1,iz1)=n1*(G2*h(iv1+1)+2*G1*H1+G*H2)
end do
do iv1=0,mv-1
  psilp(iv1+1,iz1)=psi11(iv1+1,iz1)/G
end do
end do

do iv1=1,mv
  do iz1=1,nz
    psilr(iv1,iz1)=-psi11(iv1,iz1)/2.d0/mass1
    psils(iv1,iz1)=-psilp(iv1,iz1)/2.d0/mass1
  end do
end do

c kinetic energy for ion 2

do iz2=1,nz
  y2=z2(iz2)
  call othpl(4,mv,y2,h,dh)
  G=exp(-1*y2**2/2.d0)
  G1=-1*alpha2*y2*exp(-1*y2**2/2.d0)
  G2=alpha2**2*exp(-1*y2**2/2.d0)*(y2**2-1)
  iv2=0
  psi22(iv2+1,iz2)=dsqrt(alpha2/dsqrt(pi))*G2
  do iv2=1,mv-1
    n=iv2
    call nvj(n,b)
    n2=dsqrt(alpha2/dsqrt(pi)/(2**n)/b)
    H1=alpha2*dh(iv2+1)
    H2=2*iv2*dh(iv2)*alpha2**2
    psi22(iv2+1,iz2)=n2*(G2*h(iv2+1)+2*G1*H1+G*H2)
  end do
  do iv2=0,mv-1
    psi2p(iv2+1,iz2)=psi22(iv2+1,iz2)/G
  end do
end do

do iv2=1,mv
  do iz2=1,nz
    psi2r(iv2,iz2)=-psi22(iv2,iz2)*ek(2)/ek(1)/2.d0/mass1
    psi2s(iv2,iz2)=-psi2p(iv2,iz2)*ek(2)/ek(1)/2.d0/mass1
  end do
end do
c kinetic energy for ion 3

do iz3=1,nz
  y3=z3(iz3)
  call othpl(4,mv,y3,h,dh)
  G=exp(-1*y3**2/2.d0)
  G1=-1*alpha3*y3*exp(-1*y3**2/2.d0)
  G2=alpha3**2*exp(-1*y3**2/2.d0)*(y3**2-1)
  iv3=0
  psi33(iv3+1,iz3)=dsqrt(alpha3/dsqrt(pi))*G2
  do iv3=1,mv-1
    n=iv3
    call nvj(n,b)
    n3=dsqrt(alpha3/dsqrt(pi)/(2**n)/b)
    H1=alpha3*dh(iv3+1)
    H2=2*iv3*dh(iv3)*alpha3**2
    psi33(iv3+1,iz3)=n3*(G2*h(iv3+1)+2*G1*H1+G*H2)
  end do
  do iv3=0,mv-1

```

```

psi3p(iv3+1,iz3)=psi33(iv3+1,iz3)/G
end do
end do

do iv3=1,mv
do iz3=1,nz
  psi3r(iv3,iz3)=-psi33(iv3,iz3)*ek(mz)/ek(1)/2.d0/mass1
  psi3s(iv3,iz3)=-psi3p(iv3,iz3)*ek(mz)/ek(1)/2.d0/mass1
end do
end do

c second derivative of first ion wavefunction
if(mype.eq.0) then

open(20,file='secwavr1.dat',status='unknown')
do iz1=1,nz
  write(20,30) zp1(iz1),(psilr(iv1,iz1),iv1=1,mv)
end do
close(20)

open(40,file='secwavr2.dat',status='unknown')
do iz2=1,nz
  write(40,30) zp2(iz2),(psi2r(iv2,iz2),iv2=1,mv)
end do
close(40)

open(60,file='secwavr3.dat',status='unknown')
do iz3=1,nz
  write(60,30) zp3(iz3),(psi3r(iv3,iz3),iv3=1,mv)
end do
close(60)

end if
call MPI_BARRIER(comm,ierror)

c basis set

do iz1=1,nz
do iz2=1,nz
do iz3=1,nz
  za1=am(1,1)*zp1(iz1)+am(1,2)*zp2(iz2)*dsqrt(ek(1)/
$ ek(2))+am(1,3)*zp3(iz3)*dsqrt(ek(1)/ek(mz))
  za2=am(2,1)*zp1(iz1)+am(2,2)*zp2(iz2)*dsqrt(ek(1)/
$ ek(2))+am(2,3)*zp3(iz3)*dsqrt(ek(1)/ek(mz))
  za3=am(3,1)*zp1(iz1)+am(3,2)*zp2(iz2)*dsqrt(ek(1)/
$ ek(2))+am(3,3)*zp3(iz3)*dsqrt(ek(1)/ek(mz))
  V(iz1,iz2,iz3)=
    $ alpha*0.5d0*dk1**2*(za1+cz(1))**2
    $ +beta*dk1**2*(za1+cz(1))**4
    $ +alpha*0.5d0*dk1**2*(za2+cz(2))**2
    $ +beta*dk1**2*(za2+cz(2))**4
    $ +alpha*0.5d0*dk1**2*(za3+cz(mz))**2
    $ +beta*dk1**2*(za3+cz(mz))**4
    $ +1/abs((za2-za1)+(cz(2)-cz(1)))
    $ +1/abs((za3-za1)+(cz(mz)-cz(1)))
    $ +1/abs((za3-za2)+(cz(mz)-cz(2)))
    $ -alpha*0.5d0*dk1**2*cz(1)**2
    $ -alpha*0.5d0*dk1**2*cz(2)**2
    $ -alpha*0.5d0*dk1**2*cz(mz)**2
    $ -beta*dk1**2*cz(1)**4
    $ -beta*dk1**2*cz(2)**4-beta*dk1**2*cz(mz)**4
    $ -1/abs(cz(2)-cz(1))
    $ -1/abs(cz(mz)-cz(1))-1/abs(cz(mz)-cz(2))
  end do
end do
end do

if(mype.eq.mv) then

```

```

do iv=1,mv
  do jv=1,mv
    do kv=1,mv
      do iv1=1,mv
        do jv1=1,mv
          do kv1=1,mv
            sum4=0.d0
            sum5=0.d0
            sum6=0.d0
            call delta(iv,iv1,delta1)
            call delta(jv,jv1,delta2)
            call delta(kv,kv1,delta3)
            do iz1=1,nz
              sum4=sum4+ps1(iv,iz1)*psi1s(iv1,iz1)*delta2*delta3
                $      *weight1(iz1)/alpha1
              end do
              do iz2=1,nz
                sum5=sum5+ps2(jv,iz2)*psi2s(jv1,iz2)*delta1*delta3
                  $      *weight2(iz2)/alpha2
              end do
              do iz3=1,nz
                sum6=sum6+ps3(kv,iz3)*psi3s(kv1,iz3)*delta1*delta2
                  $      *weight3(iz3)/alpha3
              end do
              KE((kv-1)*mv**2+(jv-1)*mv+iv, (kv1-1)*mv**2+(jv1-
              1)*mv+iv1)=sum4+sum5+sum6
              end do
              end do
              end do
            end do
          end do
        end do
      end do
    end do
  end do
else
  do iv=mype+1,mype+1
    do jv=1,mv
      call mysecond(tf)
      filetime='cputime_ '
      write(filetime(9:10),'(i2.2)') mype+1
      open(6,file=filetime,status='unknown')
      write(6,807) 'CPU Time= ',(tF-tS)/3600.0d0,' (hour)'
      do kv=1,mv
        do iv1=1,mv
          do jv1=1,mv
            do kv1=kv,mv
              sum1=0.d0
              sum2=0.d0
              sum3=0.d0
              do iz1=1,nz
                comm1=ps1(iv,iz1)
                commt1=ps1(iv1,iz1)
              do iz2=1,nz
                comm2=ps2(jv,iz2)
                commt2=ps2(jv1,iz2)
              do iz3=1,nz
                comm3=ps3(kv,iz3)
                commt3=ps3(kv1,iz3)
              sum3=sum3+comm1*comm2*comm3*V(iz1,iz2,iz3)*commt1*commt2*
                $      commt3*weight3(iz3)/alpha3*weight2(iz2)/alpha2
                $      *weight1(iz1)/alpha1
              end do
              end do
              end do
            PE1((kv-1)*mv**2+(jv-1)*mv+iv, (kv1-1)*mv**2+(jv1-
            1)*mv+iv1)=sum3
            end do
            end do
            end do

```



```

call othpl(4,mv,y1,h,dh)
do iv1=1,mv-1,1
  n=iv1
  call nvj(n,b)
  n1=dsqrt(alpha1/dsqrt(pi)/(2**n)/b)
  bsi1(iv1+1,is1)=n1*h(iv1+1)*dexp(-y1**2/2.d0)
  bsi1(iv1+1,is1)=n1*h(iv1+1)
end do
end do

cc Normalization of wavefunctions for ion 1.
do iv1=1,mv
  sum1=0.d0
  do is1=1,ns
    sum1=sum1+bs1(iv1,is1)**2*wt1(is1)/alpha1
  end do
  do is1=1,ns
    bsi1(iv1,is1)=bsi1(iv1,is1)/dsqrt(sum1)
  end do
end do

c Hamonic parameters for ion 2 (in a.u.)
w2=dsqrt(ek(2))
alpha2=dsqrt(mass1*w2*ek(1)/ek(2))
do is2=1,ns
  zfx2(is2)=zf2(is2)/alpha2
end do
c Hamonic wavefunctions for ion 2
do is2=1,ns
  y2=zf2(is2)
  iv2=0
  bsi2(iv2+1,is2)=dsqrt(alpha2)/(pi**0.25d0)*dexp(-
y2**2/2.d0)
  bs2(iv2+1,is2)=dsqrt(alpha2)/(pi**0.25d0)
  !!!!!!! call the subroutine which will give the value
of Hermite.
  call othpl(4,mv,y2,h,dh)
  do iv2=1,mv-1,1
    n=iv2
    call nvj(n,b)
    n2=dsqrt(alpha2/dsqrt(pi)/(2**n)/b)
    bsi2(iv2+1,is2)=n2*h(iv2+1)*dexp(-y2**2/2.d0)
    bs2(iv2+1,is2)=n2*h(iv2+1)
  end do
end do

cc Normalization of wavefunctions for ion 2.
do iv2=1,mv
  sum2=0.d0
  do is2=1,ns
    sum2=sum2+bs2(iv2,is2)**2*wt2(is2)/alpha2
  end do
  do iz2=1,nz
    bsi2(iv2,is2)=bsi2(iv2,is2)/dsqrt(sum2)
  end do
end do

c Hamonic parameters for ion 3 (in a.u.)
w3=dsqrt(ek(mz))
alpha3=dsqrt(mass1*w3*ek(1)/ek(mz))
do is3=1,ns
  zfx3(is3)=zf3(is3)/alpha3
end do
c Hamonic wavefunctions for ion 3
do is3=1,ns
  y3=zf3(is3)

```

```

iv3=0
bsi3(iv3+1,is3)=dsqrt(alpha3) / (pi**0.25d0) *dexp(-
y3**2/2.d0)
bs3(iv3+1,is3)=dsqrt(alpha3) / (pi**0.25d0)
!!!!!! call the subroutine which will give the value
of Hermite.
call othpl(4,mv,y3,h,dh)
do iv3=1,mv-1,1
n=iv3
call nvj(n,b)
n3=dsqrt(alpha3/dsqrt(pi)/(2**n)/b)
bsi3(iv3+1,is3)=n3*h(iv3+1)*dexp(-y3**2/2.d0)
bs3(iv3+1,is3)=n3*h(iv3+1)
end do
end do

cc Normalization of wavefunctions for ion 3.
do iv3=1,mv
sum3=0.d0
do is3=1,ns
sum3=sum3+bs3(iv3,is3)**2*wt3(is3)/alpha3
end do
do is3=1,ns
bsi3(iv3,is3)=bsi3(iv3,is3)/dsqrt(sum3)
end do
end do

c Test of wavefunction

open(10,file='bset1.dat',status='unknown')
do is1=1,ns
write(10,10) zfx1(is1),(bsi1(iv1,is1),iv1=1,mv)
end do
close(10)

open(30,file='bset2.dat',status='unknown')
do is2=1,ns
write(30,10) zfx2(is2),(bsi2(iv2,is2),iv2=1,mv)
end do
close(30)

open(50,file='bset3.dat',status='unknown')
do is3=1,ns
write(50,10) zfx3(is3),(bsi3(iv3,is3),iv3=1,mv)
end do
close(50)

call MPI_BARRIER(comm,ierror)

allocate(bsi_j(mv**3))
allocate(bs_j(mv**3))
allocate(wavef_j(ns,ns,ns))
allocate(wavefp_j(ns,ns,ns))

do j=1,lp

do is3=1,ns
do is2=1,ns
do is1=1,ns

c calculate bs(1:mv**3,iz1,iz2,iz3) for a fixed iz1, iz2,
iz3
do iv=1,mv
do jv=1,mv
do kv=1,mv
bsi_j((kv-1)*mv**2+(jv-1)*mv+iv)=bsi1(iv,is1)
$ *bsi2(jv,is2)*bsi3(kv,is3)
bs_j((kv-1)*mv**2+(jv-1)*mv+iv)=bs1(iv,is1)

```

```

      $ *bs2(jv,is2)*bs3(kv,is3)
    end do
  end do
end do
sum5=0.d0
sum6=0.d0
do i=1,mv**3
  sum5=sum5+Hamil(i,j)*bsi_j(i)
  sum6=sum6+Hamil(i,j)*bs_j(i)
end do
wavef_j(is1,is2,is3)=sum5
wavefp_j(is1,is2,is3)=sum6
wavefp(j,is1,is2,is3)=sum6
end do
end do
end do

end do

do i=1,lp
  if(wavefp(i,13,13,13).lt.0) then
    do is1=1,ns
      do is2=1,ns
        do is3=1,ns
          wavefp(i,is1,is2,is3)=-1.d0*wavefp(i,is1,is2,is3)
        end do
      end do
    end do
  end if
end do

c Transition dipol moments:
do is1=1,ns
  do is2=1,ns
    do is3=1,ns
      do i=1,lp
        do j=1,lp
          sum=0.d0
          do is1=1,ns
            do is2=1,ns
              do is3=1,ns
                sum=sum+wavefp(i,is1,is2,is3)*mu*tdm(is1,is2,is3)
                $ *wavefp(j,is1,is2,is3)
                $ *wt3(is3)/alpha3*wt2(is2)/alpha2*wt1(is1)/alpha1
              end do
            end do
            dipole(i,j)=sum
          end do
        end do
      end do
    end do
  end do
end do

open(160,file='transitiondipole.dat',status='unknown')
do i=1,lp
  write(160,60) (dipole(i,j),j=1,lp)
end do
close(160)

```

```

open(161,file='dipol.dat',status='unknown')
write(161,*) lm
do i=1,lm
  write(161,60) (dipole(i,j),j=1,lm)
end do
close(161)

deallocate(bsi_j)
deallocate(bs_j)
deallocate(wavef_j)
deallocate(wavefp_j)

end if
call MPI_BARRIER(comm,ierror)

10   format(e24.16,150(x,f24.16))
20   format(150(x,f24.16))
30   format(e24.16,150(x,f24.16))
40   format(150(x,e24.16))
50   format(1000(x,e21.13))
60   format(400(x,e24.16))
70   format(200(x,i4))
807  format(a20,f7.2,2x,a8)

call MPI_BARRIER(comm,ierror)
call MPI_FINALIZE(ierror)

End
c-----
subroutine delta(ii,ji,deltav)
integer ii,ji
real*8 deltav
deltav=0.d0

if(ii.eq.ji) then
  deltav=1.d0
end if

end
c-----
subroutine nvj(m,A)
real*8 i,m,A

if(m.eq.0) then
  A=1.0
else
  A=1.0
  do i=1,m
    A=A*i
  end do
end if

end
c-----
SUBROUTINE OTHPL(KF,N,X,PL,DPL)
C
C      =====
C      Purpose: Compute orthogonal polynomials: Tn(x) or
C      Un(x),
C                  or Ln(x) or Hn(x), and their derivatives
C      Input : KF --- Function code
C                  KF=1 for Chebyshev polynomial Tn(x)
C                  KF=2 for Chebyshev polynomial Un(x)
C                  KF=3 for Laguerre polynomial Ln(x)
C                  KF=4 for Hermite polynomial Hn(x)
C      n --- Order of orthogonal polynomials
C      x --- Argument of orthogonal polynomials
C      Output: PL(n) --- Tn(x) or Un(x) or Ln(x) or Hn(x)

```

```

C           DPL(n)--- Tn'(x) or Un'(x) or Ln'(x) or
Hn'(x)
C =====
C
IMPLICIT DOUBLE PRECISION (A-H,O-Z)
DIMENSION PL(0:N),DPL(0:N)
A=2.0D0
B=0.0D0
C=1.0D0
Y0=1.0D0
Y1=2.0D0*X
DY0=0.0D0
DY1=2.0D0
PL(0)=1.0D0
PL(1)=2.D0*X
DPL(0)=0.0D0
DPL(1)=2.0D0
IF (KF.EQ.1) THEN
  Y1=X
  DY1=1.0D0
  PL(1)=X
  DPL(1)=1.0D0
ELSE IF (KF.EQ.3) THEN
  Y1=1.D0-X
  DY1=-1.0D0
  PL(1)=1.0D0-X
  DPL(1)=-1.0D0
END IF
DO 10 K=2,N
  IF (KF.EQ.3) THEN
    A=-1.0D0/K
    B=2.0D0+A
    C=1.0D0+A
  ELSE IF (KF.EQ.4) THEN
    C=2.0D0*(K-1.0D0)
  END IF
  YN=(A*X+B)*Y1-C*Y0
  DYN=A*Y1+(A*X+B)*DY1-C*DY0
  PL(K)=YN
  DPL(K)=DYN
  Y0=Y1
  Y1=YN
  DY0=DY1
10          DY1=DYN
RETURN
END
C=====
subroutine mysecond(time)

real*8 time

time=MPI_WTIME()
return
end
C=====

Subroutine gauher(x,w,n)
Integer n,MAXIT
Real*8 x(n),w(n)
Double precision EPS,PIM4
Parameter (EPS=3.d-14,PIM4=.7511255444649425d0,MAXIT=10)
Integer i,its,j,m
Double precision p1,p2,p3,pp,z,z1
m=(n+1)/2
do i=1,m
  if(i.eq.1) then

```

```
z=sqrt(float(2*n+1))-1.85575d0*(2*n+1)**(-.16667d0)
else if(i.eq.2)then
  z=z-1.14d0*n**.426d0/z
else if(i.eq.3)then
  z=1.86d0*z-.86d0*x(1)
else if(i.eq.4)then
  z=1.91d0*z-.91d0*x(2)
else
  z=2.d0*z-x(i-2)
end if

do its=1,MAXIT
  p1=PIM4
  p2=0.d0
  do j=1,n
    p3=p2
    p2=p1
    p1=z*dsqrt(2.d0/j)*p2-dsqrt(dble(j-1)/dble(j))*p3
  end do
  pp=dsqrt(2.d0*n)*p2
  z1=z
  z=z1-p1/pp
  if(abs(z-z1).le.EPS) goto 1
end do
1      x(i)=z
x(n+1-i)=-z
w(i)=2.d0/(pp*pp)
w(n+1-i)=w(i)
end do
return
end
```